UNIVERSITY OF CALIFORNIA,
IRVINE

Precise Navigation with Cellular Signals: Receiver Design, Differential and Non-Differential Frameworks, and Performance Analysis

DISSERTATION

submitted in partial satisfaction of the requirements
for the degree of

DOCTOR OF PHILOSOPHY

in Electrical Engineering and Computer Science

by

Joe Khalife

Dissertation Committee:
Professor Zaher (Zak) M. Kassas, Chair
Professor A. Lee Swindlehurst
Professor Tryphon T. Georgiou

2020

DEDICATION

To my parents Joseph and Jeanette, my brother Paul, my sister Maria, and Ceren. You are with me every second.

TABLE OF CONTENTS

LIST OF FIGURES

Page

LIST OF TABLES

LIST OF ALGORITHMS

ACKNOWLEDGMENTS

I would like to thank my advisor Prof. Zak Kassas for his guidance and support during my doctoral studies. I am grateful for his time and all the work he put to acquire funding to support me and my colleagues and to build the ASPIN Lab. I would also like to thank Prof. Kassas for giving me the opportunity to attend and present at many conferences in the field and for providing all necessary equipment and material needed for my research. Building the Lab with Prof. Kassas and my colleagues was a very challenging journey and sometimes pushed me to my limits. However, it was in times like these that I found the greatest rewards.

I would like to thank Prof. Samer Saab who believed in me and inspired me to pursue doctoral studies. I am forever grateful for all the time I spent working with Prof. Saab and for everything I learned from him, academically and personally. I will always cherish the times we spent together talking about research, music, philosophy, and life.

I would like to thank my Ph.D. committee members Prof. Lee Swindlehurst and Prof. Tryphon Georgiou for taking time to serve in the committee and for all their helpful advice throughout my Qualifying exam and Ph.D. Defense.

I would like to thank the National Center for Sustainable Transportation (NCST), the Office of Naval Research (ONR), and the National Science Foundation (NSF) for supporting my research.

I would like to thank Institute of Electrical and Electronics Engineers (IEEE) and Institute of Navigation (ION) for giving me the chance to present my work to the rest of the community by publishing my conference and journal papers.

I would like to thank my friends and colleagues: Joshua, Kimia, Ali, and Mahdi for their support throughout the Ph.D. journey and for all the helpful discussions and help with experiments.

I would like to thank my parents Joseph and Jeanette, my brother Paul, and my sister Maria for being the best family anyone can ask for. I cannot express how much I love them and how much I miss them. They are my absolute support and the reason I came so far. I hope they are proud of me.

Finally, I would like to thank the love of my life, Ceren. She was there for me and supported me during the hard times. She made a lot of sacrifices so I can get through this tough journey. I am forever grateful to her and I hope I can make her as happy as she deserves. Seni çok seviyorum.

VITA

Joe Khalife

EDUCATION

Doctor of Philosophy in Electrical Engineering **2020**
University of California, Irvine *Irvine, California*

Master of Science in Computer Engineering **2014**
Lebanese American University *Byblos, Lebanon*

Bachelor of Engineering in Electrical Engineering **2011**
Lebanese American University *Byblos, Lebanon*

RESEARCH EXPERIENCE

Graduate Research Assistant **2019–2020**
University of California, Irvine *Irvine, California*

Graduate Research Assistant **2015–2019**
University of California, Riverside *Riverside, California*

Graduate Research Assistant **2011–2014**
Lebanese American University *Byblos, Lebanon*

TEACHING EXPERIENCE

Teaching Assistant **2019–2020**
University of California, Irvine *Irvine, California*

Teaching Assistant **2015–2019**
University of California, Riverside *Riverside, California*

Teaching Assistant **2011–2014**
Lebanese American University *Byblos, Lebanon*

REFEREED JOURNAL PUBLICATIONS

[J7] **J. Khalife**, C. Sevinç, and Z. Kassas (2020) "Performance evaluation of TOA Positioning in asynchronous 4G and 5G networks: A stochastic geometry approach," *IEEE Wireless Communication Letters*, in preparation.

[J6] **J. Khalife** and Z. Kassas (2019) "Opportunistic UAV navigation with carrier phase measurements from asynchronous cellular signals," *IEEE Transactions on Aerospace and Electronic Systems*, accepted.

[J5] **J. Khalife** and Z. Kassas (2019) "Optimal sensor placement for dilution of precision minimization via quadratically constrained fractional programming," *IEEE Transactions on Aerospace and Electronic Systems*, Vol. 55, Issue 4, pp. 2086–2096.

[J4] M. Maaref, **J. Khalife**, and Z. Kassas (2019) "Lane-level localization and mapping in GNSS-challenged environments by fusing lidar data and cellular pseudoranges," *IEEE Transactions on Intelligent Vehicles*, Vol. 4, Issue 1, pp. 73-89.

[J3] **J. Khalife**, K. Shamaei, and Z. Kassas (2018) "Navigation with cellular CDMA signals – part I: signal modeling and software-defined receiver design," *IEEE Transactions on Signal Processing*, Vol. 66, Issue 8, Apr. 2018, pp. 2204–2218.

[J2] **J. Khalife** and Z. Kassas (2018) "Navigation with cellular CDMA signals – part II: performance analysis and experimental results," *IEEE Transactions on Signal Processing*, Vol. 66, Issue 8, Apr. 2018, pp. 2191–2203.

[J1] K. Shamaei, **J. Khalife**, and Z. Kassas (2018) "Exploiting LTE signals for navigation: theory to implementation," *IEEE Transactions on Wireless Communications*, Vol. 17, Issue 4, Apr. 2018, pp. 2173–2189.

CONFERENCE PUBLICATIONS

[C25]**J. Khalife**, M. Neinavaie, and Z. Kassas (2020) " Navigation with Differential Carrier Phase Measurements from Megaconstellation LEO Satellites," *in Proceedings of IEEE/ION Position, Location, and Navigation Symposium*, Apr. 20–23, 2020, Portland, OR, accepted.

[C24]**J. Khalife** and Z. Kassas (2019) "Assessment of differential carrier phase measurements from Orbcomm LEO satellite signals for opportunistic navigation," *in Proceedings of ION GNSS Conference*, Sep. 16–20, 2019, Miami, FL, pp. 4053–4063.

[C23] J. Morales, **J. Khalife**, U. Santa Cruz, and Z. Kassas (2018) "Orbit modeling for simultaneous tracking and navigation using LEO satellite signals," *in Proceedings of ION GNSS Conference*, Sep. 16–20, Miami, FL, pp. 2090–2099.

[C22] **J. Khalife** and Z. Kassas (2019) "Receiver design for Doppler positioning with LEO satellites," *in Proceedings of IEEE ICASSP*, May 12–17, Brighton, UK, pp. 5506–5510.

[C21] **J. Khalife**, and Z. Kassas (2019) "Simultaneous tracking of Orbcomm LEO satellites and inertial navigation system aiding using Doppler measurements," *in Proceedings of IEEE Vehicular Technology Conference*, Apr. 28–May 1, Kuala Lumpur, Malaysia, pp. 1–6.

[C20] M. Maaref, **J. Khalife**, and Z. Kassas (2019) "Pseudorange measurement outlier detection for navigation with cellular signals," *in Proceedings of ACM/IEEE International Conference on Cyber-Physical Systems*, Apr. 16–18, Montreal, Canada, pp. 346–347.

[C19] C. Ardito, J. Morales, **J. Khalife**, A. Abdallah, and Z. Kassas (2019) "Performance evaluation of navigation using LEO satellite signals with periodically transmitted satellite positions," *in Proceedings of ION International Technical Meeting (ITM)*, Jan. 28 – 31, Reston, VA, pp. 306–318.

[C18] **J. Khalife**, S. Bhattacharya, and Z. Kassas (2018) "Centimeter-accurate UAV navigation with cellular signals," *in Proceedings of ION GNSS Conference*, Sep. 24–28, Miami, FL, pp.2321–2331.

[C17] M. Maaref, **J. Khalife**, and Z. Kassas (2018) "Integrity monitoring of signal of opportunity-based navigation for autonomous ground vehicles," [C01] *in Proceedings of ION GNSS Conference*, Sep. 24–28, 2018, Miami, FL, pp. 2456–2466.

[C16] J. Morales, **J. Khalife**, A. Abdallah, C. Ardito, and Z. Kassas (2018) "Inertial navigation system aiding with Orbcomm LEO satellite Doppler measurements," *in Proceedings of ION GNSS Conference*, Sep. 24–28, 2018, Miami, FL, pp. 2718–2725.

[C15] **J. Khalife** and Z. Kassas (2018) "Precise UAV navigation with cellular carrier phase measurements," *in Proceedings of IEEE/ION Position, Location, and Navigation Symposium*, Apr. 23–26, 2018, Monterey, CA, pp. 978–989.

[C14] K. Shamaei, **J. Khalife**, and Z. Kassas (2018) "A joint TOA and DOA approach for positioning with LTE signals," *in Proceedings of IEEE/ION Position, Location, and Navigation Symposium*, Apr. 23–26, Monterey, CA, pp. 81–91.

[C13] K. Shamaei, **J. Khalife**, and Z. Kassas (2018) "Pseudorange and multipath analysis of positioning with LTE secondary synchronization signals," *in Proceedings of IEEE Wireless Communications and Networking Conference*, Apr. 15-18 Barcelona, Spain, pp. 286–291 (special session).

[C12] K. Shamaei, **J. Khalife**, S. Bhattacharya, and Z. Kassas (2017) "Computationally efficient receiver design for mitigating multipath for positioning with LTE signals," *in Proceedings of ION GNSS Conference*, Sep. 25–29, Portland, OR, pp. 3751–3760.

[C11] **J. Khalife** and Z. Kassas (2017) "Evaluation of relative clock stability in cellular networks," *in Proceedings of ION GNSS Conference*, Sep. 25–29, Portland, OR, pp. 2554–2559.

[C10] K. Shamaei, **J. Khalife**, and Z. Kassas (2017) "Ranging precision analysis of LTE signals," *in Proceedings of European Signal Processing Conference*, Aug. 28–Sep. 2, Kos Island, Greece, pp. 2788–2792 (special session).

[C09] **J. Khalife**, S. Ragothaman, and Z. Kassas (2017) "Pose estimation with lidar odometry and cellular pseudoranges," *in Proceedings of IEEE Intelligent Vehicles Symposium*, Jun. 11–14, Redondo Beach, CA, pp. 1722–1727.

[C08] **J. Khalife** and Z. Kassas (2017) "Modeling and analysis of sector clock bias mismatch for navigation with cellular signals," *in Proceedings of American Control Conference*, May 24–26, Seattle, WA, pp. 3573–3578.

[C07] J. Morales, **J. Khalife**, and Z. Kassas (2017) "Collaborative autonomous vehicles with signals of opportunity aided inertial navigation systems," *in Proceedings of ION International Technical Meeting (ITM)*, Jan. 30 – Feb. 2, Monterey, CA, pp. 805–818.

[C06] K. Shamaei, **J. Khalife**, and Z. Kassas (2017) "Comparative results for positioning with secondary synchronization signal versus cell specific reference signal in LTE systems," *in Proceedings of ION ITM*, Jan. 30 – Feb. 2, Monterey, CA, pp. 1256–1268.

[C05] K. Shamaei, **J. Khalife**, and Z. Kassas (2016) "Performance characterization of positioning in LTE systems," *in Proceedings of ION GNSS*, Sep. 12–16, Portland, OR, pp. 2262–2270.

[C04] **J. Khalife** and Z. Kassas (2016) "Characterization of sector clock biases in cellular CDMA systems," *in Proceedings of ION GNSS Conference*, Sep. 12–16, Portland, OR, pp. 2281–2285.

[C03] **J. Khalife**, K. Shamaei, and Z. Kassas (2016) "A software-defined receiver architecture for cellular CDMA-based navigation," *in Proceedings of IEEE/ION Position, Location, and Navigation Symposium*, Apr. 11–14, Savannah, GA, pp. 816–826.

[C02] J. Morales, **J. Khalife**, and Z. Kassas (2016) "GNSS vertical dilution of precision reduction using terrestrial signals of opportunity," *in Proceedings of ION ITM*, Jan. 25–28, Monterey, CA, pp. 664–669.

[C01] **J. Khalife**, Z. Kassas, and S. Saab (2016) "Indoor localization based on floor plans and power maps: non-line of sight to virtual line of sight," *in Proceedings of ION GNSS Conference*, Sep. 14–18, 2015, Tampa, FL, pp. 2291–2300.

SOFTWARE

LabVIEW, MATLAB, C++; LaTeX; MS: Word, Excel.

PATENTS

Z. Kassas, J. Morales, and **J. Khalife** (2019) "Receiver design for Doppler positioning with low Earth orbit satellites," U.S. Patent Application No. 62/834,317.

Z. Kassas, J. Morales, and **J. Khalife** (2019) "Low Earth orbit satellite signal aided inertial navigation system," U.S. Patent Application No. 62/834,313.

Z. Kassas, M. Maaref, and **J. Khalife** (2019) "Lane-level navigation system for ground vehicles with lidar and cellular signals," U.S. Patent Application No. 62/663,209.

Z. Kassas, K. Shamaei, and **J. Khalife** (2017) "A real-time, multipath-mitigating receiver design for navigation with LTE signals," U.S. Patent Application No. 62/561,023.

Z. Kassas, K. Shamaei, and **J. Khalife** (2016) "Software-defined radio for navigation with LTE signals," U.S. Patent Application No. 62/398,403.

Z. Kassas, **J. Khalife**, and K. Shamaei (2016) "Software-defined radio for navigation with cellular CDMA signals," U.S. Patent Application No. 62/294,758.

AWARDS

Best Presentation Award, "Assessment of differential carrier phase measurements from Orbcomm LEO satellite signals for opportunistic navigation," *ION GNSS Conference*, Miami, FL, 2019.

Best Presentation Award, "Centimeter-accurate UAV navigation with cellular signals," *ION GNSS Conference*, Miami, FL, 2018.

Best Presentation Award, "Tightly-coupled inertial navigation system using LEO satellite signals," *ION GNSS Conference*, Miami, FL, 2018.

IEEE Walter Fried Award for Best Paper, "Precise UAV navigation with cellular carrier phase measurements," *IEEE/ION Position, Location, and Navigation Symposium*, Monterey, CA, 2018.

Best presentation award, "Computationally efficient receiver design for mitigating multipath for positioning with LTE signals," *ION GNSS Conference*, 2017.

National Center for Sustainable Transportation (NCST) 2016 Outstanding Graduate Student of the Year at the University of California at Riverside.

Best Student Paper Award, "A software-defined receiver architecture for cellular CDMA-based navigation," *IEEE/ION Position, Location, and Navigation Symposium*, Savannah, GA, 2016.

Best Presentation Award, "Performance characterization of positioning in LTE systems," *ION GNSS Conference*, Portland, OR, 2016.

Best research poster finalist, "Navigation with cellular CDMA signals," *Southern California Robotics (SCR) Symposium*, San Diego, CA, 2016.

NCST Fellowship Award, UCR, 2015.

Dean's Distinguished Fellowship Award, UCR, 2015.

Distinguished List, LAU, Byblos, Lebanon, 2006–2011.

ABSTRACT OF THE DISSERTATION

Precise Navigation with Cellular Signals: Receiver Design, Differential and Non-Differential Frameworks, and Performance Analysis

By

Joe Khalife

Doctor of Philosophy in Electrical Engineering and Computer Science

University of California, Irvine, 2020

Professor Zaher (Zak) M. Kassas, Chair

Autonomous vehicles (AVs) will demand a resilient, accurate, and tamper-proof navigation system. Current AV navigation systems will not meet these demands as they are dependent on global navigation satellite system (GNSS) signals, which are jammable, spoofable, and may not be usable in certain environments (e.g., indoors and deep urban canyons). Dead-reckoning sensors (e.g., inertial measurements units, lidars, or cameras) are typically used to aid GNSS signals in challenged environment. However, such sensors accumulate errors with time and can only provide a navigation solution in a local frame, i.e., relative to the AV's initial position. Alternatively, signals of opportunity (SOPs) (e.g., AM/FM radio, low Earth orbit satellite signals, Wi-Fi, and cellular) may be used as a global navigation source in GNSS-challenged environment.

Cellular signals, particularly code-division multiple access (CDMA), long-term evolution (LTE), and fifth generation (5G) new radio (NR) signals, are among the most promising SOP candidates for navigation. These signals are (i) abundant, (ii) received at a much higher power and bandwidth than GNSS signals, (iii) offer a favorable horizontal geometry, (iv) are diverse in the radio frequency spectrum, (v) and are free to use. These inherent attributes make them attractive navigation sources for AVs in GNSS-challenged environments.

However, since SOPs are not intended for navigation, there are several challenges associated with using cellular signals and SOPs in general for navigation: (1) the unavailability of appropriate low-level signal and error models for optimal extraction of states and parameters of interest for positioning and timing purposes, (2) the absence of published receiver architectures capable of producing navigation observables, (3) the unknown fundamental performance bounds, (4) and the lack of frameworks for high accuracy navigation with such signals. This dissertation addresses the aforementioned challenges for cellular SOPs, focusing on CDMA systems, with extensions to LTE and 5G. The foundational contributions of this dissertation are demonstrated on ground vehicles and unmanned aerial vehicles (UAVs), showing meter-level accurate navigation for the former and sub-meter-level accurate navigation for the latter.

Chapter 1

Introduction

1.1 Background

Global navigation satellite systems (GNSSs) have been the prevalent positioning, navigation, and timing technology over the past few decades. However, GNSS signals suffer from four main limitations:

1. They are extremely weak and unusable in certain environments (e.g., indoors and deep urban canyons) [3].
2. They are susceptible to unintentional interference and intentional jamming [4, 5].
3. Civilian signals are unencrypted, unauthenticated, and specified in publicly available documents, making them spoofable (i.e., hackable) [5].
4. Their position estimate suffers from a large vertical estimation uncertainty due to the lack of GNSS space vehicle angle diversity, which is particularly problematic for aerial vehicles [6].

As such, standalone GNSSs will not deliver the stringent demands of future systems such as autonomous vehicles (Avs), intelligent transportation systems, and location-based services. Traditional approaches to aid GNSS in challenging environments mainly rely on dead-reckoning sensors (e.g., inertial measurements units, lidars, or cameras). However, such sensors accumulate errors with time and can only provide a navigation solution in a local frame, i.e., relative to the AV's initial position. Alternatively, signals of opportunity (SOPs) may be used as a global navigation source in GNSS-challenged environment. Signals of opportunity are ambient signals not intended for positioning, navigation, and timing, such as cellular, AM/FM radio, satellite communication, digital television, and Wi-Fi. Cellular signals, particularly code-division multiple access (CDMA), long-term evolution (LTE), and fifth generation (5G) new radio (NR) signals, are among the most promising SOP candidates for navigation due to their following qualities

- Abundance: cellular base transceiver stations (BTSs) are plentiful due to the ubiquity of cellular and smartphones.
- Geometric diversity: the cell configuration by construction yields favorable BTS geometry—unlike certain terrestrial transmitters, which tend to be colocated, e.g., digital television.
- High carrier frequency: cellular carrier frequency ranges 800–2,500 MHz and in millimeter-wave (mmW) bands, which yields precise carrier phase navigation observables.
- Large bandwidth: cellular signals have a bandwidth up to 100 MHz for LTE Advanced and will go to as high as to 1 GHz for mmW 5G signals, which yields accurate time-of-arrival (TOA) estimates.
- High received power: cellular signals are often available and usable in GNSS-challenged environments—the received carrier-to-noise ratio C/N_0 from nearby cellular BTSs is more than 20 dB higher than GPS satellites.

Besides the aforementioned advantages, there is no deployment cost associated with using cellular signals for positioning and navigation—the signals are practically free to use. Specifically, the receiver, also referred to as the user equipment (UE), could eavesdrop on the transmitted cellular signals without communicating with the BTS, extract necessary positioning and timing information from received signals, and calculate the navigation solution locally. While other navigation approaches requiring two-way communication between the UE and BTS (i.e., network based) exist, this dissertation focuses on explaining how precise UE-based navigation can be achieved with cellular signals, focusing on CDMA systems, with extensions to LTE and 5G. The foundational contributions of this dissertation are demonstrated on ground vehicles and unmanned aerial vehicles (UAVs), showing meter-level accurate navigation for the former and sub-meter-level accurate navigation for the latter.

1.2 Related Work

Traditional approaches to enable navigation in GNSS-challenged environments [7, 8, 9] have focused on coupling GNSS receivers with inertial navigation systems and advanced signal processing algorithms [3, 10, 11, 12]. Recently, ambient radio frequency (RF) SOPs have been considered as a stand-alone alternative to GNSS or to complement GNSS-based navigation [13, 14, 15, 16].

Different studies have been conducted for specific types of SOPs including AM/FM radio [17, 18], iridium satellites [19, 20], digital television (DTV) [21, 22], cellular [23, 24, 25, 26], and Wi-Fi [27, 28, 29]. It has been demonstrated that AM signals could potentially provide 20 meter positioning accuracy [17]. A better localization performance could be achieved using DTV signals, where the average positioning error becomes less than 4 meters in certain favorable environments [21]. Experimental results for navigation using cellular CDMA fused with DTV signals showed a navigation solution within 2 meters from that of a GPS solution

and a maximum difference of 12 meters [25]. SOPs have also been used for indoor positioning, where it has been shown that an average positioning error of 4 meters could be achieved by coupling Wi-Fi and inertial measurement units (IMUs) in a SLAM framework [27]. Coupling observables from other signals such as GSM, digital audio broadcasting, and cellular 3G with IMU measurements also showed promising results [14]. Moreover, iridium satellite signals were considered to improve navigation performance in deep urban and indoor environments [30]. SOPs were also employed in timing applications, such as enabling longer integration time for GPS-assisted femtocells in indoor environments [31]. Besides these experimental studies, the literature on SOPs partially answers theoretical questions on the observability and estimability of the SOP signal landscape [32, 33], motion planning in the SOP landscape for optimal information gathering [34, 35, 36], and collaborative SOP landscape map building [1, 37].

Sources of error and the so-called error budget for GNSS-based navigation have been thoroughly studied [6, 38]. In contrast, navigation sources of error for SOPs are not yet fully characterized. It is important to note that while some of these errors are not harmful for communication purposes, they severely degrade the navigation performance if they are not modeled and accounted for appropriately. Moreover, the states of a cellular BTSs are unknown to a navigating receiver and need to be estimated. Although the some cellular standards (e.g., the cdma200 standard) state that a BTS should transmit its position, local wireless providers do not usually transmit such information [39, 40]. Hence, the positions of the BTSs need to be manually surveyed or estimated on-the-fly individually or collaboratively [1, 41]. The literature on navigation using cellular signals considers TOA, time difference of arrival (TDOA), and frequency of arrival (FOA) measurements [42, 43]; however, certain assumptions such as perfect synchronization or negligible variations between the transmitter and receiver clocks are made to eliminate the clock biases of the BTS and the receiver from the measurement model [23, 44, 45, 46, 47]. However, cellular CDMA and LTE networks are not perfectly synchronized, and their protocols recommend synchronization of

CDMA BTSs and LTE eNodeBs to within 3 microseconds from GPS time [48, 49]. This translates to ranging errors of about 900 meters. Several approaches in the literature have been proposed to account for the BTSs' or eNodeBs' clock biases and drifts, including using the round-trip time (RTT) instead of the TOA [50]. Although RTT-based methods could yield good results in asynchronous systems, two-way communication between the receiver and the BTSs or eNodeBs is needed. This limits the availability of RTT measurements to only paying subscribers to a particular cellular provider and compromises the privacy of the user. Some of the proposed navigation frameworks assume the BTSs' or eNodeBs' clock bias and drift to be constant [25, 51]. However, the clock bias and drift are dynamic and stochastic [52]; hence, must be continuously estimated either (i) via a reference receiver, which shares such estimates with the navigating receiver or (ii) by the navigating receiver itself by adopting a simultaneous localization and mapping approach [16, 36, 53]. In either case, the navigating receiver must have appropriate models for (i) the measurement it is drawing from the BTS, (ii) relevant BTS states' dynamics, and (iii) all relevant sources of errors.

Besides TOA measurements, one can exploit carrier phase measurements from cellular SOPs, which may yield a precise navigation solution. This technique is well known in GNSS and sub-meter-level (centimeter to decimeter) is common in carrier phase differential GNSS (CDGNSS), also known as real-time kinematic (RTK) [6, 54]. To use this technique with cellular systems, referred to as carrier phase differential cellular (CD-cellular), the deployment of base receivers is needed, which could pose a practical limitation. However, considering the need for a resilient and accurate position, navigation, and timing (PNT) alternative to GNSS in future AVs, especially unmanned aerial vehicle (UAV) applications (e.g., package delivery, environmental monitoring, search and rescue, etc.), installing a dedicated CD-cellular network is lucrative. Recent advances in software-defined radios (SDRs) and embedded computing pave the road to making such networks for precise UAV navigation a reality. SDRs are attractive because of their inherent advantages: (i) flexibility: designs are hardware in-

dependent, (ii) modularity: different functions can be implemented independently, and (iii) upgradability: minimal changes are needed to improve designs. Although most SDRs used to be limited to post-processing applications, processor-specific optimization techniques allow for real-time operation [55].

Since SOP-based navigation is a relatively new paradigm, the literature on performance characterization under system errors is scarce for navigation using SOPs. While the performance of cellular systems such as CDMA has been well studied from a communication systems perspective [56, 57, 58], the identification of sources of errors that affect the navigation performance of such systems remains a topic of research. In addition to having appropriate models for such errors, the optimal BTS–receiver geometrical configuration must be identified in order to characterize bounds on the estimation performance. Such configurations have been extensively studied; however; the literature does not provide a lower bound on the estimation error covariance for localization with TOA measurements with non-identical noise variances [59, 60].

The BTS–receiver geometrical configuration is strongly linked to the dilution of precision (DOP) and position error bound (PEB). These metrics are of extreme importance in sensor placement with applications in source localization, tracking, and navigation [61, 62, 63]. In source localization and target tracking applications, one is interested in optimally placing the receiver, which makes observations to an unknown source (e.g., emitter) or target, minimizing the estimation error uncertainty about the state of the receiver or target [64, 65, 66]. In navigation applications, one is interested in optimally placing the receiver, which makes observations to known sources (e.g., global navigation satellite system (GNSS) satellites or SOPs), minimizing the estimator error uncertainty about the receiver's state [35, 36, 67]. To this end, one aims at (i) minimizing the geometric DOP (GDOP) or more generally the weighted GDOP (WGDOP), which is equivalent to minimizing the trace of the estimation error covariance matrix [59, 68, 69, 70, 71, 72] and (ii) maximizing the determinant of the

GDOP or WGDOP matrix, which is equivalent to maximizing the determinant of the Fisher information matrix [62, 73]. However, all the aforementioned optimization problems are nonconvex, necessitating the use of numerical general-purpose optimization solvers, which tend to be computationally intensive and could converge to a local optimum.

Instead of directly optimizing a functional of the WGDOP matrix, alternative approximating metrics were proposed, such as maximizing the area of the polygon whose vertices are the endpoints of the unit line-of-sight (LOS) vectors from the source to the receiver [74]. In [75], it was shown that this criterion was piecewise concave for the problem of placing an additional sensor to a set of pre-deployed sensors localizing a *single* source using pseudorange measurements, and a closed-form expression for the optimal two-dimensional (2-D) position of the additional sensor was derived. The problem was generalized to the case of localizing *multiple* sources and it was shown that optimizing the product of areas yielded a set of parallelizable convex programs [1]. Direct minimization of the WGDOP or maximization of the WGDOP matrix in three-dimensional (3-D) space remains unsolved.

The aforementioned literature focuses on deterministic realization of the BTS–receiver or eNodeB–receiver geometry. Let the generic term base station (BS) denote noth 3G BTSs, 4G eNodeBs, and 5G next generation NodeBs (gNBs). Instead of deterministic network modeling techniques, stochastic geometry has been adapted extensively to model the location of BSs over the last decade for several reasons [76, 77]: (i) modeling BS locations with point processes captures the randomness of BS deployment and (ii) stochastic geometry approach brings analytically tractable results. These perks of stochastic geometry sparked studies to characterize the localization performance in wireless networks [78, 79]. In [80], a cellular network model with a homogeneous Poisson point process (PPP) was used to derive bounds for TOA-based positioning, while the effect of signal-to-noise ratio (SNR) heterogeneity in TOA-based localization was studied in [81] by using a binomial point process (BPP) model. Such analyses shed some light on the expected localization performance in 5G networks;

however, they make the *impractical* assumption that the UE and BTSs are synchronized.

1.3 Challenges

There are four main challenges associated with using cellular signals and SOPs in general for navigation:

- The unavailability of appropriate low-level signal and error models for optimal extraction of states and parameters of interest for positioning and timing purposes.
- The absence of published receiver architectures capable of producing navigation observables.
- The unknown fundamental performance bounds.
- The lack of frameworks for precise navigation with such signals.

To the author's knowledge, while previous work demonstrated experimental results for navigation via cellular signals, none of these four challenges has been fully addressed.

It is important to stress again that there are some error sources that are not harmful in communication systems but severely degrade the navigation performance. Such errors must be identified and modeled for precise navigation with cellular signals. Moreover, navigation frameworks must be designed around the identified error sources in order to minimize their effect.

While differential frameworks are known to yield precise navigation, the literature on such frameworks focuses on GNSSs, which are fundamentally different than cellular systems in the fact that, in contrast to GNSS satellites, the states of the cellular BTSs (position and clock

errors) may not be known. Subsequently, appropriate differential frameworks for navigation with cellular SOPs must be designed and their performance must be analyzed.

Besides differential frameworks, the literature on precise non-differential frameworks with cellular SOPs is missing. The main challenge in such problems is the dynamic and stochastic nature of the unknown BTS clock errors. To resolve this challenging problem, novel models for navigation observables that leverage certain levels of synchronization between BTSs must be established. In the case of fully asynchronous networks, robust non-differential frameworks must be designed to guarantee reliable long-term navigation with cellular SOPs.

Additionally, the performance of these novel differential and non-differential frameworks must be analyzed for two main purposes: (i) to establish fundamental performance bounds and (ii) establish relationships between these bounds and system parameters for optimal navigation framework design.

Independently of the navigation framework, the BTS–receiver geometry, measured by the GDOP or some related metric, greatly affects the navigation performance. One remaining challenge in navigation, target tracking, or source localization is the optimal placement of navigation sources or sensors as to minimize the GDOP. Specifically, the exact solution of where to place an additional receiver given a set of pre-deployed receivers remains unanswered.

Finally, with the rise of 4G and 5G networks, the literature on radionavigation began to analyze the expected localization performance in such networks using methods from stochastic geometry. However, the analyzes pertain to network-based localization, where impractical assumptions on network synchronization are made. Subsequently, the performance characterization of navigation with realistic 4G and 5G signals remains missing.

1.4 Contributions and Dissertation Outline

The dissertation is organized by contributions, which are as follows:

Chapter 2: Cellular CDMA Signal Modeling and Software Receiver Design for Navigation

This chapter presents an SDR for navigation with cellular CDMA signals. The CDMA signal structure is described and precise, low-level signal models for optimal extraction of relevant navigation and timing information from received cellular CDMA signals compatible with the latest cdma2000 standard are developed. The pseudorange from the proposed receiver is modeled and the pseudorange error is studied in an additive white Gaussian channel. Experimental results validating the proposed SDR by comparing the variation in the resulting pseudoranges and the true ranges to two BTSs are presented. Moreover, this chapter identifies an elaborate model for timing errors between BTS sectors which affect the navigation performance. The derived model is validated experimentally in different locations, at different times, and for different cellular providers.

Chapter 3: Differential Framework Design for Precise Navigation with Pseudorange Measurements from Cellular SOPs

This chapter proposes a differential framework for navigation using pseudorange measurements from cellular SOPs, which employs reference and navigating receivers. The navigation performance under this framework in the presence of sources of errors identified in the previous contribution is analyzed. Lower bounds on the navigation performance of the differential framework for static and batch estimators are derived. Moreover, a practical upper bound on the position error due to the sector clock bias discrepancy is derived. In addition, a more generic lower bound on the logarithm of the determinant of the estimation error covariance is derived for the case of uncorrelated measurement noise with non-identical variances and an optimal BTS–receiver geometrical configuration that achieves the lower bound is identified.

The results of this contributions are validated experimentally on a ground vehicle and on UAVs with meter-level accuracy.

Chapter 4: Differential Framework Design for Precise Navigation with Carrier Phase Measurements from Cellular SOPs

This chapter proposes a differential framework for navigation using CD-cellular measurements and a method for resolving carrier phase ambiguities is discussed. A batch weighted nonlinear least-squares estimator is developed to solve for the integer ambiguities and an EKF is formulated to initialize the batch estimator. The proposed framework is evaluated through Monte Carlo (MC) simulations. Important design considerations of a practical CD-cellular navigation network and their effect on the navigation performance are studied, namely: 1) the number of bases needed to cover a given cellular SOP environment and the base placement that maximizes availability, 2) communication requirements and synchronization of CD-cellular measurements shared between the bases and navigating UAVs, and 3) hardware and software consideration for real-time implementation. Experimental results are presented demonstrating a UAV navigating exclusively with CD-cellular measurements with sub-meter-level accuracy.

Chapter 5: Non-Differential Framework Design for Precise Navigation with Carrier Phase Measurements from Quasi-Synchronous Cellular SOPs

This chapter proposes a non-differential framework for navigation using carrier phase measurements from cellular SOPs transmitted by quasi-synchronous BTSs. This relative stability of quasi-synchronous BTSs is manifested as a common term driving the BTS clocks. When this common term is present, the BTSs are said to be quasi-synchronous. Cellular carrier phase measurements are modeled at a fine granularity level and parameterized by deviations from the common clock error. The deviation term is demonstrated to evolve as a stable stochastic process, which is characterized via system identification. Moreover, experimental results over long periods of time validating the identified models are presented. The paper

also discusses how to estimate the statistics of this process on-the-fly when the receiver has access to GNSS signals. A theoretical lower bound for the logarithm of the determinant of the position estimation error covariance is derived and an upper bound on the position error is provided. The results of this contribution are validated by two sets of experiments showing UAVs navigating with sub-meter-level accuracy.

Chapter 6: Non-Differential Framework Design for Precise Navigation with Carrier Phase Measurements from Asynchronous Cellular SOPs

This chapter presents an extended Kalman filter (EKF)-based non-differential framework for navigation with carrier phase measurements from cellular SOPs transmitted by asynchronous BTSs. The EKF initialization is discussed and a complete EKF estimation error and estimation error covariance analysis is conducted, performed by studying the observability of the system under consideration as well as the EKF's stochastic stability. The theoretical results produced herein can be generalized to a broader class of problems: EKF-based navigation using SOP carrier phase and pseudorange measurements. MC simulations are conducted to demonstrate the theoretical predictions about the system and study the effect of different system parameters on the estimation performance. The results of this contribution are validated by two sets of experiments showing UAVs navigating with meter-level accuracy.

Chapter 7: Optimal Receiver Placement for Dilution of Precision Minimization

This chapter presents an approach to find the global optimal solution of the DOP minimization problem. It is shown that the DOP problem can be formulated as a quadratically constrained fractional quadratic program. An algorithm for solving this program is presented and MC simulation results are given demonstrating convergence of the proposed approach to the global optimal solution. Also, the superiority of the proposed approach is demonstrated against nonlinear numerical optimization solvers and other approaches that approximate the DOP minimization problem.

Chapter 8: Performance Evaluation of TOA Positioning in Asynchronous 4G

and 5G Networks: A Stochastic Geometry Approach

This chapter analyzes the positioning of a UE in asynchronous 4g and 5G networks. Unlike existing approaches, this dissertation accounts for both UE and BS clock biases. Three different cases of prior knowledge of the UE clock bias statistics are considered. The squared-position error bound (SPEB) for each case is derived and analytical relationships between the SPEB of the three studied cases are established. The cumulative density function (cdf) of the SPEB for each case is analyzed numerically using stochastic geometry models.

Chapter 9: Conclusions

This chapter summarizes the contributions of this dissertation.

The intellectual products from this dissertation are published in the following journal and conference articles.

Journal Publications

[J1] J. Khalife, K. Shamaei, and Z. Kassas (2018) "Navigation with cellular CDMA signals – part I: signal modeling and software-defined receiver design," *IEEE Transactions on Signal Processing*, Vol. 66, Issue 8, Apr. 2018, pp. 2204–2218.

[J2] J. Khalife and Z. Kassas (2018) "Navigation with cellular CDMA signals – part II: performance analysis and experimental results," *IEEE Transactions on Signal Processing*, Vol. 66, Issue 8, Apr. 2018, pp. 2191–2203.

[J3] J. Khalife and Z. Kassas (2019) "Optimal sensor placement for dilution of precision minimization via quadratically constrained fractional programming," *IEEE Transactions on Aerospace and Electronic Systems*, Vol. 55, Issue 4, pp. 2086–2096.

[J4] J. Khalife and Z. Kassas (2019) "Opportunistic UAV navigation with carrier phase measurements from asynchronous cellular signals," *IEEE Transactions on Aerospace and*

Electronic Systems, accepted.

[J5] J. Khalife, C. Sevinç, and Z. Kassas (2020) "Performance evaluation of TOA Positioning in asynchronous 4G and 5G networks: A stochastic geometry approach," *IEEE Wireless Communication Letters*, in preparation.

Conference Publications

[C1] J. Khalife, K. Shamaei, and Z. Kassas (2016) "A software-defined receiver architecture for cellular CDMA-based navigation," *in Proceedings of IEEE/ION Position, Location, and Navigation Symposium*, Apr. 11–14, Savannah, GA, pp. 816–826.

[C2] J. Khalife and Z. Kassas (2016) "Characterization of sector clock biases in cellular CDMA systems," *in Proceedings of ION GNSS Conference*, Sep. 12–16, Portland, OR, pp. 2281–2285.

[C3] J. Khalife and Z. Kassas (2017) "Modeling and analysis of sector clock bias mismatch for navigation with cellular signals," *in Proceedings of American Control Conference*, May 24–26, Seattle, WA, pp. 3573–3578.

[C4] J. Khalife and Z. Kassas (2017) "Evaluation of relative clock stability in cellular networks," *in Proceedings of ION GNSS Conference*, Sep. 25–29, Portland, OR, pp. 2554–2559.

[C5] J. Khalife and Z. Kassas (2018) "Precise UAV navigation with cellular carrier phase measurements," *in Proceedings of IEEE/ION Position, Location, and Navigation Symposium*, Apr. 23–26, 2018, Monterey, CA, pp. 978–989.

[C6] J. Khalife, S. Bhattacharya, and Z. Kassas (2018) "Centimeter-accurate UAV navigation with cellular signals," *in Proceedings of ION GNSS Conference*, Sep. 24–28, Miami, FL, pp.2321–2331.

Chapter 2

Cellular CDMA SOP Model and Receiver Design

This chapter is organized as follows. Section 2.1 provides an overview of the cellular CDMA forward link pilot signal structure. Section 2.2 presents a complete implementation of the acquisition and tracking stages of a navigation cellular CDMA SDR. Section 2.3 analyzes the statistics of the pseudorange error of the CDMA SDR in an additive white Gaussian channel. Section 2.4 models the discrepancy between the clock biases of different sectors of the same BTS. Section 2.5 validates the proposed navigation SDR and analyzes the consistency of the obtained clock bias discrepancy model experimentally. The notation used in this chapter is confined to this chapter and the following chapter, Chapter 3.

The results of this chapter have been published in [82, 83, 84, 85].

2.1 Cellular CDMA SOP Model

In a cellular CDMA communication system, several logical channels are multiplexed on the forward link channel, including: a pilot channel, a sync channel, and 7 paging channels [2]. The following subsection presents an overview of the modulation process of the forward link pilot channel and provides models of the transmitted and received signals from which timing and positioning information can be extracted.

2.1.1 Modulation of Forward Link CDMA Pilot Signals

The data transmitted on the forward link channel in cellular CDMA systems (i.e., BTS to mobile receiver) is modulated through quadrature phase shift keying (QPSK) and then spread using direct-sequence CDMA (DS-CDMA). The in-phase and quadrature components, I and Q, respectively, of the pilot channel carry the same message $m(t)$. The spreading sequences c_I and c_Q, called the short code, are 2^{15}-chip long pseudorandom noise (PN) codes that are generated using linear feedback shift registers (LFSRs). In order to distinguish the received data from different BTSs, each station uses a shifted version of the PN codes. This shift, known as the PN offset, is unique for each BTS and is an integer multiple of 64 chips, hence a total of 512 PN offsets can be realized. It can be shown that the cross-correlation of the same PN sequence with different pilot offsets is negligible [86, 87]. The transmitted pilot signal is nothing but the short code; however, other channels, such as the sync and paging channels, carry data and are furthermore spread by Walsh codes. The CDMA signal is subsequently filtered using a digital pulse shaping filter that limits the bandwidth of the transmitted CDMA signal according to the cdma2000 standard. The signal is finally modulated by the carrier frequency ω_c to produce $s(t)$.

2.1.2 Transmitted Signal Model

The transmitted pilot signal $s(t)$ by a particular BTS can be expressed as

$$\begin{aligned} s(t) &= \sqrt{C}\left\{c'_I[t-\Delta(t)]\cos(\omega_c t) - c'_Q[t-\Delta(t)]\sin(\omega_c t)\right\} \\ &= \frac{\sqrt{C}}{2}\left\{c'_I[t-\Delta(t)] + jc'_Q[t-\Delta(t)]\right\}\cdot e^{j\omega_c t} \\ &\quad + \frac{\sqrt{C}}{2}\left\{c'_I[t-\Delta(t)] - jc'_Q[t-\Delta(t)]\right\}\cdot e^{-j\omega_c t}, \end{aligned}$$

where C is the total power of the transmitted signal; $c'_I(t) = c_I(t) * h(t)$ and $c'_Q(t) = c_Q(t) * h(t)$; h is the continuous-time impulse response of the pulse shaping filter; c_I and c_Q are the in-phase and quadrature PN sequences, respectively; $\omega_c = 2\pi f_c$ with f_c being the carrier frequency; and Δ is the absolute clock bias of the BTS from GPS time. The total clock bias Δ is defined as

$$\Delta(t) = 64 \cdot (PN_{\text{offset}}\, T_c) + \delta t_s(t),$$

where PN_{offset} is the PN offset of the BTS, $T_c = \frac{1\times10^{-6}}{1.2288}$ s is the chip interval, and δt_s is the BTS clock bias. Since the chip interval is known and the PN offset can be decoded by the receiver, only δt_s needs to be estimated. While the clock bias of the BTS can be neglected for communication purposes, it cannot be ignored for navigation purposes and must be estimated in some fashion. Chapter 3 presents a framework for estimating this clock bias that is based on reference and navigating receivers.

2.1.3 Received Signal Model After Front-End Processing

Assuming the transmitted signal to have propagated through an additive white Gaussian noise channel with a power spectral density of $\frac{N_0}{2}$, a model of the received discrete-time (DT) signal $r[m]$ after RF front-end processing: downmixing, a quadrature approach to bandpass sampling [88], and quantization can be expressed as

$$r[m] = \frac{\sqrt{C}}{2}\left\{c'_I[t_m - t_s(t_m)] - jc'_Q[t_m - t_s(t_m)]\right\} \cdot e^{j\theta(t_m)} + n[m], \tag{2.1}$$

where $t_s(t_m) \triangleq \delta t_{TOF} + \Delta(t_k - \delta t_{TOF})$ is the PN code phase of the BTS, $t_m = mT_s$ is the sample time expressed in receiver time, T_s is the sampling period, δt_{TOF} is the time-of-flight (TOF) from the BTS to the receiver, θ is the beat carrier phase of the received signal, and $n[m] = n_I[m] + jn_Q[m]$ with n_I and n_Q being independent, identically-distributed (i.i.d.) Gaussian random sequences with zero-mean and variance $\frac{N_0}{2T_s}$. The receiver developed in Section 2.2 will operate on the samples of $r[m]$ in (2.1).

2.2 Cellular CDMA Navigation Receiver Architecture

The cellular CDMA navigation receiver consists of three main stages: signal acquisition, tracking, and decoding. The proposed receiver will utilize the pilot signal to detect the presence of a CDMA signal and then track it, as will be discussed in this section. The next subsection gives a brief description of the correlation process in the cellular CDMA navigation receiver. The following subsections present a software implementation in LabVIEW of the acquisition and tracking stages. Details on decoding the sync and paging channel messages are provided in [82, 89, 90].

2.2.1 Cellular CDMA Receiver Correlator

Given samples of the baseband signal exiting the RF front-end defined in (2.1), the cellular CDMA receiver first wipes off the residual carrier phase and match-filters the resulting signal. The output of the matched-filter can be expressed as

$$x[m] = \left[r[m] \cdot e^{-j\hat{\theta}(t_m)} \right] * h[-m], \tag{2.2}$$

where $\hat{\theta}$ is the beat carrier phase estimate and h is a pulse shaping filter, which is a DT version of the one used to shape the spectrum of the transmitted signal, with a finite-impulse response (FIR) given in Table 2.1. The samples m' of the FIR in Table 2.1 are spaced by $\frac{T_c}{4}$.

Table 2.1: FIR of the Pulse-Shaping Filter used in cdma2000 [2]

m'	$h[m']$	m'	$h[m']$	m'	$h[m']$
0, 47	-0.02528832	8, 39	0.03707116	16, 31	-0.01283966
1, 46	-0.03416793	9, 38	-0.02199807	17, 30	-0.14347703
2, 45	-0.03575232	10, 37	-0.06071628	18, 29	-0.21182909
3, 44	-0.01673370	11, 36	-0.05117866	19, 28	-0.14051313
4, 43	0.02160251	12, 35	0.00787453	20, 27	0.09460192
5, 42	0.06493849	13, 34	0.08436873	21, 26	0.44138714
6, 41	0.09100214	14, 33	0.12686931	22, 25	0.78587564
7, 40	0.08189497	15, 32	0.09452834	23, 24	1.0

Next, $x[m]$ is correlated with a local replica of the spreading PN sequence. In a digital receiver, the correlation operation is expressed as

$$Z_k = \frac{1}{N_s} \sum_{m=k}^{k+N_s-1} x[k] \left\{ c_I[t_m - \hat{t}_s(t_m)] + j c_Q[t_m - \hat{t}_s(t_m)] \right\}, \tag{2.3}$$

where Z_k is the kth subaccumulation, N_s is the number of samples per subaccumulation, and $\hat{t}_s(t_m)$ is the code start time estimate over the kth subaccumulation. The code phase can be

assumed to be approximately constant over a short subaccumulation interval $T_{\text{sub}} = N_s T_s$; hence, $\hat{t}_s(t_m) \approx \hat{t}_{s_k}$. It is worth mentioning that theoretically, T_{sub} can be made arbitrarily large since no data is transmitted on the pilot channel. Practically, T_{sub} is mainly limited by the stability of the BTS and receiver oscillators. In this chapter, T_{sub} is set to one PN code period. The carrier phase estimate is modeled as $\hat{\theta}(t_m) = 2\pi \hat{f}_{D_k} t_m + \theta_0$, where $\hat{f}_{D_k}$ is the apparent Doppler frequency estimate over the ith subaccumulation, and θ_0 is the initial beat carrier phase of the received signal. As in a GPS receiver, the value of θ_0 is set to zero in the acquisition stage and is subsequently maintained in the tracking stage. The apparent Doppler frequency is assumed to be constant over a short T_{sub}. Substituting for $r[m]$ and $x[m]$, defined in (2.1) and (2.2), into (2.3), it can be shown that

$$Z_k = \sqrt{C}\, R_c(\Delta t_k) \left[\frac{1}{N_s} \sum_{m=k}^{k+N_s-1} e^{j\Delta\theta(t_m)} \right] + n_k, \tag{2.4}$$

where R_c is the autocorrelation function of the PN sequences c'_I and c'_Q, $\Delta t_k \triangleq \hat{t}_{s_k} - t_{s_k}$ is the code phase error, $\Delta\theta(t_m) \triangleq \theta(t_m) - \hat{\theta}(t_m)$ is the carrier phase error, and $n_k \triangleq n_{I_k} + j n_{Q_k}$ with n_{I_k} and n_{Q_k} being i.i.d. Gaussian random sequences with zero-mean and variance $\frac{N_0}{2T_s N_s} = \frac{N_0}{2T_{\text{sub}}}$.

2.2.2 Acquisition

The objective of this stage is to determine which BTSs are in the receiver's proximity and to obtain a coarse estimate of their corresponding code start times and Doppler frequencies. A search over the code start time and Doppler frequency is performed to detect the presence of a signal. Based on experimental data, the Doppler frequency search window is chosen to be between -500 and 500 Hz at a carrier frequency in the 800/850 MHz cellular band, with a frequency spacing Δf_D between 8 and 12 Hz if T_{sub} is only one PN code period.

The code start time search window is naturally chosen to be one PN code interval with a delay spacing of one sample. The proposed receiver performs a parallel code phase search by exploiting the optimized efficiency of the fast Fourier transform (FFT) [91]. A hypothesis test on $|Z_k|^2$ could be performed to decide whether the peak corresponds to a transmitted signal or to noise. Since there is only one PN sequence, the search needs to be performed once. Fig. 2.3(a) illustrates the front panel of the acquisition stage of the LabVIEW cellular CDMA SDR showing $|Z_k|^2$ along with $\hat{t}_{s_k}$, $\hat{f}_{D_k}$, PN offset, and carrier-to-noise ratio C/N_0 for a particular BTS.

2.2.3 Tracking

After obtaining an initial coarse estimate of the code start time and Doppler frequency, the receiver refines and maintains these estimates via tracking loops. In the proposed design, a phase-locked loop (PLL) is employed to track the carrier phase and a carrier-aided delay-locked loop (DLL) is used to track the code phase. The PLL and DLL are discussed next.

PLL

The PLL consists of a phase discriminator, a loop filter, and a numerically-controlled oscillator (NCO). Since the receiver is tracking the data-less pilot channel, an `atan2` discriminator, which remains linear over the full input error range of $\pm\pi$, could be used without the risk of introducing phase ambiguities. It was found that the receiver could easily track the carrier phase with a second-order PLL with a loop filter transfer function given by

$$F_{\mathrm{PLL}}(s) = \frac{2\zeta\omega_n s + \omega_n^2}{s}, \tag{2.5}$$

where $\zeta \equiv \frac{1}{\sqrt{2}}$ is the damping ratio and ω_n is the undamped natural frequency, which can be related to the PLL's noise-equivalent bandwidth $B_{n,\mathrm{PLL}}$ by $B_{n,\mathrm{PLL}} = \frac{\omega_n}{8\zeta}(4\zeta^2 + 1)$ [6]. The output of the loop filter v_{PLL} is the rate of change of the carrier phase error, expressed in rad/s. The Doppler frequency is deduced by dividing v_{PLL} by 2π. The loop filter transfer function in (2.5) is discretized at a sampling period T_{sub} and realized in state-space. The noise-equivalent bandwidth is chosen to range between 4 and 8 Hz.

DLL

The carrier-aided DLL employs the non-coherent dot product discriminator. In order to compute the code phase error, the dot product discriminator uses the prompt, early, and late correlations, denoted by Z_{p_k}, Z_{e_k}, and Z_{l_k}, respectively. The prompt correlation was described in Subsection 2.2.1. The early and late correlations are calculated by correlating the received signal with an early and a delayed version of the prompt PN sequence, respectively. The time shift between Z_{e_k} and Z_{l_k} is defined by an early-minus-late time t_{eml}, expressed in chips. Since the autocorrelation function of the transmitted cellular CDMA pulses is not triangular as in the case of GPS, a wider t_{eml} is preferable in order to have a significant difference between Z_{p_k}, Z_{e_k}, and Z_{l_k}. Fig. 2.1 shows the autocorrelation function of the cellular CDMA PN code as specified by the cdma2000 standard and that of the C/A code in GPS. It can be seen from Fig. 2.1 that for $t_{\mathrm{eml}} \leq 0.5$ chips, $R_c(\tau)$ in the cdma2000 standard has approximately a constant value, which is not desirable for precise tracking. In this chapter, a t_{eml} of 1 to 1.2 chips is chosen.

The DLL loop filter is a simple gain K, with a noise-equivalent bandwidth $B_{n,\mathrm{DLL}} = \frac{K}{4} \equiv 0.5$ Hz. The output of the DLL loop filter v_{DLL} is the rate of change of the code phase, expressed in s/s. Assuming low-side mixing, the code start time is updated according to

$$\hat{t}_{s_{k+1}} = \hat{t}_{s_k} - (v_{\mathrm{DLL},k} + \hat{f}_{D_k}/f_c) \cdot N_s T_s.$$

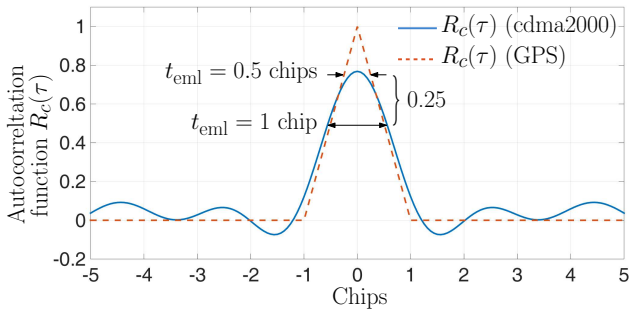

Figure 2.1: Autocorrelation function of GPS C/A code and cellular CDMA PN sequence according to the cdma2000 standard.

The pseudorange estimate ρ can therefore be deduced by multiplying the code start time by the speed-of-light c, i.e.,

$$\rho(k) = c \cdot \hat{t}_{s_k}. \tag{2.6}$$

Fig. 2.2 depicts a diagram of the tracking loops.

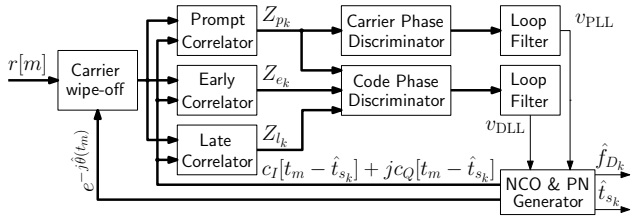

Figure 2.2: Tracking loops in the navigation cellular CDMA receiver. Thick lines represent complex quantities.

Fig. 2.3(b)–(e) shows the intermediate signals produced within the tracking loops of the LabVIEW cellular CDMA navigation receiver: phase error, code error, Doppler frequency, and pseudorange.

In the next section, the tracking performance of the DLL is studied and the closed-loop statistics of the code start time estimate are derived.

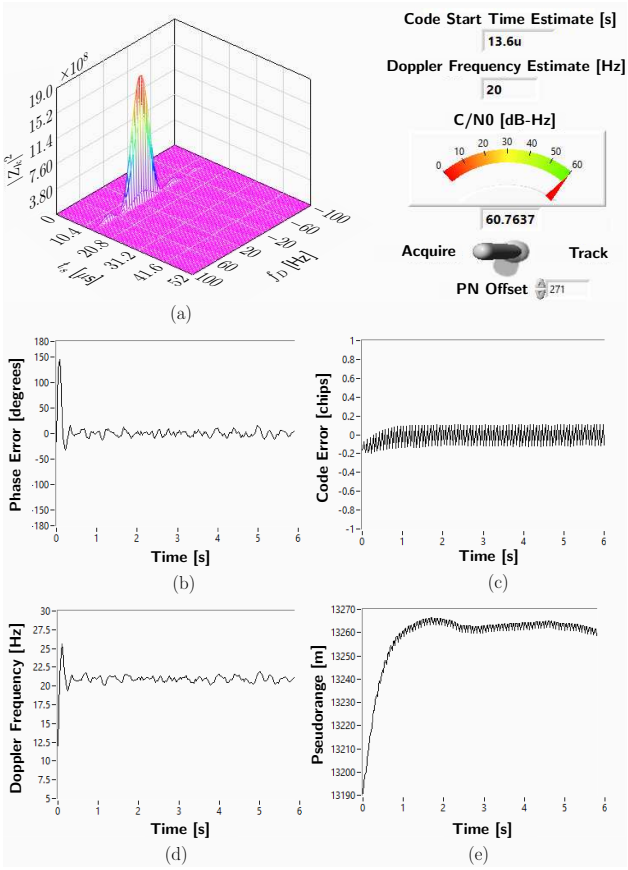

Figure 2.3: (a) Cellular CDMA signal acquisition front panel showing $|Z_k|^2$ along with $\hat{t}_{s_k}$, $\hat{f}_{D_k}$, PN offset, and C/N_0 for a particular BTS. (b)–(e) Cellular CDMA signal tracking: (b) Carrier phase error (degrees), (c) code phase error (chips), (d) Doppler frequency estimate (Hz), and (e) measured pseudorange (m).

2.3 Pseudorange Error Analysis in an Additive White Gaussian Noise Channel

Section 2.2 presented a recipe for designing a receiver that can extract a pseudorange estimate from cellular CDMA signals. This section analyzes the statistics of the error of the pseudorange estimate for a coherent DLL. It is worth noting that when the receiver is closely tracking the carrier phase, the dot-product discriminator and a coherent DLL discriminator will perform similarly. Hence, the analysis is carried for a coherent discriminator. Moreover, this subsection studies the statistics of the pseudorange error in a coherent baseband discriminator. To this end, it is assumed that t_s is constant. Therefore, the carrier aiding

term will be negligible and the code start time error Δt_k will be affected only by the channel noise. As mentioned in Subsection 2.2.3, it is enough to use a first-order loop for the DLL yielding the following closed-loop time-update error equation [92]

$$\Delta t_{k+1} = (1 - 4B_{n,\mathrm{DLL}}T_{\mathrm{sub}})\Delta t_k + KD_k, \tag{2.7}$$

where D_k is the output of the code discriminator. The discriminator statistics are discussed next.

2.3.1 Discriminator Statistics

In order to study the discriminator statistics, the received signal noise statistics must first be determined. In what follows, the received signal noise is characterized for an additive white Gaussian channel.

Received Signal Noise Statistics

In order to make the analysis more tractable, the continuous-time (CT) received signal and correlation are considered. The transmitted signal is assumed to propagate in an additive white Gaussian noise channel with a power spectral density $\frac{N_0}{2}$. The CT received signal after downmixing and bandpass sampling is given by

$$r(t) = \frac{\sqrt{C}}{2}\left[c'_I(t - t_s) - jc'_Q(t - t_s)\right] e^{j\theta(t)} + n(t),$$

and the CT matched-filtered baseband signal $x(t)$ is given by

$$x(t) = \left[r(t) \cdot e^{-j\hat{\theta}(t)}\right] * h(-t).$$

The resulting early and late correlations in the DLL are given by

$$\begin{aligned} Z_{e_k} &= \int_0^{T_{\text{sub}}} x(t)\left[c_I(t-\tau_{e_k}) + jc_Q(t-\tau_{e_k})\right] dt, \\ Z_{l_k} &= \int_0^{T_{\text{sub}}} x(t)\left[c_I(t-\tau_{l_k}) + jc_Q(t-\tau_{l_k})\right] dt, \end{aligned}$$

where $\tau_{e_k} \triangleq \hat{t}_{s_k} - \frac{t_{\text{eml}}}{2}T_c$ and $\tau_{l_k} \triangleq \hat{t}_{s_k} + \frac{t_{\text{eml}}}{2}T_c$. Assuming the receiver is closely tracking the carrier phase [6], the early and late correlations may be approximated with

$$\begin{aligned} Z_{e_k} &\approx T_{\text{sub}}\sqrt{C}R_c(\Delta t_k - \frac{t_{\text{eml}}}{2}T_c) + n_{e_k} \triangleq S_{e_k} + n_{e_k}, \\ Z_{l_k} &\approx T_{\text{sub}}\sqrt{C}R_c(\Delta t_k + \frac{t_{\text{eml}}}{2}T_c) + n_{l_k} \triangleq S_{l_k} + n_{l_k}, \end{aligned}$$

where n_{e_k} and n_{l_k} are zero-mean Gaussian random variables with the following variances and covariances

$$\begin{aligned} \text{var}\{n_{e_k}^2\} &= \text{var}\{n_{l_k}^2\} = \frac{T_{\text{sub}}N_0}{2} \quad \forall k, \\ \mathbb{E}\{n_{e_k}n_{l_k}\} &= \frac{T_{\text{sub}}N_0R_c(t_{\text{eml}}T_c)}{2}, \quad \forall k, \\ \mathbb{E}\{n_{e_k}n_{e_j}\} &= \mathbb{E}\{n_{l_k}n_{l_j}\} = \mathbb{E}\{n_{e_k}n_{l_j}\} = 0, \quad \forall k \neq j. \end{aligned}$$

Coherent Discriminator Statistics

The coherent baseband discriminator function is defined as

$$D_k \triangleq \frac{Z_{e_k} - Z_{l_k}}{\sqrt{C}} = \frac{(S_{e_k} - S_{l_k})}{\sqrt{C}} + \frac{(n_{e_k} - n_{l_k})}{\sqrt{C}}.$$

The normalized signal component of the discriminator function $\frac{(S_{e_k}-S_{l_k})}{T_{\text{sub}}\sqrt{C}}$ is shown in Fig. 2.4 for $t_{\text{eml}} = \{0.25, 0.5, 1, 1.5, 2\}$.

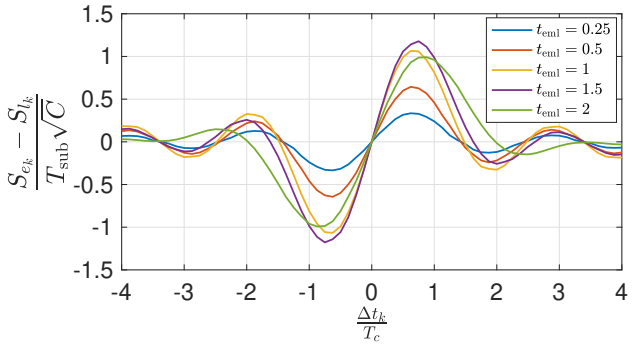

Figure 2.4: Output of the coherent baseband discriminator function for the CDMA shortcode with different correlator spacings.

It can be seen from Fig. 2.4 that for small values of $\frac{\Delta t_k}{T_c}$, the discriminator function can be approximated by a linear function given by

$$D_k \approx \alpha \Delta t_k + \frac{(n_{e_k} - n_{l_k})}{\sqrt{C}},$$

where α is the slope of the the discriminator function at $\Delta t_k = 0$ [92], which is obtained by

$$\alpha = \left.\frac{\partial D_k}{\partial \Delta t_k}\right|_{\Delta t_k = 0} = T_{\text{sub}} \left[\frac{d}{d\tau} R_c(\tau) - \frac{d}{d\tau} R_c(\tau)\right]\Bigg|_{\tau = \frac{t_{\text{eml}}}{2} T_c}.$$

Since $R_c(\tau)$ is symmetric,

$$\left.\frac{d}{d\tau} R_c(\tau)\right|_{\tau = -\frac{t_{\text{eml}}}{2} T_c} = \left.\frac{d}{d\tau} R_c(\tau)\right|_{\tau = \frac{t_{\text{eml}}}{2} T_c} \triangleq R_c'\left(\frac{t_{\text{eml}}}{2} T_c\right),$$

and the linearized discriminator output becomes

$$D_k \approx 2 T_{\text{sub}} R_c'\left(\frac{t_{\text{eml}}}{2} T_c\right) \Delta t_k + \frac{(n_{e_k} - n_{l_k})}{\sqrt{C}}. \tag{2.8}$$

It is worth noting that $R_c(\tau)$ and $R_c'(\tau)$ are obtained by numerically computing the autocor-

relation function of the pulse-shaped short code. Since the FIR of the pulse-shaping filter $h[k]$ is defined over only 48 values of k, the autocorrelation function $R_c(\tau)$ will be defined over 95 values of τ. However, interpolation may be used to evaluate $R_c(\tau)$ and $R_c'(\tau)$ at any τ. The mean and variance of D_k can be obtained from (2.8), and are given by

$$\mathbb{E}\{D_k\} = 2T_{\text{sub}}R_c'\left(\frac{t_{\text{eml}}}{2}T_c\right)\Delta t_k, \tag{2.9}$$

$$\begin{aligned}\text{var}\{D_k\} &= \frac{1}{C}\text{var}\{n_{e_k} - n_{l_k}\} \\ &= \frac{1}{C}\left[\text{var}\{n_{e_k}\} + \text{var}\{n_{l_k}\} - 2\mathbb{E}\{n_{e_k}n_{l_k}\}\right] \\ &= \frac{T_{\text{sub}}N_0}{C}\left[1 - R_c(t_{\text{eml}}T_c)\right].\end{aligned} \tag{2.10}$$

Now that the discriminator statistics are known, the closed-loop pseudorange error is characterized.

2.3.2 Closed-Loop Analysis

In order to achieve the desired loop noise-equivalent bandwidth, K in (2.7) must be normalized according to

$$K = \left.\frac{4B_{n,\text{DLL}}T_{\text{sub}}\Delta t_k}{\mathbb{E}\{D_k\}}\right|_{\Delta t_k=0} = \frac{2B_{n,\text{DLL}}}{R_c'\left(\frac{t_{\text{eml}}}{2}T_c\right)}. \tag{2.11}$$

In cellular CDMA systems, for a t_{eml} of 1.2, the loop filter gain becomes $K \approx 4B_{n,\text{DLL}}$, hence the choice of K in Subsection 2.2.3. Assuming a zero-mean tracking error, i.e., $\mathbb{E}\{\Delta t_k\} = 0$,

then the variance of the code start time error is given by

$$\begin{aligned} \mathrm{var}\{\Delta t_{k+1}\} &= (1 - 4B_{n,\mathrm{DLL}}T_{\mathrm{sub}})^2 \mathrm{var}\{\Delta t_k\} \\ &\quad + K^2 \mathrm{var}\{D_k\}. \end{aligned} \tag{2.12}$$

At steady-state, $\mathrm{var}\{\Delta\tau_{k+1}\}$ becomes

$$\mathrm{var}\{\Delta\tau_{k+1}\} = \mathrm{var}\{\Delta\tau_k\} = \mathrm{var}\{\Delta\tau\}, \tag{2.13}$$

where Δt is the steady-state code start time error. Combining (2.11)–(2.13) yields

$$\mathrm{var}\{\Delta t\} = \frac{B_{n,\mathrm{DLL}}\, q(t_{\mathrm{eml}})}{2(1 - 2B_{n,\mathrm{DLL}}T_{\mathrm{sub}})C/N_0}, \tag{2.14}$$

where

$$q(t_{\mathrm{eml}}) \triangleq \frac{1 - R_c(t_{\mathrm{eml}}T_c)}{\left[R_c'(\frac{t_{\mathrm{eml}}}{2}T_c)\right]^2}.$$

The pseudorange can hence be expressed as

$$\rho(k) = c \cdot t_{s_k} + c \cdot \Delta t_k \triangleq c \cdot t_{s_k} + v(k),$$

where $v(k)$ is a zero-mean random variable with variance $\sigma^2 = c^2 \cdot \mathrm{var}\,\{\Delta t\}$. Fig. 2.5 shows a plot of σ as a function of the carrier-to-noise ratio $\frac{C}{N_0}$ for $t_{\mathrm{eml}} = 1.25$ chips.

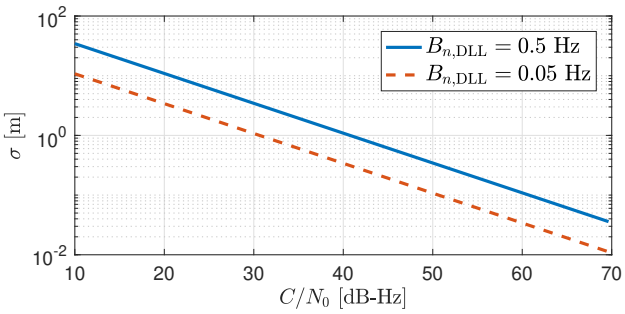

Figure 2.5: Plot of σ as a function of the carrier-to-noise ratio $\frac{C}{N_0}$ for $t_{\mathrm{eml}} = 1.25$ chips and $B_{n,\mathrm{DLL}} = \{0.5 \text{ Hz}, 0.05 \text{ Hz}\}$.

2.4 Clock Bias Discrepancy Model between Different Sectors of a BTS Cell

A typical CDMA BTS transmits into three different sectors within a particular cell. Ideally, all sectors' clocks should be driven by the same oscillator, which implies that the same clock bias (after correcting for the PN offset) should be observed in all sectors of the same cell. However, factors such as unknown distance between the phase-center of the sector antennas, delays due to RF connectors and other components (e.g., cabling, filters, amplifiers, etc.) cause the clock biases corresponding to different BTS sectors to be slightly different. This behavior was consistently observed experimentally in different locations, at different times, and for different cellular providers [82, 83]. In this section, the model for the pseudorange produced by the cellular CDMA navigation receiver developed in Section 2.2 is given. Subsequently, a stochastic dynamic model for the observed clock bias mismatch for different sectors of the same BTS cell is identified and experimentally validated.

2.4.1 Pseudorange Measurement Model

The pseudorange can be obtained from the proposed cellular CDMA navigation SDR by multiplying the code phase estimate by the speed-of-light. A model for this produced pseu-

dorange can be parameterized as a function of the receiver and BTS position and clock bias states. For simplicity, a planar environment will be assumed, with the receiver and BTS three-dimensional (3-D) position states appropriately projected onto such planar environment. The subsequent discussion can be straightforwardly generalized to 3-D. The state of the receiver is defined as $\boldsymbol{x}_r \triangleq \left[\boldsymbol{r}_r^{\mathsf{T}}, c\delta t_r\right]^{\mathsf{T}}$, where $\boldsymbol{r}_r = [x_r, y_r]^{\mathsf{T}}$ is the position vector of the navigating receiver, δt_r is the navigating receiver's clock bias, and c is the speed-of-light. Similarly, the state of the ith BTS is defined as $\boldsymbol{x}_{s_i} \triangleq \left[\boldsymbol{r}_{s_i}^{\mathsf{T}}, c\delta t_{s_i}\right]^{\mathsf{T}}$, where $\boldsymbol{r}_{s_i} = [x_{s_i}, y_{s_i}]^{\mathsf{T}}$ is the position vector of the ith BTS and δt_{s_i} is the clock bias. After mild approximations discussed in [33], the pseudorange measurement to the ith BTS at time k, $\rho_i(k)$, can be expressed as

$$\rho_i(k) = \|\boldsymbol{r}_r(k) - \boldsymbol{r}_{s_i}\| + c \cdot [\delta t_r(k) - \delta t_{s_i}(k)] + v_i(k), \tag{2.15}$$

where v_i is the observation noise, which is modeled as a zero-mean white Gaussian random sequence with variance σ_i^2.

2.4.2 Sector Clock Bias Discrepancy Detection

In order to detect the discrepancy between sectors' clock biases, the proposed cellular CDMA receiver was placed at the border of two sectors of a BTS cell and was drawing pseudorange measurements from both sector antennas. The receiver had full knowledge of its state and of the BTS's position. Subsequently, the receiver solved for the BTS clock biases $\delta t_{s_i}^{(p_i)}$ and $\delta t_{s_i}^{(q_i)}$ observed in sectors p_i and q_i, respectively. A realization of $\delta t_{s_i}^{(p_i)}$ and $\delta t_{s_i}^{(q_i)}$ is depicted in Fig. 2.6.

Fig. 2.6 suggests that the clock biases $\delta t_{s_i}^{(p_i)}$ and $\delta t_{s_i}^{(q_i)}$ can be related through

$$\delta t_{s_i}^{(q_i)}(k) = \delta t_{s_i}^{(p_i)}(k) + [1 - 1_{q_i}(p_i)]\, \epsilon_i(k),$$

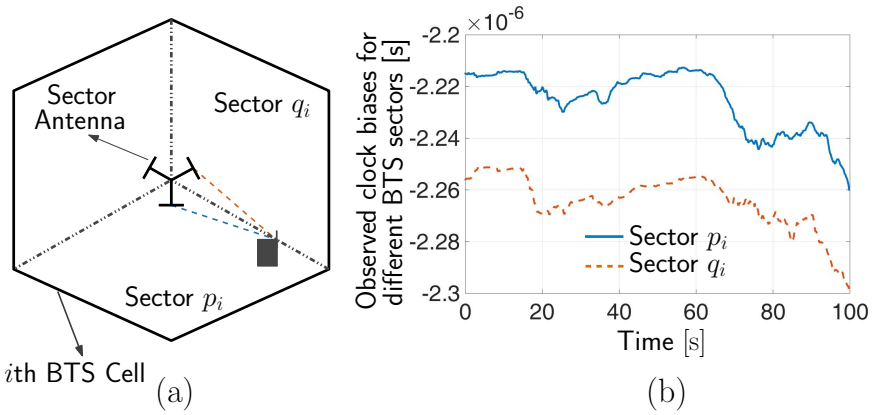

Figure 2.6: (a) A cellular CDMA receiver placed at the border of two sectors of a BTS cell, making pseudorange observations on both sector antennas simultaneously. The receiver has knowledge of its own states and has knowledge of the BTS position states. (b) Observed BTS clock bias corresponding to two different sectors from a real BTS (Verizon Wireless).

where ϵ_i is a random sequence that models the discrepancy between the sectors' clock biases and

$$1_{q_i}(p_i) = \begin{cases} 1, & \text{if } p_i = q_i, \\ 0, & \text{otherwise}, \end{cases}$$

is the indicator function.

Remark The cdma2000 protocol requires all PN offsets to be synchronized to within 10 μs from GPS time; however, synchronization to within 3 μs is recommended [48]. Since each sector of a BTS uses a different PN offset, then the clock biases $\delta t_{s_i}^{(p_i)}$ and $\delta t_{s_i}^{(q_i)}$ will be bounded according to $-10\ \mu\text{s} \leq \delta t_{s_i}^{(p_i)}(k) \leq 10\ \mu\text{s}$ and $-10\ \mu\text{s} \leq \delta t_{s_i}^{(q_i)}(k) \leq 10\mu\text{s}$. Therefore, ϵ_i will be within 20 μs from GPS time, namely

$$-20\ \mu\text{s} \leq \epsilon_i \leq 20\ \mu\text{s}.$$

The discrepancy $\{\epsilon_i\}_{i=1}^2$ between the clock biases observed in two different sectors of some BTS cell over a 24-hour period is shown in Figs. 2.7(a) and 2.7(b) for two different BTSs. Both cellular towers pertain to the U.S. cellular provider Verizon Wireless and are located

near the University of California, Riverside campus. The cellular signals were recorded between September 23 and 24, 2016. It can be seen from Fig. 2.7 that $|\epsilon_i|$ is bounded by approximately 2.02 μs and 0.65 μs, respectively, which is well below 20 μs.

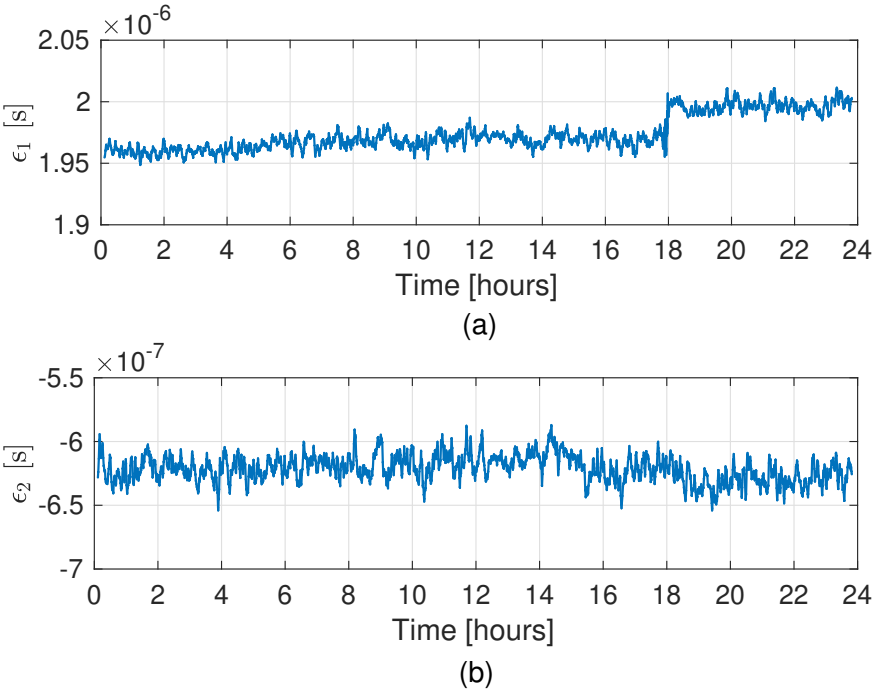

Figure 2.7: The discrepancies ϵ_1 and ϵ_2 between the clock biases observed in two different sectors of some BTS cell over a 24-hour period. (a) and (b) correspond to ϵ_1 and ϵ_2 for BTSs 1 and BTS 2, respectively. Both BTSs pertain to the U.S. cellular provider Verizon Wireless and are located near the University of California, Riverside campus. The cellular signals were recorded between September 23 and 24, 2016. It can be seen that $|\epsilon_i|$ is well below 20 μs.

In what follows, a stochastic dynamic model for ϵ_i is identified.

2.4.3 Model Identification

It is hypothesized that the discrepancy $\epsilon_i(k) = \delta t_{s_i}^{(q_i)}(k) - \delta t_{s_i}^{(p_i)}(k)$ for $p_i \neq q_i$ adheres to an autoregressive (AR) model of order n [93], which can be expressed as

$$\epsilon_i(k) + \sum_{j=1}^{n} a_{i,j}\epsilon_i(k-j) = \zeta_i(k),$$

where ζ_i is a white sequence. The objective is to find the order n and the coefficients $\{a_{i,j}\}_{j=1}^{n}$ that will minimize the sum of the squared residuals $\sum_{l=0}^{k} \zeta_i^2(l)$. To find the order n, several AR models were identified and for a fixed order, a least-squares estimator was used to solve for $\{a_{i,j}\}_{j=1}^{n}$. It was noted that the sum of the squared residuals corresponding to each $n \in \{1, \ldots, 10\}$ were comparable, suggesting that the minimal realization of the AR model is of first-order. For $n = 1$, it was found that $a_{i,1} = -(1 - \beta_i)$, where $0 < \beta_i \ll 1$ (on the order of 8×10^{-5} to 3×10^{-4}). This implies that ϵ_i is an exponentially correlated random variable (ECRV) with the continuous-time (CT) dynamics given by

$$\dot{\epsilon}_i(t) = -\alpha_i \epsilon_i(t) + \tilde{\zeta}_i(t), \tag{2.16}$$

where $\alpha_i \triangleq \frac{1}{\tau_i}$, τ_i is the time constant of the discrepancy dynamical model, and $\tilde{\zeta}_i$ is a CT white process with variance $\sigma^2_{\tilde{\zeta}_i}$. Discretizing (2.16) at a sampling period T yields the DT model

$$\epsilon_i(k+1) = \phi_i \, \epsilon_i(k) + \zeta_i(k), \tag{2.17}$$

where $\phi_i = e^{-\alpha_i T}$. The variance of ζ_i is given by $\sigma^2_{\zeta_i} = \frac{\sigma^2_{\tilde{\zeta}_i}}{2\alpha_i}\left(1 - e^{-2\alpha_i T}\right)$. Fig. 2.8 shows an experimental realization of ϵ_i and the corresponding residual ζ_i.

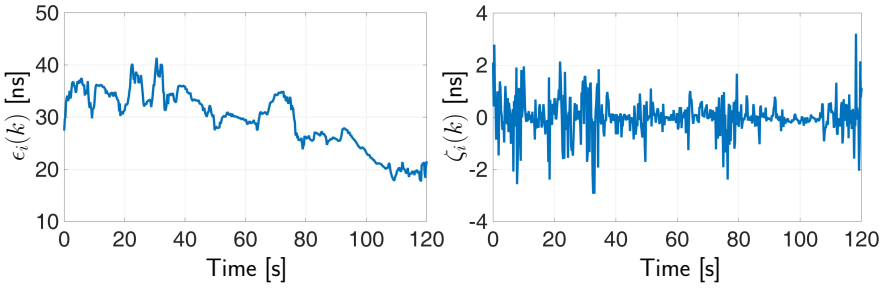

(a) (b)

Figure 2.8: (a) A realization of the discrepancy ϵ_i between the observed clock biases of two BTS sectors and (b) the corresponding residual ζ_i.

2.4.4 Model Validation

The identified model in (2.17) was validated through residual analysis [93]. To this end, the autocorrelation function (acf) and power spectral density (psd) of the residual error e_i defined as the difference between the measured data ϵ_i' and predicted value from the identified model ϵ_i in (2.17), i.e., $e_i \triangleq \epsilon_i' - \epsilon_i$, were computed. Fig. 2.9 shows the acf and psd of e_i computed from a different realization of ϵ_i. The psd was computed using Welch's method [94]. It can be seen from Fig. 2.9 that the residual error e_i is nearly white; hence, the identified model is capable of describing the true system.

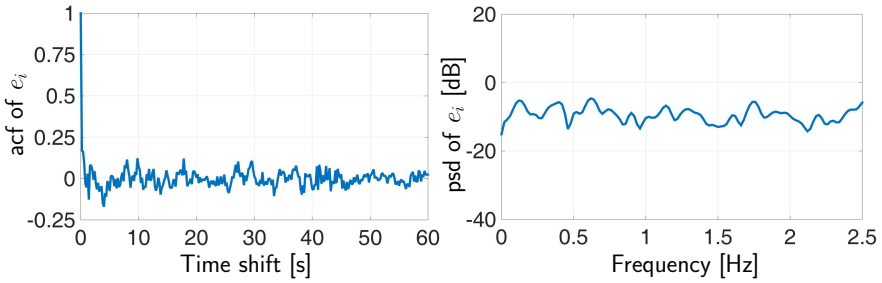

(a) (b)

Figure 2.9: The (a) acf and (b) psd of e_i with a sampling frequency of 5 Hz.

2.4.5 Residual Statistics Characterization

Next, the probability density function (pdf) of ζ_i will be characterized, assuming that ζ_i is an ergodic process. It was found that the Laplace distribution best matches the actual distribution of ζ_i obtained from experimental data, i.e., the pdf of ζ_i is given by

$$p(\zeta_i) = \frac{1}{2\lambda_i} \exp\left(-\frac{|\zeta_i - \mu_i|}{\lambda_i}\right), \tag{2.18}$$

where μ_i is the mean of ζ_i and λ_i is the parameter of the Laplace distribution, which can be related to the variance by $\sigma_{\zeta_i}^2 = 2\lambda_i^2$. A maximum likelihood estimator (MLE) was adopted to calculate the parameters μ_i and λ_i of $p(\zeta_i)$ [95]. Fig. 2.10 shows the actual distribution of

the data along with the estimated pdf. For comparison purposes, a Gaussian and Logistic pdf fits obtained via an MLE are plotted as well.

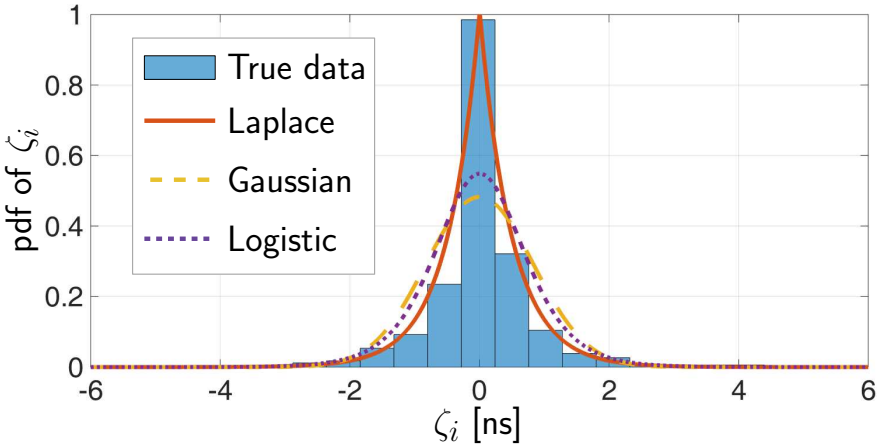

Figure 2.10: Distribution of ζ_i from experimental data and the estimated Laplace pdf via MLE. For comparison purposes, a Gaussian (dashed) and Logistic (dotted) pdf fits are plotted as well.

It was noted that $\mu_i \approx 0$ from several batches of collected experimental data; therefore, ζ_i is appropriately modeled as a zero-mean white Laplace-distributed random sequence with variance $2\lambda_i^2$.

2.4.6 Statistics of the Discrepancy Between Sector Clock Biases

The solution to the dynamic model (2.17) can be expressed as

$$\epsilon_i(k) = \phi_i^k \epsilon_i(0) + \sum_{l=0}^{k-1} \phi_i^{k-1-l} \zeta_i(l),$$

where $\epsilon_i(0)$ is the known initial discrepancy. Without loss of generality, $\epsilon_i(0)$ is assumed to be zero. Therefore, $\epsilon_i(k)$ has mean $\mathbb{E}[\epsilon_i(k)] = 0$ and variance $\text{var}[\epsilon_i(k)] = \frac{\sigma_{\zeta_i}^2}{2\alpha_i}\left(1 - e^{-2\alpha_i kT}\right)$. Note that the discrepancy ϵ_i is the weighted sum of uncorrelated Laplace-distributed random variables. The central limit theorem asserts that the pdf of ϵ_i converges to a Gaussian pdf. It was noted that the convergence happens for $k \geq 9$ for $\phi_i \geq 0.95$, as depicted in Fig. 2.11.

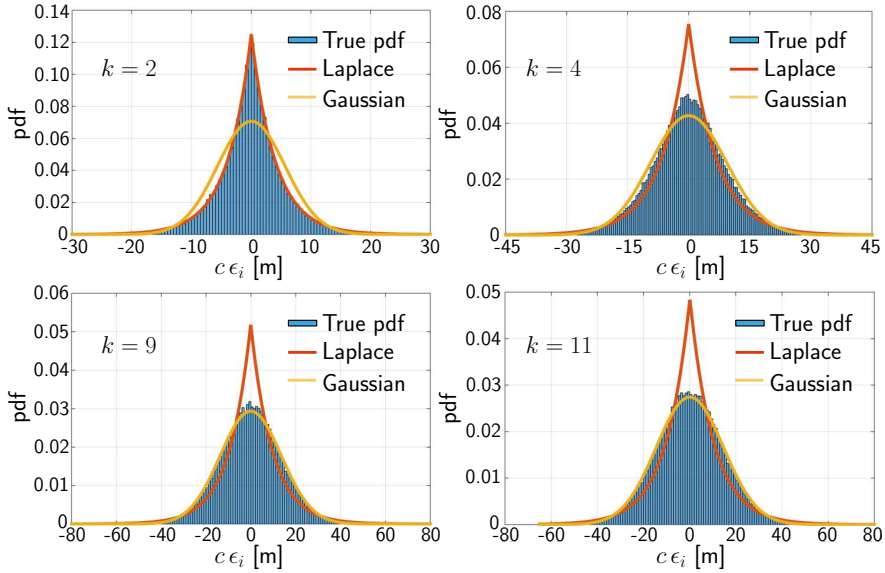

Figure 2.11: Simulation of the distribution of $c\epsilon_i$ (expressed in meters) for $\phi_i = 0.95$, $\mu_i = 0$, and $\lambda_i = 13$ns. The true distribution is fitted to a Gaussian distribution (yellow) and a Laplace distribution (red).

2.4.7 Approximation with a Random Walk

When $\alpha_i \to 0$, the dynamics of $\epsilon_i(k)$ converge to that of a random walk. Since the values of α_i obtained experimentally are very small, studying the RW model as an approximation becomes relevant. The mean of the RW process is also zero and the variance is given by $\sigma^2_{\tilde{\zeta}_i} kT$. It can be readily shown that $\sigma^2_{\tilde{\zeta}_i} kT > \frac{\sigma^2_{\tilde{\zeta}_i}}{2\alpha_i}\left(1 - e^{-2\alpha_i kT}\right), \forall\, \alpha_i > 0$, $k > 0$, and $T > 0$. Denote the relative error between the variances of the ECRV and RW models by γ, then the following can be established

$$\frac{1}{2\alpha_i kT}\left(1 - e^{-2\alpha_i kT}\right) \geq 1 - \gamma. \tag{2.19}$$

Note that (2.19) may also be expressed as

$$f(x, \gamma) \geq 0,$$

where

$$x \triangleq 2\alpha_i kT \quad \text{and} \quad f(x,\gamma) \triangleq 1-(1-\gamma)x - e^{-x}.$$

Fig. 2.12(a) shows $f(x,\gamma)$ as a function of x for different values of γ. Let $x^\star = g(\gamma)$ denote the solution to $f(x,\gamma)=0$ for a given γ. According to Fig. 2.12(a), for a given γ, $f(x,\gamma) \geq 0$ is satisfied $\forall\, x \in (0, g(\gamma)]$. Fig. 2.12(b) depicts the solution $x^\star = g(\gamma)$ as a function of γ. Note that $g(\gamma)$ does not have a closed form but can be calculated using iterative methods, e.g., Newton's method.

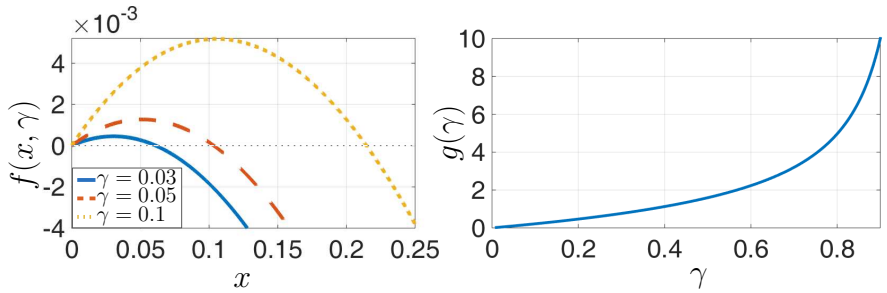

Figure 2.12: (a) Plot of $f(x,\gamma)$ for $\gamma = \{0.03, 0.05, 0.1\}$. (b) Plot of $g(\gamma)$.

Subsequently, for a desired γ and a known α_i, one can solve for k that guarantees the relative error between the RW and ECRV variances to be less than γ using $2\alpha_i kT \leq g(\gamma)$. For example, given that $\gamma = 0.01$ and $\alpha_i = 3\times 10^{-4}$ Hz, then for $kT \leq \frac{g(0.01)}{2\times 3\times 10^{-4}} = 33.55$ s, the relative error between the RW and ECRV variances will remain less than 1 %.

2.5 Experimental Results

In this section, experimental results on an aerial and ground vehicle, validating the proposed cellular CDMA navigation SDR are presented. Next, the consistency of the clock bias discrepancy model derived in Section 2.4 is analyzed experimentally.

2.5.1 Cellular CDMA Navigation SDR Experimental Results

In order to test the proposed cellular CDMA SDR, the variation in the pseudorange obtained by the receiver was compared to the variation in true range between the moving receiver and cellular CDMA BTSs. For this purpose, two experiments are conducted where the proposed receiver was mounted on (1) an unmanned aerial vehicle (UAV) and (2) a ground vehicle.

UAV Results

In the first experiment, a DJI Matrice 600 UAV was equipped with the proposed SDR, a consumer-grade 800/1900 MHz cellular antenna, and a small consumer-grade GPS antenna to discipline the on-board oscillator. The cellular signals were down-mixed and sampled via a single-channel universal software radio peripheral (USRP) driven by a GPS-disciplined oscillator (GPSDO). The cellular receiver was tuned to a carrier frequency of 883.98 MHz, which is a channel allocated for the U.S. cellular provider Verizon Wireless. Samples of the received signals were stored for off-line post-processing. The cellular CDMA signals were processed by the proposed LabVIEW-based SDR. The ground-truth reference for the UAV trajectory was taken from its on-board navigation system, which uses GPS, an inertial navigation system, and other sensors. Fig. 2.13 shows the SOP BTS environment in which the UAV was present as well as the experimental hardware setup.

Over the course of the experiment, the receiver was listening to two BTSs, whose position states were mapped prior to the experiment according to the framework discussed in [1]. The distance D between the UAV and the BTS was calculated using the navigation solution produced by the UAV's navigation system and the known BTS position, and the pseudorange ρ was obtained from the proposed cellular CDMA SDR mounted on the UAV over the trajectory shown in Fig. 2.14.

Figure 2.13: SOP BTS environment and experimental hardware setup for the UAV experiment. Map data: Google Earth.

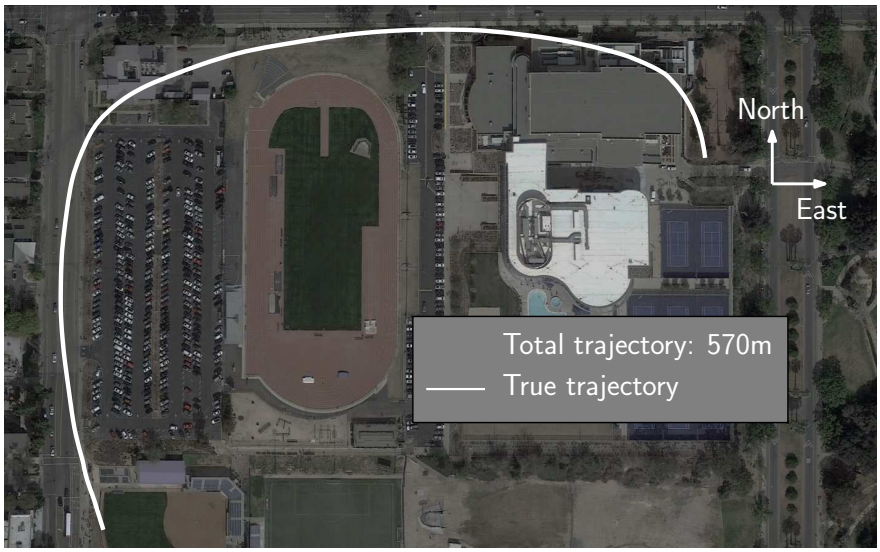

Figure 2.14: Trajectory taken by the UAV over the course of the experiment. Map data: Google Earth.

In order to validate the resulting pseudoranges, the variation of the pseudorange $\Delta\rho \triangleq \rho - \rho(0)$, where $\rho(0)$ is the initial value of the pseudorange, and the variation in distance $\Delta D \triangleq D - D(0)$, where $D(0)$ is the initial distance between the UAV and the BTS are plotted in Fig. 2.15 for the two BTSs.

It can be seen from Fig. 2.15 that the variations in the pseudoranges follow closely the variations in distances. The difference between ΔD and $\Delta\rho$ for a particular BTS is due to the variation in the clock bias difference $c\,(\delta t_r - \delta t_{s_i})$ and the noise terms v_i.

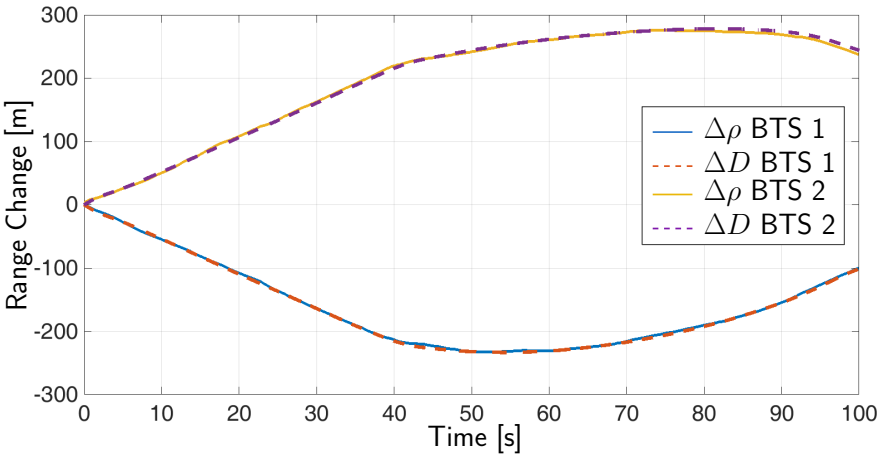

Figure 2.15: Variation in pseudoranges and the variation in distances between the receiver and two cellular CDMA BTSs for the UAV experiment.

Ground Vehicle Results

In the second experiment, a car was equipped with the proposed SDR, a consumer-grade 800/1900 MHz cellular antenna, and a surveyor-grade GPS antenna to collect GPS L1 signal and to discipline the on-board oscillator. The cellular and GPS signals were down-mixed and synchronously sampled via a dual-channel USRP driven by a GPSDO. The cellular receiver was tuned to a carrier frequency of 882.75 MHz, which is also a channel allocated for the U.S. cellular provider Verizon Wireless. Samples of the received signals were stored for off-line post-processing. The cellular CDMA signals were processed by the proposed LabVIEW-based SDR. The GPS signal was processed by the Generalized Radionavigation Interfusion Device (GRID) SDR [96] and the resulting GPS solution was assumed to be the ground-truth reference for the car trajectory. Fig. 2.16 shows the SOP BTS environment, car trajectory, and the experimental hardware setup.

Over the course of the experiment, the receiver was listening to two BTSs, whose position states were mapped prior to the experiment according to the framework discussed in [1]. The change in the true range and the change in pseudorange are plotted in Fig. 2.17, similarly to the UAV experiment.

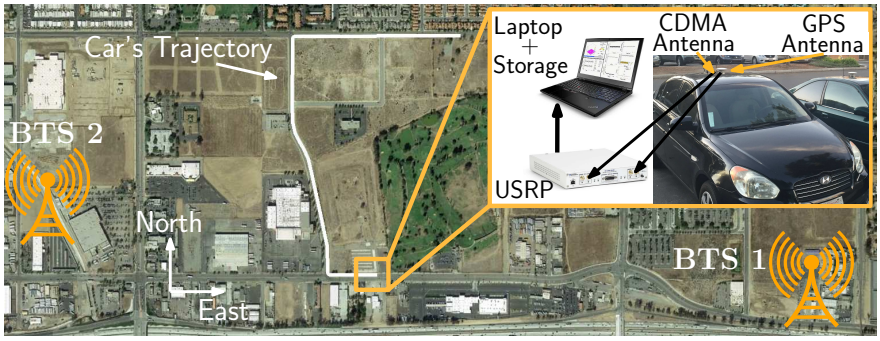

Figure 2.16: SOP BTS environment, true trajectory, and experimental hardware setup for the ground vehicle experiment. Map data: Google Earth.

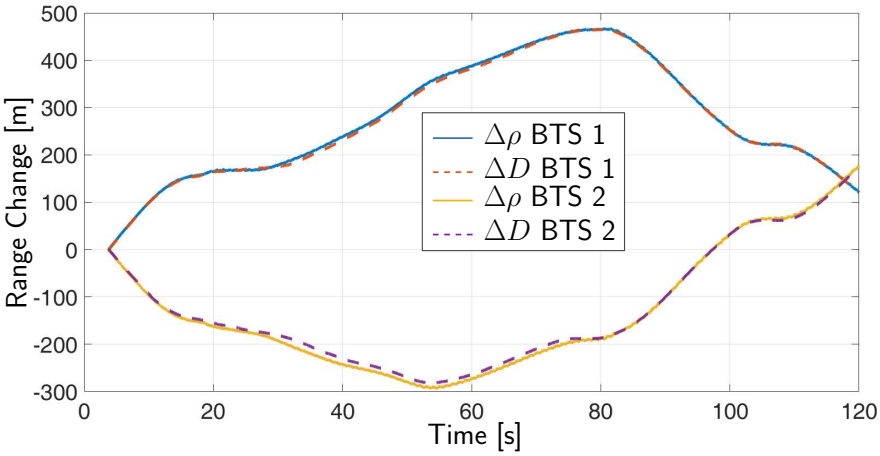

Figure 2.17: Variation in pseudoranges and the variation in distances between the receiver and two cellular CDMA BTSs for the ground vehicle experiment.

It can be seen from Fig. 2.17 that the variations in the pseudoranges follow closely the variations in distances. The difference between ΔD and $\Delta\rho$ for a particular BTS is due to the variation in the clock bias difference $c\,(\delta t_r - \delta t_{s_i})$ and the noise terms v_i. Chapter 3 studies the navigation performance and estimation of the clock bias in further detail.

2.5.2 Clock Bias Discrepancy Model Consistency Analysis

The consistency of the clock bias discrepancy model was analyzed experimentally in different locations, at different times, and for different cellular providers. The results are presented in this section.

Cellular CDMA SOP Test Scenarios and Hardware Setup

The tests were performed twice at three different locations. There is a six-day period between each test at each of the three locations. A total of three carrier frequencies were considered, two of them pertaining to Verizon Wireless and one to Sprint. The test scenarios are summarized in Table 2.2 and Fig. 2.18. The date field in Table 2.2 shows the date in which the test was conducted in MM/DD/YYYY format.

Table 2.2: Test Dates, Locations, and Carrier Frequencies

Test	Date	Location	Frequency	Provider
(a)	01/14/2016	1	882.75 MHz	Verizon
(b)	01/20/2016	1	882.75 MHz	Verizon
(c)	08/28/2016	2	883.98 MHz	Verizon
(d)	09/02/2016	2	883.98 MHz	Verizon
(e)	08/28/2016	3	1940.0 MHz	Sprint
(f)	09/02/2016	3	1940.0 MHz	Sprint

Figure 2.18: Locations of the cellular CDMA BTSs: Colton, CA; Riverside, CA; and the University of California, Riverside (UCR). Map data: Google Earth.

For the purpose of collecting data, a receiver that was placed close to the border of two sectors for each BTS was equipped with two antennas to acquire and track: (1) GPS signals and (2) signals from the cellular CDMA BTS sector antennas. The CDMA antenna used for the experiments in location 1 was a consumer-grade 800/1900 MHz cellular antenna and a high-gain tri-band cellular antenna for locations 2 and 3. Both GPS antennas were surveyor-grade Leica antennas. The GPS and cellular signals were simultaneously down-mixed and synchronously sampled at 2.5 MS/s via a dual channel USRP driven by a GPSDO. Samples of the received signals were stored for off-line post-processing. The GPS signal was processed by GRID and the cellular CDMA signals were processed by the proposed LabVIEW-based SDR. The receiver's clock bias obtained from the GPS solution was used to solve for the BTS sector clock bias. Fig. 2.19 shows the experimental hardware setup.

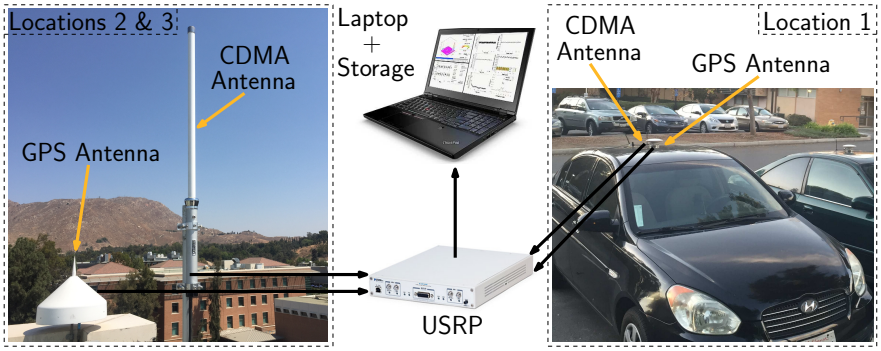

Figure 2.19: Experimental hardware setup for each location. Left: hardware setup for locations 2 and 3. Center: data collection equipment. Right: hardware setup for location 1.

Analysis of Sector Clock Bias Discrepancy Realizations

Fig. 2.20 shows six realizations, five minutes each, of the discrepancy corresponding to Tests (a)–(f) in Table 2.2. It can be seen from Fig. 2.20 that the behavior of the discrepancy is consistent across the tests. The initial discrepancy is subtracted out so that all realizations start at the origin. The inverse of the time constant for each realization was found to be $\{\alpha_i\}_{i=1}^{6} = \{2.08, 1.66, 1.77, 1.70, 1.39, 2.53\} \times 10^{-4}$ Hz.

Next, the process noise driving the discrepancy is characterized. The process noise was calculated according to

$$\zeta_i(k) = \epsilon_i(k+1) - \phi_i \epsilon_i(k),$$

where $\phi_i = e^{-\alpha_i T}$ and $T = 0.2$ s. The acf of each of the six realizations of ζ_i corresponding to the six realizations of ϵ_i from Fig. 2.20 are shown in Fig. 2.21. Similarly to Fig. 2.9(a), the shape of the acfs in Fig. 2.21 exhibits very quick de-correlation, validating that ζ_i is approximately a white sequence.

Fig. 2.22 shows a histogram of each realization of ζ_i along with the estimated pdf $p(\zeta_i)$. The pdfs were obtained by estimating the μ_i and λ_i parameters associated with the Laplace pdf (2.18). It can be seen that the Laplace pdf consistently matched the experimental data.

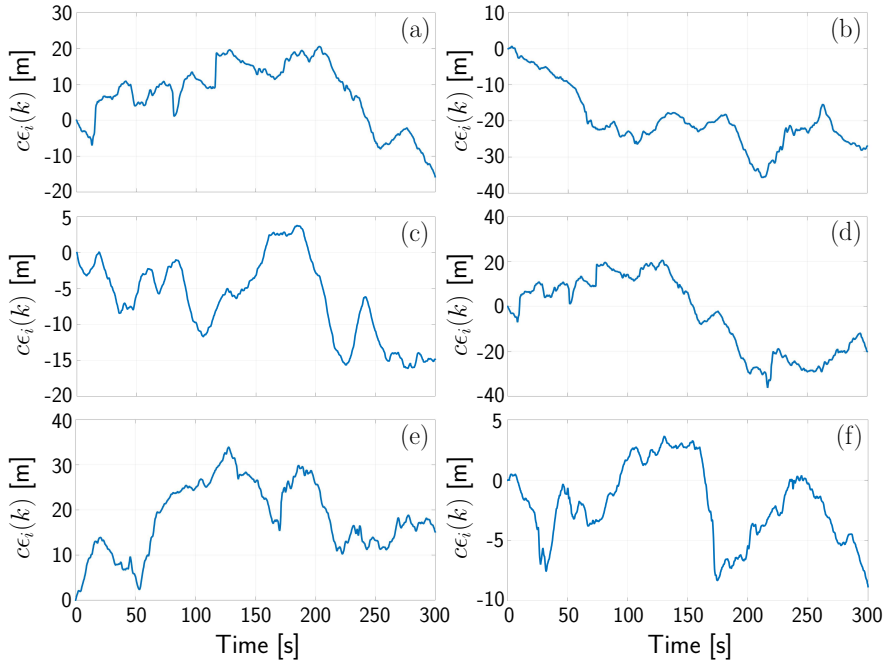

Figure 2.20: Six realizations, five minutes each, of the sector clock bias discrepancy for the tests in Table 2.2.

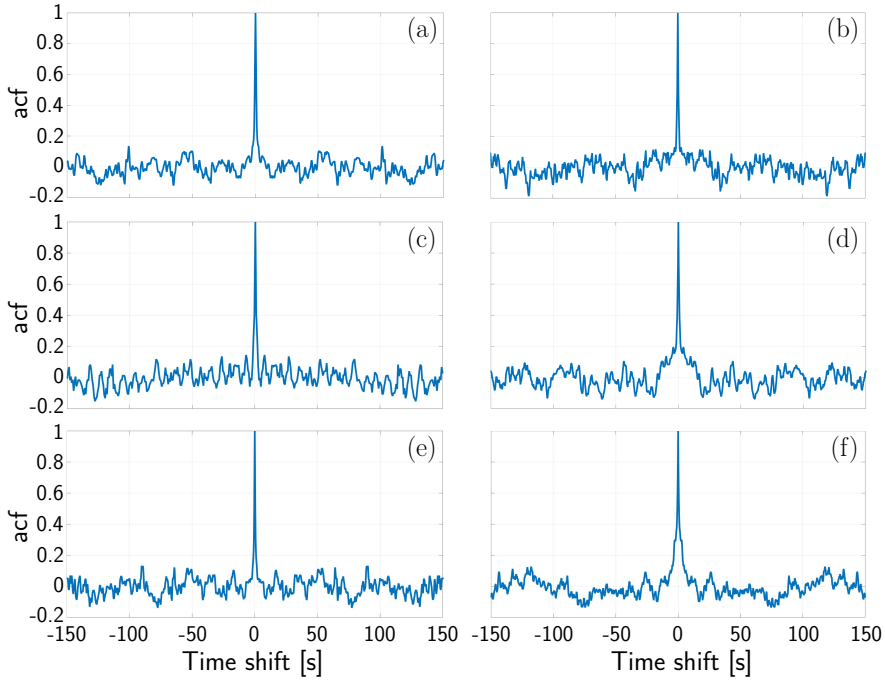

Figure 2.21: The acf of the six realizations of the process noise ζ_i corresponding to the discrepancies in Fig. 2.20.

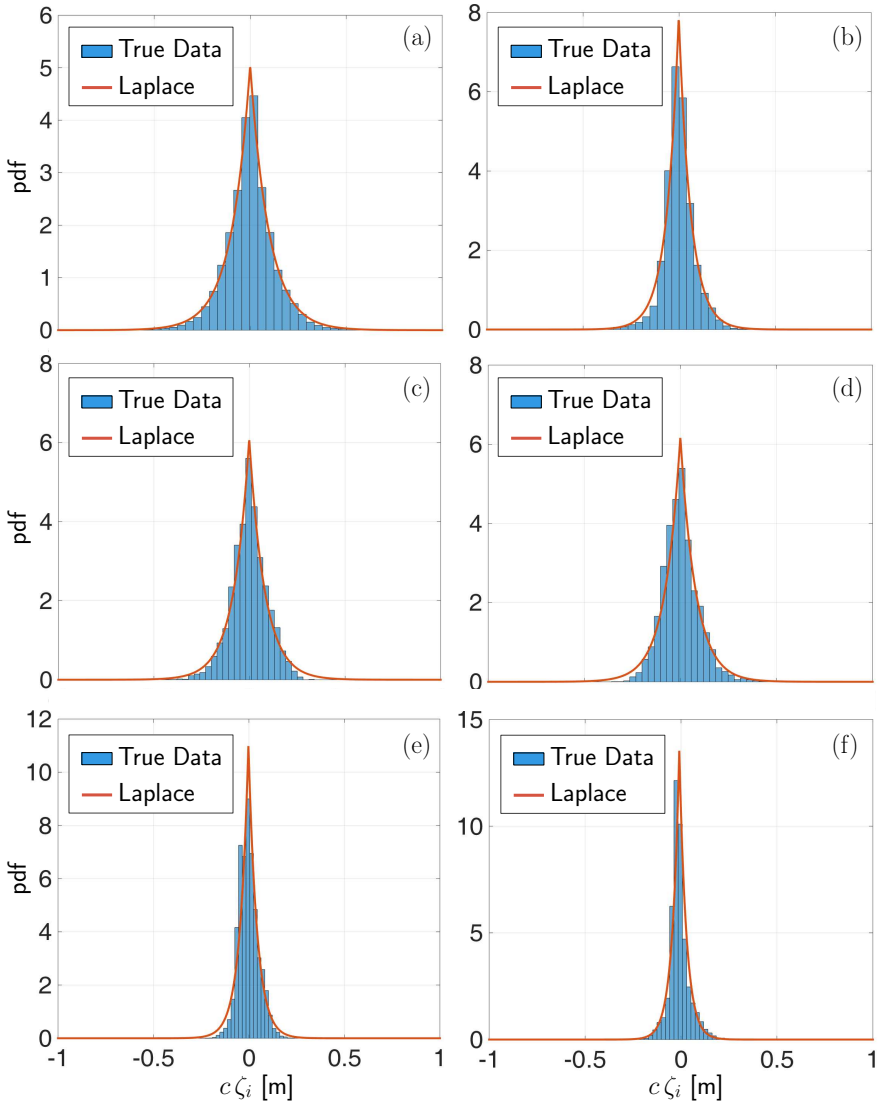

Figure 2.22: A histogram of each realization of the process noise along with the estimated Laplace distribution.

Chapter 3

Differential Framework for Navigation With Pseudorange Measurements from Cellular SOPs

This chapter is organized as follows. Section 3.1 studies a base/rover receiver framework for navigation with cellular CDMA signals. Section 3.2 derives a lower bound on the determinant of the estimation error covariance for pseudorange measurements with uncorrelated measurement noise and analyzes the navigation performance using cellular CDMA signals in the presence of clock bias discrepancies between BTS sectors. Section 3.3 shows experimental results of navigation using cellular CDMA signals for (1) a mobile ground vehicle and stationary base, (2) a UAV with a stationary base, and (3) a UAV with a mobile base. Note that the same notation of Chapter 2 is adopted in this chapter.

The results of this chapter have been published in [82, 97].

3.1 Base/Rover Navigation Framework

By making pseudorange observations to 3 or more BTSs, one may estimate the two-dimensional (2-D) position and clock bias of a cellular CDMA receiver, provided that the BTS locations and their clock biases are known. The observability of environments comprising multiple receivers making pseudorange observations on terrestrial SOPs was studied in [33] and the estimation of unknown cellular CDMA SOP states was addressed in [41]. This section describes a framework for navigating with cellular CDMA signals. The framework consists of two receivers: a reference receiver and a navigating receiver, referred to as the base and rover, respectively [85]. Each receiver is capable of producing pseudorange measurements to nearby SOP BTSs. The base could be deployed on top of a building; therefore, it has access to GNSS signals. However, the rover is located between the buildings where GNSS signals are severely attenuated and cannot be used to produce a navigation solution. Note that cellular CDMA signals are orders of magnitude more powerful that GNSS signals (carrier-to-noise ratio around 60 dB-Hz, see Fig. 2.3 in Chapter 2 [85], while the carrier-to-noise ratio of GNSS signals outdoors is around 41-46 dB-Hz [6]). Alternatively, the rover may lose access to GNSS signals in a situation where it is located in the vicinity of a personal privacy device (i.e., GNSS jammer [4]), which makes GNSS signals unusable. Subsequently, the base is assumed to have knowledge of its own state vector and is estimating the states of the unknown SOP BTSs. These estimates are shared with the rover, which has *no* knowledge of its own states. This section considers the estimation of receiver and SOP states in a static framework. As such, the time argument will be dropped for simplicity of notation.

3.1.1 BTS State Estimation

Consider a base with knowledge of its own state vector (by having access to GPS signals, for example) to be present in the rover's environment as depicted in Fig. 3.1 [82].

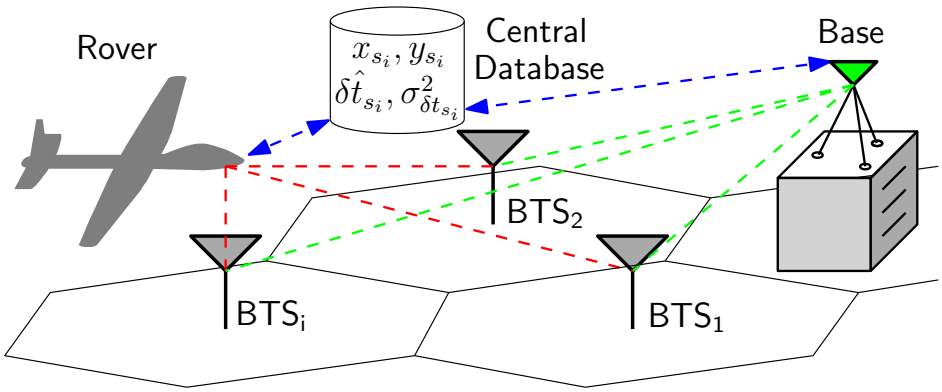

Figure 3.1: Base and rover in a cellular SOP environment.

The base's objective is to estimate the BTSs' position and clock bias states and share these estimates with the rover through a central database. The position states of the BTSs are assumed to be known and stored in a database. The position states could be readily obtained via multiple bases in the environment, estimating the position states of the BTSs for a sufficiently long period of time. These estimates are physically verifiable via surveying or satellite images. Unlike the position state estimates, the clock bias state estimates are time-varying and difficult to verify. Therefore, in the sequel, it is assumed that the base is only producing for the ith BTS an estimate $\delta\hat{t}_{s_i}$ and an associated estimation error variance $\sigma^2_{\delta t_{s_i}}$.

Consider M bases and N SOP BTSs. Denote the state vector of the jth base by $\boldsymbol{x}_{r_j}$, the pseudorange measurement by the jth base on the ith BTS by $\rho_i^{(j)}$, and the corresponding measurement noise by $v_i^{(j)}$. Assume $v_i^{(j)}$ to be independent for all i and j with a corresponding variance ${\sigma_i^{(j)}}^2$. The measurement $\rho_i^{(j)}$ is hence given by

$$\rho_i^{(j)} = \left\|\boldsymbol{r}_{r_j} - \boldsymbol{r}_{s_i}\right\|_2 + c\left(\delta t_{r_j} - \delta t_{s_i}\right) + v_i^{(j)}.$$

The base knows $\boldsymbol{r}_{r_j}$, $\boldsymbol{r}_{s_i}$, and $c\delta t_{r_j}$. Subsequently, define the set of measurements made by

all bases on the ith BTS as

$$\begin{aligned}\boldsymbol{z}_i &\triangleq \begin{bmatrix} \|\boldsymbol{r}_{r_1} - \boldsymbol{r}_{s_i}\| + c\delta t_{r_1} - \rho_i^{(1)} \\ \vdots \\ \|\boldsymbol{r}_{r_M} - \boldsymbol{r}_{s_i}\| + c\delta t_{r_M} - \rho_i^{(M)} \end{bmatrix} = \begin{bmatrix} c\delta t_{s_i} - v_i^{(1)} \\ \vdots \\ c\delta t_{s_i} - v_i^{(M)} \end{bmatrix} \\ &= c\delta t_{s_i}\mathbf{1}_M + \boldsymbol{v}_i,\end{aligned}$$

where $\mathbf{1}_M \triangleq [1, \ldots, 1]^\mathsf{T}$ and $\boldsymbol{v}_i \triangleq -\left[v_i^{(1)}, \ldots, v_i^{(M)}\right]^\mathsf{T}$. The clock bias δt_{s_i} is estimated by solving a weighted least-squares (WLS) problem, resulting in the estimate

$$\hat{\delta} t_{s_i} = \frac{1}{c}\left(\mathbf{1}_M^\mathsf{T}\mathbf{W}\mathbf{1}_M\right)^{-1}\mathbf{1}_M^\mathsf{T}\mathbf{W}\boldsymbol{z}$$

and associated estimation error variance $\sigma^2_{\delta t_{s_i}} = \frac{1}{c}\left(\mathbf{1}_M^\mathsf{T}\mathbf{W}\mathbf{1}_M\right)^{-1}$, where $\mathbf{W} = \text{diag}\left[\frac{1}{\sigma_i^{(1)^2}}, \ldots, \frac{1}{\sigma_i^{(M)^2}}\right]$ is the weighting matrix. The true clock bias of the ith BTS can now be expressed as $\delta t_{s_i} = \hat{\delta} t_{s_i} + w_i$, where w_i is a zero-mean Gaussian random variable with variance $\sigma^2_{\delta t_{s_i}}$.

3.1.2 Pseudorange Model in the Presence of Sector Mismatch

Since the rover is using the BTS clock bias estimate produced by the base(s), the pseudorange measured by the rover in sector q_i of the ith BTS, using the discrepancy model identified in Chapter 2, can be expressed as

$$\rho_i^{(q_i)} = \hat{h}_i^{(p_i)} + \eta_i - \left[1 - 1_{q_i}(p_i)\right] \cdot \left[c\epsilon_i\right],$$

where $\hat{h}_i^{(p_i)} \triangleq h_i\left(\boldsymbol{x}_r, \hat{\boldsymbol{x}}_{s_i}^{(p_i)}\right)$, $h_i(\boldsymbol{x}_r, \boldsymbol{x}_{s_i}) \triangleq \|\boldsymbol{r}_r - \boldsymbol{r}_{s_i}\|_2 + c \cdot [\delta t_r - \delta t_{s_i}]$, $\hat{\boldsymbol{x}}_{s_i}^{(p_i)} = \left[\boldsymbol{r}_{s_i}^\mathsf{T}, c\hat{\delta} t_{s_i}^{(p_i)}\right]^\mathsf{T}$, $\hat{\delta} t_{s_i}^{(p_i)}$ is the ith BTS clock bias estimate produced by the base in sector p_i, and $\eta_i \triangleq v_i - w_i$ models the overall uncertainty in the pseudorange measurement, which is a zero-mean Gaussian random variable with variance $\sigma^2_{\eta_i} = \sigma_i^2 + c^2\sigma^2_{\delta t_{s_i}}$. The quantities ϵ_i, η_i, and $\hat{\delta} t_{s_i}^{(p_i)}$

are time-varying quantities with $\hat{\delta}t_{s_i}^{(p_i)}$ known at all times. Therefore, the pseudorange at time-step k is given by

$$\rho_i^{(q_i)}(k) = \hat{h}_i^{(p_i)}(k) + \eta_i(k) - [1 - 1_{q_i}(p_i)] \cdot [c\epsilon_i(k)]\,, \tag{3.1}$$

where $\hat{h}_i^{(p_i)}(k) = h_i\left[\boldsymbol{x}_r(k), \hat{\boldsymbol{x}}_{s_i}^{(p_i)}(k)\right]$ indicates that the observation estimate is calculated using the base estimates and the receiver state at time k. After nine time steps, ϵ_i can be modeled as a zero-mean Gaussian random variable with variance $\frac{\lambda_i^2}{\alpha_i}\left(1 - e^{-2\alpha_i kT}\right)$ [85], as shown in Chapter 2. In the sequel, $\lambda_i \equiv \lambda$ and $\alpha_i \equiv \alpha$, $\forall\ i$.

3.1.3 Fusion of BTS Clock State Estimates into the Navigation Solution

The rover is assumed to be drawing pseudorange measurements from N BTSs, N_s of which have a mismatch between the base and rover sectors. Without loss of generality, the set of pseudorange measurements are assumed to be sorted such that the first N_s measurements correspond to ones coming from the BTSs with sector mismatch between the base and rover. If the rover is either stationary or mobile but has perfect knowledge of the change in its position, it can solve through a batch LS estimator for its: (1) initial position state $\boldsymbol{r}_r(k_0)$ and (2) clock bias at time-steps k_0 to $k_0 + K - 1$ by utilizing all the measurements from k_0 to $k_0 + K - 1$. Alternatively, the rover may solve for its current position and clock bias through a LS estimator (point solution with $K = 1$). In either case, the estimator is estimating the state vector $\boldsymbol{x}_r'$ given by

$$\boldsymbol{x}_r' = [x_r(k_0), y_r(k_0), c\delta t_r(k_0), \ldots, c\delta t_r(k_0 + K - 1)]^{\mathsf{T}}\,.$$

The measurement model is therefore given by

$$\boldsymbol{\rho} = \hat{\boldsymbol{h}} + c\boldsymbol{\epsilon} + \boldsymbol{\eta}, \tag{3.2}$$

where

$$\boldsymbol{\rho} \triangleq \left[{}^{K}\boldsymbol{\rho}_1^{\mathsf{T}}, \ldots, {}^{K}\boldsymbol{\rho}_N^{\mathsf{T}}\right]^{\mathsf{T}},\ {}^{K}\boldsymbol{\rho}_i \triangleq \left[\rho_i^{(q_i)}(k_0), \ldots, \rho_i^{(q_i)}(k_0+K-1)\right]^{\mathsf{T}},$$

$$\hat{\boldsymbol{h}} \triangleq \left[{}^{K}\hat{\boldsymbol{h}}_1^{\mathsf{T}}, \ldots, {}^{K}\hat{\boldsymbol{h}}_N^{\mathsf{T}}\right]^{\mathsf{T}},\ {}^{K}\hat{\boldsymbol{h}}_i \triangleq \left[\hat{h}_i^{(p_i)}(k_0), \ldots, \hat{h}_i^{(p_i)}(k_0+K-1)\right]^{\mathsf{T}},$$

$$\boldsymbol{\epsilon} \triangleq \left[{}^{K}\boldsymbol{\epsilon}_1^{\mathsf{T}}, \ldots, {}^{K}\boldsymbol{\epsilon}_N^{\mathsf{T}}, \mathbf{0}_{\bar{K}\times 1}^{\mathsf{T}}\right]^{\mathsf{T}},\ {}^{K}\boldsymbol{\epsilon}_i \triangleq \left[\epsilon_i(k_0), \ldots, \epsilon_i(k_0+K-1)\right]^{\mathsf{T}},$$

$$\boldsymbol{\eta} \triangleq \left[{}^{K}\boldsymbol{\eta}_1^{\mathsf{T}}, \ldots, {}^{K}\boldsymbol{\eta}_N^{\mathsf{T}}\right]^{\mathsf{T}},\ {}^{K}\boldsymbol{\eta}_i \triangleq \left[\,\eta_i(k_0), \ldots, \eta_i(k_0+K-1)\,\right]^{\mathsf{T}},$$

and $\bar{K} \triangleq K \cdot (N - N_s)$. The Jacobian matrix $\mathbf{H}$ of the set of observations with respect to $\boldsymbol{x}_r'$ is given by $\mathbf{H} = \begin{bmatrix}\mathbf{G} & \bar{\mathbf{I}}_N\end{bmatrix}$, where $\mathbf{G} \triangleq \begin{bmatrix}\frac{\boldsymbol{r}_r - \boldsymbol{r}_{s_1}}{\|\boldsymbol{r}_r - \boldsymbol{r}_{s_1}\|}\mathbf{1}_K^{\mathsf{T}} & \ldots & \frac{\boldsymbol{r}_r - \boldsymbol{r}_{s_N}}{\|\boldsymbol{r}_r - \boldsymbol{r}_{s_N}\|}\mathbf{1}_K^{\mathsf{T}}\end{bmatrix}^{\mathsf{T}}$ and $\bar{\mathbf{I}}_N \triangleq \begin{bmatrix}\mathbf{I}_{K\times K} & \ldots & \mathbf{I}_{K\times K}\end{bmatrix}^{\mathsf{T}}$ where $\mathbf{I}_{K\times K}$ indicates the $K \times K$ identity matrix. The "overall" measurement noise, $(c\boldsymbol{\epsilon} + \boldsymbol{\eta})$, captures the errors due to measurement noise, base estimation errors, and discrepancies between the sectors' clock biases. It is modeled as a zero-mean random variable with a covariance matrix $\mathbf{R}$. The structure of $\mathbf{R}$ will be discussed in Subsections 3.2.2–3.2.3. The rover's state can now be estimated by solving a WNLS problem, to obtain an estimate of its state $\hat{\boldsymbol{x}}_r'$ and an associated estimation error covariance $\mathbf{P}$. The iterated WNLS equations are given by

$$\begin{aligned}\hat{\boldsymbol{x}}_r'^{(l+1)} &= \hat{\boldsymbol{x}}_r'^{(l)} + \left(\mathbf{H}^{\mathsf{T}}\mathbf{R}^{-1}\mathbf{H}\right)^{-1}\mathbf{H}^{\mathsf{T}}\mathbf{R}^{-1}\left(\boldsymbol{\rho} - \hat{\boldsymbol{\rho}}\right)\\ \mathbf{P}^{(l)} &= \left(\mathbf{H}^{\mathsf{T}}\mathbf{R}^{-1}\mathbf{H}\right)^{-1},\end{aligned}$$

where l is the iteration number and $\hat{\boldsymbol{\rho}}$ is $\hat{\boldsymbol{h}}$ evaluated at the current estimate $\hat{\boldsymbol{x}}_r'^{(l)}$.

3.2 Performance Characterization of the Base/Rover Framework with Pseudorange Measurements in the Presence of Sector Clock Bias Discrepancies

In this section, the estimation performance in the presence of the discrepancy discussed in Subsection 2.4 of Chapter 2 is analyzed as a function of time and the number of mismatches between the BTS cell sectors which the bases are listening to and those cell sectors which the rover is listening to. The estimation performance was characterized for a special case of this problem and for a static estimator only, where the discrepancy model was assumed to adhere to a random walk [98]. This section derives lower bounds on the determinant of the estimation error covariance for point and batch estimators with uncorrelated measurements between sets of sensors (SOPs), where each set has an arbitrary measurement noise covariance, and for a discrepancy that is modeled as an exponentially correlated random sequence. First, a general lower bound on the determinant of the estimation error covariance in the case of uncorrelated measurement noise is derived. Next, analytical expressions of the lower bounds on the determinant of the estimation error covariance in the presence of sector mismatch for two estimation frameworks are presented, namely a point solution and a batch solution. Finally, a practical upper bound on the position error is derived.

3.2.1 Estimation Error Covariance Lower Bound

This subsection derives the lower bound on the determinant of the estimation error covariance (D-optimality criterion) in the case of uncorrelated measurement noise and specifies an optimal BTS configuration that achieves this bound. The D-optimality criterion is chosen, since it is equivalent to minimizing the volume of the uncertainty ellipsoid [99] and is also a commonly used metric when studying the geometric dilution of precision [73]. The results

are captured in the following two theorems. It is important to note that the results presented in these two theorems are applicable beyond cellular CDMA systems. In fact, they apply to the general problem of a set of sensors (receiver) making pseudorange measurements on a source (transmitter). This problem is encountered in navigation and source localization.

Theorem 3.1. *Given $N \geq 3$ sets of K pseudorange measurements modeled according to (3.2) with a measurement noise covariance $\mathbf{R} = \mathrm{diag}[\mathbf{R}_1, \ldots, \mathbf{R}_N]$ where $\{\mathbf{R}_i\}_{i=1}^N$ is a set of $K \times K$ positive definite matrices, the determinant of the estimation error covariance $\mathbf{P}$ is lower bounded by*

$$\det[\mathbf{P}] \geq \frac{4}{\left(\sum_{i=1}^{N} \mathbf{1}_K^{\mathsf{T}} \mathbf{R}_i^{-1} \mathbf{1}_K\right)^2 \det\left[\sum_{i=1}^{N} \mathbf{R}_i^{-1}\right]}. \tag{3.3}$$

Proof. First, the Jacobian matrix $\mathbf{H}$ is re-parameterized by the bearing angles $\{\theta_i\}_{i=1}^N$ between the receiver and the N BTSs, as shown in Fig. 3.2(a). Subsequently, the matrix $\mathbf{G}$ can be re-expressed as $\mathbf{G} = [\boldsymbol{x} \quad \boldsymbol{y}]$, where $\boldsymbol{x} \triangleq \left[\cos\theta_1 \mathbf{1}_K^{\mathsf{T}}, \ldots, \cos\theta_N \mathbf{1}_K^{\mathsf{T}}\right]^{\mathsf{T}}$ and $\boldsymbol{y} \triangleq \left[\sin\theta_1 \mathbf{1}_K^{\mathsf{T}}, \ldots, \sin\theta_N \mathbf{1}_K^{\mathsf{T}}\right]^{\mathsf{T}}$. The information matrix $\mathbf{M}$ is given by

$$\mathbf{M} = \mathbf{P}^{-1} = \mathbf{H}^{\mathsf{T}} \mathbf{R}^{-1} \mathbf{H} = \begin{bmatrix} \mathbf{G}^{\mathsf{T}} \mathbf{R}^{-1} \mathbf{G} & \mathbf{G}^{\mathsf{T}} \mathbf{R}^{-1} \bar{\mathbf{I}}_N \\ \bar{\mathbf{I}}_N^{\mathsf{T}} \mathbf{R}^{-1} \mathbf{G} & \bar{\mathbf{I}}_N^{\mathsf{T}} \mathbf{R}^{-1} \bar{\mathbf{I}}_N \end{bmatrix}.$$

Assuming that $\mathbf{G}$ is full column-rank, which is guaranteed whenever at least three of the BTSs are non-collinear, and from the Schur complement properties, the determinant of $\mathbf{M}$ can be expressed as

$$\det[\mathbf{M}] = \det[\mathbf{M}_1] \det[\mathbf{M}_2 - \mathbf{M}_3],$$

where $\mathbf{M}_1 \triangleq \mathbf{G}^{\mathsf{T}} \mathbf{R}^{-1} \mathbf{G}$, $\mathbf{M}_2 \triangleq \bar{\mathbf{I}}_N^{\mathsf{T}} \mathbf{R}^{-1} \bar{\mathbf{I}}_N = \sum_{i=1}^{N} \mathbf{R}_i^{-1}$, and $\mathbf{M}_3 \triangleq \bar{\mathbf{I}}_N^{\mathsf{T}} \mathbf{R}^{-1} \mathbf{G} \left(\mathbf{G}^{\mathsf{T}} \mathbf{R}^{-1} \mathbf{G}\right)^{-1} \mathbf{G}^{\mathsf{T}} \mathbf{R}^{-1} \bar{\mathbf{I}}_N$.

By definition, $\mathbf{M}$ is a positive definite matrix, hence

$$\mathbf{M}_1 \succ \mathbf{0} \quad \text{and} \quad \mathbf{M}_2 - \mathbf{M}_3 \succ \mathbf{0}.$$

Also by definition, $\mathbf{M}_2$ is a positive definite matrix. Since $\mathbf{G}$ is full column-rank and $\mathbf{R}^{-1}$ is positive-definite, then $\left(\mathbf{G}^{\mathsf{T}}\mathbf{R}^{-1}\mathbf{G}\right)^{-1}$ will be positive-definite as well. The matrix $\mathbf{M}_3$ may also be expressed as $\mathbf{M}_3 = \mathbf{B}^{\mathsf{T}}\left(\mathbf{G}^{\mathsf{T}}\mathbf{R}^{-1}\mathbf{G}\right)^{-1}\mathbf{B}$, where $\mathbf{B} \triangleq \mathbf{G}^{\mathsf{T}}\mathbf{R}^{-1}\bar{\mathbf{I}}_N$; which readily shows that $\mathbf{M}_3$ is positive semi-definite. Therefore, it can be deduced that

$$\mathbf{M}_2 \succeq \mathbf{M}_2 - \mathbf{M}_3,$$

and hence

$$\det\left[\mathbf{M}_2\right] \geq \det\left[\mathbf{M}_2 - \mathbf{M}_3\right].$$

Subsequently, the following upper bound may be established on $\det\left[\mathbf{M}\right]$

$$\det\left[\mathbf{M}\right] \leq \det\left[\mathbf{G}^{\mathsf{T}}\mathbf{R}^{-1}\mathbf{G}\right] \det\left[\sum_{i=1}^{N} \mathbf{R}_i^{-1}\right]. \tag{3.4}$$

The matrix $\mathbf{M}_1 = \mathbf{G}^{\mathsf{T}}\mathbf{R}^{-1}\mathbf{G}$ may be expressed as

$$\mathbf{G}^{\mathsf{T}}\mathbf{R}^{-1}\mathbf{G} = \begin{bmatrix} \boldsymbol{x}^{\mathsf{T}}\mathbf{R}^{-1}\boldsymbol{x} & \boldsymbol{x}^{\mathsf{T}}\mathbf{R}^{-1}\boldsymbol{y} \\ \boldsymbol{y}^{\mathsf{T}}\mathbf{R}^{-1}\boldsymbol{x} & \boldsymbol{y}^{\mathsf{T}}\mathbf{R}^{-1}\boldsymbol{y} \end{bmatrix},$$

which has the determinant

$$\begin{aligned} \det\left[\mathbf{G}^{\mathsf{T}}\mathbf{R}^{-1}\mathbf{G}\right] &= \left(\boldsymbol{x}^{\mathsf{T}}\mathbf{R}^{-1}\boldsymbol{x}\right)\left(\boldsymbol{y}^{\mathsf{T}}\mathbf{R}^{-1}\boldsymbol{y}\right) - \left(\boldsymbol{x}^{\mathsf{T}}\mathbf{R}^{-1}\boldsymbol{y}\right)^2 \\ &\leq \left(\boldsymbol{x}^{\mathsf{T}}\mathbf{R}^{-1}\boldsymbol{x}\right)\left(\boldsymbol{y}^{\mathsf{T}}\mathbf{R}^{-1}\boldsymbol{y}\right). \end{aligned} \tag{3.5}$$

Equations (3.4) and (3.5) yield

$$\det\left[\mathbf{M}\right] \leq \left(\boldsymbol{x}^{\mathsf{T}}\mathbf{R}^{-1}\boldsymbol{x}\right)\left(\boldsymbol{y}^{\mathsf{T}}\mathbf{R}^{-1}\boldsymbol{y}\right)\det\left[\sum_{i=1}^{N}\mathbf{R}_i^{-1}\right]. \tag{3.6}$$

Using the definition of $\boldsymbol{x}$ and $\boldsymbol{y}$ and noting that $\mathbf{R}^{-1} = \operatorname{diag}\left[\mathbf{R}_1^{-1},\ldots,\mathbf{R}_N^{-1}\right]$, the following can be deduced

$$\begin{aligned}\boldsymbol{x}^{\mathsf{T}}\mathbf{R}^{-1}\boldsymbol{x} + \boldsymbol{y}^{\mathsf{T}}\mathbf{R}^{-1}\boldsymbol{y} &= \sum_{i=1}^{N}\mathbf{1}_K^{\mathsf{T}}\mathbf{R}_i^{-1}\mathbf{1}_K\cos^2\theta_i \\ &\quad + \sum_{i=1}^{N}\mathbf{1}_K^{\mathsf{T}}\mathbf{R}_i^{-1}\mathbf{1}_K\sin^2\theta_i \\ &= \sum_{i=1}^{N}\mathbf{1}_K^{\mathsf{T}}\mathbf{R}_i^{-1}\mathbf{1}_K. \end{aligned}\tag{3.7}$$

Defining $u \triangleq \boldsymbol{x}^{\mathsf{T}}\mathbf{R}^{-1}\boldsymbol{x}$ and $a \triangleq \sum_{i=1}^{N}\mathbf{1}_K^{\mathsf{T}}\mathbf{R}_i^{-1}\mathbf{1}_K$ and incorporating the geometric constraint (3.7) into (3.6) yields

$$\det\left[\mathbf{M}\right] \leq u\left(a-u\right)\det\left[\sum_{i=1}^{N}\mathbf{R}_i^{-1}\right]. \tag{3.8}$$

The right-hand side of (3.8) is maximized when $u^\star = \frac{a}{2} = \frac{1}{2}\sum_{i=1}^{N}\mathbf{1}_K^{\mathsf{T}}\mathbf{R}_i^{-1}\mathbf{1}_K$. This finally yields

$$\det[\mathbf{P}] = \frac{1}{\det[\mathbf{M}]} \geq \frac{4}{\left(\sum_{i=1}^{N}\mathbf{1}_K^{\mathsf{T}}\mathbf{R}_i^{-1}\mathbf{1}_K\right)^2\det\left[\sum_{i=1}^{N}\mathbf{R}_i^{-1}\right]}.$$

□

Corollary 3.1.1. *If $K = 1$, i.e., $\mathbf{R}_i = \sigma_i^2$, the lower bound simplifies to*

$$\det\left[\mathbf{P}\right] \geq \frac{4}{\left[\operatorname{trace}\left(\mathbf{R}^{-1}\right)\right]^3}.$$

Proof. This can be seen by noting that $\sum_{i=1}^{N} \mathbf{1}_K^{\mathsf{T}} \mathbf{R}_i^{-1} \mathbf{1}_K = \sum_{i=1}^{N} \mathbf{R}_i^{-1} = \sum_{i=1}^{N} \frac{1}{\sigma_i^2} = \text{trace}\,(\mathbf{R}^{-1})$. □

Theorem 3.2. *Given a total of N BTSs grouped into L sets with $N_l \geq 3$ BTSs in each set, where $l = 1, \ldots, L$, and given that the receiver is drawing K pseudorange measurements from each set of BTSs with noise covariance $\{\mathbf{\Sigma}_l = \text{diag}[\mathbf{R}_l, \ldots, \mathbf{R}_l]\}_{l=1}^{L}$ where $\{\mathbf{R}_l\}_{l=1}^{L}$ is a set of $K \times K$ positive definite matrices, the optimal estimation performance that minimizes the determinant of the estimation error covariance is achieved when each set of BTSs forms a regular polygon around the receiver, i.e.,*

$$\theta_{i_l}^{(l)} = \frac{2\pi}{N_l} i_l + \theta_0^{(l)}, \quad i_l = 1, \ldots, N_l,$$

where $\theta_{i_l}^{(l)}$ is the bearing angle between the receiver and the i_lth BTS in lth set and $\theta_0^{(l)}$ is an arbitrary offset angle.

The optimal BTS configuration is illustrated in Fig. 3.2(b).

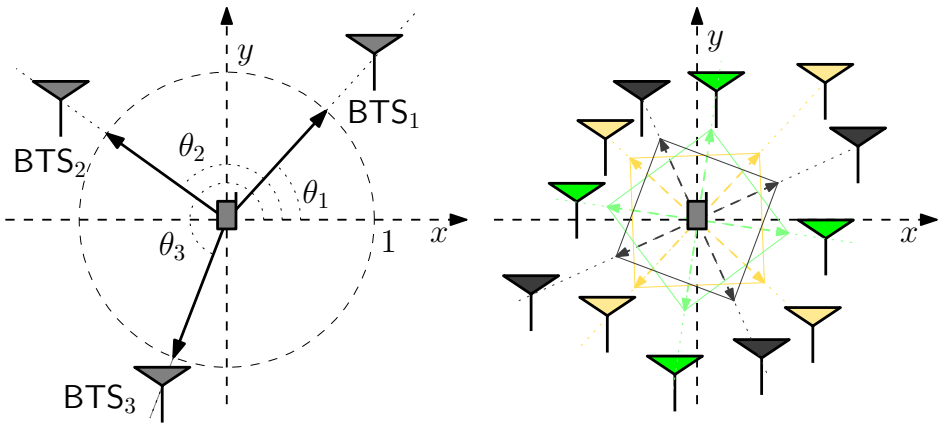

(a) (b)

Figure 3.2: (a) Re-parametrization of the unit line-of-sight (LOS) vectors by the bearing angles. (b) Optimal distribution of the BTSs around the receiver where each color represents a different set of BTSs.

Proof. In general, for $\left\{\theta_{i_l} = \frac{2\pi i_l}{N_l} + \theta_{i_0}\right\}_{i_l=1}^{N_l}$ and any integer $N_l \geq 3$ and constant offset angle

θ_{i_0}, the following holds [69]

$$\sum_{i_l=1}^{N_l} \cos^2 \theta_{i_l} = \sum_{i_l=1}^{N_l} \sin^2 \theta_{i_l} = \frac{N_l}{2}, \tag{3.9}$$

$$\sum_{i_l=1}^{N_l} \cos \theta_{i_l} \sin \theta_{i_l} = \sum_{i_l=1}^{N_l} \cos \theta_{i_l} = \sum_{i_l=1}^{N_l} \sin \theta_{i_l} = 0. \tag{3.10}$$

Note that (3.9) and (3.10) hold for any offset angle θ_{i_0}. The information matrix can be expressed as

$$\mathbf{M} = \begin{bmatrix} \boldsymbol{x}^{\mathsf{T}}\mathbf{R}^{-1}\boldsymbol{x} & \boldsymbol{x}^{\mathsf{T}}\mathbf{R}^{-1}\boldsymbol{y} & \boldsymbol{x}^{\mathsf{T}}\mathbf{R}^{-1}\bar{\mathbf{I}}_N \\ \boldsymbol{y}^{\mathsf{T}}\mathbf{R}^{-1}\boldsymbol{x} & \boldsymbol{y}^{\mathsf{T}}\mathbf{R}^{-1}\boldsymbol{y} & \boldsymbol{y}^{\mathsf{T}}\mathbf{R}^{-1}\bar{\mathbf{I}}_N \\ \bar{\mathbf{I}}_N^{\mathsf{T}}\mathbf{R}^{-1}\boldsymbol{x} & \bar{\mathbf{I}}_N^{\mathsf{T}}\mathbf{R}^{-1}\boldsymbol{y} & \bar{\mathbf{I}}_N^{\mathsf{T}}\mathbf{R}^{-1}\bar{\mathbf{I}}_N \end{bmatrix}.$$

Define the partitioned vectors

$$\boldsymbol{x} \triangleq \begin{bmatrix} \boldsymbol{x}_1 \\ \vdots \\ \boldsymbol{x}_L \end{bmatrix}, \quad \boldsymbol{y} \triangleq \begin{bmatrix} \boldsymbol{y}_1 \\ \vdots \\ \boldsymbol{y}_L \end{bmatrix}, \quad \mathbf{1}_N \triangleq \begin{bmatrix} \mathbf{1}_{N_1} \\ \vdots \\ \mathbf{1}_{N_L} \end{bmatrix},$$

where $\boldsymbol{x}_l = \left[\cos\theta_1^{(l)}\mathbf{1}_K^{\mathsf{T}}, \ldots, \cos\theta_{N_l}^{(l)}\mathbf{1}_K^{\mathsf{T}}\right]^{\mathsf{T}}$ and $\boldsymbol{y}_l = \left[\sin\theta_1^{(l)}\mathbf{1}_K^{\mathsf{T}}, \ldots, \sin\theta_{N_l}^{(l)}\mathbf{1}_K^{\mathsf{T}}\right]^{\mathsf{T}}$, where $l = 1, \ldots, L$. The overall measurement noise covariance is defined as

$$\mathbf{R} \triangleq \operatorname{diag}\left[\boldsymbol{\Sigma}_1, \ldots, \boldsymbol{\Sigma}_L\right],$$

where $\boldsymbol{\Sigma}_l = \operatorname{diag}[\mathbf{R}_l, \ldots, \mathbf{R}_l]$ (repeated N_l times). Subsequently, $\boldsymbol{x}^{\mathsf{T}}\mathbf{R}^{-1}\boldsymbol{x}$ can be expressed

as

$$\begin{aligned}
\boldsymbol{x}^{\mathsf{T}}\mathbf{R}^{-1}\boldsymbol{x} &= \sum_{l=1}^{L}\boldsymbol{x}_l^{\mathsf{T}}\boldsymbol{\Sigma}_l^{-1}\boldsymbol{x}_l \\
&= \sum_{l=1}^{L}\sum_{i_l=1}^{N_l}\mathbf{1}_K^{\mathsf{T}}\mathbf{R}_l^{-1}\mathbf{1}_K\cos^2\theta_{i_l}^{(l)} \\
&= \sum_{l=1}^{L}\mathbf{1}_K^{\mathsf{T}}\mathbf{R}_l^{-1}\mathbf{1}_K\sum_{i_l=1}^{N_l}\cos^2\theta_{i_l}^{(l)}. \qquad (3.11)
\end{aligned}$$

Similarly, it can be shown that

$$\begin{aligned}
\boldsymbol{x}^{\mathsf{T}}\mathbf{R}^{-1}\boldsymbol{x} &= \sum_{l=1}^{L}\mathbf{1}_K^{\mathsf{T}}\mathbf{R}_l^{-1}\mathbf{1}_K\sum_{i_l=1}^{N_l}\sin^2\theta_{i_l}^{(l)}, \qquad (3.12)\\
\boldsymbol{x}^{\mathsf{T}}\mathbf{R}^{-1}\boldsymbol{y} &= \sum_{l=1}^{L}\mathbf{1}_K^{\mathsf{T}}\mathbf{R}_l^{-1}\mathbf{1}_K\sum_{i_l=1}^{N_l}\cos\theta_{i_l}^{(l)}\sin\theta_{i_l}^{(l)}, \qquad (3.13)\\
\boldsymbol{x}^{\mathsf{T}}\mathbf{R}^{-1}\bar{\mathbf{I}}_N &= \sum_{l=1}^{L}\mathbf{1}_K^{\mathsf{T}}\mathbf{R}_l^{-1}\sum_{i_l=1}^{N_l}\cos\theta_{i_l}^{(l)}, \qquad (3.14)\\
\boldsymbol{y}^{\mathsf{T}}\mathbf{R}^{-1}\bar{\mathbf{I}}_N &= \sum_{l=1}^{L}\mathbf{1}_K^{\mathsf{T}}\mathbf{R}_l^{-1}\sum_{i_l=1}^{N_l}\sin\theta_{i_l}^{(l)}, \qquad (3.15)\\
\bar{\mathbf{I}}_N^{\mathsf{T}}\mathbf{R}^{-1}\bar{\mathbf{I}}_N &= \sum_{l=1}^{L}N_l\mathbf{R}_l^{-1}. \qquad (3.16)
\end{aligned}$$

From (3.9)–(3.16) and the optimal BTS configuration, i.e., each set of BTSs forms a regular polygon around the receiver, the information matrix can be expressed as,

$$\mathbf{M}=\begin{bmatrix}
\sum_{l=1}^{L}\frac{N_l}{2}\mathbf{1}_K^{\mathsf{T}}\mathbf{R}_l^{-1}\mathbf{1}_K & 0 & \mathbf{0}_{K\times 1}^{\mathsf{T}} \\
0 & \sum_{l=1}^{L}\frac{N_l}{2}\mathbf{1}_K^{\mathsf{T}}\mathbf{R}_l^{-1}\mathbf{1}_K & \mathbf{0}_{K\times 1}^{\mathsf{T}} \\
\mathbf{0}_{K\times 1} & \mathbf{0}_{K\times 1} & \sum_{l=1}^{L}N_l\mathbf{R}_l^{-1}
\end{bmatrix},$$

hence

$$\mathbf{P} = \begin{bmatrix} \frac{2}{\sum_{l=1}^{L} N_l \mathbf{1}_K^{\mathsf{T}} \mathbf{R}_l^{-1} \mathbf{1}_K} & 0 & \mathbf{0}_{K\times 1}^{\mathsf{T}} \\ 0 & \frac{2}{\sum_{l=1}^{L} N_l \mathbf{1}_K^{\mathsf{T}} \mathbf{R}_l^{-1} \mathbf{1}_K} & \mathbf{0}_{K\times 1}^{\mathsf{T}} \\ \mathbf{0}_{K\times 1} & \mathbf{0}_{K\times 1} & \left[\sum_{l=1}^{L} N_l \mathbf{R}_l^{-1}\right]^{-1} \end{bmatrix}. \tag{3.17}$$

By noting that $\sum_{i=1}^{N} \mathbf{1}_K^{\mathsf{T}} \mathbf{R}_i^{-1} \mathbf{1}_K = \sum_{l=1}^{L} N_l \mathbf{1}_K^{\mathsf{T}} \mathbf{R}_l^{-1} \mathbf{1}_K$ and that $\sum_{i=1}^{N} \mathbf{R}_i^{-1} = \sum_{l=1}^{L} N_l \mathbf{R}_l^{-1}$, the determinant of the estimation error covariance may be expressed as

$$\det[\mathbf{P}] = \frac{4}{\left(\sum_{i=1}^{N} \mathbf{1}_K^{\mathsf{T}} \mathbf{R}_i^{-1} \mathbf{1}_K\right)^2 \det\left[\sum_{i=1}^{N} \mathbf{R}_i^{-1}\right]}. \tag{3.18}$$

Therefore, the configuration described in Theorem 3.2 (with determinant computed in (3.18)) indeed achieves the lower bound established in Theorem 3.1 (cf. (3.3)). □

It is worth noting that the results in Theorem 3.2 are applicable beyond cellular CDMA systems and the base/rover framework. The problem can be regarded as an optimal sensor placement problem, where it is desired to place sensors (bases) in a way that minimizes the uncertainty in the SOP's state. Moreover, these results can provide an insight on the minimum requirements of the system. If the required performance happens to violate the bound, the system designer will know that this performance is not achievable and either more SOPs or sensors must be employed or more measurements must be taken. Hence, Theorem 3.2 could be used to deduce necessary system settings to make a desired performance achievable. The optimal performance based on minimizing the determinant of the estimation error covariance in the presence of sector mismatch is analyzed next.

3.2.2 Lower Bound on the Determinant of the Estimation Error Covariance in the Presence of Sector Mismatch: Point Solution

In this scenario, the rover is solving for its state at time k using the measurements made at time k, i.e., $k_0 = k$ and $K = 1$. The overall measurement noise covariance in this case is given by

$$\mathbf{R} = \text{diag}\left[\left(\sigma_\eta^2 + \sigma_\epsilon^2(k)\right)\mathbf{I}_{N_s \times N_s}, \sigma_\eta^2 \mathbf{I}_{(N-N_s)\times(N-N_s)}\right], \tag{3.19}$$

where $\sigma_\epsilon^2(k) \triangleq \frac{c^2\lambda^2}{\alpha}\left(1 - e^{-2\alpha k T}\right)$. By applying Theorem 3.2 and Corollary 3.1.1, the optimal estimation error covariance under sector clock bias discrepancies can be found from (3.17) to yield

$$\mathbf{P}^\star = \begin{bmatrix} \mathbf{P}_{x,y}^\star & \mathbf{0}_{2\times 1} \\ \mathbf{0}_{1\times 2} & \left(\sigma_{c\delta t_r}^\star\right)^2 \end{bmatrix} = \begin{bmatrix} 2\sigma_{\text{eq}}^2 \mathbf{I}_{2\times 2} & \mathbf{0}_{2\times 1} \\ \mathbf{0}_{1\times 2} & \sigma_{\text{eq}}^2 \end{bmatrix}, \tag{3.20}$$

where

$$\begin{aligned} \sigma_{\text{eq}}^2 &\triangleq \frac{1}{\text{trace}\left(\mathbf{R}^{-1}\right)} = \frac{1}{\frac{N_s}{\sigma_\eta^2 + \sigma_\epsilon^2(k)} + \frac{N-N_s}{\sigma_\eta^2}} \\ &= \frac{\left[\sigma_\eta^2 + \frac{c^2\lambda^2}{\alpha}\left(1 - e^{-2\alpha k T}\right)\right]\sigma_\eta^2}{N\sigma_\eta^2 + (N - N_s)\frac{c^2\lambda^2}{\alpha}\left(1 - e^{-2\alpha k T}\right)}. \end{aligned} \tag{3.21}$$

In order to demonstrate the result in (3.20), Monte Carlo simulations were conducted for several N_s and k values. The logarithm of the determinant of each resulting position estimation error covariance $\mathbf{P}_{x,y}$, namely $\log\det\left[\mathbf{P}_{x,y}\right]$, for 500 runs were plotted along with $\log\det\left[\mathbf{P}_{x,y}^\star\right]$ obtained in (3.20). A surface plot of $\log\det\left[\mathbf{P}_{x,y}^\star\right]$ and the Monte Carlo simulation results for $\log\det\left[\mathbf{P}_{x,y}\right]$ are shown in Fig. 3.3.

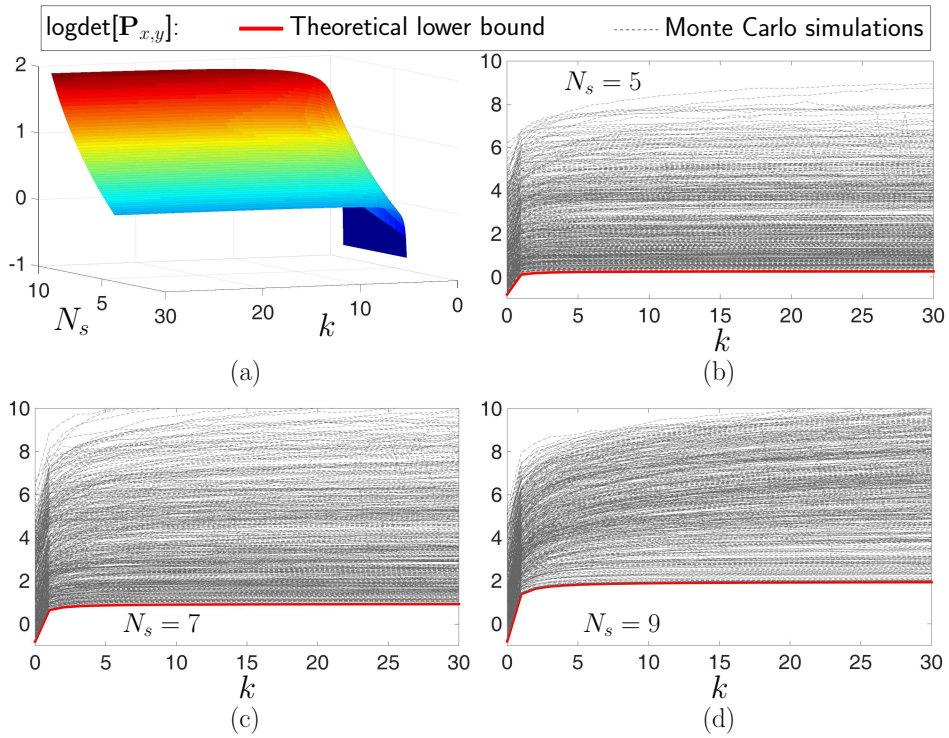

Figure 3.3: (a) Surface plot of $\log\det\left[\mathbf{P}^{\star}_{x,y}\right]$ as a function of N_s and k. (b)–(d) Plots of $\log\det\left[\mathbf{P}_{x,y}\right]$ for 500 Monte Carlo simulations along with the theoretical lower bound $\log\det\left[\mathbf{P}^{\star}_{x,y}\right]$. Simulation parameters: $N = 12$, $T = 0.2$s, $\alpha = 10^{-3}$Hz, $\sigma_\eta^2 = 4$ m^2, and $\lambda = 66$ ns/s.

The following remarks can be concluded from these simulations.

Remark 1. For a fixed $N_s < N$, $\log\det\left[\mathbf{P}^{\star}_{x,y}\right]$ becomes almost constant after five to ten time steps and converges to a constant value that can be approximated to be

$$\lim_{k\to\infty} \log\det\left[\mathbf{P}^{\star}_{x,y}\right] \approx \log\left[4\left(\frac{\sigma_\eta^2}{N-N_s}\right)^2\right]. \tag{3.22}$$

The derivation of (3.22) is given in Appendix A. The same expression is obtained when the rover uses only the measurements from the $N-N_s$ BTSs with no sector mismatch to estimate its state. This is attributed to the fact that the variance of the error in the measurements coming from the BTSs with sector mismatch increases with time until it reaches a steady value (cf. (3.19)). This steady state value is much larger than σ_η^2 and therefore these measurements will be "almost neglected" by the estimator.

Remark 2. For large k, one can approximate $\log\det\left[\mathbf{P}^{\star}_{x,y}\right]$

$$\log\det\left[\mathbf{P}^{\star}_{x,y}\right] \approx -2\log\left(1-\frac{N_s}{N}\right)+\xi, \tag{3.23}$$

where ξ is a finite constant. The derivation of (3.23) is given in Appendix B. It can be readily seen that (3.23) approaches ∞ as N_s approaches N. It is therefore imperative to have at least one BTS with no sector mismatch in order for the estimation error covariance to be bounded.

3.2.3 Lower Bound on the Determinant of the Estimation Error Covariance in the Presence of Sector Mismatch: Batch Estimator

In this scenario, the rover is assumed to be either stationary or mobile but has perfect knowledge of the change in its position with $k_0 = 1$ and $K > 1$. Starting at $k_0 = 1$ ensures that the pseudorange measurements are affected by the error due to clock bias discrepancy in the case of sector mismatch. In order to make the analysis more tractable, the exponentially correlated model in the batch estimator is approximated by a random walk, i.e., $\alpha \to 0$. For small values of α and k, the relative error between the variances of these processes is guaranteed to be less than an arbitrary small threshold [85]. Subsequently, $\sigma^2_{\epsilon}(k)$ is approximated by

$$\sigma^2_{\epsilon}(k) \approx \bar{\sigma}^2_{\epsilon}(k) \triangleq \lim_{\alpha\to 0}\sigma^2_{\epsilon}(k) = 2kTc^2\lambda^2, \tag{3.24}$$

where $k = 1,\ldots,K$. The overall measurement noise covariance in this case is given by

$$\mathbf{R} = \mathrm{diag}[\mathbf{R}_1,\ldots,\mathbf{R}_N],$$

where $\{\mathbf{R}_i\}_{i=1}^{N}$ is a set of $K \times K$ positive definite matrices with

$$\mathbf{R}_i = \begin{cases} \sigma_\eta^2 \mathbf{I}_{K\times K} + \mathbf{R}_\epsilon, & \text{if } i \leq N_s, \\ \sigma_\eta^2 \mathbf{I}_{K\times K}, & \text{otherwise,} \end{cases}$$

where

$$[\mathbf{R}_\epsilon]_{m,n} = \sigma_\epsilon^2 \left[\min\{m,n\}\right], \quad m,n = 1,\dots K,$$

and $[\mathbf{\Psi}]_{m,n}$ denotes the element in the mth row and nth column of matrix $\mathbf{\Psi}$. Using this approximation of $\sigma_{\eta_s}^2(k)$ and by applying Theorem 3.2, the optimal estimation error covariance under sector clock bias discrepancies for a batch estimator can be approximated by

$$\mathbf{P}'^{\star} \approx \begin{bmatrix} \mathbf{P}'^{\star}_{x,y} & \mathbf{0}_{K\times 1}^{\mathsf{T}} \\ \mathbf{0}_{K\times 1} & \mathbf{P}'^{\star}_{c\delta t_r} \end{bmatrix},$$

where

$$\mathbf{P}'^{\star}_{x,y} = \frac{4c^2\lambda^2 T \sigma_\eta^2 \mathbf{I}_{2\times 2}}{f(\beta)\sigma_\eta^2 N_s + 2c^2(N-N_s)K\lambda^2 T}, \tag{3.25}$$

$$\mathbf{P}'^{\star}_{c\delta t_r} = \left[N_s {\mathbf{R}_\epsilon}^{-1} + \frac{N-N_s}{\sigma_\eta^2}\mathbf{I}_{K\times K}\right]^{-1}, \quad \beta \triangleq \frac{\sigma_{\eta_s}^2}{\sigma_\epsilon^2(1)},$$

and $f(\beta)$ is a function of β. The expression of $f(\beta)$ and the derivation of (3.25) are outlined in Appendix C.

Monte Carlo simulations for several N_s and k values were conducted to demonstrate the result in (3.25). The logarithm of the determinant of each resulting position estimation error covariance $\mathbf{P}'_{x,y}$, namely $\log\det\left[\mathbf{P}'_{x,y}\right]$, for 500 runs were plotted along with $\log\det\left[\mathbf{P}'^{\star}_{x,y}\right]$ obtained in (3.25). A surface plot of $\log\det\left[\mathbf{P}'^{\star}_{x,y}\right]$ and the Monte Carlo simulation results for $\log\det\left[\mathbf{P}'_{x,y}\right]$ are shown in Fig. 3.4.

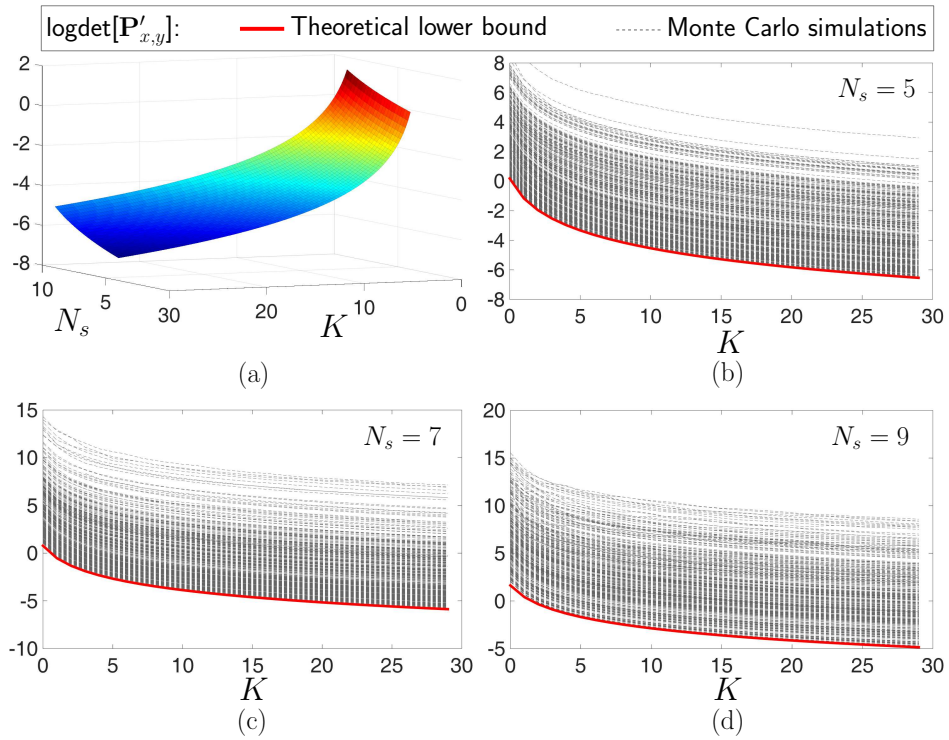

Figure 3.4: (a) Surface plot of $\log\det\left[\mathbf{P}'^{\star}_{x,y}\right]$ as a function of N_s and k. (b)–(d) Plots of $\log\det\left[\mathbf{P}'_{x,y}\right]$ for 500 Monte Carlo simulations along with the theoretical lower bound $\log\det\left[\mathbf{P}'^{\star}_{x,y}\right]$. Simulation parameters: $N = 12$, $T = 0.2$ s, $\alpha = 10^{-3}$ Hz, $\sigma_\eta^2 = 4$ m^2, and $\lambda = 66$ ns/s.

The following remarks can be concluded from these simulations.

Remark 1. For a fixed $N_s < N$, $\log\det\left[\mathbf{P}'^{\star}_{x,y}\right]$ is a strictly decreasing function of K, and it can be concluded that (3.25) approaches zero as $K \to \infty$. This implies that a good strategy for the rover in the presence of sector mismatch is to stand still if it does not have exact knowledge on the change in its position.

Remark 2. For large K, the approximation $f(\beta)N_s\sigma_\eta^2 + 2c^2(N - N_s)K\lambda^2 T \approx 2c^2(N - N_s)K\lambda^2 T$ can be made, since $f(\beta)N_s\sigma_\eta^2$ is constant for a given σ_η^2 and $\bar{\sigma}_\epsilon^2(1)$, and therefore $2c^2(N - N_s)K\lambda^2 T >> f(\beta)N_s\sigma_\eta^2$ for large K. Subsequently, (3.25) can be approximated by

$$\mathbf{P}'^{\star}_{x,y} \approx \frac{2\sigma_\eta^2 \mathbf{I}_{2\times 2}}{(N - N_s)\,K}. \tag{3.26}$$

The same expression is obtained when the rover uses only the measurements from the $N-N_s$ BTSs with no sector mismatch to estimate its state. This results from the fact that the measurements coming from the N_s BTSs with sector mismatch are highly correlated in time and the uncertainty associated with these measurements is a strictly increasing function of K. Thus, subsequent measurements from BTSs with sector mismatch will bring little to no contribution in estimating the state of the rover and will therefore be "neglected" by the estimator.

Remark 3. It is also worth noting that when $N_s = N$, the optimal position estimation error covariance becomes

$$\mathbf{P}'^{\star}_{x,y} = \frac{4c^2K\lambda^2T\mathbf{I}_{2\times 2}}{f(\beta)\sigma_\eta^2 N},$$

which is a finite constant. In contrast to the point solution case, the need to have at least one measurement coming from a BTS with no mismatch between the base and rover sectors is eliminated in the batch estimator.

3.2.4 Practical Upper Bound on the Position Error

This subsection characterizes an upper bound on the position error due to the discrepancy between sectors' clock biases. To this end, it is assumed that $N_s = N$, i.e., the base receivers are listening to different sectors than the navigating receiver, and the latter is not aware of the presence of these discrepancies. It is also assumed that the WNLS is in steady state, and the discrepancies $\boldsymbol{\epsilon} = [\epsilon_1, \ldots, \epsilon_N]^\mathsf{T}$ are suddenly introduced into the measurements, which will induce an incremental change in the receiver state estimate $\delta\boldsymbol{x}_r = c\left(\mathbf{H}^\mathsf{T}{\mathbf{R}_\eta}^{-1}\mathbf{H}\right)^{-1}\mathbf{H}^\mathsf{T}{\mathbf{R}_\eta}^{-1}\boldsymbol{\epsilon}$. In general, the discrepancy vector $\boldsymbol{\epsilon}$ can be expressed as

$$\boldsymbol{\epsilon} = b\mathbf{1}_N + \boldsymbol{\psi}, \tag{3.27}$$

where $b \triangleq \frac{1}{N}\sum_{i=1}^{N}\epsilon_i = \frac{1}{N}\mathbf{1}_N^{\mathsf{T}}\boldsymbol{\epsilon}$, and $\boldsymbol{\psi} \triangleq [\epsilon_1 - b, \ldots, \epsilon_N - b]^{\mathsf{T}}$. The term b is referred to as the common error and the vector $\boldsymbol{\psi}$ as the unbiased error. It follows from this definition that $\sum_{i=1}^{N}\psi_i = 0$. By replacing the expression of $\boldsymbol{\epsilon}$ in a WNLS step, the incremental change in the receiver state estimate can be expressed as $\delta\boldsymbol{x}_r = \delta\boldsymbol{x}_r^{(b)} + \delta\boldsymbol{x}_r^{(\psi)}$, where $\delta\boldsymbol{x}_r^{(b)} = cb\left(\mathbf{H}^{\mathsf{T}}{\mathbf{R}_\eta}^{-1}\mathbf{H}\right)^{-1}\mathbf{H}^{\mathsf{T}}{\mathbf{R}_\eta}^{-1}\mathbf{1}_N$ is the effect of the common error and $\delta\boldsymbol{x}_r^{(\psi)} = c\left(\mathbf{H}^{\mathsf{T}}{\mathbf{R}_\eta}^{-1}\mathbf{H}\right)^{-1}\mathbf{H}^{\mathsf{T}}{\mathbf{R}_\eta}^{-1}\boldsymbol{\psi}$ is the effect of the unbiased error.

Effect of Common Error on Navigation Solution

The common error term will only affect the receiver clock bias estimate. This can be shown by realizing that

$$\mathbf{H}\boldsymbol{e}_3 = [\mathbf{G} \quad \mathbf{1}_N]\,\boldsymbol{e}_3 = \mathbf{1}_N, \tag{3.28}$$

where $\boldsymbol{e}_3 = [0, 0, 1]^{\mathsf{T}}$. Then, using (3.28), the incremental change due to the common term becomes

$$\begin{aligned}\delta\boldsymbol{x}_r^{(b)} &= cb\left(\mathbf{H}^{\mathsf{T}}{\mathbf{R}_\eta}^{-1}\mathbf{H}\right)^{-1}\mathbf{H}^{\mathsf{T}}{\mathbf{R}_\eta}^{-1}\mathbf{1}_N \\ &= cb\left(\mathbf{H}^{\mathsf{T}}{\mathbf{R}_\eta}^{-1}\mathbf{H}\right)^{-1}\mathbf{H}^{\mathsf{T}}{\mathbf{R}_\eta}^{-1}\mathbf{H}\boldsymbol{e}_3 = cb\boldsymbol{e}_3,\end{aligned} \tag{3.29}$$

which has a non-zero component only in the clock bias state. Thus, if the individual discrepancies ϵ_i happen to be all equal, the receiver's position estimate will be unaffected.

Effect of Unbiased Error on Navigation Solution

Unlike the common error, the unbiased error will affect all receiver states. The following theorem establishes a bound on the error introduced by the unbiased error in the receiver's position estimate.

Theorem 3.3. *In a cellular environment comprising N BTSs in which the base and the rover are experiencing bounded sector mismatches ϵ_i, such that $|\epsilon_i| \leq \alpha$, $\forall\, i$, the error induced by the mismatches in the receiver's position estimate is bounded by*

$$\|\delta \boldsymbol{r}_r\| \leq \begin{cases} \sqrt{N}\alpha\,\kappa, & \text{if } N \text{ is even,} \\ \sqrt{\frac{N^2-1}{N}}\alpha\,\kappa, & \text{if } N \text{ is odd,} \end{cases}$$

where $\kappa \triangleq c \left\| \left(\mathbf{H}^{\mathsf{T}} {\mathbf{R}_\eta}^{-1} \mathbf{H}\right)^{-1} \mathbf{H}^{\mathsf{T}} {\mathbf{R}_\eta}^{-1} \right\|$.

Proof. The incremental change in the receiver position state estimate can be expressed as $\delta \boldsymbol{r}_r = \mathbf{T}\delta \boldsymbol{x}_r = \mathbf{T}\delta \boldsymbol{x}_r^{(b)} + \mathbf{T}\delta \boldsymbol{x}_r^{(\psi)}$, where $\mathbf{T} = [\mathbf{I}_{2\times 2} \quad \mathbf{0}_{2\times 1}]$. By replacing $\delta \boldsymbol{x}_r^{(b)}$ with its expression from (3.29), the change in position becomes

$$\delta \boldsymbol{r}_r = cb\mathbf{T}\boldsymbol{e}_3 + \mathbf{T}\delta \boldsymbol{x}_r^{(\psi)} = \mathbf{T}\delta \boldsymbol{x}_r^{(\psi)}. \tag{3.30}$$

Taking the 2-norm on both sides of (3.30) yields

$$\begin{aligned} \|\delta \boldsymbol{r}_r\| &= \left\|\mathbf{T}\delta \boldsymbol{x}_r^{(\psi)}\right\| \\ &\leq \|\mathbf{T}\| \cdot \left\|\delta \boldsymbol{x}_r^{(\psi)}\right\| = \left\|\delta \boldsymbol{x}_r^{(\psi)}\right\|, \end{aligned} \tag{3.31}$$

since $\|\mathbf{T}\| = 1$. Replacing $\delta \boldsymbol{x}_r^{(\psi)}$ by its expression in the WNLS update, (3.31) becomes

$$\begin{aligned} \|\delta \boldsymbol{r}_r\| &\leq \left\| c \left(\mathbf{H}^{\mathsf{T}} {\mathbf{R}_\eta}^{-1} \mathbf{H}\right)^{-1} \mathbf{H}^{\mathsf{T}} {\mathbf{R}_\eta}^{-1} \left(\boldsymbol{\epsilon} - b\mathbf{1}_N\right) \right\| \\ &\leq \kappa \left\|\boldsymbol{\epsilon} - b\mathbf{1}_N\right\|. \end{aligned} \tag{3.32}$$

Therefore, to determine the upper bound of (3.32), the term $\|\boldsymbol{\epsilon} - b\mathbf{1}_N\|$, or equivalently its square, must be maximized, leading to

$$\underset{\boldsymbol{\epsilon}}{\text{maximize}} \quad \left\|\boldsymbol{\epsilon} - b\mathbf{1}_N\right\|^2 = \left\|\mathbf{A}\boldsymbol{\epsilon}\right\|^2, \tag{3.33}$$

$$\mathbf{A} \triangleq \begin{bmatrix} (1-\frac{1}{N}) & -\frac{1}{N} & \cdots & -\frac{1}{N} \\ -\frac{1}{N} & (1-\frac{1}{N}) & \cdots & -\frac{1}{N} \\ \vdots & \vdots & \ddots & \vdots \\ -\frac{1}{N} & -\frac{1}{N} & \cdots & (1-\frac{1}{N}) \end{bmatrix}.$$

Motivated by experimental data collected in different BTS cell sectors and for various cells, it is reasonable to assume that

$$|\epsilon_i| \leq \alpha, \quad \forall\, i, \tag{3.34}$$

where α is some positive constant. As such, the maximization problem in (3.33) becomes constrained by (3.34). The function in (3.33) is convex, since it is the composition of the norm with a linear base, and the box constraints in (3.34) form a convex set. Therefore, the maximizer of (3.33) subject to the constraints (3.34) lies on the extreme points of the feasibility region, namely $|\epsilon_i^\star| = \alpha$, $\forall\ i$.

If N is even, the maximum is achieved whenever $\sum_{i=1}^{N} \epsilon_i = 0$; hence, the maximizer is $\epsilon_i^\star = (-1)^i\, \alpha$, $\forall\ i$. If N is odd, the maximum is achieved whenever $\sum_{i=1}^{N} \epsilon_i = \alpha$; hence, the maximizer is $\epsilon_i^\star = (-1)^i\, \alpha$ for $i = 1, \ldots, N-1$, and $\epsilon_N^\star = \pm\alpha$. Therefore, the maximum error introduced in the receiver's position is bounded by

$$\|\delta \boldsymbol{r}_r\| \leq \begin{cases} \sqrt{N}\alpha\, \kappa, & \text{if } N \text{ is even,} \\ \sqrt{\frac{N^2-1}{N}}\alpha\, \kappa, & \text{if } N \text{ is odd.} \end{cases}$$

□

3.3 Experimental Results

Navigation using the proposed base/rover framework discussed in Section 3.1 was tested in three experiments with (1) a mobile ground vehicle and a stationary base, (2) a UAV and a stationary base, and (3) a UAV and a mobile base. In both experiments, the cellular CDMA module of the LabVIEW-based Multichannel Adaptive TRansceiver Information eXtractor (MATRIX) SDR developed in [82] was used to process the cellular CDMA signals, and the Generalized Radionavigation Interfusion Device (GRID) SDR [96] was used to process the GPS signals. The measurement noise variance for the base and rover was calculated from [85]

$$\sigma_i^2 = \frac{c^2 \, B_{n,\mathrm{DLL}} \, q\left(t_{\mathrm{eml}}\right)}{2 \left(C/N_0\right)_i \left(1 - 2 B_{n,\mathrm{DLL}} \, T_{CO}\right)}, \tag{3.35}$$

where t_{eml} is the early-minus-late time in the CDMA receiver's delay-locked loop (DLL) correlators (expressed in chips), $B_{n,\mathrm{DLL}}$ is the DLL loop noise bandwidth (expressed in Hertz), $(C/N_0)_i$ is the measured carrier-to-noise ratio for the ith BTS (expressed in Hertz), $T_{CO} = \frac{1}{37.5}$ s is the predetection coherent integration time, and $q\left(t_{eml}\right)$ is a function of the autocorrelation of the cellular CDMA short code, whose expression is given in [85]. Moreover, the three-dimensional (3–D) position states of the BTSs involved in the experiments were mapped prior to the experiments according to the framework discussed in [1]. The following subsections present results for each experiment.

3.3.1 Ground Vehicle Results

In this experiment, two cars (a base and a rover) were equipped with two antennas each to acquire and track: (1) GPS signals and (2) signals from nearby cellular CDMA BTSs. The receivers' CDMA antennas used for the experiment were consumer-grade 800/1900 MHz

cellular antennas, and the GPS antennas were surveyor-grade Leica antennas. The GPS and cellular signals were simultaneously down-mixed and synchronously sampled via two universal software radio peripherals (USRPs) driven by the same GPS-disciplined oscillator (GSPDO). The receivers were tuned to the cellular carrier frequency 882.75 MHz, which is a channel allocated for U.S. cellular provider Verizon Wireless. Samples of the received signals were stored for off-line post-processing. Over the course of the experiment, both receivers were listening to the same 3 BTSs. The base receiver and the rover receiver were listening to the same sectors; hence, there were no additional errors due to the discrepancies between sector clocks. The base receiver was stationary during the experiments and was estimating the clock biases of the 3 BTSs with known position states via a WLS estimator as discussed in Subsection 3.1.1. The BTSs' position states were expressed in a local 3–D frame whose horizontal plane passes through the three BTSs and is centered at the mean of the BTSs' positions. The height of the rover was known and constant in the local 3–D frame over the trajectory driven and was passed as a constant parameter to the estimator. Hence, only the rover's two-dimensional (2–D) position and its clock bias were estimated through the WNLS described in Subsection 3.1.3. The weights of the WNLS were calculated using (3.35). For the first pseudorange measurement, the WNLS iterations were initialized by setting the rover's initial horizontal position states at the origin of the 3–D local frame and the initial clock bias to zero. For each subsequent pseudorange measurement, the WNLS iterations were initialized at the solution from the previous WNLS. The experimental hardware setup, the environment layout, and the true and estimated rover trajectories are shown in Fig. 3.5.

It can be seen from Fig. 3.5 that the navigation solution obtained from the cellular CDMA signals follows closely the navigation solution obtained using GPS signals. The mean distance difference along the traversed trajectory between the GPS and CDMA navigation solutions was calculated to be 5.51 m with a standard deviation of 4.01 m and a maximum error of 11.11 m. The mean receiver clock estimate difference between the GPS and CDMA

Figure 3.5: Experimental hardware setup, rover trajectory, and base and BTS locations for ground experiments. Map data: Google Earth.

navigation solutions was calculated to be -45 ns with a standard deviation of 23.03 ns.

3.3.2 UAV Results

Two UAV experiments were conducted: (1) one with a stationary base and (2) one with a mobile base.

UAV Results with a Stationary Base

In this experiment, the base consisted of a GPSDO-driven dual-channel USRP connected to a high-gain tri-band cellular antenna and a surveyor-grade Leica GPS antenna deployed on the roof of Winston Chung Hall at the University of California, Riverside. A DJI Matrice 600 UAV was used as the rover, which was equipped with a consumer-grade 800/1900 MHz cellular antenna and a small consumer-grade GPS antenna to discipline the on-board oscillator. The cellular signals on the rover side were down-mixed and sampled by a single-channel Ettus 312 USRP driven by a GPS-disciplined temperature compensated crystal oscillator (TCXO). The cellular receivers were tuned to the cellular carrier frequency 883.98 MHz, which is also a channel allocated for Verizon Wireless. Samples of the received signals were stored for off-line post-processing. The ground-truth reference for the rover trajectory was taken from the UAV's on-board navigation system, which uses GPS, inertial navigation system, and other sensors. Fig. 3.6 shows the SOP BTS environment in which the base and rover were present as well as the experimental hardware setup, which is similar to the one employed in [85, 98].

Over the course of the experiment, the base and the rover were listening to the same 2 BTSs. Since only 2 BTSs were available for processing, an extended Kalman filter (EKF) framework was adopted (for observability considerations) to estimate the rover's state $\boldsymbol{x}_r$, which is composed of its 2-D position $\boldsymbol{r}_r$, velocity $\dot{\boldsymbol{r}}_r$, clock bias δt_r, and clock drift $\dot{\delta} t_r$, namely $\boldsymbol{x}_r \triangleq \left[\boldsymbol{r}_r^{\mathsf{T}}, \dot{\boldsymbol{r}}_r^{\mathsf{T}}, c\delta t_r, c\dot{\delta} t_r\right]^{\mathsf{T}}$. Similarly to the ground experiment, all position states were expressed in a local 3–D frame whose horizontal plane is defined by the two BTSs and the base and is centered at the mean of two BTSs' and the base's positions. The UAV was programmed to fly at a constant height and at a constant speed. Hence, similarly to the ground experiment, the height of the rover was passed as a constant parameter to the filter. The rover's position and velocity states were assumed to evolve according to velocity random walk dynamics, and the clock bias and clock drift dynamics were modeled

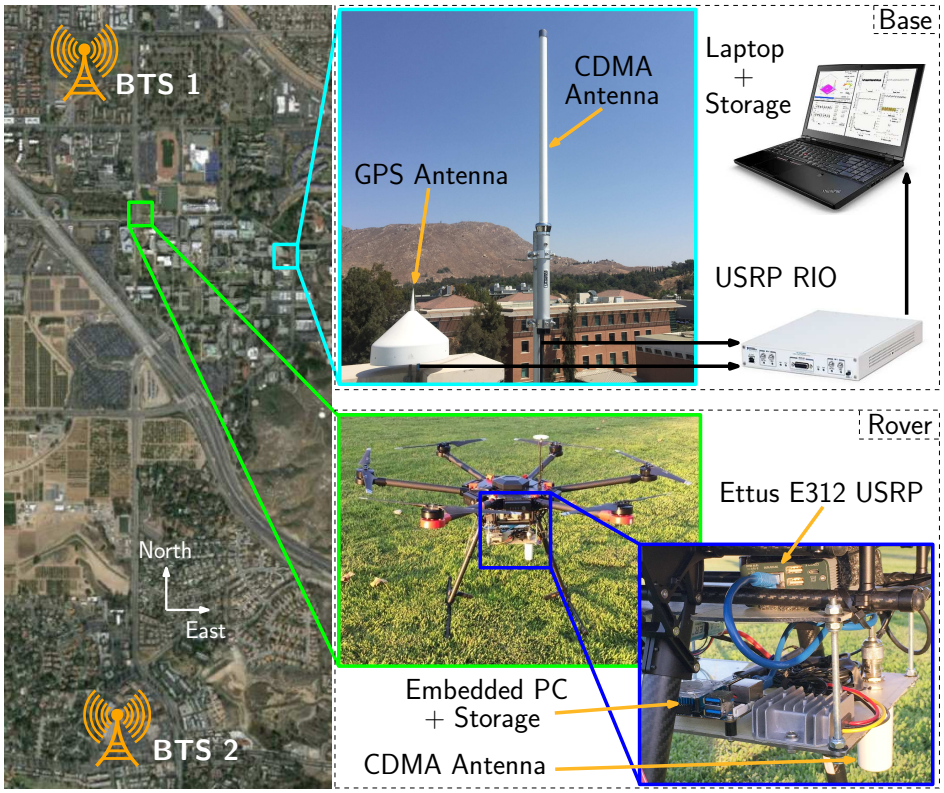

Figure 3.6: SOP BTS environment and experimental hardware setup with stationary base. Map data: Google Earth.

according to the standard clock error model: double integrator driven by noise, as discussed in [33]. The power spectral densities of the process noise driving $\ddot{x}_r$ and $\ddot{y}_r$ were obtained by post-processing the data sampled from the UAV's on-board navigation system. The time averages of the x and y accelerations were approximately zero with time variances $\sigma^2_{\ddot{x}} \approx 0.36$ $(\mathrm{m/s^2})^2$ and $\sigma^2_{\ddot{y}} \approx 0.24$ $(\mathrm{m/s^2})^2$. These variances were used to form the covariance matrix of the process noise driving the position and velocity states [33]. Alternatively, the power spectra of the acceleration process noise may be estimated adaptively [41], or an inertial measurement unit (IMU) may be used to propagate the position and orientation states of the rover. The process noise covariance of the clock error states can be parameterized by the white frequency coefficient h_0 and the frequency random walk coefficient h_{-2} [100, 101]. Since the USRP on-board the rover is equipped with a TCXO, the aforementioned coefficients were chosen to be $h_0 = 9.4 \times 10^{-20}$ and $h_{-2} = 3.8 \times 10^{-21}$ [41]. The EKF states corresponding to the UAV's position and velocity were initialized with the values obtained from the on-board

navigation system with a zero initial uncertainty. The EKF state corresponding to the clock bias was initialized according to

$$c\hat{\delta}t_r(0|-1) = \rho_1(0) - \|\boldsymbol{r}_r(0) - \boldsymbol{r}_{s_1}\|_2 + c\hat{\delta}t_{s_1}(0),$$

where $\boldsymbol{r}_r(0)$ is the UAV's initial position obtained from the on-board navigation system and $\hat{\delta}t_{s_1}(0)$ is the first BTS's clock bias estimate given by the base at $k = 0$. The initial uncertainty associated with $c\hat{\delta}t_r(0|-1)$ was set equal to the estimation error variance $\sigma^2_{\delta t_{s_1}}$ given by the base. The EKF state corresponding to the clock drift was initialized to zero with an initial uncertainty of 10 $(\text{m/s})^2$. The measurement noise covariance matrix was obtained using (3.19) and (3.35). Three scenarios were tested. In the first scenario, the base and the rover were listening to the same sectors; hence, there were no additional errors due to the discrepancies between sector clocks. In the second scenario, the base was forced to listen to a different sector of BTS 1 than the rover; however, the measurement noise covariance was not modified to compensate for the discrepancy introduced. The third scenario is similar to the second, except that the measurement noise covariance was modified to account for the sector clock bias discrepancy, as defined in (3.19). The initial discrepancy was calculated and was known to the EKF for scenarios 2 and 3. Moreover, the parameters λ and α were calculated offline by the base and were found to be $\lambda = 13$ ns/s and $\alpha = 8 \times 10^{-4}$ Hz. The rover's true trajectory and estimated trajectory for each scenario are shown in Fig. 3.7 and the resulting RMSEs are tabulated in Table 3.1.

Table 3.1: Experimental Results for UAV with Stationary Base

	Scenario 1	**Scenario 2**	**Scenario 3**
RMSE (m)	9.39	23.99	13.42
Standard deviation (m)	3.42	11.24	5.18
Maximum error (m)	18.96	38.93	31.98

Fig. 3.7 and Table 3.1 show a significant improvement in the estimation performance when

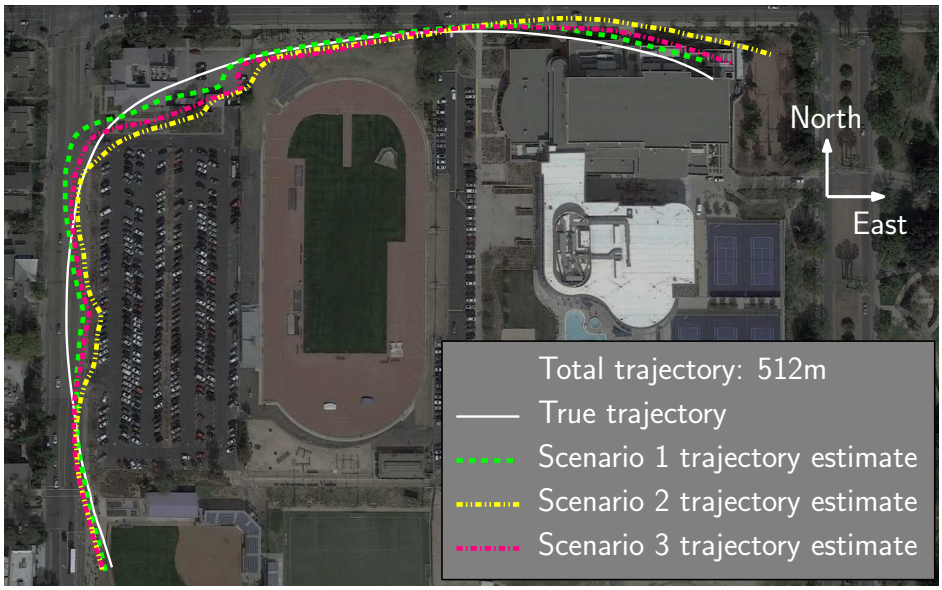

Figure 3.7: UAV's true and estimated trajectories. Map data: Google Earth.

the sector clock bias error model identified in this chapter is used, which is reflected in a reduction of around 11 m in the RMSE, 6 m in the standard deviation, and 7 m in the maximum error. Note that the UAV position estimate deviates from the true trajectory initially even though the UAV had not performed sharp maneuvers. This is due to the error in the pseudorange measurements caused by multipath. These multipath errors are not negligible, since the UAV is flying slightly lower than the BTSs, which are located around 1 and 2.3 km away from the UAVs.

UAV Results with a Mobile Base

In this experiment, the base and the rover were identical Autel Robotics X-Star Premium UAVs equipped with a single-channel Ettus 312 USRP driven by a GPS-disciplined TCXO connected to a consumer-grade 800/1900 MHz cellular antenna and a small consumer-grade GPS antenna to discipline the on-board oscillator. The cellular receivers were tuned to the cellular carrier frequency 882.75 MHz, which is also a channel allocated for Verizon Wireless. Samples of the received signals were stored for off-line post-processing. The ground-truth

references for the base and rover trajectories were taken from the UAVs' on-board navigation systems, which use GPS, inertial navigation system, and other sensors. Note that in this scenario, the clock biases were taken with respect to the base's clock bias. Fig. 3.8 shows the SOP BTS environment in which the base and rover were present as well as the experimental hardware setup.

Over the course of the experiment, the base and the rover were listening to the same 4 BTSs. The same three scenarios performed in the stationary base experiment were considered. In this case, SOP BTS 4 was the BTS cell in which the base and the rover were listening to different sectors. The framework discussed in Subsection 3.1.3 was adopted. The initial discrepancy was calculated and was known to the WNLS for scenarios 2 and 3. Moreover, the parameters λ and α were calculated offline by the base and were found to be $\lambda = 15.28$ ns/s and $\alpha = 2.2 \times 10^{-4}$ Hz. The rover's true trajectory and estimated trajectory for each scenario are shown in Fig. 3.9 and the resulting RMSEs are tabulated in Table 3.2.

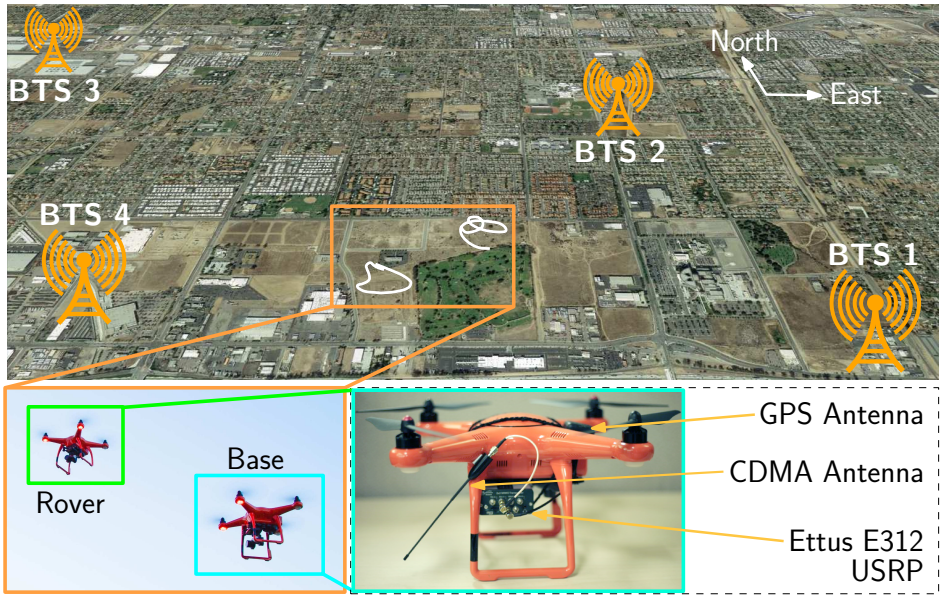

Figure 3.8: SOP BTS environment and experimental hardware setup with a mobile base. Map data: Google Earth.

Fig. 3.9 and Table 3.2 show a significant improvement in the estimation performance when the sector clock bias error model identified in this chapter is used, which is reflected in a

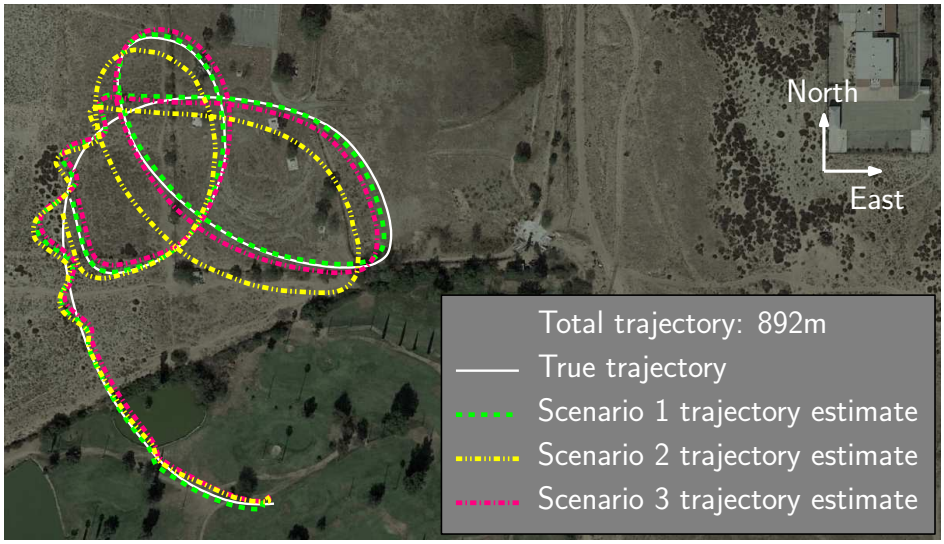

Figure 3.9: UAV's true and estimated trajectories. Map data: Google Earth.

Table 3.2: Experimental Results for UAV with a Mobile Base

	Scenario 1	**Scenario 2**	**Scenario 3**
RMSE (m)	5.05	13.70	6.66
Standard deviation (m)	3.12	7.00	3.27
Maximum error (m)	16.67	23.77	16.86

reduction of around 7 m in the RMSE, a reduction of 3.7 m in the standard deviation, and a reduction of 7 m in the maximum error. It is worth mentioning that the position RMSE obtained by not using SOP BTS 4 was around 11 m. This indicates that not using the BTS in case of sector mismatch is not the best strategy. A better performance may be obtained by exploiting all available BTSs' and incorporating the rigorous error models derived in this chapter.

Fig. 3.10 shows $\log\det\left[\mathbf{P}_{x,y}\right]$ and $\log\det\left[\mathbf{P}'_{x,y}\right]$ for a point solution and a batch estimator, respectively, corresponding to the experimental results of scenarios 2 and 3 along with the theoretical lower bounds derived in Subsections 3.2.2 and 3.2.3. It can be seen that scenario 3 outperforms scenario 2 in terms of estimation error uncertainty for both estimators. Moreover, the lower bounds are never violated. The difference between the experimental logarithm of the determinant of the position estimation error covariance and the theoretical

lower bound is attributed to the geometrical configuration of the BTSs, which does not meet the optimal requirements in Theorem 3.2.

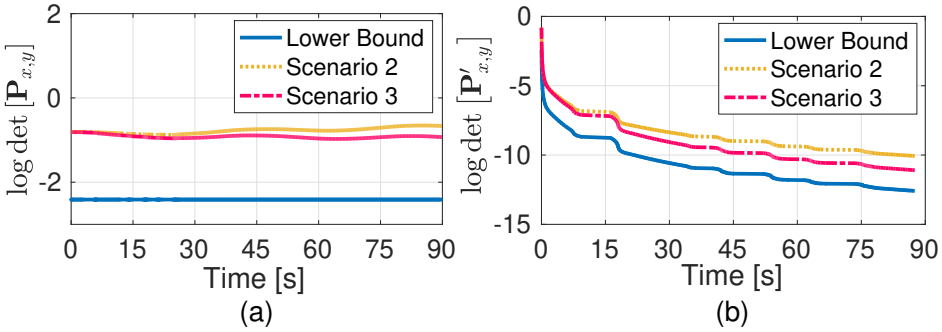

Figure 3.10: Logarithm of the determinant of the position estimation error covariance for (a) the point solution and (b) the batch estimator for scenarios 2 and 3. The theoretical lower bounds are also plotted.

Remark Comparing the proposed navigation approach with the state-of-the-art in the literature is not straightforward, since cellular CDMA navigation receivers were not documented in a way that facilitates reproduction (they are mainly proprietary, e.g., [25]). Chapter 2 extensively discusses a receiver architecture for navigation with cellular CDMA signals. Moreover, the navigation frameworks proposed in the literature are significantly different than the base/rover framework proposed in this work. In addition, to the authors' knowledge, this work is the first to demonstrate UAVs navigating with cellular CDMA signals. While a 1.68 m error has been reported by combining cellular CDMA and digital television signals in the literature [25], this paper reports 5 m accuracy using cellular CDMA signals exclusively.

Chapter 4

Differential Framework for Navigation with Carrier Phase Measurements from Cellular SOPs

This chapter is organized as follows. Section 4.1 describes the carrier phase measurement model and the pseudorange model parameterized by the receiver and BTS states. Section 4.2 describes the CD-cellular navigation framework. Section 4.3 provides Monte Carlo simulation results to assess the performance of the proposed framework. Section 4.4 provides a preliminary CD-cellular network design analysis and software and hardware considerations for real-time implementation of a CD-cellular network. Section4.5 shows experimental results demonstrating centimeter-level-accurate UAV navigation via the proposed CD-cellular framework. Note that the notation in this chapter is independent from the one in previous chapter and is confined to this chapter and the following chapter, Chapter 5.

The results of this chapter have been published in [102, 103].

4.1 Model Description

4.1.1 UAV-Mounted Receiver Dynamics Model

The navigating UAV-mounted receiver state consists of its unknown two-dimensional (2–D) position $\boldsymbol{r}_{r_{\mathrm{U}}} \triangleq [x_{r_{\mathrm{U}}}, y_{r_{\mathrm{U}}}]^{\mathsf{T}}$ and velocity $\dot{\boldsymbol{r}}_{r_{\mathrm{U}}}$. An altimeter may be used to estimate the UAV's altitude. The subsequent analysis may be readily extended to 3–D; however, the vertical position estimate will suffer from large uncertainties due to the poor vertical diversity of cellular SOPs. Hence, the state vector of the UAV-mounted receiver is given by $\boldsymbol{x}_{r_{\mathrm{U}}} = \left[\boldsymbol{r}_{r_{\mathrm{U}}}^{\mathsf{T}}, \dot{\boldsymbol{r}}_{r_{\mathrm{U}}}^{\mathsf{T}}\right]^{\mathsf{T}}$. The navigating UAV's position $\boldsymbol{r}_{r_{\mathrm{U}}}$ and velocity $\dot{\boldsymbol{r}}_{r_{\mathrm{U}}}$ will be assumed to evolve according to a continuous-time velocity random walk model [104]. Therefore, the navigating UAV dynamics is modeled according to the discretized model

$$\boldsymbol{x}_{r_{\mathrm{U}}}(k+1) = \mathbf{F}_{r_{\mathrm{U}}}\, \boldsymbol{x}_{r_{\mathrm{U}}}(k) + \boldsymbol{w}_{r_{\mathrm{U}}}(k), \quad k = 0, 1, 2, \ldots, \tag{4.1}$$

where $\boldsymbol{w}_{r_{\mathrm{U}}}$ is a discrete-time zero-mean white noise sequence with covariance $\mathbf{Q}_{r_{\mathrm{U}}}$, with

$$\mathbf{F}_{r_{\mathrm{U}}} = \begin{bmatrix} \mathbf{I}_{2\times 2} & T\mathbf{I}_{2\times 2} \\ \mathbf{0}_{2\times 2} & \mathbf{I}_{2\times 2} \end{bmatrix}, \qquad \mathbf{Q}_{r_{\mathrm{U}}} = \begin{bmatrix} \tilde{q}_x \frac{T^3}{3} & 0 & \tilde{q}_x \frac{T^2}{2} & 0 \\ 0 & \tilde{q}_y \frac{T^3}{3} & 0 & \tilde{q}_y \frac{T^2}{2} \\ \tilde{q}_x \frac{T^2}{2} & 0 & \tilde{q}_x T & 0 \\ 0 & \tilde{q}_y \frac{T^2}{2} & 0 & \tilde{q}_y T \end{bmatrix},$$

where T is the sampling time and $\tilde{q}_x$ and $\tilde{q}_y$ are the power spectral densities of the continuous-time x– and y– acceleration noise, respectively.

4.1.2 Cellular Carrier Phase Observation Model

In Chapter 2, a receiver that can produce pseudorange and carrier phase measurements from cellular CDMA BTSs was discussed. Several known signals may be transmitted for synchronization or channel estimation purposes in other cellular systems, from which navigation observables may be drawn. In long-term evolution (LTE) systems, two synchronization signals (primary synchronization signal (PSS) and secondary synchronization signal (SSS)) are broadcast by each evolved node B (eNodeB) [105]. In addition to the PSS and SSS, a reference signal known as the cell-specific reference signal (CRS) is transmitted by each eNodeB for channel estimation purposes [105]. The PSS, SSS, and CRS may be exploited to draw carrier phase and pseudorange measurements on neighboring eNodeBs [26, 106]. In the rest of this chapter, it is assumed that Doppler frequency measurements are available to cellular CDMA or LTE signals (e.g., from specialized navigation receivers [25, 82, 85, 107, 108]).

The continuous-time carrier phase observable can be obtained by integrating the Doppler measurement over time [6]. The carrier phase (expressed in cycles) made by the i-th receiver on the n-th SOP is given by

$$\phi_n^{(i)}(t) = \phi_n^{(i)}(t_0) + \int_{t_0}^{t} f_{D_n}^{(i)}(\tau) d\tau, \quad n = 1, \ldots, N, \tag{4.2}$$

where $f_{D_n}^{(i)}$ is the Doppler measurement made by the i-th receiver on the n-th cellular SOP, $\phi_n^{(i)}(t_0)$ is the initial carrier phase, and N is the total number of SOPs. In (4.2), the index identifier i denotes either the base (B) or the UAV (U), which are discussed in Subsection 4.2.1. Assuming a constant Doppler during a subaccumulation period T, (4.2) can be discretized to yield

$$\phi_n^{(i)}(t_k) = \phi_n^{(i)}(t_0) + \sum_{l=0}^{k-1} f_{D_n}^{(i)}(t_l) T, \tag{4.3}$$

where $t_k \triangleq t_0 + kT$. In what follows, the time argument t_k will be replaced by k for simplicity of notation. Note that the receiver will make noisy carrier phase measurements. Adding measurement noise to (4.3) and expressing the carrier phase observable in meters yields

$$z_n^{(i)}(k) = \lambda\phi_n^{(i)} + \lambda T \sum_{l=0}^{k-1} f_{D_n}^{(i)}(l) + v_n^{(i)}(k), \tag{4.4}$$

where λ is the carrier signal wavelength and $v_n^{(i)}$ is the measurement noise, which is modeled as a discrete-time zero-mean white Gaussian sequence with variance $\left[\sigma_n^{(i)}(k)\right]^2$, which can be shown for a coherent second-order phase-locked loop (PLL) to be given by [6]

$$\left[\sigma_n^{(i)}(k)\right]^2 = \lambda^2 \frac{B_{i,\mathrm{PLL}}}{C/N_{0_n}(k)},$$

where $B_{i,\mathrm{PLL}}$ is the receiver's PLL noise equivalent bandwidth and C/N_{0_n} is the cellular SOP's measured carrier-to-noise ratio. Note that a coherent PLL may be employed in CDMA and LTE navigation receivers since the cellular synchronization and reference signals do not carry any data. The carrier phase in (4.4) can be parameterized in terms of the receiver and cellular SOP states as

$$z_n^{(i)}(k) = \left\|\boldsymbol{r}_{r_i}(k) - \boldsymbol{r}_{s_n}\right\|_2 + c \cdot [\delta t_{r_i}(k) - \delta t_{s_n}(k)] + \lambda N_n^{(i)} + v_n^{(i)}(k), \tag{4.5}$$

where $\boldsymbol{r}_{r_i} \triangleq [x_{r_i}, y_{r_i}]^\mathsf{T}$ is the receiver's position vector; $\boldsymbol{r}_{s_n} \triangleq [x_{s_n}, y_{s_n}]^\mathsf{T}$ is the cellular BTS's position vector; c is the speed of light; δt_{r_i} and δt_{s_n} are the receiver's and cellular BTS's clock biases, respectively; and $N_n^{(i)}$ is the carrier phase ambiguity.

4.2 Navigation with SOP Carrier Phase Differential Cellular Measurements

In this section, a framework for CD-cellular navigation is developed.

4.2.1 CD-Cellular Framework

The framework consists of a navigating UAV and a reference receiver in an environment comprising N cellular BTSs. The UAV and reference receiver are assumed to be listening to the same BTSs with the BTS locations being known. The reference receiver, referred to as the base (B), is assumed to have knowledge of its own position state, e.g., a stationary receiver deployed at a surveyed location. Note that instead of a stationary receiver, the base may be another UAV with access to GNSS and a high-end sensor suite enabling to know its location precisely (e.g., high-flyer). The navigating UAV (U) does not have knowledge of its position nor its velocity. The base communicates its own position and carrier phase observables with the UAV. Fig. 4.1 illustrates the base/UAV framework.

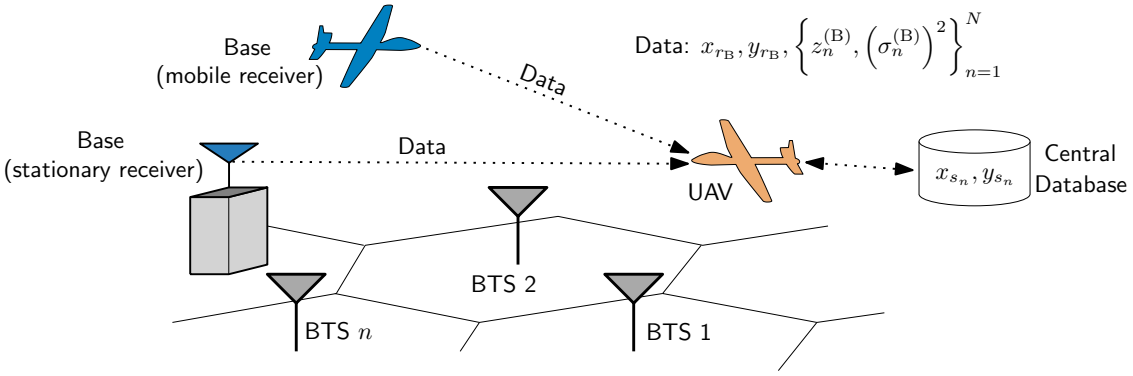

Figure 4.1: Base/UAV framework. The base could be either a stationary receiver or another UAV.

In what follows, the objective is to estimate the UAV's position, which will be achieved by double-differencing the measurements (4.5). Without loss of generality, let the measurements

to the first SOP be taken as references to form the single difference

$$z_{n,1}^{(i)}(k) \triangleq z_n^{(i)}(k) - z_1^{(i)}(k).$$

Subsequently, define the double difference between U and B as

$$\begin{aligned} z_{n,1}^{(\mathrm{U,B})}(k) &\triangleq z_{n,1}^{(\mathrm{U})}(k) - z_{n,1}^{(\mathrm{B})}(k) + \|\boldsymbol{r}_{r_\mathrm{B}}(k) - \boldsymbol{r}_{s_n}\| - \|\boldsymbol{r}_{r_\mathrm{B}}(k) - \boldsymbol{r}_{s_1}\| \\ &\triangleq h_{n,1}^{(\mathrm{U})}(k) + \lambda N_{n,1}^{(\mathrm{U,B})} + v_{n,1}^{(\mathrm{U,B})}(k), \end{aligned} \tag{4.6}$$

where $n = 1, \ldots, N$, ${h_{n,1}}^{(\mathrm{U})}(k) \triangleq \|\boldsymbol{r}_{r_\mathrm{U}}(k) - \boldsymbol{r}_{s_n}\| - \|\boldsymbol{r}_{r_\mathrm{U}}(k) - \boldsymbol{r}_{s_1}\|$, $N_{n,1}^{(\mathrm{U,B})} \triangleq N_n^{(\mathrm{U})} - N_n^{(\mathrm{B})} - N_1^{(\mathrm{U})} + N_1^{(\mathrm{B})}$, and $v_{n,1}^{(\mathrm{U,B})}(k) \triangleq v_n^{(\mathrm{U})}(k) - v_n^{(\mathrm{B})}(k) - v_1^{(\mathrm{U})}(k) + v_1^{(\mathrm{B})}(k)$. Define the vector of measurements as

$$\boldsymbol{z}(k) \triangleq \boldsymbol{h}\left[\boldsymbol{r}_{r_\mathrm{U}}(k)\right] + \lambda \boldsymbol{N} + \boldsymbol{v}(k),$$

where

$$\boldsymbol{z}(k) \triangleq \left[z_{2,1}^{(\mathrm{U,B})}(k), \ldots, z_{N,1}^{(\mathrm{U,B})}(k)\right]^\mathsf{T}, \quad \boldsymbol{h}\left[\boldsymbol{r}_{r_\mathrm{U}}(k)\right] \triangleq \left[h_{2,1}^{(\mathrm{U})}(k), \ldots, h_{N,1}^{(\mathrm{U})}(k)\right]^\mathsf{T},$$

$$\boldsymbol{N} \triangleq \left[N_{2,1}^{(\mathrm{U,B})}, \ldots, N_{N,1}^{(\mathrm{U,B})}\right]^\mathsf{T}, \quad \boldsymbol{v}(k) \triangleq \left[v_{2,1}^{(\mathrm{U,B})}(k), \ldots, v_{N,1}^{(\mathrm{U,B})}(k)\right]^\mathsf{T}$$

where $\boldsymbol{v}(k)$ has a covariance $\mathbf{R}_{\mathrm{U,B}}(k)$ which can be readily shown to be

$$\mathbf{R}_{\mathrm{U,B}}(k) = \mathbf{R}^{(1)}(k) + \left\{\left[\sigma_1^{(\mathrm{B})}(k)\right]^2 + \left[\sigma_1^{(\mathrm{U})}(k)\right]^2\right\} \boldsymbol{\Xi},$$

where

$$\mathbf{R}^{(1)}(k) \triangleq \mathrm{diag}\left\{\left[\sigma_2^{(\mathrm{B})}(k)\right]^2 + \left[\sigma_2^{(\mathrm{U})}(k)\right]^2, \ldots, \left[\sigma_N^{(\mathrm{B})}(k)\right]^2 + \left[\sigma_N^{(\mathrm{U})}(k)\right]^2\right\}$$

and $\boldsymbol{\Xi}$ is a matrix of ones.

4.2.2 Batch Solution

The vector $\boldsymbol{N}$ is now a vector of integers and has to be solved for along with the UAV's position. Using only one set of carrier phase measurement with no *a priori* knowledge on the UAV position results in an underdetermined system: $(N+1)$ unknowns with only $(N-1)$ measurements. In GNSS, when no *a priori* information on the position of the UAV (rover) is known, the UAV could remain stationary for a period of time such that enough variation in satellite geometry is observed. Subsequently, the UAV (rover) uses measurements collected at different times in a batch estimator, resulting in an overdetermined system [6]. Other approaches to deal with integer ambiguity resolution for GNSS include [109]. However, cellular SOP transmitters are stationary. Hence, no variation in geometry will be observed unless the navigating UAV is moving. In this case, cellular carrier phase measurements collected at several time-steps could be used in a batch estimator to solve for the positions of the UAV over the different time-steps as well as for the integer ambiguities. Denote K the number of time-steps in which carrier phase measurements are collected to be processed in a batch. Then, the total number of measurements will be $K \times (N-1)$, while the total number of unknowns will be $2K + N - 1$. Note that for $N \geq 3$, the resulting system is overdetermined for $K \geq 3$.

Define the collection of measurements from time-step 0 to $K-1$ as

$$\mathbf{z}^K \triangleq \left[\boldsymbol{z}^\mathsf{T}(0), \ldots, \boldsymbol{z}^\mathsf{T}(K-1)\right]^\mathsf{T},$$

which can be expressed as

$$\mathbf{z}^K = \mathbf{h}\left[\mathbf{r}_{r_\mathrm{U}}^K\right] + \lambda \bar{\mathbf{I}}^K \boldsymbol{N} + \mathbf{v}^K, \tag{4.7}$$

$$\mathbf{r}_{r_{\mathrm{U}}}^{K} \triangleq \begin{bmatrix} \boldsymbol{r}_{r_{\mathrm{U}}}(0) \\ \vdots \\ \boldsymbol{r}_{r_{\mathrm{U}}}(K-1) \end{bmatrix}, \ \mathbf{h}\left[\mathbf{r}_{r_{\mathrm{U}}}^{K}\right] \triangleq \begin{bmatrix} \boldsymbol{h}\left[\boldsymbol{r}_{r_{\mathrm{U}}}(0)\right] \\ \vdots \\ \boldsymbol{h}\left[\boldsymbol{r}_{r_{\mathrm{U}}}(K-1)\right] \end{bmatrix}, \ \bar{\mathbf{I}}^{K} \triangleq \begin{bmatrix} \mathbf{I}_{(N-1)\times(N-1)} \\ \vdots \\ \mathbf{I}_{(N-1)\times(N-1)} \end{bmatrix}, \ \mathbf{v}^{K} \triangleq \begin{bmatrix} \boldsymbol{v}(0) \\ \vdots \\ \boldsymbol{v}(K-1) \end{bmatrix},$$

where $\mathbf{v}^K$ is the overall measurement noise with covariance

$$\mathbf{R}^{K} \triangleq \mathrm{blkdiag}\left[\mathbf{R}_{\mathrm{U,B}}(0), \ldots, \mathbf{R}_{\mathrm{U,B}}(K-1)\right],$$

where blkdiag is a block-diagonal matrix. A weighted nonlinear least-squares (WNLS) estimator is used to estimate $\mathbf{r}_{r_{\mathrm{U}}}^{K}$ along with the float solution of $\boldsymbol{N}$. Then, an integer least-squares (ILS) estimator is employed to fix the integer ambiguities $\boldsymbol{N}$ and the estimate of $\mathbf{r}_{r_{\mathrm{U}}}^{K}$ is subsequently corrected using the fixed ambiguities. However, the WNLS has to be initialized properly such that 1) the measurement Jacobian with respect to the receiver positions is full column-rank and 2) the WNLS converges to the right basin of attraction. In order to provide a proper initialization, an extended Kalman filter (EKF) will be used to estimate $\mathbf{r}_{r_{\mathrm{U}}}^{K}$ and $\boldsymbol{N}$ for some $K \geq 3$. Next, the EKF estimates are used to initialize the batch WNLS. For $k > K$, the fixed ambiguities are used to estimate the UAV's position $\boldsymbol{r}_{r_{\mathrm{U}}}(k)$. The EKF model is discussed next.

4.2.3 EKF Model

Define the vector $\boldsymbol{x} \triangleq \left[\boldsymbol{x}_{r_{\mathrm{U}}}^{\mathsf{T}}, \boldsymbol{N}^{\mathsf{T}}\right]^{\mathsf{T}}$ as the state vector to be estimated. Note that at this point, only the float solution of $\boldsymbol{N}$ is estimated. The EKF will produce an estimate $\hat{\boldsymbol{x}}(k|j)$, i.e., an estimate of $\boldsymbol{x}(k)$ using all measurements up to time-step $j \leq k$, along with an estimation error covariance $\mathbf{P}(k|j) \triangleq \mathbb{E}\left[\tilde{\boldsymbol{x}}(k|j)\tilde{\boldsymbol{x}}^{\mathsf{T}}(k|j)\right]$ where $\tilde{\boldsymbol{x}}(k|j) \triangleq \boldsymbol{x}(k) - \hat{\boldsymbol{x}}(k|j)$ is the estimation error. The EKF estimate and covariance time update equations are readily obtained from

(4.1) and are given by

$$\hat{\boldsymbol{x}}(k+1|k) = \mathbf{F}\hat{\boldsymbol{x}}(k|k), \qquad \mathbf{P}(k+1|k) = \mathbf{F}\mathbf{P}(k|k)\mathbf{F}^{\mathsf{T}} + \mathbf{Q},$$

$$\mathbf{F} \triangleq \operatorname{diag}\left[\mathbf{F}_{r_{\mathrm{U}}}, \mathbf{I}_{(N-1)\times(N-1)}\right], \quad \mathbf{Q} \triangleq \operatorname{diag}\left[\mathbf{Q}_{r_{\mathrm{U}}}, \epsilon\mathbf{I}_{(N-1)\times(N-1)}\right],$$

where ϵ is some small positive number that ensures that $\mathbf{Q}$ is positive definite [101, 110]. The EKF state and covariance measurement update is performed according to

$$\hat{\boldsymbol{x}}(k+1|k+1) = \hat{\boldsymbol{x}}(k+1|k) + \mathbf{K}\boldsymbol{\nu}(k+1), \qquad \mathbf{P}(k+1|k+1) = [\mathbf{I} - \mathbf{K}\mathbf{H}]\,\mathbf{P}(k+1|k),$$

$$\begin{aligned}
\boldsymbol{\nu}(k+1) &\triangleq \boldsymbol{z}(k+1) - \left[\boldsymbol{h}\left[\hat{\boldsymbol{r}}_{r_{\mathrm{U}}}(k+1|k)\right] + \lambda\hat{\boldsymbol{N}}(k+1|k)\right], \\
\mathbf{K} &\triangleq \mathbf{P}(k+1|k)\mathbf{H}^{\mathsf{T}}\mathbf{S}^{-1}, \\
\mathbf{S} &\triangleq \mathbf{H}\mathbf{P}(k+1|k)\mathbf{H}^{\mathsf{T}} + \mathbf{R}_{\mathrm{U,B}}(k+1),
\end{aligned}$$

where $\mathbf{H}$ is the measurement Jacobian given by

$$\mathbf{H} \triangleq \left[\mathbf{T}\mathbf{G} \quad \mathbf{0}_{(N-1)\times 2} \quad \mathbf{I}_{(N-1)\times(N-1)}\right], \ \mathbf{G} \triangleq \begin{bmatrix} \frac{\hat{\boldsymbol{r}}_{r_{\mathrm{U}}}^{\mathsf{T}}(k+1|k) - \boldsymbol{r}_{s_1}^{\mathsf{T}}}{\left\|\hat{\boldsymbol{r}}_{r_{\mathrm{U}}}(k+1|k) - \boldsymbol{r}_{s_1}\right\|} \\ \vdots \\ \frac{\hat{\boldsymbol{r}}_{r_{\mathrm{U}}}^{\mathsf{T}}(k+1|k) - \boldsymbol{r}_{s_N}^{\mathsf{T}}}{\left\|\hat{\boldsymbol{r}}_{r_{\mathrm{U}}}(k+1|k) - \boldsymbol{r}_{s_N}\right\|} \end{bmatrix}, \ \mathbf{T} \triangleq \left[-\mathbf{1}_{N-1} \quad \mathbf{I}_{(N-1)\times(N-1)}\right],$$

and $\mathbf{1}_{N-1}$ is an $(N-1)\times 1$ vector of ones.

4.2.4 EKF Initialization

In order to initialize the EKF, i.e., obtain $\hat{\boldsymbol{x}}(0|0)$ and $\mathbf{P}(0|0)$, a centroid positioning method is used based on the hearable cell IDs[111]. To this end, the UAV position is initialized at the centroid of the SOP positions, denoted $\boldsymbol{r}_c$. The UAV initial position's 3σ bound is set to be

the maximum distance at which the SOP signals can be acquired and tracked reliably by the receiver, which from experimental results was determined to be 7 km. The initial velocity is set to zero and its corresponding 3σ bound is set to be that of the maximum velocity with which the UAV can fly (e.g., specified by the manufacturer's specification sheet). The initial estimate and uncertainty of the float solution of $\boldsymbol{N}$ can be deduced from the initial position estimates and $\boldsymbol{z}(0)$.

4.3 Simulation Results

In this section, the following aspects of the framework described in Section 4.2 are studied through Monte Carlo simulations: 1) the effect of K on the navigation performance and 2) and the effect of N on the navigation performance. A total of 500 Monte Carlo runs were performed and the total position root mean-squared error (RMSE) was calculated for each value of N and K. The BTS layout, the base's position, and a sample UAV trajectory are plotted in Fig. 4.2. The UAV was set to start at the same initial position indicated in Fig. 4.2 for all the Monte Carlo runs. The cellular carrier phase measurements were simulated at 1 Hz for both receivers. The total position RMSEs are shown in Fig. 4.3 for varying values of N and K. Note that the Least-Squares AMBiguity Decorrelation Adjustment (LAMBDA) method [112] implemented at the Delft University of Technology was used to solve for the integer ambiguities [113].

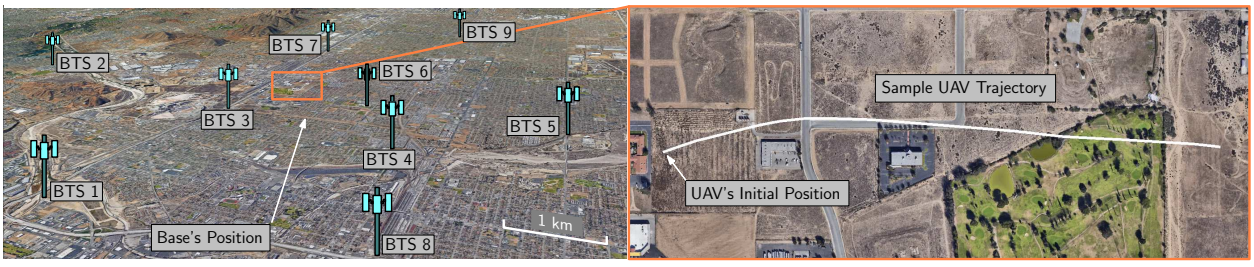

Figure 4.2: The BTS layout, the base's position, and a sample UAV trajectory used for 500 Monte Carlo runs.

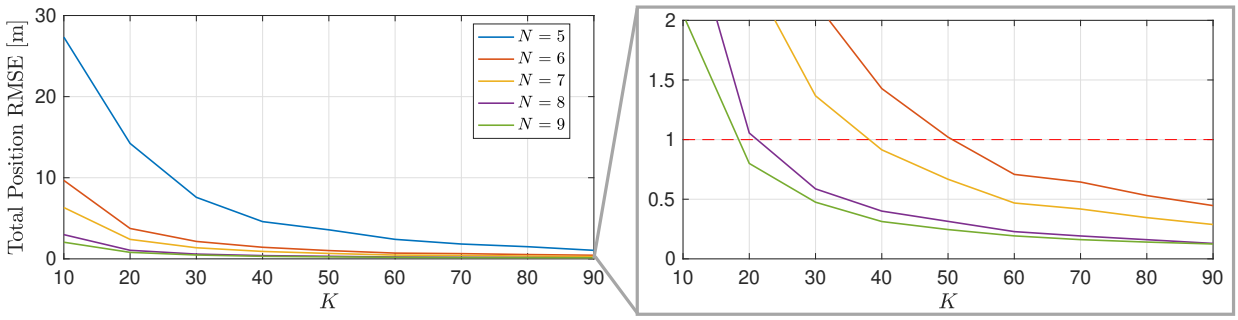

Figure 4.3: Total position RMSEs for 500 Monte Carlo runs of the CD-cellular framework described in Section 4.2 for varying values of K and N.

The following can be deduced from Fig. 4.3. First, it can be readily seen, as expected, that the total RMSE decreases as K and N increase. However, the decrease in RMSE becomes less significant for large values of K and N. For a given K, the change in the RMSE becomes very small when $N \geq 8$. For a given N, the change in RMSE becomes very small when $K \geq 60$. Subsequently, when 8 or more BTSs are available, little improvement is expected over $K \geq 60$. Second, to achieve centimeter-level performance for a reasonable value of K, e.g., for $K \leq 60$, 6 or more BTSs are needed.

4.4 CD-Cellular Network Design

In this section, preliminary CD-cellular network design considerations and a feasible base architecture are discussed.

4.4.1 Number of Bases and Placement

In order to determine the number of bases needed in an area A, the minimum distance d_0 above which received cellular signals become unreliable for navigation must be determined. In this chapter, reliable signals are defined as signals received at a C/N_0 above 35 dB-Hz on average [114]. Experimental data collected in a semi-urban environment in Colton,

California, shows that d_0 in such environments is 6 km. A C/N_0 plot for 9 cellular BTSs within 6 km of the receiver are shown for a period of 3 minutes in Fig. 4.4. It can be seen that the C/N_0 is above 35 dB-Hz most of the time for $d_0 = 6$ km. For a true urban environment, it is assumed that the maximum distance is halved. Moreover, a cellular (hexagonal)-type coverage for each base is considered since it was proven efficient in cellular systems. Subsequently, 0.0107 bases/km^2 will be needed in a semi-urban environment and 0.0428 bases/km^2 will be needed in a true urban environment. To put things into perspective, 52 bases will be needed to cover the 1,214 km^2 land area of the city of Los Angeles, California.

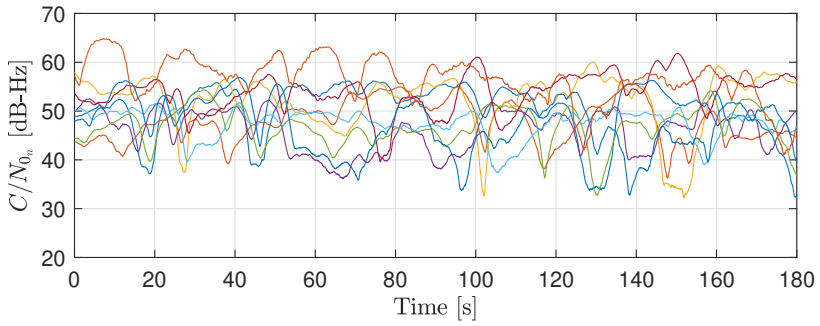

Figure 4.4: Carrier-to-noise ratios $\{C/N_{0_n}\}_{n=1}^{9}$ of all the cellular BTSs measured by the UAV. The C/N_0 measured by the base were of similar values.

4.4.2 Communication Requirements and Synchronization

The base can produce carrier phase observables from cellular signals at a rate of 100 Hz. In typical navigation systems, pseudorange or carrier phase updates are usually performed at up to 10 Hz. However, even at 100 Hz, these rates can be trivially achieved using today's wireless technology. Moreover, cellular base stations are required to be synchronized to within 10 μs from GPS time. Subsequently, the base and UAV can align the observables in time based on the cellular system time without introducing significant latencies. Accounting for the distances between the base and UAV and each base station, a maximum latency of 60 μs could be observed. This latency is way below the time interval in which navigation

observables are being produced and will introduce errors below 8mm in the CD-cellular measurements.

4.4.3 Software-Defined Radio Architecture

The cellular navigation receiver on-board the base is broken up into three main components. The first component is the front-end (FE) abstraction layer (FEAL). The FEAL is primarily responsible for interfacing with the FEs which can be universal software radio peripherals (USRPs). Each type of FE is exposed to the rest of the system as an FE object (FEO), which consists of certain configuration methods. In the exact implementation, the FEO is responsible for configuring the various devices using the data provided in the configuration methods. The FEO creates Sample Frames by reading the sample data from the device. A Sample Frame consists of a vector of complex numbers (the raw in-phase and quadrature (IQ) components) and a sequence number. The next component is the channel bank (CB). A CB performs cellular signal acquisition and tracking, which are spread across two different objects. The CB itself is responsible for conducting acquisition. Once a cellular SOP is acquired, a channel object (CO) is created. A CO contains all the necessary functions and algorithms necessary to track the signal and produce pseudorange and carrier phase observables, which are eventually transmitted to the UAV.

The core architecture of the base consists of an array of Pipeline Objects (POs). A PO consists of a single FEO and a single CB. Data communication between the two objects uses a lockless queue. The data passed between the two objects is a shared pointer to a sample frame object (SFO), which is a set or raw IQ samples. Then, each of the outputs of the pipelines are passed to the communication device that will transmit the observables to the UAV. This architecture is illustrated in Fig. 4.5.

Each object and component described above are implemented as abstract classes in C++,

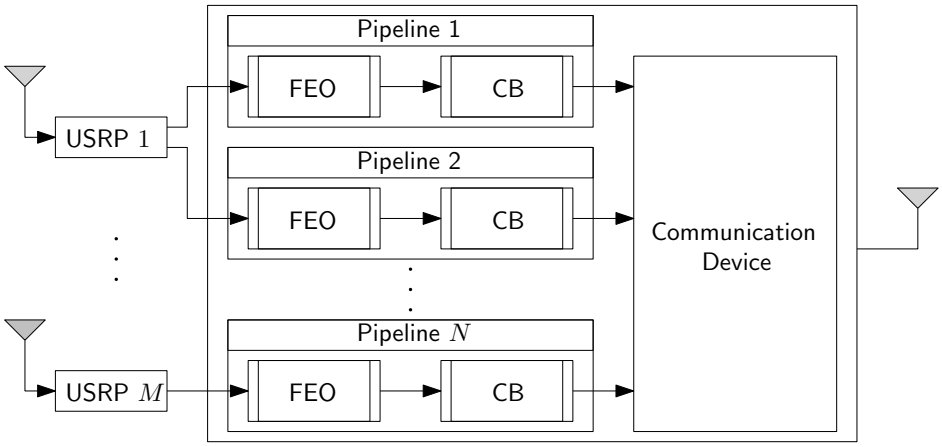

Figure 4.5: Base SDR core architecture.

which can be extended into more concrete classes depending on the cellular signal structure. For example, a CB can be extended to a cellular CDMA CB, in which the tracking and acquisition functions are modified according to [82]. This can be applied to various other objects throughout the base's SDR. This abstracts the specific cellular SOP signal structure from the rest of the receiver architecture. Furthermore, each channel within the CBs, the IQ sample gathering function in the FEO, and the acquisition operation in a CB are set to run in independent threads with different priorities. The IQ sample gathering threads in the FEO are given the highest priority because of the hardware dependence. This means that a "slow" channel implementation will not impact the rest of the receiver. Also, each of the components are decoupled from one another using queues. This allows for simultaneous development of the base's receiver and its components independently of the architecture. This is a result of using queues to communicate data, which represent standard interfaces for each component to interact with.

Due to the relatively large number of hearable SOPs in the base's environment, the base's receiver needs to maintain a high throughput rate. This is achieved using several key technologies. The first is the Single Instruction Multiple Data (SIMD) technology, which effectively allows the same instruction to be performed on multiple pieces of data in a single clock cycle. This is implemented as Advanced Vector eXtensions (AVX) on Intel processors. This

allows for multiple samples to be processed simultaneously in a single clock cycle, increasing the throughput tremendously. The SDR could also leverage multicore processors. Due to the highly parallelizable nature of the receiver's architecture, the more cores available to the program, the faster it runs. This is due to the fact that there are generally more threads than there are cores, creating a backlog of threads that require processor time. The number of threads that can be executed in parallel increases as the number of cores increases. The receiver uses highly optimized computing libraries to assist in several calculations. Libraries such as EIGEN and FFTW can easily take advantage of SIMD instructions. In addition, EIGEN is compiled to leverage the use of Intel's Math Kernel Library which contains several high performance matrix and signal processing operations.

4.5 Experimental Results

In this section, experimental results are presented demonstrating centimeter-level-accurate UAV navigation results using the CD-cellular framework developed in this chapter. As mentioned in Section 4.1, only the 2–D position of the UAV is estimated as its altitude may be obtained using other sensors (e.g., an altimeter). In the following experiments, the altitude of the UAV was obtained from its on-board navigation system. Moreover, the noise equivalent bandwidths of the receivers' PLLs were set to $B_{\mathrm{N,PLL}} = B_{\mathrm{M,PLL}} = B_{\mathrm{PLL}} = 3$ Hz. In order to demonstrate the CD-cellular framework discussed in Section 4.2, two Autel Robotics X-Star Premium UAVs were equipped each with an Ettus E312 USRP, a consumer-grade 800/1900 MHz cellular antenna, and a small consumer-grade GPS antenna to discipline the on-board oscillator. Note that one UAV acted as a base and the other as a navigating UAV. The receivers were tuned to a 882.75 MHz carrier frequency (i.e., $\lambda = 33.96$ cm), which is a cellular CDMA channel allocated for the U.S. cellular provider Verizon Wireless. Samples of the received signals were stored for off-line post-processing. The cellular carrier

phase measurements were given at a rate of 37.5 Hz, i.e., $T = 0.0267$ ms. The ground-truth reference for each UAV trajectory was taken from its on-board integrated navigation system, which uses GPS, an inertial measurement unit (IMU), and other sensors. The navigating UAV's total traversed trajectory was 1.72 km, which was completed in 3 minutes. Over the course of the experiment, the receivers on-board the UAVs were listening to 9 BTSs, whose positions were mapped prior to the experiment according to the framework discussed in [1]. A plot of C/N_0 of all the BTSs measured by the UAV is given in Fig. 4.4. The base measured similar C/N_0 values.

The CD-cellular measurements were used to estimate the navigating UAV's trajectory via the base/UAV framework developed in Section 4.2. The experimental setup, the SOP BTS layout, and the true (from the UAV's on-board integrated navigation system) and estimated (from the proposed CD-cellular) navigating UAV trajectories are shown in Fig. 4.6. The position RMSE was found to be 62.11 cm over a trajectory of 1.72 km flown over a period of 3 minutes. The LAMBDA method was used to solve for the integer ambiguities [113].

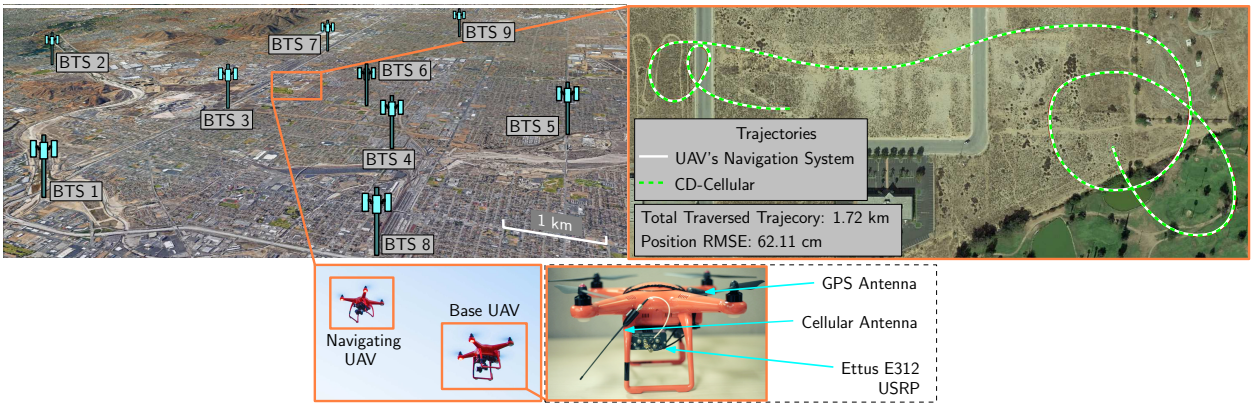

Figure 4.6: Experimental setup, the SOP BTS layout, and the true (from the UAV's on-board integrated navigation system) and estimated (from the proposed CD-cellular) navigating UAV trajectories via CD-cellular measurements in the base/UAV framework. The true and estimated trajectories are shown in solid and dashed lines, respectively. Map data: Google Earth.

It is important to note that the RMSE was calculated with respect to the trajectory returned by the UAV's on-board navigation system. Although these systems use multiple navigation

sensors, they are not equipped with high-precision GPS receivers, e.g., RTK. Therefore, some errors are expected in what is considered to be "true" trajectories taken from the UAV's on-board navigation system. Moreover, the base was mobile during the experiment and the position returned by its on-board navigation system was used as ground-truth. Consequently, any errors in the base's GPS solution would have degraded the navigating UAV's estimate.

Chapter 5

Non-Differential Framework for Navigation with Carrier Phase Measurements from Quasi-Synchronous Cellular SOPs

This chapter is organized as follows. Section 5.1 describes the single receiver navigation framework that leverages the relative stability of cellular SOPs. Section 5.2 derives stochastic models for the clock deviations of quasi-synchronous SOPs and validates these models experimentally. Section 5.3 establishes performance bounds for the single receiver navigation framework. Section 5.4 provides experimental results demonstrating the proposed framework, showing sub-meter level receiver navigation accuracy. Note that the notation in this chapter follows the one in Chapter 4, and all new notation used herein will be defined when necessary.

The results of this chapter have been published in [102].

5.1 Navigation with SOP Carrier Phase Measurements: Single receiver

This section discusses a cellular carrier phase navigation framework that alleviates the need of a base, i.e., employable on a single receiver. The same carrier phase measurement model as in Subsection 4.1.2 in Chapter 4 is used. Note that since what follows only pertains to single receiver navigation, the receiver index i will be dropped for simplicity of notation.

The terms $c\left[\delta t_r(k) - \delta t_{s_n}(k) + \frac{\lambda}{c}N_n\right]$ are combined into one term defined as

$$c\delta t_n(k) \triangleq c\left[\delta t_r(k) - \delta t_{s_n}(k) + \frac{\lambda}{c}N_n\right].$$

It was noted in [84] that cellular BTSs possess tighter carrier frequency synchronization then time (code phase) synchronization (the code phase synchronization requirement as per the cellular protocol is to be within 3 μs). Therefore, the resulting clock biases in the carrier phase estimates will be very similar, up to an initial bias, as shown in Fig. 5.1. Consequently, one may leverage this relative frequency stability to eliminate parameters that need to be estimated. BTSs with such relative frequency stability are said to be quasi-synchronous. This allows one to use a static estimator (e.g., a WNLS) to estimate the position of the receiver. To achieve this, in what follows, the carrier phase measurement is first re-parameterized and a WNLS estimation framework is subsequently developed.

5.1.1 Carrier Phase Measurement Re-Parametrization

Motivated by the experimental results in [84], the following re-parametrization is proposed

$$c\bar{\delta}t_n(k) \triangleq c\delta t_n(k) - c\delta t_n(0) \equiv c\delta t(k) + \epsilon_n(k), \tag{5.1}$$

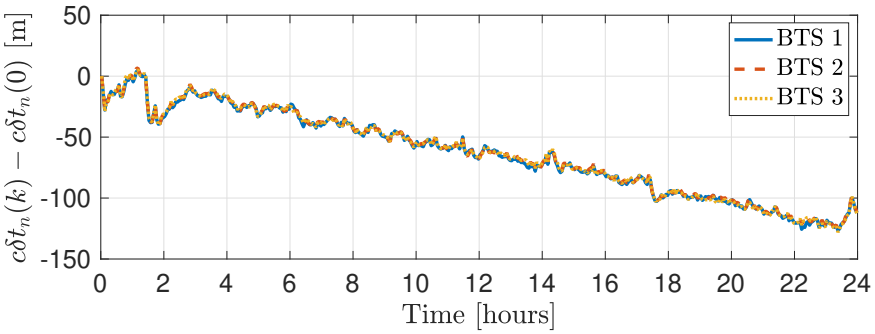

Figure 5.1: Experimental data showing $c\delta t_n(k) - c\delta t_n(0)$ obtained from carrier phase measurements over 24 hours for three neighboring BTSs. It can be seen that the clock biases $c\delta t_n(k)$ in the carrier phase measurement are very similar up to an initial bias $c\delta t_n(0)$ which has been removed.

where $c\delta t$ is a time-varying common bias term and ϵ_n is the deviation of $c\bar{\delta} t_n$ from this common bias and is treated as measurement noise. Using (5.1), the carrier phase measurement (4.5) from Chapter 4 can be re-parameterized as

$$z_n(k) = \|\boldsymbol{r}_r(k) - \boldsymbol{r}_{s_n}\| + c\delta t(k) + c\delta t_{0_n} + \eta_n(k), \tag{5.2}$$

where $c\delta t_{0_n} \triangleq c\delta t_n(0)$ and $\eta_n(k) \triangleq \epsilon_n(k) + v_n(k)$ is the overall measurement noise. The statistics of ϵ_n will be discussed in Section 5.2. Note that $c\delta t_{0_n}$ can be obtained knowing the initial position and given the initial measurement $z_n(0)$ according to $c\delta t_{0_n} \approx z_n(0) - \|\boldsymbol{r}_r(0) - \boldsymbol{r}_{s_n}\|$. This approximation ignores the contribution of the initial measurement noise. If the receiver is initially stationary for a period $k_0 T$ seconds, which is short enough such that $\delta t(k) \approx 0$ for $k = 1, \ldots, k_0$, then the first k_0 samples may be averaged to obtain a more accurate estimate of $c\delta t_{0_n}$.

It is proposed that instead of lumping all N clock biases into one bias $c\delta t$ to be estimated, several clusters of clocks get formed, each of size N_l (i.e., $\sum_{l=1}^{L} N_l = N$, where L is the total number of clusters), and the clocks in each cluster are lumped into one bias $c\delta t_l$ to be estimated. This gives finer granularity for the parametrization (5.1), since naturally, certain groups of cellular SOPs will be more synchronized with each other than with other

groups (e.g., corresponding to the same network provider, transmission protocol, etc.). An illustrative experimental plot is shown in Fig. 5.2. Note that since the 2–D position vector of the receiver is being estimated along with L clock biases, the number of clusters L cannot exceed $N-2$, otherwise there would be more unknowns than measurements.

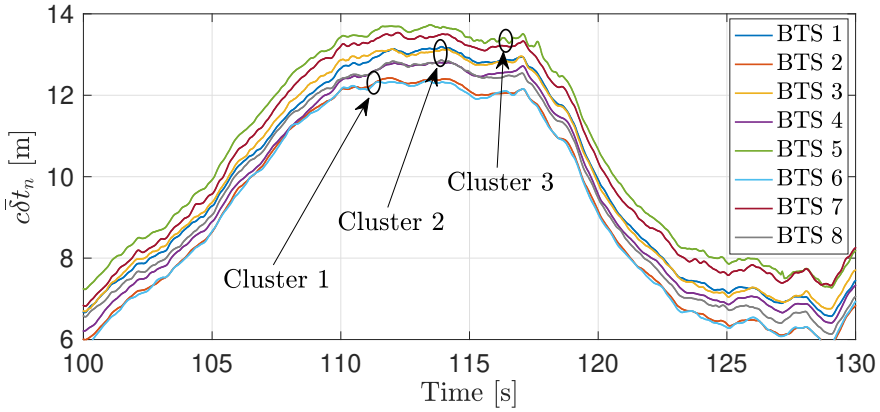

Figure 5.2: Experimental data for $c\bar{\delta}t_n(k)$ over 30 seconds for 8 BTSs. The clock biases have been visually clustered into three clusters as an illustrative example.

Without loss of generality, it assumed that the carrier phase measurements have been ordered such that the first N_1 measurements were grouped into the first cluster, the second N_2 measurements were grouped into the second cluster, and so on. Next, obtaining the navigation solution with a WNLS is discussed.

5.1.2 Navigation Solution

Given $N \geq 3$ pseudoranges modeled according to (5.2) and $L \leq N-2$ SOP clusters, the receiver may solve for its current position $\boldsymbol{r}_r$ and the current set of common biases $c\boldsymbol{\delta}t \triangleq [c\delta t_1, \ldots, c\delta t_L]^\mathsf{T}$ using a WNLS estimator. The state to be estimated is defined by $\boldsymbol{x} \triangleq \left[\boldsymbol{r}_r^\mathsf{T}, c\boldsymbol{\delta}t^\mathsf{T}\right]^\mathsf{T}$. An estimate $\hat{\boldsymbol{x}}$ may be obtained using the iterated WNLS equations given

by

$$\hat{\boldsymbol{x}}^{(j+1)}(k) = \hat{\boldsymbol{x}}^{(j)}(k) + \left(\mathbf{H}^{\mathsf{T}}\mathbf{R}_{\eta}^{-1}\mathbf{H}\right)^{-1}\mathbf{H}^{\mathsf{T}}\mathbf{R}_{\eta}^{-1}\delta\boldsymbol{z}(k), \tag{5.3}$$

where $\delta\boldsymbol{z}(k) \triangleq [\delta z_1(k), \ldots, \delta z_N(k)]^{\mathsf{T}}$ and $\delta z_n(k) \triangleq z_n(k) - \left[\left\|\hat{\boldsymbol{r}}_r^{(j)}(k) - \boldsymbol{r}_{s_n}\right\| + c\hat{\delta}t_{l_n}^{(j)}(k) + c\delta t_{0_n}\right]$, $\mathbf{R}_{\eta} = \operatorname{diag}\left[\sigma_1^2 + \sigma_{\epsilon_1}^2, \ldots, \sigma_N^2 + \sigma_{\epsilon_N}^2\right]$ is the measurement noise covariance where $\sigma_{\epsilon_n}^2$ will be discussed in Section 5.2, j is the WNLS iteration index, and $\mathbf{H}$ is the measurement Jacobian given by

$$\mathbf{H} \triangleq [\mathbf{G} \quad \boldsymbol{\Gamma}], \qquad \boldsymbol{\Gamma} \triangleq \begin{bmatrix} \mathbf{1}_{N_1} & \ldots & \mathbf{0} \\ \vdots & \ddots & \vdots \\ \mathbf{0} & \ldots & \mathbf{1}_{N_L} \end{bmatrix}, \tag{5.4}$$

$$\mathbf{G} \triangleq \begin{bmatrix} \dfrac{\hat{\boldsymbol{r}}_r^{(j)} - \boldsymbol{r}_{s_1}}{\|\hat{\boldsymbol{r}}^{(j)} - \boldsymbol{r}_{s_1}\|} & \ldots & \dfrac{\hat{\boldsymbol{r}}_r^{(j)} - \boldsymbol{r}_{s_N}}{\|\hat{\boldsymbol{r}}^{(j)} - \boldsymbol{r}_{s_N}\|} \end{bmatrix}^{\mathsf{T}}, \tag{5.5}$$

and $\mathbf{1}_{N_l} \triangleq [1, \ldots, 1]^{\mathsf{T}}$. Note that

$$l_n = \begin{cases} 1, & \text{for } n = 1, \ldots, N_1, \\ 2, & \text{for } n = N_1 + 1, \ldots, \sum_{l=1}^{2} N_l, \\ \vdots & \vdots \\ L, & \text{for } n = \sum_{l=1}^{L-1} N_l + 1, \ldots, N. \end{cases}$$

After convergence (i.e., $\hat{\boldsymbol{x}}^{(j+1)}(k) \approx \hat{\boldsymbol{x}}^{(j)}(k)$) the final estimate is obtained by setting $\hat{\boldsymbol{x}}(k) \equiv \hat{\boldsymbol{x}}^{(j+1)}(k)$. In the rest of the chapter, it is assumed that $\mathbf{H}$ is always full column rank.

5.1.3 Common Clock Bias Parametrization

Note that the clock bias clusters $\{c\delta t_l\}_{l=1}^{L}$ are "virtual clock biases", which are introduced to group SOPs whose carrier frequency is more synchronized than others. This would in turn yield more precise measurement models, reducing the estimation error. This subsection parameterizes $c\delta t_l$ as a function of $c\delta t_n$. This parametrization is based on the following theorem.

Theorem 5.1. *Consider $N \geq 3$ carrier phase measurements. Assume that the contribution of the relative clock deviation ϵ_n is much larger than the carrier phase measurement noise v_n and that ϵ_n are uncorrelated with identical variances σ^2. Then, the position error at any time instant $\delta \boldsymbol{r}_r(k)$ due to relative clock deviations is independent of $c\delta t_l$.*

Proof. Denote the measurement noise covariance of $\boldsymbol{\eta} \triangleq [\eta_1 \ldots, \eta_n]^{\mathsf{T}}$ as $\mathbf{R}_\eta$. It is assumed that the WNLS had converged very closely to the true state in the absence of clock deviations. The clock deviations are then suddenly introduced into the measurements, which will induce an incremental change in the receiver state estimate given by

$$\begin{aligned}\delta \boldsymbol{x}(k) &= -\left(\mathbf{H}^{\mathsf{T}}\mathbf{R}_\eta^{-1}\mathbf{H}\right)^{-1}\mathbf{H}^{\mathsf{T}}\mathbf{R}_\eta^{-1}\boldsymbol{\epsilon}(k) \\ &= -\left(\bar{\mathbf{H}}^{\mathsf{T}}\bar{\mathbf{H}}\right)^{-1}\bar{\mathbf{H}}^{\mathsf{T}}\bar{\boldsymbol{\epsilon}}(k),\end{aligned}$$

where

$$\bar{\mathbf{H}} \triangleq \mathbf{R}_\eta^{-\frac{1}{2}}\mathbf{H}, \quad \bar{\boldsymbol{\epsilon}}(k) \triangleq \mathbf{R}_\eta^{-\frac{1}{2}}\boldsymbol{\epsilon}(k),$$

and $\boldsymbol{\epsilon} \triangleq [\epsilon_1, \ldots, \epsilon_N]^{\mathsf{T}}$. The matrix product $\bar{\mathbf{H}}^{\mathsf{T}}\bar{\boldsymbol{\epsilon}}(k)$ can be further expressed as

$$\bar{\mathbf{H}}^{\mathsf{T}}\bar{\boldsymbol{\epsilon}}(k) = \begin{bmatrix} \bar{\mathbf{G}}^{\mathsf{T}} \\ \bar{\boldsymbol{\Gamma}}^{\mathsf{T}} \end{bmatrix}\bar{\boldsymbol{\epsilon}}(k) = \begin{bmatrix} \bar{\mathbf{G}}^{\mathsf{T}}\bar{\boldsymbol{\epsilon}}(k) \\ \bar{\boldsymbol{\Gamma}}^{\mathsf{T}}\bar{\boldsymbol{\epsilon}}(k) \end{bmatrix},$$

where

$$\bar{\mathbf{G}} \triangleq \mathbf{R}_\eta^{-\frac{1}{2}}\mathbf{G}, \quad \bar{\mathbf{\Gamma}} \triangleq \mathbf{R}_\eta^{-\frac{1}{2}}\mathbf{\Gamma}.$$

Next, $\left(\bar{\mathbf{H}}^\mathsf{T}\bar{\mathbf{H}}\right)^{-1}$ is expressed as

$$\left(\bar{\mathbf{H}}^\mathsf{T}\bar{\mathbf{H}}\right)^{-1} = \begin{bmatrix} \bar{\mathbf{G}}^\mathsf{T}\bar{\mathbf{G}} & \bar{\mathbf{G}}^\mathsf{T}\bar{\mathbf{\Gamma}} \\ \bar{\mathbf{\Gamma}}^\mathsf{T}\bar{\mathbf{G}} & \bar{\mathbf{\Gamma}}^\mathsf{T}\bar{\mathbf{\Gamma}} \end{bmatrix}^{-1} \triangleq \begin{bmatrix} \mathbf{A} & \mathbf{B} \\ \mathbf{B}^\mathsf{T} & \mathbf{D} \end{bmatrix},$$

where $\mathbf{A}$ is a 2×2 symmetric matrix, $\mathbf{B}$ is a $2 \times L$ matrix, and $\mathbf{D}$ is an $L \times L$ symmetric matrix. The estimation error becomes

$$\delta\boldsymbol{x}(k) = \begin{bmatrix} \delta\boldsymbol{r}_r(k) \\ \delta\left(c\boldsymbol{\delta}t(k)\right) \end{bmatrix} = -\begin{bmatrix} \left(\mathbf{A}\bar{\mathbf{G}}^\mathsf{T} + \mathbf{B}\bar{\mathbf{\Gamma}}^\mathsf{T}\right)\bar{\boldsymbol{\epsilon}}(k) \\ \left(\mathbf{B}^\mathsf{T}\bar{\mathbf{G}}^\mathsf{T} + \mathbf{D}\bar{\mathbf{\Gamma}}^\mathsf{T}\right)\bar{\boldsymbol{\epsilon}}(k) \end{bmatrix}.$$

Using the matrix block inversion lemma, the following may be obtained

$$\begin{aligned}
\mathbf{A} &= \left(\bar{\mathbf{G}}^\mathsf{T}\bar{\mathbf{\Psi}}\bar{\mathbf{G}}\right)^{-1} \\
\mathbf{B} &= -\left(\bar{\mathbf{G}}^\mathsf{T}\bar{\mathbf{\Psi}}\bar{\mathbf{G}}\right)^{-1}\bar{\mathbf{G}}^\mathsf{T}\bar{\mathbf{\Gamma}}\left(\bar{\mathbf{\Gamma}}^\mathsf{T}\bar{\mathbf{\Gamma}}\right)^{-1} \\
\mathbf{D} &= \left(\bar{\mathbf{\Gamma}}^\mathsf{T}\bar{\mathbf{\Gamma}}\right)^{-1}\left[\mathbf{I} + \bar{\mathbf{\Gamma}}^\mathsf{T}\bar{\mathbf{G}}\left(\bar{\mathbf{G}}^\mathsf{T}\bar{\mathbf{\Psi}}\bar{\mathbf{G}}\right)^{-1}\bar{\mathbf{G}}^\mathsf{T}\bar{\mathbf{\Gamma}}\left(\bar{\mathbf{\Gamma}}^\mathsf{T}\bar{\mathbf{\Gamma}}\right)^{-1}\right],
\end{aligned}$$

where $\bar{\mathbf{\Psi}} \triangleq \mathbf{I} - \bar{\mathbf{\Gamma}}\left(\bar{\mathbf{\Gamma}}^\mathsf{T}\bar{\mathbf{\Gamma}}\right)^{-1}\bar{\mathbf{\Gamma}}^\mathsf{T}$. This yields the position error given by

$$\delta\boldsymbol{r}_r(k) = -\left(\bar{\mathbf{G}}^\mathsf{T}\bar{\mathbf{\Psi}}\bar{\mathbf{G}}\right)^{-1}\bar{\mathbf{G}}^\mathsf{T}\bar{\mathbf{\Psi}}\bar{\boldsymbol{\epsilon}}(k).$$

When $\mathbf{R}_\eta = \sigma^2\mathbf{I}$, the above simplifies to

$$\delta\boldsymbol{r}_r(k) = -\left(\mathbf{G}^\mathsf{T}\mathbf{\Psi}\mathbf{G}\right)^{-1}\mathbf{G}^\mathsf{T}\mathbf{\Psi}\boldsymbol{\epsilon}(k), \tag{5.6}$$

$$\boldsymbol{\epsilon}(k) \triangleq [\epsilon_1(k), \ldots, \epsilon_N(k)]^{\mathsf{T}}, \quad \boldsymbol{\Psi} \triangleq \mathbf{I} - \boldsymbol{\Gamma}\left(\boldsymbol{\Gamma}^{\mathsf{T}}\boldsymbol{\Gamma}\right)^{-1}\boldsymbol{\Gamma}^{\mathsf{T}}. \tag{5.7}$$

Note that $\boldsymbol{\Psi}$ is the annihilator matrix of $\boldsymbol{\Gamma}$ and satisfies $\boldsymbol{\Psi}\boldsymbol{\Psi} = \boldsymbol{\Psi}$. It can be readily shown that

$$\boldsymbol{\Psi} = \operatorname{diag}\left[\mathbf{I}_{N_1} - \frac{1}{N_1}\mathbf{1}_{N_1}\mathbf{1}_{N_1}^{\mathsf{T}}, \ldots, \mathbf{I}_{N_L} - \frac{1}{N_L}\mathbf{1}_{N_L}\mathbf{1}_{N_L}^{\mathsf{T}}\right].$$

Consequently, (5.6) implies that the effect on the position error $\delta\boldsymbol{r}_r$ comes from the vector

$$\tilde{\boldsymbol{\epsilon}}(k) \triangleq \boldsymbol{\Psi}\boldsymbol{\epsilon}(k) = -\begin{bmatrix} \boldsymbol{\epsilon}_1(k) - \mu_1(k)\mathbf{1}_{N_1} \\ \vdots \\ \boldsymbol{\epsilon}_L(k) - \mu_L(k)\mathbf{1}_{N_L} \end{bmatrix},$$

where $\boldsymbol{\epsilon}(k) = \left[\boldsymbol{\epsilon}_1^{\mathsf{T}}(k), \ldots, \boldsymbol{\epsilon}_L^{\mathsf{T}}(k)\right]^{\mathsf{T}}$, $\boldsymbol{\epsilon}_l(k) = \left[\epsilon_{l_1}, \ldots, \epsilon_{l_{N_l}}\right]^{\mathsf{T}}$, and $\mu_l(k) \triangleq \frac{1}{N_l}\sum_{i=1}^{N_l}\epsilon_{l_i}(k)$. Noting that $\epsilon_n(k) = c\delta t_{l_n}(k) - c\bar{\delta}t_n(k)$, the following holds

$$\begin{aligned}\tilde{\epsilon}_n(k) &= \frac{1}{N_l}\sum_{i=1}^{N_l}\left[c\delta t_l(k) - c\bar{\delta}t_{l_i}(k)\right] - \left[c\delta t_l(k) - c\bar{\delta}t_n(k)\right] \\ &= c\bar{\delta}t_n(k) - \frac{1}{N_l}\sum_{i=1}^{N_l} c\bar{\delta}t_{l_i}(k),\end{aligned} \tag{5.8}$$

which is independent of $c\delta t_l(k)$. □

The assumption that the contribution of the relative clock deviation ϵ_n is much larger than the carrier phase measurement noise v_n comes from experimental data, where $\|\boldsymbol{\epsilon}\|$ was observed to be within 0.2 and 4 m, whereas σ_n was on the order of a few cm. Form Theorem 5.1, it can be implied that while the position error is independent of $c\delta t_l$, it depends on the

clustering. Following the result in (5.8), the following parametrization is adopted

$$c\delta t_l(k) \equiv \frac{1}{N_l}\sum_{i=1}^{N_l} c\bar{\delta} t_{l_i}(k), \quad \epsilon_n(k) \equiv c\bar{\delta} t_n(k) - c\delta t_l(k). \tag{5.9}$$

The following section models the dynamics of ϵ_n.

5.2 Frequency Stability and Modeling the Dynamics of Clock Deviations

In this section, the frequency stability and the deviations ϵ_n in cellular CDMA systems are characterized.

5.2.1 Observed Frequency Stability in Cellular CDMA Systems

In order to study the stability of cellular CDMA BTS clocks, real CDMA signals were collected over a period of 24 hours via a stationary universal software radio peripheral (USRP) driven by a GPS-disciplined oscillator (GPSDO). Since the USRP clock is driven by a GPSDO, the apparent Doppler frequency will be mainly caused by the drift in the BTS clock. The Allan deviations were calculated for each BTS using: (1) the absolute Doppler frequencies and (2) the beat Doppler frequencies. The absolute Doppler frequencies are the frequencies directly observed by the receiver on each BTS. The beat Doppler frequency is defined as

$$f_{bD_n} \triangleq f_{D_n} - \frac{1}{N}\sum_{n=1}^{N} f_{D_n},$$

following the parametrization in (5.9). The Allan deviations of the absolute and beat frequencies for three cellular CDMA BTSs nearby the campus of the University of California, Riverside (UCR) are shown in Fig. 5.3. Note that the absolute and beat Doppler frequencies were normalized by the nominal carrier frequency f_c; hence, the Allan deviations are unitless.

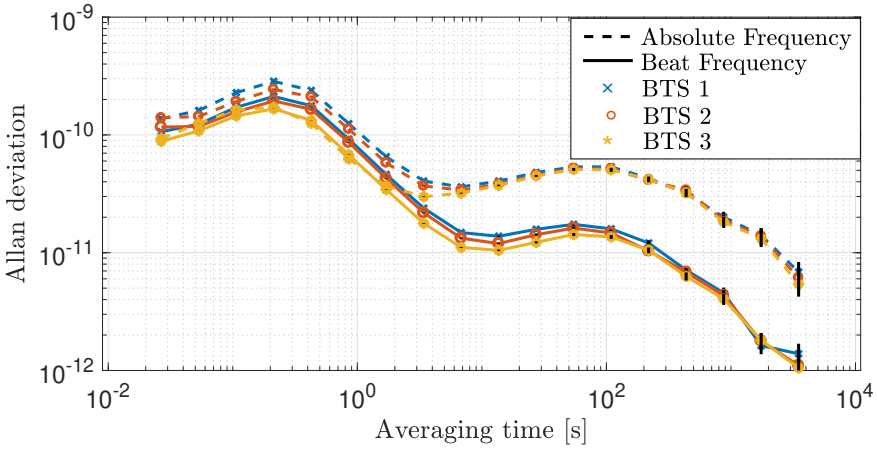

Figure 5.3: Allan deviations of absolute and beat frequencies for three CDMA BTSs near UCR. The Allan deviations were calculated from data collected over 24 hours. The carrier frequency was $f_c = 883.98$ MHz.

Two main conclusions may be drawn from Fig. 5.3. First, the beat frequencies are an order of magnitude more stable than the absolute frequencies. Second, the stability of the beat frequencies approaches that of atomic standards for periods of hundreds to a few thousands seconds. This implies that cellular CDMA signals may be exploited for precise navigation for several minutes using carrier phase measurements.

A similar experiment was conducted at a different time in Colton, California. However, only ten minutes of data were collected. The Allan deviations for two cellular CDMA BTSs in Colton, California, are shown in Fig. 5.4. Similar conclusions are drawn from Fig. 5.4.

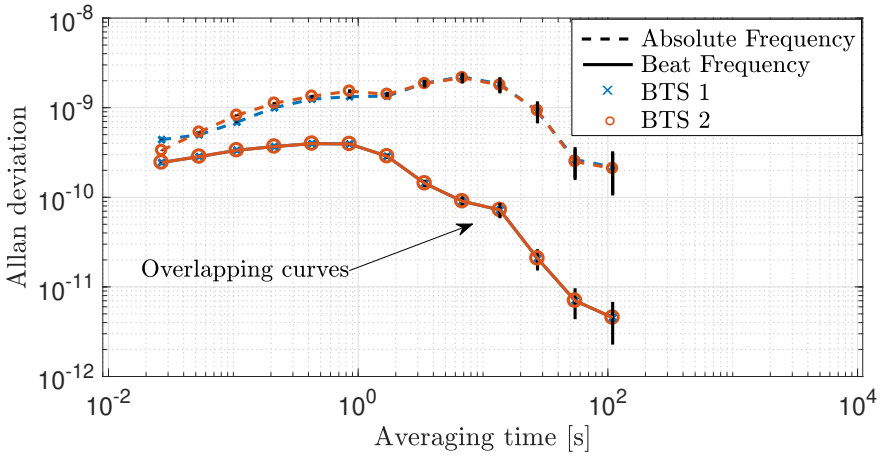

Figure 5.4: Allan deviations of absolute and beat frequencies for two CDMA BTSs in Colton, California. The Allan deviations were calculated from data collected over ten minutes. The carrier frequency was $f_c = 882.75$ MHz.

5.2.2 Modeling the Dynamics of Clock Deviations

Fig. 5.5 shows the clock bias deviations $\{\epsilon_n\}_{n=1}^{3}$ for the three cellular BTSs nearby UCR over 24 hours.

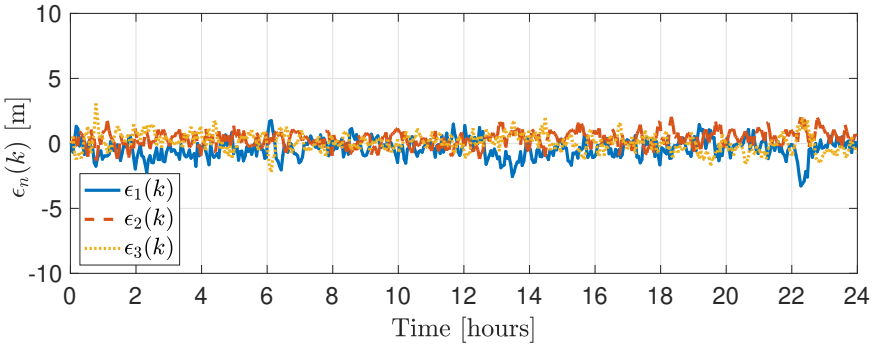

Figure 5.5: Plot of the deviations $\epsilon_n(k)$ from the common clock bias for three BTSs near UCR over 24 hours.

The receiver can perform an exhaustive search over the different clustering possibilities to minimize its position error while it has access to GPS. The number of possible clusters is given by $N_{\text{clus}} = \sum_{L=1}^{N-2} \left(\begin{array}{c} N \\ L \end{array} \right) = \sum_{L=1}^{N-2} \frac{N!}{L!(N-L)!}$. It can be seen that this number becomes impractically large as N increases. A rule-of-thumb that significantly reduces N_{num} is discussed in Subsection 5.3.3. Subsequently, it is assumed that a clustering is given. Next, ϵ_n

are calculated according to (5.9). It can be seen from Fig. 5.5 that ϵ_n is bounded. It can be readily verified (e.g., through spectral analysis) that ϵ_n is not a white sequence. An auto regressive moving average (ARMA) model is proposed to describe the dynamics of ϵ_n, which is generically expressed as

$$\epsilon_n(k+1) = \sum_{i=1}^{p} \phi_i \epsilon_n(k-i+1) + \sum_{i=1}^{q} \psi_i w_{\epsilon_n}(k-i+1) + w_{\epsilon_n}(k), \tag{5.10}$$

where p and $\{\phi_i\}_{i=1}^{p}$ are the order and the coefficients of the autoregressive (AR) part, respectively; q and $\{\psi_i\}_{i=1}^{q}$ are the order and the coefficients of the moving average (MA) part, respectively; and w_ϵ is a white sequence. Identifying p and q and their corresponding coefficients can be readily obtained with standard system identification techniques [93]. Here, the MATLAB System Identification Toolbox was used to identify (5.10), where it was found that $p = q = 6$ was usually enough to whiten w_{ϵ_n}.

5.2.3 Statistics of the Residuals

In this subsection, the resulting residuals w_ϵ are studied. To this end, the autocorrelation function (acf) and the probability density function (pdf) of the residuals are computed for the three realizations of ϵ_n shown in Fig. 5.5. Note that half of the data was used for system identification and the other half was used to validate the model. The acf and pdf of the residuals obtained with the second half of the data are plotted in Figs. 5.6(a)–(c). A Gaussian pdf fit (red) was also plotted. It can be seen that $\{w_{\epsilon_n}\}_{n=1}^{3}$ are zero-mean white Gaussian sequences, with variances $\left\{\sigma^2_{w_{\epsilon n}}\right\}_{n=1}^{3}$.

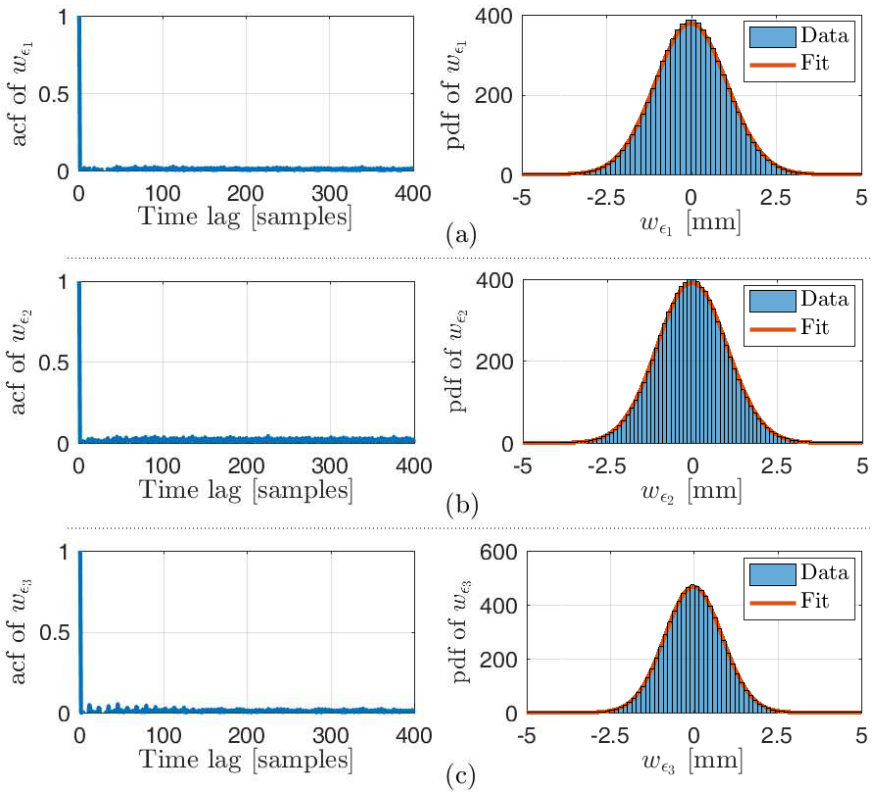

Figure 5.6: (a), (b), and (c) show the acfs and pdfs of w_{ϵ_1}, w_{ϵ_2}, and w_{ϵ_3}, respectively. The acfs show that the sequences $\{w_{\epsilon_n}\}_{n=1}^{3}$ are approximately white and the pdfs show that the sequences are Gaussian.

5.2.4 Statistics of the Clock Deviations

Since $w_{\epsilon_n}(k)$ was found to be a Gaussian sequence, then ϵ_n, which is a linear combination of $w_{\epsilon_n}(k)$ will also be Gaussian. Without loss of generality, it is assumed that $\epsilon_n(i-p)=0$ for $i=1,\ldots,p$. Subsequently, $\mathbb{E}\left[\epsilon_n(k)\right]=0$. The variance of $\epsilon_n(k)$ is discussed next. The ARMA process identified earlier may be represented in state-space according to

$$\begin{aligned}\boldsymbol{\xi}_n(k+1) &= \mathbf{F}_{\xi_n}\boldsymbol{\xi}_n(k)+\boldsymbol{\Gamma}_{\xi_n}w_{\epsilon_n}(k)\\ \epsilon_n(k) &= \boldsymbol{h}_{\epsilon_n}^{\mathsf{T}}\boldsymbol{\xi}_n(k)\end{aligned}$$

where $\boldsymbol{\xi}_n$ is the underlying dynamic AR process, $\mathbf{F}_{\xi_n}$ is its state transition matrix, $\boldsymbol{\Gamma}_{\xi_n}$ is the input matrix, and $\boldsymbol{h}_{\epsilon_n}^{\mathsf{T}}$ is the output matrix. The eigenvalues of $\mathbf{F}_{\xi_n}$ were computed to be

inside the unit circle, implying stability of $\boldsymbol{\xi}_n$. The covariance of $\boldsymbol{\xi}_n$, denoted $\mathbf{P}_{\xi_n}$, evolves according to

$$\mathbf{P}_{\xi_n}(k+1) = \mathbf{F}_{\xi_n}\mathbf{P}_{\xi_n}(k)\mathbf{F}_{\xi_n}^{\mathsf{T}} + \mathbf{Q}_{\xi_n},$$

where $\mathbf{Q}_{\xi_n} \triangleq \sigma_{w_{\epsilon_n}}^2 \boldsymbol{\Gamma}_{\xi_n}\boldsymbol{\Gamma}_{\xi_n}^{\mathsf{T}}$ and the variance of the clock deviation ϵ_n at any given time-step is given by

$$\sigma_{\epsilon_n}^2(k) = \boldsymbol{h}_{\epsilon_n}^{\mathsf{T}}\mathbf{P}_{\xi_n}(k)\boldsymbol{h}_{\epsilon_n}.$$

Since $\boldsymbol{\xi}_n$ is stable, $\mathbf{P}_{\xi_n}(k)$ will converge to a finite steady-state covariance denoted $\mathbf{P}_{\xi_n,\mathrm{ss}}$ given by the solution to the discrete-time matrix Lyapunov equation

$$\mathbf{P}_{\xi_n,\mathrm{ss}} = \mathbf{F}_{\xi_n}\mathbf{P}_{\xi_n,\mathrm{ss}}\mathbf{F}_{\xi_n}^{\mathsf{T}} + \mathbf{Q}_{\xi_n}.$$

Subsequently, the steady-state variance of the clock deviation is given by

$$\sigma_{\epsilon_n}^2 = \boldsymbol{h}_{\epsilon_n}^{\mathsf{T}}\mathbf{P}_{\xi_n,\mathrm{ss}}\boldsymbol{h}_{\epsilon_n}.$$

5.3 Performance Characterization

This section derives performance bounds for the single receiver navigation framework using SOP carrier phase measurements presented in Section 5.1. Also, clustering of the clock bias biases is investigated and an upper bound on the position error is derived.

5.3.1 A Note on the Optimal BTS Geometric Configuration

As seen in Chapter 3, the measurement Jacobian $\mathbf{G}$ with respect to the position states (cf. (5.5)) could be re-parameterized in terms of the bearing angles θ_n between each SOP and the receiver, given by

$$\mathbf{G} = \begin{bmatrix} \cos\theta_1 & \dots & \cos\theta_N \\ \sin\theta_1 & \dots & \sin\theta_N \end{bmatrix}^{\mathsf{T}},$$

as illustrated in Fig. 5.7(a). The optimal geometric configuration of sensors (or navigation sources) around an emitter (or receiver) has been well studied in the literature. This problem is also similar to the geometric dilution of precision (GDOP) minimization problem in GPS. It was found that the GDOP is minimized when the end points of the unit line of sight vectors pointing from the receiver to each navigation source form a regular polygon around the receiver, as shown in Fig. 5.7(b). In the sequel, the aforementioned configuration will be referred to as the optimal configuration, where the bearing angles are given by $\theta_n = \frac{2\pi(n-1)}{N}$, $n = 1, \dots, N$. Note that these results hold for $N \geq 3$ in the 2-D case.

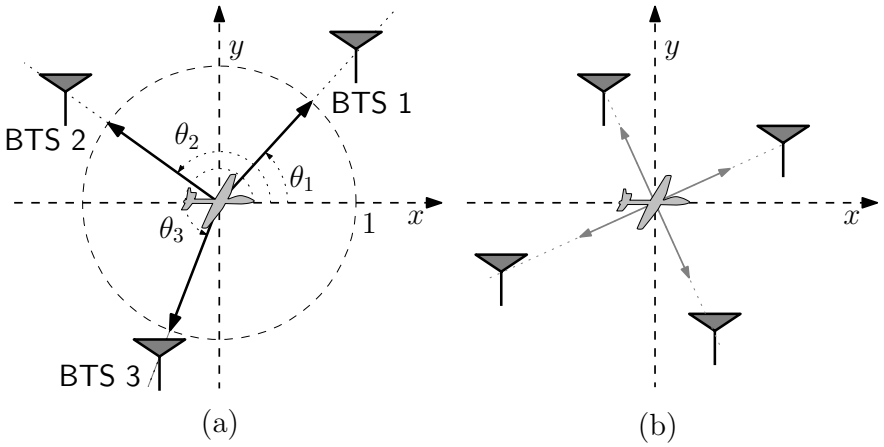

Figure 5.7: (a) Re-parametrization of the measurement Jacobian as a function of the bearing angles θ_n. (b) Optimal geometric configuration of the BTSs around the receiver.

5.3.2 Lower Bound on the logarithm of the Determinant of the Position Estimation Error Covariance

It can be readily seen that optimal performance is achieved when all clocks are perfectly synchronized, i.e., $\epsilon_n(k) = 0$, $\forall\, k$, and therefore $\mathbf{R}_\eta = \mathbf{R}$. In this case, only one clock bias is estimated, and this problem becomes similar to the one discussed in [97], in which it is shown that the logarithm of the determinant of the position estimation error covariance $\mathbf{P}_{x,y}$ is bounded by

$$\log\det\left[\mathbf{P}_{x,y}\right] \geq -2\log\left[\mathrm{trace}\left(\mathbf{R}^{-1}\right)\right].$$

5.3.3 Clustering of the Clock Biases

It was mentioned in Subsection 5.2.2 that an exhaustive search may be performed to cluster the clock biases $c\delta t_n$ in order to minimize the position estimation error. This amounts to finding the matrix $\mathbf{\Gamma}$ that minimizes

$$J_p(\mathbf{\Gamma}) \triangleq \sum_{k=1}^{k_0} \left\|\delta \boldsymbol{r}_r(k)\right\|^2 =$$
$$\sum_{k=1}^{k_0} \left\| \left[\mathbf{G}^\mathsf{T}\left(\mathbf{I}-\mathbf{\Gamma}\left(\mathbf{\Gamma}^\mathsf{T}\mathbf{\Gamma}\right)^{-1}\mathbf{\Gamma}^\mathsf{T}\right)\mathbf{G}\right]^{-1}\mathbf{G}^\mathsf{T}\left(\mathbf{I}-\mathbf{\Gamma}\left(\mathbf{\Gamma}^\mathsf{T}\mathbf{\Gamma}\right)^{-1}\mathbf{\Gamma}^\mathsf{T}\right)\boldsymbol{\epsilon}(k)\right\|^2$$
$$= \sum_{k=1}^{k_0} \left\| \left(\mathbf{G}^\mathsf{T}\mathbf{\Psi}\mathbf{G}\right)^{-1}\mathbf{G}^\mathsf{T}\mathbf{\Psi}\boldsymbol{\epsilon}(k)\right\|^2,$$

where $\mathbf{\Gamma}$ and $\mathbf{\Psi}$ are defined in (5.4) and (5.7), respectively. This optimization problem is non-convex and intractable. Instead of optimizing $J_p(\mathbf{\Gamma})$, a tractable rule-of-thumb is provided

next. First, consider the modified cost function

$$\begin{aligned} J(\mathbf{\Gamma}) &\triangleq \left\| \left(\mathbf{G}^{\mathsf{T}}\mathbf{\Psi}\mathbf{G}\right)^{-1}\mathbf{G}^{\mathsf{T}}\mathbf{\Psi}\boldsymbol{\epsilon}(k_0)\right\|^2 \\ &= \left\| \left(\mathbf{G}^{\mathsf{T}}\mathbf{\Psi}\mathbf{\Psi}\mathbf{G}\right)^{-1}\mathbf{G}^{\mathsf{T}}\mathbf{\Psi}\mathbf{\Psi}\boldsymbol{\epsilon}(k_0)\right\|^2 \\ &\leq \left\| \left(\mathbf{G}_{\Gamma}^{\mathsf{T}}\mathbf{G}_{\Gamma}\right)^{-1}\mathbf{G}_{\Gamma}^{\mathsf{T}}\right\|^2 \left\|\mathbf{\Psi}\boldsymbol{\epsilon}(k_0)\right\|^2, \end{aligned}$$

where $\mathbf{G}_{\Gamma} \triangleq \mathbf{\Psi}\mathbf{G}$. Let the singular value decomposition (svd) of $\mathbf{G}_{\Gamma}$ be

$$\mathbf{G}_{\Gamma} = \mathbf{U}\mathbf{\Sigma}_{\Gamma}\mathbf{V}^{\mathsf{T}},$$

where $\mathbf{U}$ is an $N \times N$ unitary matrix, $\mathbf{V}$ is a 2×2 unitary matrix, and $\mathbf{\Sigma}_{\Gamma} = [\mathbf{\Sigma} \quad \mathbf{0}]^{\mathsf{T}}$, where $\mathbf{\Sigma}$ is a nonsingular 2×2 diagonal matrix containing the nonzero singular values of $\mathbf{G}_{\Gamma}$. It can be readily shown that

$$\left(\mathbf{G}_{\Gamma}^{\mathsf{T}}\mathbf{G}_{\Gamma}\right)^{-1}\mathbf{G}_{\Gamma}^{\mathsf{T}} = \mathbf{V}\mathbf{\Sigma}'\mathbf{U}^{\mathsf{T}}, \tag{5.11}$$

where $\mathbf{\Sigma}' \triangleq [\mathbf{\Sigma}^{-1} \quad \mathbf{0}]^{\mathsf{T}}$. This implies that (5.11) is the svd of $\left(\mathbf{G}_{\Gamma}^{\mathsf{T}}\mathbf{G}_{\Gamma}\right)^{-1}\mathbf{G}_{\Gamma}^{\mathsf{T}}$ and its singular values are the inverses of the singular values of $\mathbf{G}_{\Gamma}$, yielding

$$\left\| \left(\mathbf{G}_{\Gamma}^{\mathsf{T}}\mathbf{G}_{\Gamma}\right)^{-1}\mathbf{G}_{\Gamma}^{\mathsf{T}}\right\|^2 = \left[\sigma_{\max}\left(\mathbf{G}_{\Gamma}\right)\right]^2 = \left[\frac{1}{\sigma_{\min}\left(\mathbf{G}_{\Gamma}\right)}\right]^2,$$

where $\sigma_{\max}(\cdot)$ and $\sigma_{\min}(\cdot)$ denote the maximum and minimum singular values of a matrix, respectively. Note that the singular values of $\mathbf{G}_{\Gamma}$ are the square root of the eigenvalues of $\mathbf{G}_{\Gamma}^{\mathsf{T}}\mathbf{G}_{\Gamma} = \mathbf{G}^{\mathsf{T}}\mathbf{\Psi}\mathbf{G}$, and hence

$$\left\| \left(\mathbf{G}_{\Gamma}^{\mathsf{T}}\mathbf{G}_{\Gamma}\right)^{-1}\mathbf{G}_{\Gamma}^{\mathsf{T}}\right\|^2 = \frac{1}{\lambda_{\min}\left(\mathbf{G}^{\mathsf{T}}\mathbf{\Psi}\mathbf{G}\right)} = \lambda_{\max}\left(\mathbf{P}_{x,y}\right),$$

where $\lambda_{\max}(\cdot)$ and $\lambda_{\min}(\cdot)$ denote the maximum and minimum eigenvalues of a matrix, respectively. Consequently, the cost $J(\mathbf{\Gamma})$ may be bounded by

$$J(\mathbf{\Gamma}) \leq \lambda_{\max}(\mathbf{P}_{x,y}) \left\| \mathbf{\Psi}\boldsymbol{\epsilon}(k_0) \right\|^2. \tag{5.12}$$

Next, two theorems are presented that will help derive the rule-of-thumb for clustering the clock biases.

Theorem 5.2. *Assume a clock bias clustering with $L < N-2$ clusters and denote $J_L \triangleq \left\| \mathbf{\Psi}\boldsymbol{\epsilon}(k) \right\|^2$. Then, there exists a clustering with $L+1$ clusters such that $J_L \geq J_{L+1}$.*

Proof. First, note that J_L may be expressed as

$$\begin{aligned}
J_L = \left\| \mathbf{\Psi}\boldsymbol{\epsilon}(k) \right\|^2 &= \left\| \begin{bmatrix} \boldsymbol{\epsilon}_1(k) - \mu_1(k)\mathbf{1}_{N_1} \\ \vdots \\ \boldsymbol{\epsilon}_L(k) - \mu_L(k)\mathbf{1}_{N_L} \end{bmatrix} \right\|^2 \\
&= \sum_{l=1}^{L} \left\| \boldsymbol{\epsilon}_l - \mu_l(k)\mathbf{1}_{N_l} \right\|^2 = \sum_{l=1}^{L} \sum_{j=1}^{N_l} \left[\epsilon_{l_j}(k) - \mu_l(k) \right]^2 \\
&= \sum_{l=1}^{L-1} \sum_{j=1}^{N_l} \left[\epsilon_{l_j}(k) - \mu_l(k) \right]^2 + \sum_{j=1}^{N_L} \left[\epsilon_{L_j}(k) - \mu_l(k) \right]^2 \\
&= a + \sum_{j=1}^{N_L} (\epsilon_{L_j}(k) - \mu_L(k))^2,
\end{aligned}$$

where $a \triangleq \sum_{l=1}^{L-1} \sum_{j=1}^{N_l} \left[\epsilon_{l_j}(k) - \mu_l(k) \right]^2$. In what follows, the time argument k will be dropped for simplicity of notation. Now add an additional cluster by partitioning $\boldsymbol{\epsilon}_L$ according to $\boldsymbol{\epsilon}_L = \left[\boldsymbol{\epsilon}'^{\mathsf{T}}_L, \epsilon_{L+1} \right]^{\mathsf{T}}$ and define

$$J_{L+1} = a + \sum_{j=1}^{N_L - 1} \left(\epsilon_{L_j} - \mu'_L \right)^2 + \left(\epsilon_{L+1} - \mu_{L+1} \right)^2,$$

where $\mu'_L \triangleq \frac{1}{N_L-1}\sum_{j=1}^{N_L-1}\epsilon_{L_j}$ and $\mu_{L+1} = \epsilon_{L+1}$. Subsequently, J_{L+1} may be expressed as

$$J_{L+1} = a + \sum_{j=1}^{N_L-1}(\epsilon_{L_j} - \mu_L)^2.$$

The second term in J_L may be expressed as

$$\begin{aligned}\sum_{j=1}^{N_L}(\epsilon_{L_j} - \mu_L)^2 &= \sum_{j=1}^{N_L}\epsilon_{L_j}^2 - N_L\mu_L^2 \\ &= \sum_{j=1}^{N_L-1}\epsilon_{L_j}^2 - N_L\mu_L^2 + \epsilon_{L_{N_L}}^2.\end{aligned}$$

The term $N_L\mu_L^2$ may be expressed as

$$\begin{aligned}N_L\mu_L^2 &= N_L\left(\frac{1}{N_L}\sum_{j=1}^{N_L}\epsilon_{L_j}\right)^2 \\ &= \frac{1}{N_L}\left(\sum_{j=1}^{N_L-1}\epsilon_{L_j} + \epsilon_{L_{N_L}}\right)^2 \\ &= \frac{1}{N_L}\left[(N_L-1)\,\mu'_L + \epsilon_{L_{N_L}}\right]^2 \\ &= \frac{(N_L-1)^2\,\mu'^2_L}{N_L} + \frac{2(N_L-1)\mu'_L\epsilon_{L_{N_L}}}{N_L} + \frac{\epsilon^2_{L_{N_L}}}{N_L}\end{aligned}$$

$$\begin{aligned}&= (N_L-1)\,\mu'^2_L - \frac{(N_L-1)\,\mu'^2_L}{N_L} \\ &\quad + \frac{2(N_L-1)\mu'_L\epsilon_{L,N_L}}{N_L} + \frac{\epsilon^2_{L_{N_L}}}{N_L} + \epsilon^2_{L_{N_L}} - \epsilon^2_{L_{N_L}} \\ &= (N_L-1)\,\mu'^2_L - \frac{(N_L-1)}{N_L}(\epsilon_{L_{N_L}} - \mu'_L)^2 + \epsilon^2_{L_{N_L}}.\end{aligned}$$

Substituting back in the second term of J_L yields

$$\sum_{j=1}^{N_L}(\epsilon_{L_j}-\mu_L)^2=\sum_{j=1}^{N_L-1}(\epsilon_{L_j}-\mu'_L)^2+\frac{(N_L-1)}{N_L}(\epsilon_{L_{N_L}}-\mu'_L)^2.$$

Substituting back in J_L yields

$$\begin{aligned}J_L&=a+\sum_{j=1}^{N_L-1}(\epsilon_{L_j}-\mu'_L)^2+\frac{(N_L-1)}{N_L}(\epsilon_{L_{N_L}}-\mu'_L)^2\\&=J_{L+1}+\frac{(N_L-1)}{N_L}(\epsilon_{L_{N_L}}-\mu'_L)^2.\end{aligned}$$

Since $\frac{(N_L-1)}{N_L}(\epsilon_{L_{N_L}}-\mu'_L)^2\geq 0$, then $J_L\geq J_{L+1}$. □

From Theorem 5.2, it can be implied that $\|\boldsymbol{\Psi\epsilon}(k)\|^2$ is minimized when $L=N-2$, i.e., the maximum number of clusters is used. This also implies that using more SOP clusters will decrease $\|\boldsymbol{\Psi\epsilon}(k_0)\|^2$ in the upper bound expression of $J(\boldsymbol{\Gamma})$ given in (5.12).

Theorem 5.3. *Consider $N\geq 3$ carrier phase measurements for estimating the receiver's position $\boldsymbol{r}_r$ and a clustering of L clock states $c\boldsymbol{\delta}t$. Adding a carrier phase measurement from an additional cellular SOP while augmenting the clock state vector $c\boldsymbol{\delta}t$ by its corresponding additional clock state will neither change the position error nor the position error uncertainty.*

Proof. The augmented Jacobian matrix is given by

$$\mathbf{H}'=\begin{bmatrix}\mathbf{G}&\boldsymbol{\Gamma}&\mathbf{0}\\ \boldsymbol{g}^{\mathsf{T}}&\mathbf{0}^{\mathsf{T}}&1\end{bmatrix},$$

where $\boldsymbol{g} \triangleq \frac{\hat{\boldsymbol{r}}_r - \boldsymbol{r}_{s_{N+1}}}{\left\|\hat{\boldsymbol{r}}_r - \boldsymbol{r}_{s_{N+1}}\right\|}$. The new information matrix is subsequently given by

$$\mathbf{H}'^{\mathsf{T}}\mathbf{H}' = \begin{bmatrix} \mathbf{G}^{\mathsf{T}}\mathbf{G} + \boldsymbol{g}\boldsymbol{g}^{\mathsf{T}} & \mathbf{G}^{\mathsf{T}}\boldsymbol{\Gamma} & \boldsymbol{g} \\ \boldsymbol{\Gamma}^{\mathsf{T}}\mathbf{G} & \boldsymbol{\Gamma}^{\mathsf{T}}\boldsymbol{\Gamma} & \mathbf{0} \\ \boldsymbol{g}^{\mathsf{T}} & \mathbf{0}^{\mathsf{T}} & 1 \end{bmatrix} = \begin{bmatrix} \mathbf{M}_{11} & \boldsymbol{m}_{12} \\ \boldsymbol{m}_{12}^{\mathsf{T}} & 1 \end{bmatrix},$$

where

$$\mathbf{M}_{11} \triangleq \begin{bmatrix} \mathbf{G}^{\mathsf{T}}\mathbf{G} + \boldsymbol{g}\boldsymbol{g}^{\mathsf{T}} & \mathbf{G}^{\mathsf{T}}\boldsymbol{\Gamma} \\ \boldsymbol{\Gamma}^{\mathsf{T}}\mathbf{G} & \boldsymbol{\Gamma}^{\mathsf{T}}\boldsymbol{\Gamma} \end{bmatrix}, \boldsymbol{m}_{12} \triangleq \begin{bmatrix} \boldsymbol{g} \\ \mathbf{0} \end{bmatrix}.$$

The new covariance is given by

$$\mathbf{P}' = \left(\mathbf{H}'^{\mathsf{T}}\mathbf{H}'\right)^{-1} = \begin{bmatrix} \mathbf{A}' & \boldsymbol{b}' \\ \boldsymbol{b}'^{\mathsf{T}} & d' \end{bmatrix},$$

where

$$\begin{aligned} \mathbf{A}' &= \left(\mathbf{M}_{11} - \boldsymbol{m}_{12}\boldsymbol{m}_{12}^{\mathsf{T}}\right)^{-1} \\ \boldsymbol{b}' &= -\left(\mathbf{M}_{11} - \boldsymbol{m}_{12}\boldsymbol{m}_{12}^{\mathsf{T}}\right)^{-1}\boldsymbol{m}_{12} \\ d' &= 1 + \boldsymbol{m}_{12}^{\mathsf{T}}\left(\mathbf{M}_{11} - \boldsymbol{m}_{12}\boldsymbol{m}_{12}^{\mathsf{T}}\right)^{-1}\boldsymbol{m}_{12} \end{aligned}$$

The matrix $\mathbf{A}'$ may be expressed as

$$\begin{aligned} \mathbf{A}' &= \left(\begin{bmatrix} \mathbf{G}^{\mathsf{T}}\mathbf{G} + \boldsymbol{g}\boldsymbol{g}^{\mathsf{T}} & \mathbf{G}^{\mathsf{T}}\boldsymbol{\Gamma} \\ \boldsymbol{\Gamma}^{\mathsf{T}}\mathbf{G} & \boldsymbol{\Gamma}^{\mathsf{T}}\boldsymbol{\Gamma} \end{bmatrix} - \begin{bmatrix} \boldsymbol{g}\boldsymbol{g}^{\mathsf{T}} & \mathbf{0} \\ \mathbf{0}^{\mathsf{T}} & \mathbf{0} \end{bmatrix}\right)^{-1} \\ &= \begin{bmatrix} \mathbf{G}^{\mathsf{T}}\mathbf{G} & \mathbf{G}^{\mathsf{T}}\boldsymbol{\Gamma} \\ \boldsymbol{\Gamma}^{\mathsf{T}}\mathbf{G} & \boldsymbol{\Gamma}^{\mathsf{T}}\boldsymbol{\Gamma} \end{bmatrix}^{-1} = \mathbf{P}, \end{aligned}$$

which indicates that the new uncertainty in the position state is unchanged. The new covariance can be expressed as

$$\mathbf{P}' = \begin{bmatrix} \mathbf{P} & -\mathbf{P}\boldsymbol{m}_{12} \\ -\boldsymbol{m}_{12}^{\mathsf{T}}\mathbf{P} & 1+\boldsymbol{m}_{12}^{\mathsf{T}}\mathbf{P}\boldsymbol{m}_{12} \end{bmatrix} = \begin{bmatrix} \mathbf{P}'_{11} & \mathbf{P}'_{12} & \mathbf{P}'_{13} \\ \mathbf{P}'^{\mathsf{T}}_{12} & \mathbf{P}'_{22} & \mathbf{P}'_{23} \\ \mathbf{P}'^{\mathsf{T}}_{13} & \mathbf{P}'^{\mathsf{T}}_{23} & \mathbf{P}'_{33} \end{bmatrix},$$

where

$$\begin{aligned}
\mathbf{P}'_{11} &= \left(\mathbf{G}^{\mathsf{T}}\boldsymbol{\Psi}\mathbf{G}\right)^{-1} \\
\mathbf{P}'_{12} &= -\left(\mathbf{G}^{\mathsf{T}}\boldsymbol{\Psi}\mathbf{G}\right)^{-1}\mathbf{G}^{\mathsf{T}}\boldsymbol{\Gamma}\left(\boldsymbol{\Gamma}^{\mathsf{T}}\boldsymbol{\Gamma}\right)^{-1} \\
\mathbf{P}'_{13} &= -\left(\mathbf{G}^{\mathsf{T}}\boldsymbol{\Psi}\mathbf{G}\right)^{-1}\boldsymbol{g} \\
\mathbf{P}'_{22} &= \left(\boldsymbol{\Gamma}^{\mathsf{T}}\boldsymbol{\Gamma}\right)^{-1}\boldsymbol{\Gamma}^{\mathsf{T}}\left[\mathbf{I}+\mathbf{G}\left(\mathbf{G}^{\mathsf{T}}\boldsymbol{\Psi}\mathbf{G}\right)^{-1}\mathbf{G}^{\mathsf{T}}\right]\boldsymbol{\Gamma}\left(\boldsymbol{\Gamma}^{\mathsf{T}}\boldsymbol{\Gamma}\right)^{-1} \\
\mathbf{P}'_{23} &= \left(\boldsymbol{\Gamma}^{\mathsf{T}}\boldsymbol{\Gamma}\right)^{-1}\boldsymbol{\Gamma}^{\mathsf{T}}\mathbf{G}\left(\mathbf{G}^{\mathsf{T}}\boldsymbol{\Psi}\mathbf{G}\right)^{-1}\boldsymbol{g} \\
\mathbf{P}'_{33} &= 1+\boldsymbol{g}^{\mathsf{T}}\left(\mathbf{G}^{\mathsf{T}}\boldsymbol{\Psi}\mathbf{G}\right)^{-1}\boldsymbol{g}
\end{aligned}$$

The new estimation error is given by

$$\delta\boldsymbol{r}'_r(k) = -\mathbf{P}'\mathbf{H}'^{\mathsf{T}}\boldsymbol{\epsilon}'(k),$$

where $\boldsymbol{\epsilon}'(k) \triangleq \left[\boldsymbol{\epsilon}^{\mathsf{T}}(k), \epsilon_{N+1}(k)\right]^{\mathsf{T}}$ and $\epsilon_{N+1}(k)$ is the error from the $(N+1)^{\text{st}}$ measurement. Using the expressions of $\mathbf{P}'$, $\mathbf{H}'$, and $\boldsymbol{\epsilon}'$, it can be readily shown that

$$\delta\boldsymbol{r}'_r(k) = -\left(\mathbf{G}^{\mathsf{T}}\boldsymbol{\Psi}\mathbf{G}\right)^{-1}\mathbf{G}^{\mathsf{T}}\boldsymbol{\Psi}\boldsymbol{\epsilon}(k) = \delta\boldsymbol{r}_r(k).$$

Therefore, the addition of a measurement while augmenting the clock state vector by one state will not improve the position estimate nor the position error uncertainty. □

From Theorem 5.3, it can be implied that it is required that $N_l \geq 2$ in order for cluster l to contribute in estimating the position state. Therefore, $\lambda_{\max}(\mathbf{P}_{x,y})$ can be made smaller by decreasing the number of clusters L. Combining the conclusions of Theorems 5.2 and 5.3 and referring to (5.12), one can see that there is a tradeoff between estimating more clock biases and uncertainty reduction: less bias for more uncertainty and vice versa. Subsequently, a good rule of thumb is to have at least on cluster with $N_l \geq 3$ (to ensure observability) and $N_l \geq 2$ for the remaining clusters. This implies that $L \leq \frac{N-3}{2}+1$, which significantly reduces the number of possible clusters in the exhaustive search algorithm.

5.3.4 Upper Bound on the Position Error

Note that for a given number of SOPs, one will choose a clustering that will yield a performance that is at least as good as estimating one clock bias. Therefore, a bound on the position error may be established according to

$$\|\delta \boldsymbol{r}_r(k)\| \leq \left\| \left(\mathbf{G}^{\mathsf{T}}\boldsymbol{\Psi}_1\mathbf{G}\right)^{-1}\mathbf{G}^{\mathsf{T}}\boldsymbol{\Psi}_1\boldsymbol{\epsilon}(k) \right\|,$$

where $\boldsymbol{\Psi}_1 \triangleq \mathbf{I} - \frac{1}{N}\mathbf{1}_N\mathbf{1}_N^{\mathsf{T}}$.

5.4 Experimental Results

In this section, experimental results are presented demonstrating precise, sub-meter level receiver navigation results via the single receiver framework developed in this chapter with precise carrier phase measurements. Only the 2–D positions of the receivers are estimated as their height may be obtained using other sensors (e.g., altimeter). In the following experiments, the height of the receivers was obtained from their on-board navigation systems. Moreover, the noise equivalent bandwidth of the receivers' PLL was set to $B_{\mathrm{N,PLL}} = B_{\mathrm{M,PLL}} =$

$B_{\text{PLL}} = 3$ Hz in all experiments.

Two experiments were conducted with two different drones. In the first experiment, the same setup described in Section 4.5 of Chapter 4 was used, except that the receiver was navigating without the base and was employing the framework developed in Section 5.1. In the second experiment, a DJI Matrice 600 was equipped with the same hardware described in Section 4.5 of Chapter 4 and the on-board USRP was tuned to the same carrier frequency. The cellular carrier phase measurements were also given at a rate of 37.5 Hz, i.e., $T = 0.0267$ ms. The ground-truth reference for the receiver trajectory was taken from its on-board navigation system, which also uses GPS, an IMU, and other sensors. The experimental setup and SOP BTS layout for the second experiment are shown in Fig. 5.8.

In both experiments, the receivers had access to GPS for 10 seconds, then GPS was cut off. During the time where GPS was available, the cellular signals were used to cluster the cellular SOPs and characterize the clock deviations, as described in Subsection 5.2.2. In the first experiment, the receiver traversed a trajectory of 1.72 Km, which was completed in 3 minutes. The receiver was listening to the same 9 CDMA BTSs as in Fig. 4.6 of Chapter 4, with the same carrier-to-noise ratios as in Fig. 4.4 of Chapter 4. The navigation results are shown in Fig. 5.9. The optimal clustering was found to be $\mathcal{C}_1 = \{\text{BTS 1 , BTS 5, BTS 7, BTS 8}\}, \mathcal{C}_2 = \{\text{BTS 2, BTS 3, BTS 6 }\}$, and $\mathcal{C}_3 = \{\text{BTS 4, BTS 9}\}$. The position RMSE was calculated to be 36.61 cm.

In the second experiment, the receiver traversed a trajectory of 3.07 Km completed in 325 seconds. The receiver was listening to the 7 CDMA BTSs shown in Fig. 5.8. The carrier-to-noise ratios of all the BTSs measured by the navigating receiver in the second experiment are given in Fig. 5.10 and the navigation results are shown in Fig. 5.11. The optimal clustering was found to be $\mathcal{C}_1 = \{\text{BTS 1, BTS 2, BTS 3, BTS 4, BTS 6}\}$ and $\mathcal{C}_2 = \{\text{BTS 5, BTS 7}\}$. The position RMSE was calculated to be 88.58 cm.

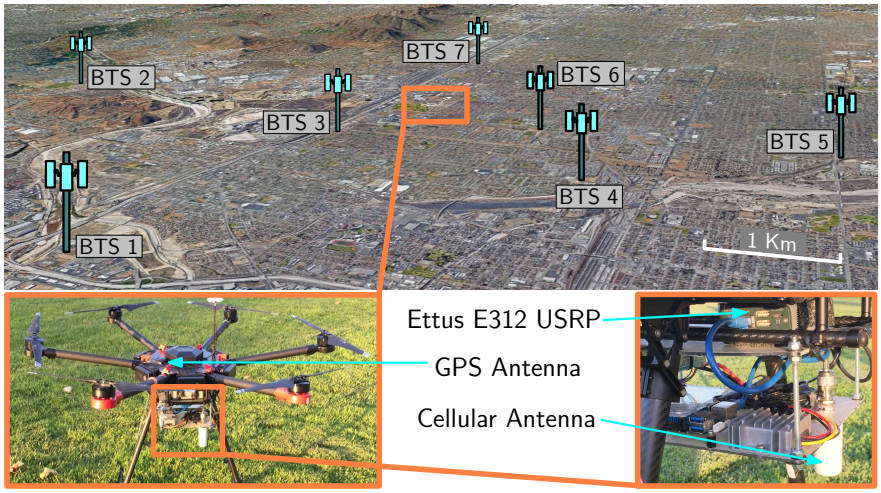

Figure 5.8: Experimental setup and the SOP BTS layout for the second experiment demonstrating a single receiver navigating with precise cellular carrier phase measurements. Map data: Google Earth.

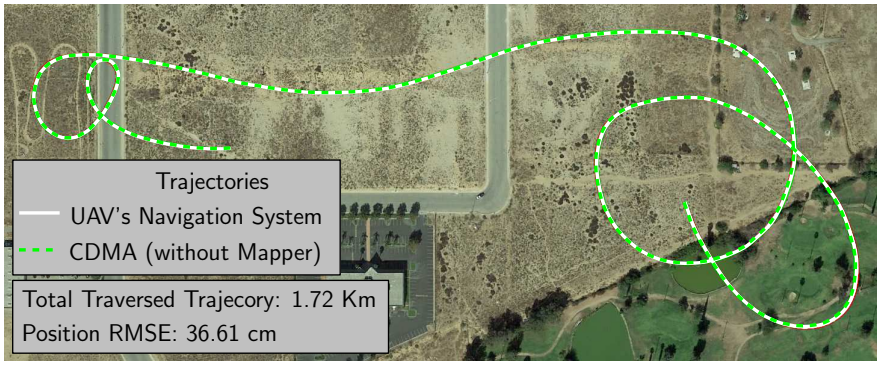

Figure 5.9: First experiment demonstrating a single receiver navigating with precise cellular carrier phase measurements. The true and estimated trajectories are shown in solid and dashed lines, respectively. Map data: Google Earth.

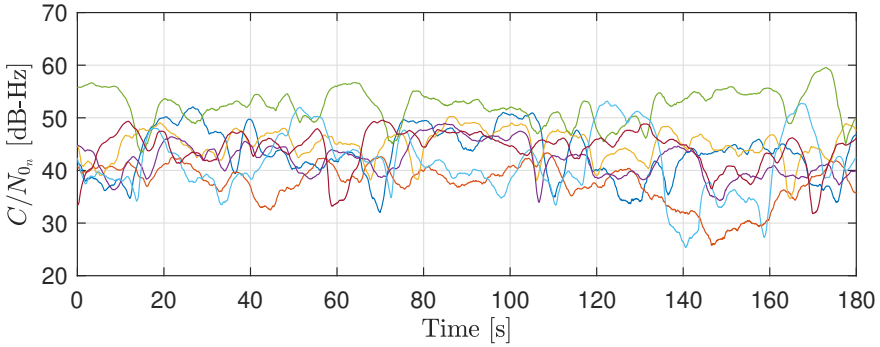

Figure 5.10: Carrier-to-noise ratios of all $\{C/N_{0_n}\}_{n=1}^{7}$ the cellular BTSs measured by the navigating receiver for the second experiment.

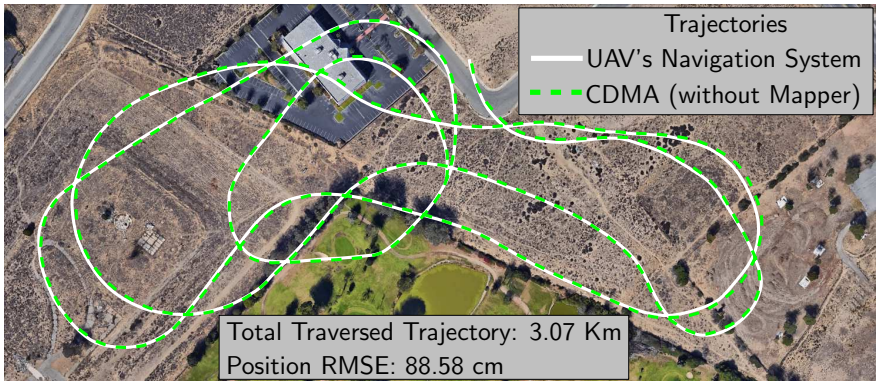

Figure 5.11: Second experiment demonstrating a single receiver navigating with precise cellular carrier phase measurements. The true and estimated trajectories are shown in solid and dashed lines, respectively. Map data: Google Earth.

5.4.1 Discussion

First, it is important to note that all RMSEs were calculated with respect to the trajectory returned by the receivers' on-board navigation system. Although these systems use multiple sensors for navigation, they are not equipped with high precision GPS receivers, e.g., Real Time Kinematic (RTK) systems. Therefore, some errors are expected in what is considered to be "true" trajectories taken from the on-board sensors. The hovering horizontal precision of the receivers are reported to be 2 meters for the X-Star Premium by Autel Robotics and 1.5 meters for the Matrice 600 by DJI.

Second, it can be noted that the CD-cellular with base/rover framework from Chapter 4 under-performed compared to the single receiver framework. This can be due to: (1) poor synchronization between the base's and rover measurements and (2) errors in the base position. It is important to note that the base was mobile during the experiment and the position returned by its on-board navigation system was used as ground-truth. Consequently, any errors in the GPS solution would have degraded the rover's estimate.

Third, the RMSEs reported in this section are for optimal clustering. In the 10 seconds during which GPS was available, a search was performed to optimally cluster the clock biases using the rule-of-thumb discussed in Subsection 5.3.3. The search took less than 3

seconds. The RMSEs without clustering (only one bias is estimated) are 48 cm and 97 cm for the first and second experiments, respectively.

Chapter 6

Non-Differential Framework for Navigation with Carrier Phase Measurements from Asynchronous Cellular SOPs

This chapter is organized as follows. Section 6.1 describes the cellular SOP and receiver dynamics models. Section 6.2 describes the EKF-based navigation framework. Section 6.3 analyzes the observability and the EKF error boundedness of the proposed framework. Section 6.4 characterizes the performance of the proposed framework via MC simulations. Section 6.5 provides experimental results showing meter-level UAV navigation accuracy. The notation in this chapter is independent from the one used in previous chapters.

The results of this chapter have been published in [115].

6.1 Model Description

This section presents the dynamics model of the UAV-mounted receiver and cellular SOP as well as the cellular carrier phase measurement model. Note that an altimeter could be used to estimate the UAV's altitude. Therefore, only the UAV's two-dimensional (2–D) position is estimated in this chapter. The subsequent analysis is readily extendable to 3–D; however, the vertical position estimate will suffer from large uncertainty due to the poor vertical diversity of cellular towers.

6.1.1 Cellular SOP Dynamics Model

The cellular SOPs emanate from spatially-stationary terrestrial BTSs or eNodeBs, and their states will consist of their *known* 2–D positions and *unknown* clock error states, namely the clock bias and clock drift. For simplicity of notation, let the term BTS denote any type of cellular SOP transmitter (CDMA BTS, LTE eNodeB, etc.), unless explicitly stated otherwise. The position vector of the n-th BTS is given by $\boldsymbol{r}_{s_n} = [x_{s_n}, y_{s_n}]^{\mathsf{T}}$. The state of the n-th BTS will only consist of its clock error state and is given by $\boldsymbol{x}_{\text{clk},s_n}(k) \triangleq \left[c\delta t_{s_n}(k), c\dot{\delta} t_{s_n}(k)\right]^{\mathsf{T}}$, where $\delta t_{s_n}(k)$ and $\dot{\delta} t_{s_n}(k)$ are the clock bias and clock drift at time-step k, respectively, and c is the speed-of-light. The n-th BTS's dynamics can be described by the discretized state space model

$$\boldsymbol{x}_{\text{clk},s_n}(k+1) = \mathbf{F}_{\text{clk}}\, \boldsymbol{x}_{\text{clk},s_n}(k) + \boldsymbol{w}_{\text{clk},s_n}(k), \quad k = 0, 1, \ldots,$$

where $n = 1, \ldots, N$, with N being the total number of BTSs, and $\boldsymbol{w}_{\text{clk},s_n}(k)$ is a zero-mean white noise sequence with covariance $\mathbf{Q}_{\text{clk},s_n}$, with

$$\mathbf{F}_{\text{clk}} = \begin{bmatrix} 1 & T \\ 0 & 1 \end{bmatrix}, \; \mathbf{Q}_{\text{clk},s_n} = c^2 \begin{bmatrix} S_{\tilde{w}_{\delta t_s,n}} T + S_{\tilde{w}_{\dot{\delta} t_s,n}} \frac{T^3}{3} & S_{\tilde{w}_{\dot{\delta} t_s,n}} \frac{T^2}{2} \\ S_{\tilde{w}_{\dot{\delta} t_s,n}} \frac{T^2}{2} & S_{\tilde{w}_{\dot{\delta} t_s,n}} T \end{bmatrix},$$

where T is the sampling time and $S_{\tilde{w}_{\delta t_s,n}}$ and $S_{\tilde{w}_{\dot{\delta} t_s,n}}$ are the power spectra of the continuous-time process noise driving the clock bias and clock drift, respectively. These spectra can be related to the power-law coefficients $\{h_\alpha\}_{\alpha=-2}^{2}$, which have been shown through laboratory experiments to be adequate to characterize the power spectral density of the fractional frequency deviation $y(t)$ of an oscillator from nominal frequency, which takes the form $S_y(f) = \sum_{\alpha=-2}^{2} h_\alpha f^\alpha$ [100]. It is common to approximate the clock error dynamics by considering only the frequency random walk coefficient h_{-2} and the white frequency coefficient h_0, which leads to $S_{\tilde{w}_{\delta t_s,n}} \approx \frac{h_{0,s_n}}{2}$ and $S_{\tilde{w}_{\dot{\delta} t_s,n}} \approx 2\pi^2 h_{-2,s_n}$ [116].

6.1.2 UAV-Mounted Receiver Dynamics Model

The UAV-mounted receiver state consists of its unknown position $\boldsymbol{r}_r(k) \triangleq [x_r(k), y_r(k)]^{\mathsf{T}}$, velocity $\dot{\boldsymbol{r}}_r(k)$, and clock error states $\boldsymbol{x}_{\text{clk},r}(k) \triangleq \left[c\delta t_r(k), c\dot{\delta} t_r(k)\right]^{\mathsf{T}}$. Hence, the state vector of the receiver is given by $\boldsymbol{x}_r(k) = \left[\boldsymbol{r}_r^{\mathsf{T}}(k), \dot{\boldsymbol{r}}_r^{\mathsf{T}}(k), \boldsymbol{x}_{\text{clk},r}^{\mathsf{T}}(k)\right]^{\mathsf{T}}$. The receiver's position $\boldsymbol{r}_r(k)$ and velocity $\dot{\boldsymbol{r}}_r(k)$ will be assumed to evolve according to a velocity random walk model [104]. Therefore, the UAV-mounted receiver dynamics is modeled according to the discretized model

$$\boldsymbol{x}_r\,(k+1) = \mathbf{F}_r\,\boldsymbol{x}_r(k) + \boldsymbol{w}_r(k), \quad k = 0, 1, \ldots,$$

where $\boldsymbol{w}_r(k) = \left[\boldsymbol{w}_{\text{pv}}^{\mathsf{T}}(k), \boldsymbol{w}_{\text{clk},r}^{\mathsf{T}}\right]^{\mathsf{T}}(k)$ is a discrete-time zero-mean white noise sequence with covariance $\mathbf{Q}_r = \text{diag}\left[\mathbf{Q}_{\text{pv}}, \mathbf{Q}_{\text{clk},r}\right]$, with

$$\mathbf{F}_r = \begin{bmatrix} \mathbf{I}_{2\times 2} & T\mathbf{I}_{2\times 2} & \mathbf{0}_{2\times 2} \\ \mathbf{0}_{2\times 2} & \mathbf{I}_{2\times 2} & \mathbf{0}_{2\times 2} \\ \mathbf{0}_{2\times 2} & \mathbf{0}_{2\times 2} & \mathbf{F}_{\text{clk}} \end{bmatrix}, \quad \mathbf{F}_{\text{clk}} = \begin{bmatrix} 1 & T \\ 0 & 1 \end{bmatrix}$$

$$\mathbf{Q}_{\text{clk},r} = c^2 \begin{bmatrix} S_{\tilde{w}_{\delta t_r}} T + S_{\tilde{w}_{\dot{\delta} t_r}} \frac{T^3}{3} & S_{\tilde{w}_{\dot{\delta} t_r}} \frac{T^2}{2} \\ S_{\tilde{w}_{\dot{\delta} t_r}} \frac{T^2}{2} & S_{\tilde{w}_{\dot{\delta} t_r}} T \end{bmatrix}$$

$$\mathbf{Q}_{\text{pv}} = \begin{bmatrix} \tilde{q}_x \frac{T^3}{3} & 0 & \tilde{q}_x \frac{T^2}{2} & 0 \\ 0 & \tilde{q}_y \frac{T^3}{3} & 0 & \tilde{q}_y \frac{T^2}{2} \\ \tilde{q}_x \frac{T^2}{2} & 0 & \tilde{q}_x T & 0 \\ 0 & \tilde{q}_y \frac{T^2}{2} & 0 & \tilde{q}_y T \end{bmatrix},$$

where $\tilde{q}_x$ and $\tilde{q}_y$ are the power spectral densities of the continuous-time x and y acceleration noise, respectively. The spectra $S_{\tilde{w}_{\delta t_r}}$ and $S_{\tilde{w}_{\dot{\delta} t_r}}$ are modeled similarly to the BTS spectra, but with receiver-specific $h_{0,r}$ and $h_{-2,r}$.

6.2 Navigation with Cellular SOP Carrier Phase Measurements

This section formulates an EKF-based framework for standalone navigation with carrier phase measurements from asynchronous BTSs.

6.2.1 Motivation

In GNSS, the satellites' positions and clock biases are known to the receiver. Subsequently, with $N \geq 4$ satellites, one can use a static estimator (e.g., least squares) to solve for the receiver's 3–D position and its clock bias without the need of a dynamic estimator. A similar approach can be taken in a generic radionavigation systems where the receiver is making pseudorange-type measurements and the navigation source locations (i.e., transmitters) and their clock biases are known to the estimator. This chapter considers the case of opportunistic navigation with cellular signals, where BTSs may be asynchronous and have unknown clock biases. As a result, one has to account for the receiver and BTS clock biases, leading to an under-determined system. To address this, a dynamic estimator must be employed to obtain a navigation solution. In this chapter, an EKF is used as a navigation filter. The EKF relies on the dynamics model of the receiver motion and the clock errors. With minimal knowledge of the state dynamics, one can use kinematic models to propagate the state estimate between measurement updates [101]. The choice of the kinematic model order depends on the application. In the case of a maneuvering target, i.e., when there is some control input on a derivative of the position coordinates, this control input can be made available to the EKF since it is generated by the vehicle's on-board controller. As a result, the EKF implementation will not change except for incorporating the control input in the state time-update equations. The next subsections describe a detailed implementation of an EKF that estimates the state of the system defined in (6.1)–(6.2).

6.2.2 Modified Clock Error States

Estimating the terms $c\delta t_r(k)$, $c\delta t_{s_n}(k)$, and λN_n in (4.5) in Chapter 4 individually is unnecessary; hence, they will be lumped into one bias term defined as

$$c\delta t_n(k) \triangleq c\left[\delta t_r(k) - \delta t_{s_n}(k) + \frac{\lambda}{c}N_n\right],$$

with an associated drift state $c\dot{\delta}t_n(k)$ given by

$$c\dot{\delta}t_n(k) \triangleq c\left[\dot{\delta}t_r(k) - \dot{\delta}t_{s_n}(k)\right].$$

One may subsequently conclude that the dynamics of $\boldsymbol{x}_{\text{clk},n}(k) \triangleq \left[c\delta t_n(k), c\dot{\delta}t_n(k)\right]^{\mathsf{T}}$ is given by

$$\boldsymbol{x}_{\text{clk},n}(k+1) = \mathbf{F}_{\text{clk}}\,\boldsymbol{x}_{\text{clk},n}(k) + \boldsymbol{w}_{\text{clk},n}(k), \quad n = 1, \ldots, N,$$

where $\boldsymbol{w}_{\text{clk},n}(k)$ is a discrete-time zero-mean white noise sequence with covariance $\mathbf{Q}_{\text{clk},n} = \mathbf{Q}_{\text{clk},r} + \mathbf{Q}_{\text{clk},s_n}$. Note that now $\boldsymbol{w}_{\text{clk},n}(k)$ and $\boldsymbol{w}_{\text{clk},m}(k)$ are correlated, with

$$\mathbb{E}\left[\boldsymbol{w}_{\text{clk},n}(k)\boldsymbol{w}_{\text{clk},m}^{\mathsf{T}}(k)\right] = \begin{cases} \mathbf{Q}_{\text{clk},n}, & \text{if } n = m, \\ \mathbf{Q}_{\text{clk},r}, & \text{otherwise.} \end{cases}$$

6.2.3 EKF Model

The EKF estimates the UAV-mounted receiver's position and velocity and the modified clock error states for all BTSs, namely

$$\begin{aligned}\boldsymbol{x}(k) \triangleq \big[\, &\boldsymbol{r}_r^{\mathsf{T}}(k),\, c\delta t_1(k),\, \ldots,\, c\delta t_N(k),\\ &\dot{\boldsymbol{r}}_r^{\mathsf{T}}(k),\, c\dot{\delta} t_1(k),\, \ldots,\, c\dot{\delta} t_N(k) \,\big]^{\mathsf{T}}.\end{aligned}$$

Note that $\boldsymbol{x}(k)$ may be expressed as $\boldsymbol{x}(k) = \boldsymbol{\Pi}\boldsymbol{x}'(k)$, where

$$\boldsymbol{x}'(k) \triangleq \left[\boldsymbol{r}_r^{\mathsf{T}}(k), \dot{\boldsymbol{r}}_r^{\mathsf{T}}(k), \boldsymbol{x}_{\mathrm{clk},1}^{\mathsf{T}}(k), \ldots, \boldsymbol{x}_{\mathrm{clk},N}^{\mathsf{T}}(k)\right]^{\mathsf{T}}$$

and $\boldsymbol{\Pi}$ is some permutation matrix that could be readily calculated. The EKF considers the system with the following dynamics and measurement model

$$\boldsymbol{x}(k+1) = \mathbf{F}\boldsymbol{x}(k) + \boldsymbol{w}(k) \tag{6.1}$$

$$\boldsymbol{z}(k) = \boldsymbol{h}\left[\boldsymbol{x}(k)\right] + \boldsymbol{v}(k), \tag{6.2}$$

with $\boldsymbol{h}\left[\boldsymbol{x}(k)\right] \triangleq \left[h_1\left[\boldsymbol{x}(k)\right], \ldots, h_N\left[\boldsymbol{x}(k)\right]\right]^{\mathsf{T}}$, $h_n\left[\boldsymbol{x}(k)\right] \triangleq \|\boldsymbol{r}_r(k) - \boldsymbol{r}_{s_n}\| + c\delta t_n(k)$, $\boldsymbol{z}(k) \triangleq \left[z_1(k), \ldots, z_N(k)\right]^{\mathsf{T}}$, $\boldsymbol{w}(k)$ is a discrete-time zero-mean white sequence with covariance $\mathbf{Q} \triangleq \boldsymbol{\Pi}\mathbf{Q}'\boldsymbol{\Pi}^{\mathsf{T}}$, where $\mathbf{Q}' \triangleq \mathrm{diag}\left[\mathbf{Q}_{\mathrm{pv}}, \mathbf{Q}_{\mathrm{clk}}\right]$,

$$\mathbf{Q}_{\mathrm{clk}} \triangleq \begin{bmatrix} \mathbf{Q}_{\mathrm{clk},1} & \mathbf{Q}_{\mathrm{clk},r} & \cdots & \mathbf{Q}_{\mathrm{clk},r} \\ \mathbf{Q}_{\mathrm{clk},r} & \mathbf{Q}_{\mathrm{clk},2} & \cdots & \mathbf{Q}_{\mathrm{clk},r} \\ \vdots & \vdots & \ddots & \vdots \\ \mathbf{Q}_{\mathrm{clk},r} & \mathbf{Q}_{\mathrm{clk},r} & \cdots & \mathbf{Q}_{\mathrm{clk},N} \end{bmatrix}, \quad \mathbf{F} \triangleq \begin{bmatrix} \mathbf{I}_{p\times p} & T\mathbf{I}_{p\times p} \\ \mathbf{0}_{p\times p} & \mathbf{I}_{p\times p} \end{bmatrix},$$

with $p = N + 2$, and $\boldsymbol{v}(k) \triangleq \left[v_1(k), \ldots, v_N(k)\right]^{\mathsf{T}}$ is a discrete-time zero-mean white Gaussian sequence with covariance $\mathbf{R}(k) \triangleq \mathrm{diag}\left[\sigma_1^2(k), \ldots, \sigma_N^2(k)\right]$. Section 6.5 discusses how the

process and measurement noise covariance matrices $\mathbf{Q}$ and $\mathbf{R}(k)$, respectively, are selected in a practical environment.

The EKF is producing an estimate $\hat{\boldsymbol{x}}(k|j) = \mathbb{E}\left[\boldsymbol{x}(k)|\,\boldsymbol{z}(1),\ldots,\boldsymbol{z}(j)\right]$, $j \leq k$, with an associated estimation error covariance $\mathbf{P}(k|j) = \mathbb{E}\left[\tilde{\boldsymbol{x}}(k|j)\tilde{\boldsymbol{x}}^{\mathsf{T}}(k|j)\right]$, where $\tilde{\boldsymbol{x}}(k|j) \triangleq \boldsymbol{x}(k) - \hat{\boldsymbol{x}}(k|j)$ is the estimation error. The current state estimate $\hat{\boldsymbol{x}}(k|k)$ and its associated estimation error covariance $\mathbf{P}(k|k)$ are obtained using the standard EKF equations. The measurement Jacobian $\mathbf{H}(k)$ used in the EKF estimation error covariance update is given by

$$\mathbf{H}(k) = \begin{bmatrix} \mathbf{G}(k) & \mathbf{I}_{N\times N} & \mathbf{0}_{(N+2)\times(N+2)} \end{bmatrix}, \tag{6.3}$$

$$\mathbf{G}(k) \triangleq \begin{bmatrix} \frac{\boldsymbol{r}_r(k)-\boldsymbol{r}_{s_1}}{\left\|\boldsymbol{r}_r(k)-\boldsymbol{r}_{s_1}\right\|} & \cdots & \frac{\boldsymbol{r}_r(k)-\boldsymbol{r}_{s_N}}{\left\|\boldsymbol{r}_r(k)-\boldsymbol{r}_{s_N}\right\|} \end{bmatrix}^{\mathsf{T}}, \tag{6.4}$$

where $\mathbf{G}(k)$ is evaluated at $\hat{\boldsymbol{x}}(k|j)$.

6.2.4 EKF Initialization

It is assumed that the UAV has access to GNSS signals at $k = 0$ and $k = 1$, from which it could estimate its position. These position estimates, denoted by $\boldsymbol{z}_{\boldsymbol{r}_r}(0)$ and $\boldsymbol{z}_{\boldsymbol{r}_r}(1)$, can be modeled as

$$\boldsymbol{z}_{\boldsymbol{r}_r}(j) = \boldsymbol{r}_r(j) + \boldsymbol{v}_{\boldsymbol{r}_r}(j), \quad j = 0, 1, \tag{6.5}$$

where $\boldsymbol{r}_r(j)$ is the UAV's true position and $\boldsymbol{v}_{\boldsymbol{r}_r}(j)$ is a random vector that captures the estimation uncertainty, which is modeled as a zero-mean white Gaussian random sequence with covariance $\boldsymbol{\Sigma}_{\boldsymbol{r}_r}(j)$. Moreover, during the same time GNSS signals are available, the receiver makes two consecutive carrier phase measurements to the N available BTSs prior to initializing the EKF, denoted by $\boldsymbol{z}(0)$ and $\boldsymbol{z}(1)$. The maximum likelihood (ML) estimate of

$\boldsymbol{x}(1)$ from $\boldsymbol{z}_{\text{ini}} \triangleq \left[\boldsymbol{z}_{\boldsymbol{r}_r}^{\mathsf{T}}(1), \boldsymbol{z}_{\boldsymbol{r}_r}^{\mathsf{T}}(0), \boldsymbol{z}^{\mathsf{T}}(1), \boldsymbol{z}^{\mathsf{T}}(0)\right]^{\mathsf{T}}$ is obtained according to Appendix D, yielding $\hat{\boldsymbol{x}}_{\text{ML}_{\text{ini}}}$ and its associated estimation error covariance $\mathbf{P}_{\text{ML}_{\text{ini}}}$. Finally, the EKF is initialized with

$$\hat{\boldsymbol{x}}(1|1) \equiv \hat{\boldsymbol{x}}_{\text{ML}_{\text{ini}}}, \qquad \mathbf{P}(1|1) \equiv \mathbf{P}_{\text{ML}_{\text{ini}}},$$

and is run for $k \geq 1$.

Remark 1 . Let v_{r_1} and $\hat{v}_{r_1}$ denote the true initial speed and its estimate, respectively, and let $\boldsymbol{u}_{r_1}$ and $\hat{\boldsymbol{u}}_{r_1}$ denote the true initial velocity direction unit vector and its estimate, respectively. Let $\sigma_{v_{r_1}}^2$ and $\mathbf{P}_{\boldsymbol{u}_{r_1}}$ denote the initial variance and covariance of the initial estimation errors $\tilde{v}_{r_1} \triangleq v_{r_1} - \hat{v}_{r_1}$ and $\tilde{\boldsymbol{u}}_{r_1} \triangleq \boldsymbol{u}_{r_1} - \hat{\boldsymbol{u}}_{r_1}$, respectively. It is shown in Appendix E that

$$\sigma_{v_{r_1}}^2 \leq \frac{\lambda_{\max,\dot{r}}}{T^2}, \ \sigma_{\boldsymbol{u}_{r_1}}^2 \triangleq \left\|\mathbf{P}_{\boldsymbol{u}_{r_1}}\right\| \leq \frac{\lambda_{\max,\dot{r}}}{\left\|\boldsymbol{r}_r(1) - \boldsymbol{r}_r(0)\right\|^2}, \tag{6.6}$$

where $\lambda_{\max,\dot{r}}$ is a positive real number that only depends on $\bar{\boldsymbol{\Sigma}}_{\boldsymbol{r}_r} \triangleq \boldsymbol{\Sigma}_{\boldsymbol{r}_r}(0) + \boldsymbol{\Sigma}_{\boldsymbol{r}_r}(1)$. It can be seen from (6.6) that increasing T reduces the uncertainty in the initial speed estimate. Increasing $\|\boldsymbol{r}_r(1) - \boldsymbol{r}_r(0)\|$ improves the estimate of the initial velocity direction unit vector. Given $\boldsymbol{\Sigma}_{\boldsymbol{r}_r}(0)$ and $\boldsymbol{\Sigma}_{\boldsymbol{r}_r}(1)$, (6.6) may be used to choose an initial sampling time T and/or distance $\|\boldsymbol{r}_r(1) - \boldsymbol{r}_r(0)\|$ that guarantee that $\sigma_{v_{r_1}}^2$ and $\sigma_{\boldsymbol{u}_{r_1}}^2$ will be below a specified threshold. Regardless of the choice of T and $\|\boldsymbol{r}_r(1) - \boldsymbol{r}_r(0)\|$, the proposed initialization scheme will always yield an initial state estimate that is consistent with its initial estimation error covariance, which is important when initializing the EKF.

6.3 Observability and EKF Estimation Error Bounds Analyses

This section shows that the system defined in (6.1)–(6.2) is observable for $N \geq 2$. Moreover, it shows that the EKF estimation error is exponentially bounded in the mean square sense and bounded with probability one. In the sequel, the following assumptions are made:

A1. The BTSs are not colocated nor are all collinear.

A2. The UAV is not stationary nor is moving along a trajectory that is collinear with the vector connecting its receiver with any of the BTSs.

A3. The UAV is at a minimum distance d from each BTS at all time, i.e., $\|\boldsymbol{r}(k) - \boldsymbol{r}_{s_n}\| \geq d$, $\forall\, k > 0$ and $\forall\, n = 1, \ldots, N$.

This chapter aims at qualitatively studying the behavior of the EKF estimation error and estimation error covariance. To this end, generic theorems and lemmas on EKF stochastic stability are applied to the opportunistic navigation system at hand, which is implemented in a real-world environment. The relevant theorems and lemmas are stated in Appendix F, which gives theoretical background on observability and boundedness of the EKF error state.

6.3.1 Observability Analysis

The observability of an environment comprising multiple receivers making pseudorange measurements on multiple BTSs, assuming different *a priori* knowledge scenarios was analyzed in [33]. The observability analysis utilized the l-step observability matrix of the linearized

system and considered the observability of the *individual* clock biases and drifts $c\delta t_r(k)$, $c\dot{\delta} t_r(k)$, $\{c\delta t_{s_n}(k)\}_{n=1}^N$, and $\left\{c\dot{\delta} t_{s_n}(k)\right\}_{n=1}^N$.

In contrast, the system in (6.1)–(6.2) considers a single receiver making carrier phase measurements on multiple BTSs, where the individual clock biases and carrier phase ambiguities are lumped into a *single* bias term $\{c\delta t_n(k)\}_{n=1}^N$ and the drifts are also lumped into a *single* drift term $\left\{c\dot{\delta} t_n(k)\right\}_{n=1}^N$.

The observability results for the system defined in (6.1)–(6.2) is captured in the following theorem.

Theorem 6.1. *Under assumptions A1 and A2, the system defined in* (6.1)–(6.2) *is completely l-step observable for $l \geq 4$ and $N \geq 2$.*

Proof. The linearization of the deterministic part of the system (6.1)–(6.2) into the form (F.22)–(F.23) yields

$$\mathbf{F}(k) \equiv \begin{bmatrix} \mathbf{I}_{(N+2)\times(N+2)} & T\mathbf{I}_{(N+2)\times(N+2)} \\ \mathbf{0}_{(N+2)\times(N+2)} & \mathbf{I}_{(N+2)\times(N+2)} \end{bmatrix}, \quad \mathbf{\Gamma}(k) \equiv \mathbf{0},$$
$$\mathbf{H}(k) \equiv \begin{bmatrix} \mathbf{H}_\xi(k) & \mathbf{0}_{N\times(N+2)} \end{bmatrix}, \quad \mathbf{H}_\xi(k) \triangleq \begin{bmatrix} \mathbf{G}(k) & \mathbf{I}_{N\times N} \end{bmatrix}.$$

In the following, it will be proven by construction that the l-step observability matrix $\boldsymbol{\mathcal{O}}(k, k+l)$ of the linearized system is full rank, i.e.,

$$\sum_{i=1}^{2L} \gamma_i \boldsymbol{\mathcal{O}}\left(k, k+l\right) \boldsymbol{e}_{2L,i} = \mathbf{0} \tag{6.7}$$

is satisfied *if and only if* $\gamma_i = 0$, $\forall\, i = 1, \ldots, 2L$, where $L = N + 2$ and $\boldsymbol{e}_{L,i} \in \mathbb{R}^L$ is the standard basis vector consisting of a one at the i-th element and zeros elsewhere. Note that since $\boldsymbol{\mathcal{O}}(k, k+l) \in \mathbb{R}^{l\cdot N\times 2(N+2)}$, then $l \geq 4$ always satisfies $l \cdot N \geq 2(N+2)$ for $N \geq 2$. Let

$l = 4$. Subsequently, $\boldsymbol{\mathcal{O}}(k, k+4)$ may be expressed as

$$\boldsymbol{\mathcal{O}}(k, k+4) = \begin{bmatrix} \boldsymbol{\mathcal{O}}_{11} & \boldsymbol{\mathcal{O}}_{12} \\ \boldsymbol{\mathcal{O}}_{21} & \boldsymbol{\mathcal{O}}_{22} \end{bmatrix},$$

$$\boldsymbol{\mathcal{O}}_{11} \triangleq \begin{bmatrix} \mathbf{H}_\xi(k) \\ \mathbf{H}_\xi(k+1) \end{bmatrix}, \quad \boldsymbol{\mathcal{O}}_{21} \triangleq \begin{bmatrix} \mathbf{H}_\xi(k+2) \\ \mathbf{H}_\xi(k+3) \end{bmatrix},$$

$$\boldsymbol{\mathcal{O}}_{12} \triangleq \begin{bmatrix} \mathbf{0} \\ T\mathbf{H}_\xi(k+1) \end{bmatrix}, \quad \boldsymbol{\mathcal{O}}_{22} \triangleq \begin{bmatrix} 2T\mathbf{H}_\xi(k+2) \\ 3T\mathbf{H}_\xi(k+3) \end{bmatrix}.$$

The matrix $\boldsymbol{\mathcal{O}}_{11}$ may also be expressed as

$$\boldsymbol{\mathcal{O}}_{11} = \begin{bmatrix} \mathbf{G}(k) & \mathbf{I}_{N\times N} \\ \mathbf{G}(k+1) & \mathbf{I}_{N\times N} \end{bmatrix}. \tag{6.8}$$

Note that $\boldsymbol{\mathcal{O}}_{11} \in \mathbb{R}^{2N\times(N+2)}$. Moreover, the inequality $2N \geq N+2$ holds, for $N \geq 2$. Therefore,

$$\text{rank}\,[\boldsymbol{\mathcal{O}}_{11}] \leq N+2. \tag{6.9}$$

From (6.8), it can be seen that $\text{rank}\,[\boldsymbol{\mathcal{O}}_{11}] \geq N$. Moreover, for $N \geq 2$, and if A1 and A2 hold, then the $(N+1)$st and $(N+2)$nd rows of $\boldsymbol{\mathcal{O}}_{11}$ will be linearly independent from the first N rows and from each other, yielding

$$\text{rank}\,[\boldsymbol{\mathcal{O}}_{11}] \geq N+2. \tag{6.10}$$

Combining (6.9) and (6.10), it can be deduced that $\text{rank}\,[\boldsymbol{\mathcal{O}}_{11}] = N+2$. Similarly, it can be

shown that rank $[\boldsymbol{\mathcal{O}}_{21}] = N + 2$. Subsequently,

$$\sum_{i=1}^{L} \alpha_i \boldsymbol{\mathcal{O}}_{11} \boldsymbol{e}_{L,i} = \mathbf{0}, \qquad \sum_{i=1}^{L} \beta_i \boldsymbol{\mathcal{O}}_{21} \boldsymbol{e}_{L,i} = \mathbf{0},$$

are satisfied *if and only if* $\alpha_i = \beta_i = 0, \forall\, i = 1, \ldots, L$. Therefore, the equality

$$\sum_{i=1}^{L} \pi_i \mathbf{H}_{\xi}\left(k + j\right) \boldsymbol{e}_{L,i} = \mathbf{0}, \quad \forall\, j = 0, \ldots, 3 \tag{6.11}$$

is satisfied *if and only if* $\pi_i = 0, \forall\, i = 1, \ldots, L$.

The left-hand side of (6.7) can be expressed as

$$\sum_{i=1}^{2L} \gamma_i \boldsymbol{\mathcal{O}}\left(k, k+4\right) \boldsymbol{e}_{2L,i} = \left[\boldsymbol{\rho}_0^{\mathsf{T}}, \ldots, \boldsymbol{\rho}_3^{\mathsf{T}}\right]^{\mathsf{T}}, \tag{6.12}$$

$$\boldsymbol{\rho}_j \triangleq \sum_{i=1}^{L} \left(\gamma_i + jT\gamma_{L+i}\right) \mathbf{H}_{\xi}(k + j) \, \boldsymbol{e}_{L,i}, \tag{6.13}$$

where $j = 0, \ldots, 3$. It can be seen from (6.11) that $\boldsymbol{\rho}_j = \mathbf{0}$ for all $j = 0, \ldots, 3$ *if and only if*

$$\gamma_i + jT\gamma_{L+i} = 0, \ \forall\, i = 1, \ldots, L; \ \forall\, j = 0, \ldots, 3. \tag{6.14}$$

Since (6.14) holds for all $j = 0, \ldots, 3$, then evaluating (6.14) at $j = 0$ yields

$$\gamma_i = 0, \qquad \forall\, i = 1, \ldots, L. \tag{6.15}$$

Combining (6.14) and (6.15) for $j > 0$ yields

$$\gamma_{L+i} = 0, \qquad \forall\, i = 1, \ldots, L. \tag{6.16}$$

Equations (6.14)–(6.16) imply (6.7); therefore, $\boldsymbol{\mathcal{O}}(k, k+4)$ is full rank. Using Theorem F.1 in Appendix F, the system is observable. □

Remark 2 . Note that the l-step observability matrix $\boldsymbol{\mathcal{O}}(k, k+l)$ is an $l \cdot N \times 2(N+2)$ matrix; hence, $\text{rank}\left[\boldsymbol{\mathcal{O}}(k, k+l)\right] \leq \min\left\{l \cdot N, 2(N+2)\right\}$. Subsequently, one necessary condition for the observability matrix to be full rank is that $l \cdot N \geq 2(N+2)$, i.e., the UAV makes carrier phase measurements at l epochs to the N cellular BTSs. For $N \geq 2$, this condition is satisfied for $l \geq 4$. For $N \geq 4$, this condition is satisfied for $l \geq 3$.

Remark 3 . The result of Theorem 6.1 is only valid locally and in a deterministic sense, i.e., with no process or measurement noise. However, this result can be extended to the stochastic system (F.27)–(F.28). Let the measurement Jacobian $\mathbf{G}(k)$ with respect to the position states (cf. (6.4)) be re-parameterized in terms of the bearing angles $\{\theta_n(k)\}_{n=1}^{N}$ between each BTS and the UAV according to

$$\mathbf{G}(k) = \begin{bmatrix} \cos\left[\theta_1(k)\right] & \dots & \cos\left[\theta_N(k)\right] \\ \sin\left[\theta_1(k)\right] & \dots & \sin\left[\theta_N(k)\right] \end{bmatrix}^{\mathsf{T}}.$$

The presence of process noise will yield new bearing angle trajectories $\theta'_n(k) = \theta_n(k) + \delta\theta_n(k)$, where $\delta\theta_n(k)$ is the bearing angle error due to process noise. With assumptions A.1 and A.2, the new bearing angles will not change the structure nor the rank of $\mathbf{H}(k)$ (cf.(6.3)), which will remain a combination of cosine and sine functions and other constants. This in turn will satisfy the observability condition of the system with process noise. More details can be found in [117] (Lemma 4.1) and [118] (Corollary 5.2).

Remark 4 . The velocity random walk model considered in this chapter is simple yet informative enough to capture the UAV dynamics between the EKF measurement updates. In particular, the EKF will use this model to perform the time-update step, and for sufficiently small T, the UAV's dynamics model would not deviate drastically from this model. Nevertheless, this model may not necessarily cover the variety of flight modes that are achievable using typical rotary wing UAVs. To address this, one may employ a multiple model approach to estimate the UAV's state, with each model matched to a different flight mode

[101, 119, 120, 121]. The observability analysis presented in this chapter can be performed for each of the dynamics model assumed by the multiple model filter, such as acceleration random walk, constant turn-rate, or even a stationary UAV. Theorem 6.1 can be extended to study the observability of higher order UAV dynamics models (e.g., acceleration random walk, jerk random walk, etc. [104]) and higher order clock error dynamics models (e.g., three-state clock error dynamics comprising time, frequency, and frequency aging [122, 123]). It can be readily shown that the system becomes unobservable when the UAV stops.

6.3.2 Lower Bound on the EKF Estimation Error Covariance

The optimal geometric configuration of sensors (or navigation sources) around an emitter (or receiver) has been well studied in the literature [1, 66]. It was found that in the presence of independent and identically distributed measurement noise, the trace of the estimation error covariance in a nonlinear least-squares estimator is minimized when the end points of the unit line of sight vectors pointing from the receiver to each navigation source form a regular polygon around the receiver, i.e., $\theta_n = \frac{2\pi(n-1)}{N}$, $n = 1, \ldots, N \geq 3$ [69]. The aforementioned configuration will be referred to as the optimal configuration.

Although the system discussed in Subsection 6.2.3 is nonlinear, one may devise a scenario for $N \geq 3$ that will define a lower bound on the estimation error covariance in the EKF. To this end, it is assumed that the optimal BTS configuration around the receiver is maintained at all time, implying that assumption A1 is satisfied. Assumption A2 implies that the measurement Jacobian can not be the same at all time. In order to satisfy A1 and A2 simultaneously, it is assumed that optimal configuration is maintained and that the BTSs rotate around the receiver on the unit circle by $2\pi/N$ at each time-step. Therefore, the

optimal bearing angles at any given time-step k will be given by

$$\theta_n^\star(k) = \frac{2\pi \cdot \mathrm{mod}(n-1+k, N)}{N},\ n = 1, \ldots, N,\ k = 1, \ldots,$$

where $\mathrm{mod}(\cdot, \cdot)$ is the modulo operator. Note that this parametrization is independent of the state. Therefore, the Riccati equation may be iterated off-line with the optimal configuration and measurement noise covariance $\mathbf{R}^\star(k) \equiv \lambda_{\min}\left[\mathbf{R}(k)\right]\mathbf{I}$ to produce a lower bound on the estimation error covariance for the EKF, denoted $\mathbf{P}_{\min}(k+1|k)$, from which a real number $\underline{p} > 0$ such that $\underline{p}\mathbf{I} \preceq \mathbf{P}_{\min}(k+1|k)$ can be deduced. Note that $\lambda_{\min}[\mathbf{A}]$ indicates the smallest eigenvalue of matrix $\mathbf{A}$. It is also important to note that while this scenario could never be physically realized, it is only used to define a lower bound on the estimation error covariance.

Remark 5 . The intuition behind obtaining this lower bound is explained next. Assume two configurations for N BTSs: (i) the optimal one and (ii) any other arbitrary configuration. Given the same prior for both configurations, i.e., $\mathbf{P}_{\mathrm{i}}(k|k) = \mathbf{P}_{\mathrm{ii}}(k|k)$, then $\mathbf{P}_{\mathrm{i}}(k+1|k) = \mathbf{P}_{\mathrm{ii}}(k+1|k)$, since the dynamics are linear time-invariant. The covariance measurement updates can be expressed in the information form as

$$\mathbf{P}_{\mathrm{i}}^{-1}(k+1|k+1) = \mathbf{P}_{\mathrm{i}}^{-1}(k+1|k) + \frac{1}{\sigma^2}\mathbf{H}_{\mathrm{i}}^{\mathsf{T}}(k+1)\mathbf{H}_{\mathrm{i}}(k+1), \tag{6.17}$$

$$\mathbf{P}_{\mathrm{ii}}^{-1}(k+1|k+1) = \mathbf{P}_{\mathrm{ii}}^{-1}(k+1|k) + \frac{1}{\sigma^2}\mathbf{H}_{\mathrm{ii}}^{\mathsf{T}}(k+1)\mathbf{H}_{\mathrm{ii}}(k+1), \tag{6.18}$$

Since (i) is the optimal configuration,

$$\mathbf{H}_{\mathrm{i}}^{\mathsf{T}}(k+1)\mathbf{H}_{\mathrm{i}}(k+1) \succeq \mathbf{H}_{\mathrm{ii}}^{\mathsf{T}}(k+1)\mathbf{H}_{\mathrm{ii}}(k+1). \tag{6.19}$$

From (6.17)–(6.19), it can be seen that $\mathbf{P}_{\mathrm{i}}(k+1|k+1) \preceq \mathbf{P}_{\mathrm{ii}}(k+1|k+1)$. Repeating this recursion yields $\mathbf{P}_{\mathrm{i}}(k+j|k+j) \preceq \mathbf{P}_{\mathrm{ii}}(k+j|k+j)$ for all $j \geq 1$.

6.3.3 EKF Estimation Error Bounds Analysis

Consider the following two notions of estimation error boundedness defined in [117].

Definition 6.3.1. *The stochastic sequence $\tilde{\boldsymbol{x}}(k|k)$ is said to be exponentially bounded in mean square, if there are real numbers $\eta, \nu > 0$ and $0 < \vartheta < 1$ such that*

$$\mathbb{E}\left[\|\tilde{\boldsymbol{x}}(k|k)\|^2\right] \leq \eta \|\tilde{\boldsymbol{x}}(1|1)\|^2 \vartheta^k + \nu \tag{6.20}$$

holds for every $k > 0$.

Definition 6.3.2. *The stochastic sequence $\tilde{\boldsymbol{x}}(k|k)$ is said to be bounded with probability one, if*

$$\sup_{k>0} \|\tilde{\boldsymbol{x}}(k|k)\| < \infty \tag{6.21}$$

holds with probability one.

Next, it is shown that the EKF estimation error for the system at hand is bounded according to Definitions 6.3.1 and 6.3.2. From the system defined in (6.1)–(6.2), it can be seen that $\mathbf{F}(k) = \mathbf{F}$ is nonsingular and

$$\|\mathbf{F}\| = 1, \tag{6.22}$$

for all $k \geq 0$. Moreover, from the definition of $\mathbf{Q}$ and $\mathbf{R}(k)$ in Subsection 6.2.3, it can be seen that $\mathbf{Q}(k) = \mathbf{Q} \succ \mathbf{0}$ and $\mathbf{R}(k) \succ \mathbf{0}$; hence, there exist real numbers $\underline{q}, \underline{r} > 0$ such that

$$\mathbf{Q} \succeq \underline{q}\mathbf{I}, \qquad \mathbf{R}(k) \succeq \underline{r}\mathbf{I}, \tag{6.23}$$

for all $k > 0$. It was established in Theorem 6.1 that the system is observable; hence, using

Lemma F.1 in Appendix F, there exist real numbers $\underline{p}, \bar{p} > 0$ such that

$$\underline{p}\mathbf{I} \preceq \mathbf{P}(k+1|k) \preceq \bar{p}\mathbf{I}, \quad \forall\, k > 0. \tag{6.24}$$

An approach for obtaining $\underline{p}$ is given in Subsection 6.3.2. Since the dynamics of the system in (6.1) are linear, then

$$\|\boldsymbol{\varphi}(k)\| = 0, \quad \forall\, k > 0. \tag{6.25}$$

The following two lemmas establish the rest of the conditions for Theorem F.2 in Appendix F to hold.

Lemma 6.3.1. *The 2-norm of the measurement Jacobian defined in* (6.3) *is bounded by*

$$\|\mathbf{H}(k)\| \leq \sqrt{N+1}, \quad \forall\, k > 0. \tag{6.26}$$

Proof. Equation (6.26) follows from showing that

$$\mathbf{H}^{\mathsf{T}}(k)\mathbf{H}(k) \preceq (N+1)\mathbf{I}. \tag{6.27}$$

The matrix $\boldsymbol{\Delta} \triangleq (N+1)\mathbf{I} - \mathbf{H}^{\mathsf{T}}(k)\mathbf{H}(k)$ is expressed as

$$\boldsymbol{\Delta} = \begin{bmatrix} \mathbf{M} & \mathbf{0} \\ \mathbf{0} & (N+1)\mathbf{I} \end{bmatrix},$$
$$\mathbf{M} \triangleq \begin{bmatrix} (N+1)\mathbf{I} - \mathbf{G}^{\mathsf{T}}(k)\mathbf{G}(k) & -\mathbf{G}^{\mathsf{T}}(k) \\ -\mathbf{G}(k) & N\mathbf{I} \end{bmatrix},$$

which implies that (6.27) is satisfied when $\mathbf{M} \succeq \mathbf{0}$. Since $N\mathbf{I} \succ \mathbf{0}$, then $\mathbf{M}$ is positive

semi-definite if the Schur complement of its bottom-right block given by

$$\mathbf{M}_{\text{Schur}} \triangleq (N+1)\mathbf{I} - \mathbf{G}^{\mathsf{T}}(k)\mathbf{G}(k) - \frac{1}{N}\mathbf{G}^{\mathsf{T}}(k)\mathbf{G}(k),$$

is positive semi-definite. For any matrix $\mathbf{A}$, the following holds

$$\mathbf{A}^{\mathsf{T}}\mathbf{A} \preceq \text{trace}\left[\mathbf{A}^{\mathsf{T}}\mathbf{A}\right]\mathbf{I}.$$

It can be readily shown that $\text{trace}\left[\mathbf{G}^{\mathsf{T}}(k)\mathbf{G}(k)\right] = N$ for all $k \geq 0$. Subsequently,

$$\mathbf{M}_{\text{Schur}} \succeq (N+1)\mathbf{I} - N\mathbf{I} - \mathbf{I} = \mathbf{0} \quad \Rightarrow \quad \mathbf{M} \succeq \mathbf{0},$$

from which (6.27) and consequently (6.26) follow. □

Lemma 6.3.2. *Consider the system defined in* (6.1)–(6.2)*. If A3 holds, then*

$$\max_{1\leq n\leq N} \sup_{\boldsymbol{x}(k)} \|\text{Hess } h_n\left[\boldsymbol{x}(k)\right]\| \leq \frac{1}{d}, \tag{6.28}$$

where Hess *denotes the Hessian operator.*

Proof. It can be readily shown that

$$\text{Hess } h_n\left[\boldsymbol{x}(k)\right] = \frac{1}{\|\boldsymbol{r}_r(k) - \boldsymbol{r}_{s_n}\|}\text{diag}\left[\mathbf{U}, \mathbf{0}_{(2N+2)\times(2N+2)}\right],$$

where $\mathbf{U} \triangleq \mathbf{I}_{2\times 2} - \boldsymbol{v}\boldsymbol{v}^{\mathsf{T}}$ and $\boldsymbol{v} \triangleq \frac{\boldsymbol{r}_r(k)-\boldsymbol{r}_{s_n}}{\|\boldsymbol{r}_r(k)-\boldsymbol{r}_{s_n}\|}$. It can be seen that the matrix $\mathbf{U}$ is an annihilator matrix and therefore its eigenvalues consist of ones and zeros. Subsequently,

$$\|\text{Hess } h_n\left[\boldsymbol{x}(k)\right]\| = \frac{1}{\|\boldsymbol{r}_r(k) - \boldsymbol{r}_{s_n}\|}.$$

Since A3 holds, i.e., $\|\boldsymbol{r}_r(k) - \boldsymbol{r}_{s_n}\| \geq d$, then $\|\text{Hess } h_n\left[\boldsymbol{x}(k)\right]\| \leq \frac{1}{d}$, which in turn implies

(6.28). □

Using Taylor's theorem and Lemma 6.3.2, it can be deduced that

$$\|\boldsymbol{\chi}(k)\| \leq \kappa_\chi \|\tilde{\boldsymbol{x}}(k|k)\|^2, \tag{6.29}$$

where $\kappa_\chi = \frac{1}{d}$ [117]. Now the main result for the EKF error bounds is stated.

Theorem 6.2. *Consider the system defined in* (6.1)–(6.2) *whose state is being estimated using an EKF as described in Subsection 6.2.3. If A1–A3 hold, then the EKF error* $\tilde{\boldsymbol{x}}(k|k)$ *is exponentially bounded in the mean square and bounded with probability one as per Definitions 6.3.1 and 6.3.2, respectively, assuming*

$$\|\tilde{\boldsymbol{x}}(1|1)\| \leq \epsilon, \quad \mathbf{R}(k) \preceq \delta \mathbf{I}, \quad \mathbf{Q} \preceq \delta \mathbf{I},$$

for some $\epsilon, \delta > 0$.

Proof. Combining (6.22)–(6.26), (6.29), and the fact that $\mathbf{F}$ is nonsingular, one can see that all the conditions of Theorem F.2 in Appendix F are satisfied, from which one concludes that $\tilde{\boldsymbol{x}}(k|k)$ is exponentially bounded and bounded with probability one. □

The significance of the results presented in Theorems 6.1 and 6.2 are in the fact that it is possible for a UAV to reliably navigate for long periods of time exclusively with cellular signals transmitted by asynchronous BTSs.

Remark 6 . While the observability and EKF stability analysis establishes bounds on the estimation error covariance, it does not specify how to obtain such bounds. However, it is worth noting that the observability analysis can be extended for higher order models or for models with known control input. It can also be shown that the system will be l-step observable for such models. Subsequently, the EKF output covariance for these dynamics

models will be bounded as well. As a result, Theorem 6.2 can be readily extended to show that an EKF using kinematic models with or without known control inputs will have bounded errors as per Definitions 6.3.1 and 6.3.2.

6.4 Simulation Results

This section presents simulations to analyze the performance of the proposed EKF framework by varying: (i) the number of available BTSs, (ii) the initial speed of the UAV, and (iii) the quality of the oscillator on-board the UAV. The simulation setup and settings are discussed first, then, the results are provided.

6.4.1 Simulation Setup

The simulated environment consisted of 12 BTSs from 2 cellular providers and is illustrated in Fig. 6.1. It can be seen that due to the cellular structure, the geometry between the UAV and BTSs is favorable. The cell size was picked to be 2 km, which is a typical value in semi-urban environments. Monte Carlo (MC) simulations were ran for different values of: (i) the number of available BTSs N, (ii) the initial speed of the UAV v_{r_1}, and (iii) the UAV-mounted receiver's clock states' process noise covariance $\mathbf{Q}_{\text{clk},r}$. The number of available BTSs was varied in $N \in \{6, 8, 10, 12\}$. The initial speed of the UAV v_{r_1} was varied in $v_{r_1} \in \{4, 9, 13\}$ m/s. The process noise covariance of the UAV-mounted receiver's oscillator was varied to correspond to that of a temperature-compensated crystal oscillator (TCXO) and to that of an oven-controlled crystal oscillator (OCXO). Subsequently, 24 cases were simulated. The UAV's position and velocity and the UAV-mounted receiver's and BTSs' clock states were simulated using the dynamics discussed in Subsections 6.1.2 and 6.1.1 with a sampling time $T = 0.1$ s. The carrier phase measurement to each BTS was simulated according to (4.5) in

Chapter 4 with $\lambda = 33.96$ cm, which corresponds to a wavelength dedicated for a cellular CDMA channel. The 3GPP2 protocol requires cellular BTSs to be synchronized within 3μs to GPS with a frequency stability of 50 ppb [48, 49]. It was assumed that the BTSs are equipped with OCXOs to meet these requirements [41, 124]. The EKF was initialized according to the framework in Subsection 6.2.4. The simulation settings are summarized in Table 6.1.

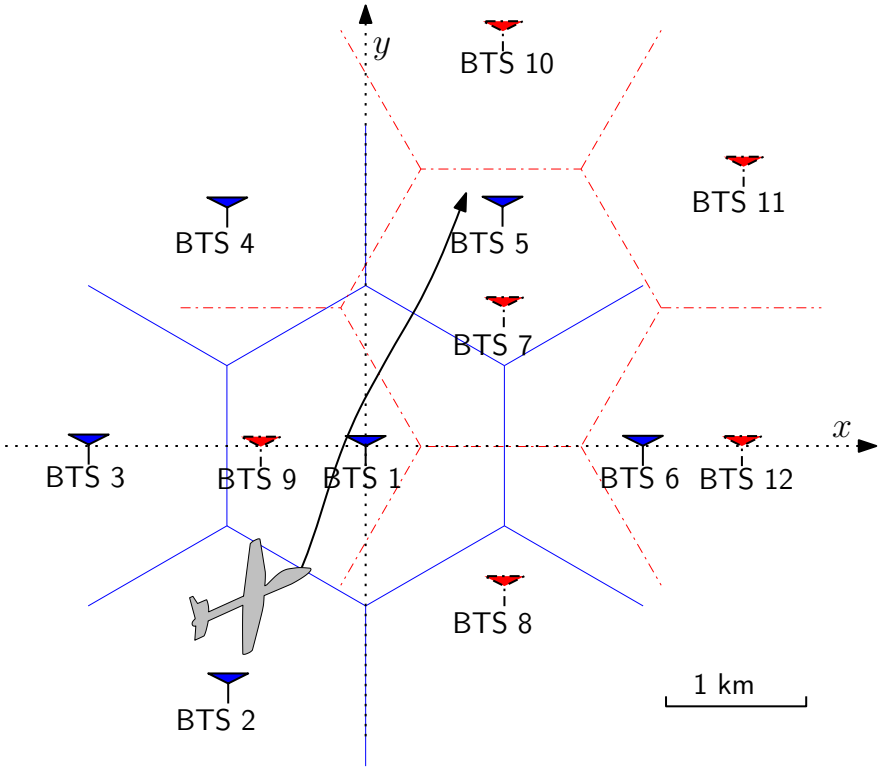

Figure 6.1: Simulation environment layout. The blue and red colors represent cells and BTSs from 2 different cellular providers. The UAV's trajectory is shown in black.

6.4.2 Single Realization Simulation Results

A single realization of the EKF errors and associated $\pm 3\sigma$ bounds for the UAV's position and velocity and the clock error states corresponding to $c\delta t_1$ and $c\dot{\delta} t_1$ are plotted in Fig. 6.2 with $N = 10$, $v_{r_1} = 9$ m/s, and an OCXO-equipped receiver. The decreasing $\pm 3\sigma$ bounds and converging errors shown in Fig. 6.2 do not contradict the main results in Subsection

Table 6.1: Simulation Settings

Parameter	Value	Unit
N	$\{6, 8, 10, 12\}$	-
λ	0.3396	m
T	0.1	s
$\mathbf{R}$	$(0.03) \cdot \mathbf{I}_{N\times N}$	m^2
$\mathbf{\Sigma}_{\boldsymbol{r}_r}(j)$	$\begin{bmatrix} 14.36 & -6.97 \\ -6.97 & 11.90 \end{bmatrix}$	m^2
j	$\{0, 1\}$	-
$\boldsymbol{r}_r(0)$	$[-500, -1500]^{\mathsf{T}}$	m
$\dot{\boldsymbol{r}}_r(0)$	$v_{r_1} \cdot [0.316, 0.949]^{\mathsf{T}}$	m/s
v_{r_1}	$\{4, 9, 13\}$	m/s
$h_{-2,r}$	$\{h_{-2,\mathrm{TCXO}}, h_{-2,\mathrm{OCXO}}\}$	s^{-1}
$h_{0,r}$	$\{h_{0,\mathrm{TCXO}}, h_{0,\mathrm{OCXO}}\}$	s
h_{-2,s_n}	$h_{-2,\mathrm{OCXO}}$	s^{-1}
h_{0,s_n}	$h_{0,\mathrm{OCXO}}$	s
$h_{-2,\mathrm{TCXO}}$	2×10^{-20}	s^{-1}
$h_{-2,\mathrm{OCXO}}$	4×10^{-23}	s^{-1}
$h_{0,\mathrm{TCXO}}$	2×10^{-19}	s
$h_{0,\mathrm{OCXO}}$	8×10^{-20}	s
$\tilde{q}_x, \tilde{q}_y$	0.03	$\mathrm{m}^2/\mathrm{s}^3$
$c\delta t_r, c\delta t_{s_n}$	$\mathcal{U}(-900, 900)^*$	m
$c\dot{\delta} t_r, c\dot{\delta} t_{s_n}$	$\mathcal{U}(-5, 5)$	m/s
N_n	$\mathcal{U}\{-500, 500\}^{**}$	cycles

* $\mathcal{U}(a, b)$ denotes the probability density function of a *continuous* uniformly-distributed random variable in (a, b).

** $\mathcal{U}\{c, d\}$ denotes the probability mass function of a *discrete* uniformly-distributed random variable in $[c, d]$.

6.3.3 that the estimation error can be exponentially bounded and bounded with probability one, as per Definitions 6.3.1 and 6.3.2. The remaining clock error states, namely $c\delta t_n$ and $c\dot{\delta} t_n$ for $n = 2, 3, \ldots, 9$, behave similarly to the ones plotted in Fig. 6.2.

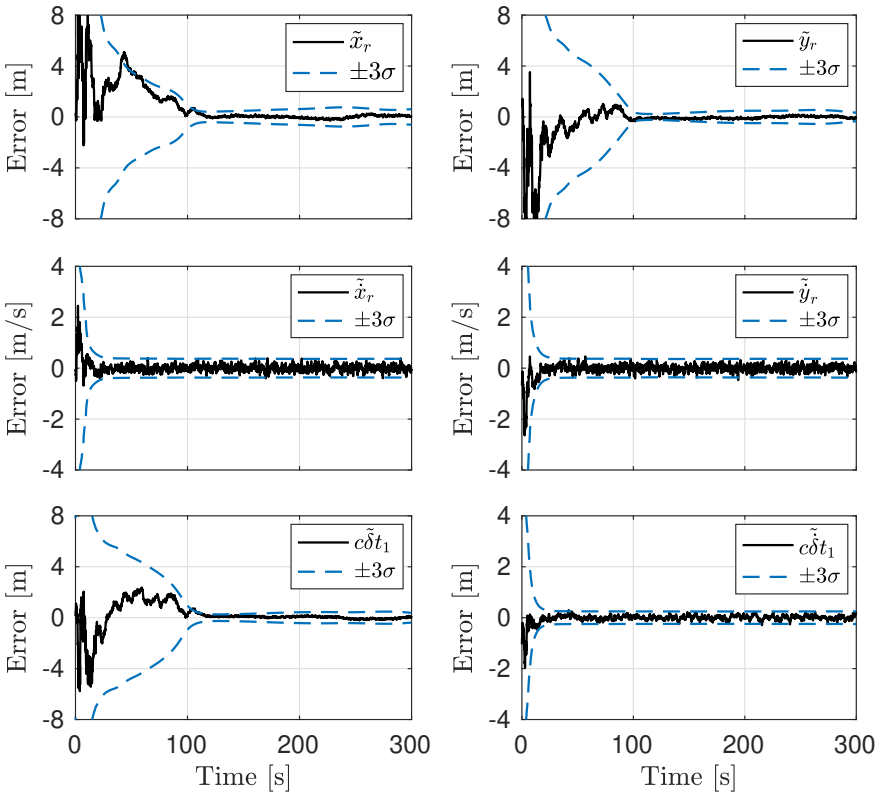

Figure 6.2: Simulation results: Single realization of EKF errors and associated $\pm 3\sigma$ bounds for the UAV position and velocity and the clock error states corresponding to $c\delta t_1$ and $c\dot{\delta}t_1$ with $N = 10$, $v_{r_1} = 9$ m/s, and an OCXO-equipped receiver.

6.4.3 Monte Carlo Simulation Results

Next, MC simulations were conducted by randomizing the process and measurement noise as well as the initial UAV position estimates $\hat{\boldsymbol{r}}_r(0)$ and $\hat{\boldsymbol{r}}_r(1)$. A total of 200 MC simulations were performed for each case described in Subsection 6.4.1. The total position RMSE and the final position error RMSE are tabulated in Table 6.2.

The following can be deduced from Table 6.2. First, as expected, the estimation performance improves as the number of available BTSs increases. Second, the receiver's clock quality significantly affects the estimation performance for $N \leq 10$. For $N > 10$, the effect of the receiver's oscillator quality becomes less significant. Third, as the initial speed increases, the estimation performance improves. Faster UAV speeds result in a faster change in the bearing angles between the UAV and the BTSs, yielding an increase in the amount of information

Table 6.2: MC Simulation Results

		Position RMSE (m)			Final position error (m)		
	N \ v_{r_1}	4	9	13	4	9	13
TCXO	6	33.47	22.85	13.15	14.28	10.23	7.29
	8	30.34	18.02	9.57	12.03	4.85	0.95
	10	27.96	17.25	9.84	9.69	4.94	1.09
	12	17.31	9.83	6.78	8.72	3.76	0.92
OCXO	6	25.97	14.84	11.18	10.15	9.65	6.52
	8	25.73	15.73	8.97	9.53	4.55	1.03
	10	24.77	13.77	5.50	8.80	2.58	0.48
	12	16.61	9.57	3.64	8.37	4.98	0.33

coming from cellular carrier phase measurements.

Next, the lower bound proposed in Subsection 6.3.2 is studied. To this end, 200 MC simulations were performed with $N = 10$, $v_{r_1} = 9$ m/s, and an OCXO-equipped receiver. The time history of the logarithm of the determinant of the estimation error covariance for each realization, denoted by $\text{logdet}\,[\mathbf{P}(k|k)]$, is plotted in Fig. 6.3 along with the logarithm of the determinant of the theoretical lower bound (LB) obtained according to Subsection 6.3.2. Note that $\text{logdet}\,[\mathbf{P}(k|k)]$ is related to the volume of the uncertainty ellipsoid [36]. Moreover, the 1σ bound calculated by the EKF is plotted for each MC realization in Fig. 6.4 for the UAV's position and velocity as well as the clock error states corresponding to $c\delta t_1$ and $c\dot{\delta}t_1$. The theoretical LB calculated using the method proposed in Subsection 6.3.2 is also plotted. Note that the σ bounds of the remaining clock error states, namely $c\delta t_n$ and $c\dot{\delta}t_n$ for $n = 2, 3, \ldots, 9$, behave similarly to the ones plotted in Fig. 6.4.

The following can be concluded from these plots. First, the $\text{logdet}\,[\mathbf{P}(k|k)]$ plot in Fig. 6.3 shows that (i) the estimation error uncertainty is decreasing for all MC realizations and (ii) the theoretical LB is not violated. Second, each component of the theoretical LB in Fig.

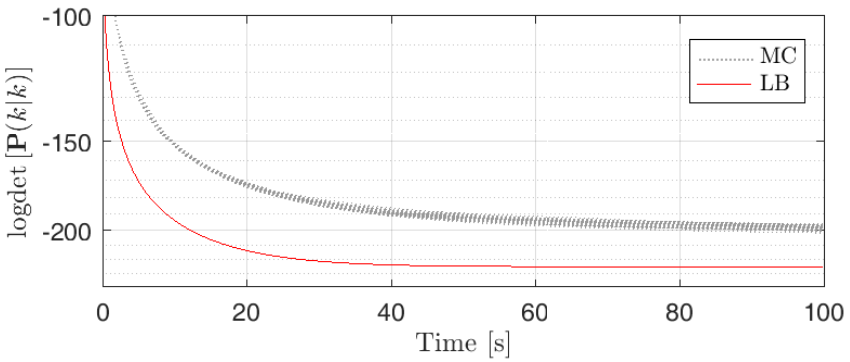

Figure 6.3: MC simulation results: 200 realizations of logdet $[\mathbf{P}(k|k)]$ along with the logarithm of the determinant of the theoretical LB obtained according to Subsection 6.3.2 with $N = 10$, $v_{r_1} = 9$ m/s, and an OCXO-equipped receiver.

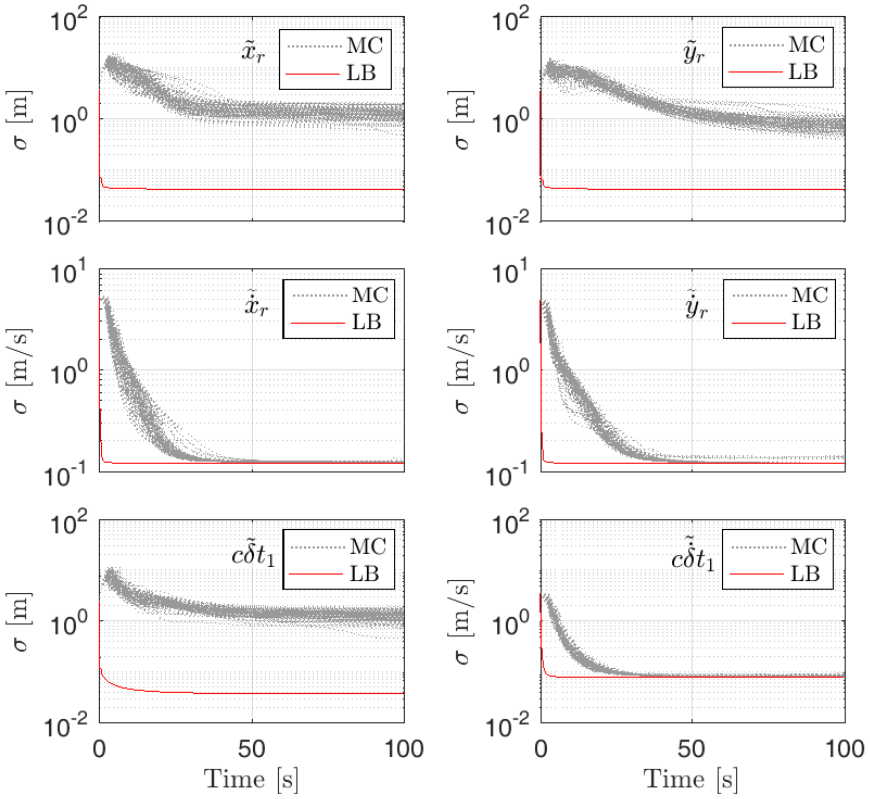

Figure 6.4: MC simulation results: 200 realizations of 1σ bound for the UAV's position and velocity as well as the clock error states corresponding to $c\delta t_1$ and $\dot{\delta}t_1$, and the corresponding theoretical LB obtained according to Subsection 6.3.2 with $N = 10$, $v_{r_1} = 9$ m/s, and an OCXO-equipped receiver.

6.4 bounds the respective component in the estimation error covariance. This result is not guaranteed to hold by the algorithm to compute the theoretical LB; however, it seems to hold. Third, the theoretical LB is tight for the velocity and clock drift states, but not tight

for the position and clock bias states.

6.5 Experimental Results

In this section, two experiments are conducted demonstrating UAV navigation via the framework developed in this chapter. In the following experiments, the altitude of the UAVs was known from their on-board navigation system.

6.5.1 Measurement Noise Statistics

The CDMA and LTE receivers employed in the experiments use second-order coherent phase-locked loops (PLLs), for which it can be shown that the measurement noise variance σ_n^2 is given by $\sigma_n^2(k) = \lambda^2 \frac{B_{\text{PLL}}}{C/N_{0_n}(k)}$, where B_{PLL} is the receiver's PLL noise equivalent bandwidth and $C/N_{0_n}(k)$ is the n-th BTS's carrier-to-noise ratio measured by the receiver [6]. In the following experiments, B_{PLL} was set to 3 Hz.

6.5.2 Hardware and Filter Description

An Autel Robotics X-Star Premium UAV was used for the first experiment and a DJI Matrice 600 was used for the second experiment. In each experiment, the UAVs were equipped with an Ettus E312 universal software radio peripheral (USRP), a consumer-grade 800/1900 MHz cellular antenna, and a small consumer-grade GPS antenna to discipline the on-board oscillator. In both experiments, the UAV-mounted receivers were tuned to listen to cellular signals in the two bands allocated for cellular communication in the U.S.: the 800 MHz and 1900 MHz bands. An E312 USRP was tuned to a 882.75 MHz carrier frequency (i.e., $\lambda = 33.96$ cm), which is a cellular CDMA channel allocated for the U.S. cellular provider

Verizon Wireless. In the second experiment, the UAV was also equipped with a second antenna and another E312 USRP, which was tuned to a 1955 MHz carrier frequency (i.e., $\lambda = 15.33$ cm), which is an LTE channel allocated for the U.S. cellular provider AT&T. Samples of the received signals were stored for off-line post-processing. The cellular carrier phase measurements were given at a rate of 37.5 Hz, i.e., $T = 26.67$ ms. The ground-truth reference for each UAV trajectory was taken from its on-board navigation system, which uses GPS, an inertial measurement unit (IMU), and other sensors. The hovering horizontal precision of the UAVs are reported to be 2 meters for the X-Star Premium by Autel Robotics and 1.5 meters for the Matrice 600 by DJI. The E312 USRPs are equipped with TCXOs with $h_{0,r} = 2 \times 10^{-19}$ and $h_{-2,r} = 2 \times 10^{-20}$ and the BTSs are assumed to be equipped with OCXOs with $h_{0,s_n} = 8 \times 10^{-20}$ and $h_{-2,s_n} = 4 \times 10^{-23}$. The x and y continuous-time acceleration noise spectra were set to $\tilde{q}_x = \tilde{q}_y = 0.03$ m^2/s^3 for both experiments. The EKF was initialized according to the framework in Subsection 6.2.4 with initial position estimates obtained from the UAVs' on-board navigation systems. The experimental setup and BTS and eNodeB layout is shown in Fig. 6.5.

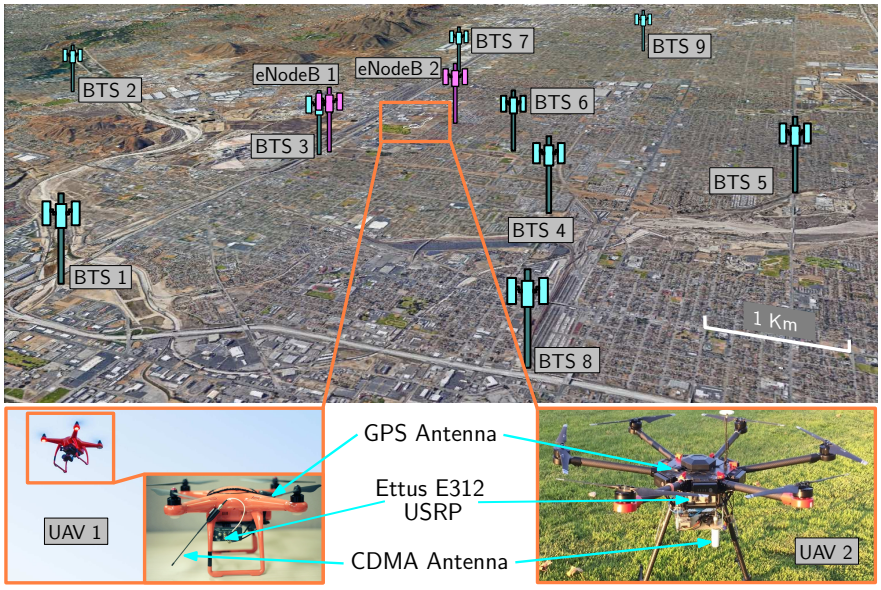

Figure 6.5: Experimental setup and BTS and eNodeB layout. The environment consists of 9 cellular CDMA BTSs (cyan towers) and 2 LTE eNodeBs (magenta towers).

6.5.3 Experiment 1: UAV Navigation Results

In the first experiment, the UAV's total traversed trajectory was 2.6 km, which was completed in 4 minutes and 40 seconds. Over the course of the experiment, the UAV-mounted receiver was listening to 8 cellular CDMA BTSs as shown in Fig. 6.5 (denoted BTSs 1–8). The positions of the BTSs were obtained in two steps: 1) the framework described in [1] was used to obtain an initial map of the cellular BTS locations then 2) Google Earth was used to determine the final position of the BTSs. Fig. 6.6 shows the true and estimated UAV trajectories. The total position RMSE was found to be 2.94 m with a final estimation error at the end of the UAV's flight of 2.23 m. The EKF position error and the associated $\pm 3\sigma$ bounds as well as the position 1σ lower bound (LB) obtained according to Subsection 6.3.2 are shown in Fig. 6.7. In order to study the effect of the number of BTSs and their relative

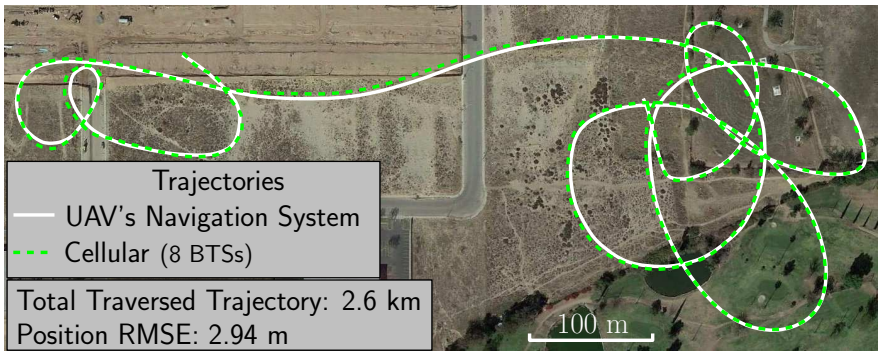

Figure 6.6: Experiment 1 ($N = 8$): True UAV trajectory and estimated UAV trajectory via cellular carrier phase measurements with the proposed EKF framework. The true and estimated trajectories are shown in solid and dashed lines, respectively. Map data: Google Earth.

geometry, the EKF was run again using BTSs 1 through 4 ($N = 4$) and then BTSs 1 through 6 ($N = 6$). The resulting EKF position errors and the associated $\pm 3\sigma$ bounds as well as the position 1σ theoretical LB obtained according to Subsection 6.3.2 are shown in Fig. 6.8. The total position RMSEs and final errors are summarized in Table 6.3.

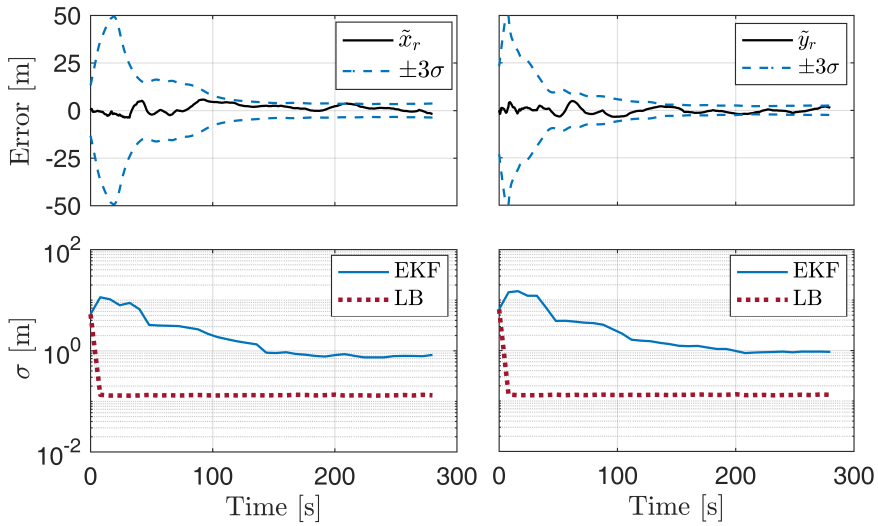

Figure 6.7: Experiment 1 ($N = 8$): Top: UAV's position estimation error trajectories and associated $\pm 3\sigma$ bounds. Bottom: Position estimation error standard deviations and the theoretical LB obtained according to Subsection 6.3.2.

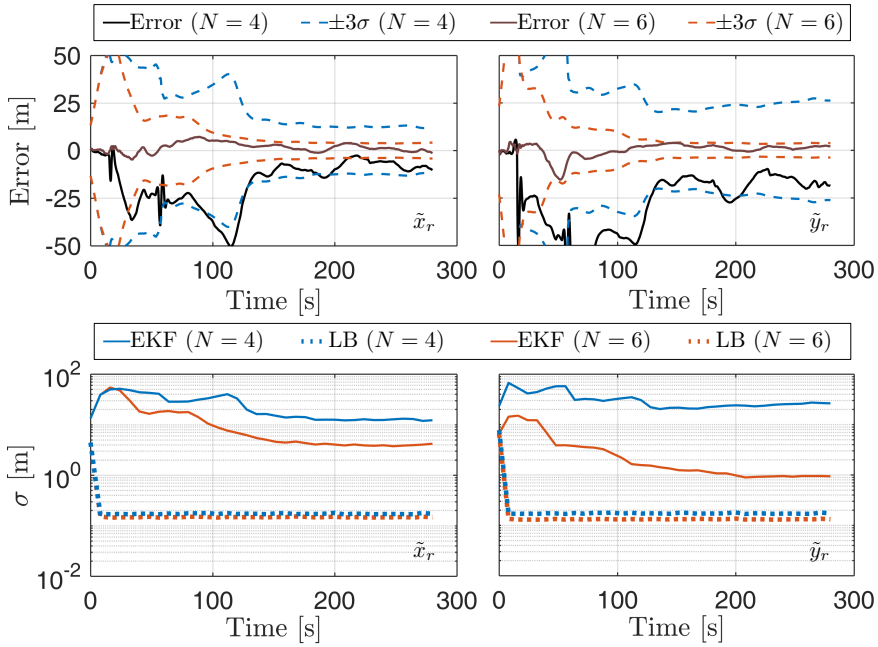

Figure 6.8: Experiment 1 ($N = 4$ and $N = 6$): Top: UAV's position estimation error trajectories and associated $\pm 3\sigma$ bounds. Bottom: Position estimation error standard deviations and the theoretical LB obtained according to Subsection 6.3.2.

6.5.4 Experiment 2: UAV Navigation Results

In the second experiment, the UAV's total traversed trajectory was 2.9 km, which was completed in 5 minutes. In this experiment, the receiver on-board the UAV was listening

to 7 cellular CDMA BTSs and 2 LTE eNodeBs shown in Fig. 6.5. The BTS and eNodeB positions were determined the same way as in the first experiment. The true and estimated UAV trajectories are shown in Fig. 6.9. The total position RMSE was found to be 5.99 m with a final estimation error at the end of the UAV's flight of 3.46 m. The EKF position error and the associated $\pm 3\sigma$ bounds as well as the position 1σ lower bound (LB) obtained according to Subsection 6.3.2 are shown in Fig. 6.10. In order to study the effect of the

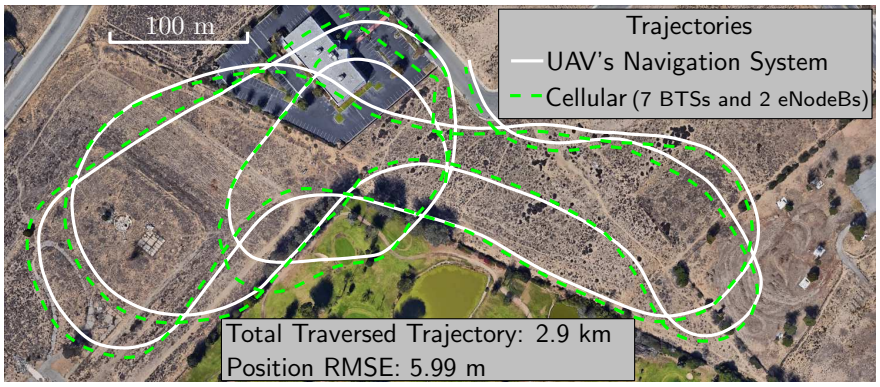

Figure 6.9: Experiment 2 ($N = 9$): True UAV trajectory and estimated UAV trajectory via cellular carrier phase measurements with the proposed EKF framework. The true and estimated trajectories are shown in solid and dashed lines, respectively. Map data: Google Earth.

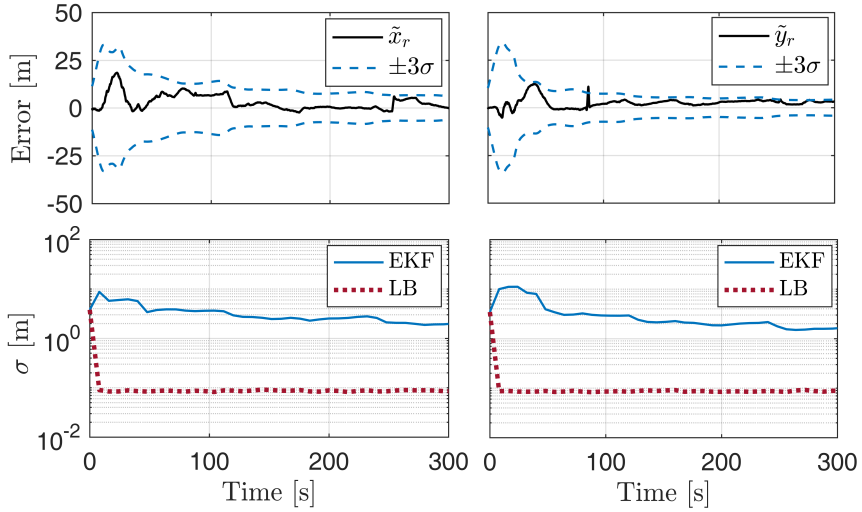

Figure 6.10: Experiment 2 ($N = 9$): Top: UAV's position estimation error trajectories and associated $\pm 3\sigma$ bounds. Bottom: Position estimation error standard deviations and the theoretical LB obtained according to Subsection 6.3.2.

number of BTSs and their relative geometry as in the first experiment, the EKF was run

again using BTSs 1 through 4 ($N = 4$) and then BTSs 1 through 5 and eNodeB 1 ($N = 6$). The resulting EKF position errors and the associated $\pm 3\sigma$ bounds as well as the position 1σ theoretical LB obtained according to Subsection 6.3.2 are shown in Fig. 6.11. The total position RMSEs and final errors are summarized in Table 6.3.

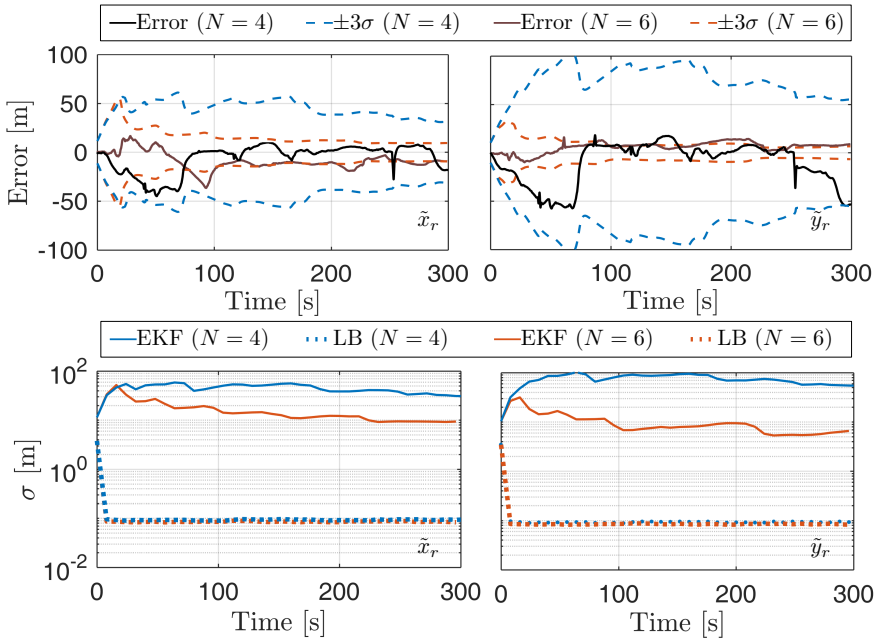

Figure 6.11: Experiment 2 ($N = 4$ and $N = 6$): Top: UAV's position estimation error trajectories and associated $\pm 3\sigma$ bounds. Bottom: Position estimation error standard deviations and the theoretical LB obtained according to Subsection 6.3.2.

Table 6.3: Experimental Results

	Experiment 1		Experiment 2	
N	Position RMSE (m)	Final position error (m)	Position RMSE (m)	Final position error (m)
4	37.39	21.29	30.77	39.81
6	4.68	2.41	14.96	12.84
8	2.94	2.23	-	-
9	-	-	5.99	3.46

6.5.5 Discussion

First, it is important to note that the favorable geometry of the BTSs and eNodeBs comes by virtue of (i) the cellular network structure where cells are typically organized in adjacent hexagons with servicing BTSs at the center of each hexagon and (ii) diversity of cellular providers. Moreover, since the wireless channel is particularly good for UAVs (line of sight is almost always maintained), it is very likely the UAV will be able to reliably listen to geometrically diverse BTSs, as shown in Fig. 6.5.

Second, it was shown in Subsection 6.3.3 that the estimation error can be exponentially bounded and bounded with probability one, as per Definitions 6.3.1 and 6.3.2 respectively; and the estimation error covariance is bounded according to (6.24). None of the experiments contradicts this result since they both show a decreasing $\pm 3\sigma$ bounds and converging errors as shown in Fig. 6.7, Fig. 6.10, Fig. 6.8, and Fig. 6.11 without violating the proposed lower bound.

Third, the UAVs in both experiments were flying at almost constant speeds of 9.3 m/s and 9.7 m/s for experiments 1 and 2, respectively. Based on the simulation results presented in Section 6.4, the RMSE and final error are expected to decrease as the UAV speed increases.

Fourth, note that the proposed framework considers imperfect knowledge of the initial state (i.e., it is initialized with an initial estimate and corresponding uncertainty). It is important that the initial estimate be consistent with the initial estimation error covariance (uncertainty). The initialization scheme proposed in Subsection 6.2.4 ensures that the initial error and the initial uncertainty are consistent.

Fifth, the framework studied in this chapter assumed the BTSs' positions to be known a priori with no uncertainty. Having uncertainty in the BTS's position does not guarantee the applicability of Theorem 6.2. Future work could extend this work to the case with

unknown/uncertain BTS positions. The reader is encouraged to look at the work in [53] and [125] for more details on how uncertainty in the BTS positions affects the performance of an opportunistic navigation framework.

Sixth, the UAV's on-board oscillator was disciplined using GPS signals during the experiment. The effect of not disciplining the on-board oscillator can be captured by increasing the clock process noise covariance matrix. Based on the results in Section 6.4, the RMSE and final error are expected to increase slightly when the on-board oscillator is not disciplined by GPS signals. It is important to note that now one has to find a new (ϵ, δ) pair for Theorem V.2 to hold. Since $\mathbf{Q}$ increases in a GPS-denied environment, then δ is likely to increase. Intuitively, one expects ϵ to decrease in this case for Theorem V.2 to hold. More details can be found in [117].

Remark 7 . The EKF employs statistical models to propagate the position and velocity of the UAV and the clock bias and drift differences. Such models will inherently mismatch the true dynamics of the UAV and clock states, possibly yielding large estimation errors. Using an IMU to propagate the position and velocity states of the UAV should yield better results [53]. Moreover, an adaptive filter may be employed to simultaneously estimate the clock states' process noise covariance to reduce the clock model mismatch [41].

Chapter 7

Optimal Receiver Placement for Dilution of Precision Minimization

This chapter is organized as follows. Section 7.1 presents two motivating problems considered by this chapter. Section 7.2 formulates the receiver placement problem and describes the models employed in the chapter. Section 7.3 proposes a method for solving the DOP minimization problem. Section 7.4 presents simulation results validating the proposed approach. The notation in this chapter is independent from the one used in previous chapters.

The results of this chapter have been published in [126].

7.1 Motivating Problems

This chapter addresses two equivalent problems. The first problem, illustrated in Fig. 7.1(a), considers a number of receivers, referred to as sensors, that are pre-deployed in some random configuration, which are collaboratively localizing a stationary source (e.g., SOP emitter) by making pseudorange observations to this source. A central estimator is used to fuse

pseudoranges from all sensors to estimate the source's 3-D position and its clock bias. Where should an additional sensor be placed so to minimize the WGDOP? If this additional sensor is a moving agent, where should it move to next?

The second problem, illustrated in Fig. 7.1(b), considers a UAV that is navigating via GNSS signals, but whose navigation solution suffers from a large vertical dilution of precision (VDOP) or WVDOP. This problem is inherent to GNSS-based navigation, due to the geometric configuration of GNSS satellites being above the UAV. It has been demonstrated that utilizing terrestrial SOP transmitters significantly reduce the VDOP or WVDOP, since now the elevation angle from which the signals are received spans $-90°$ to $+90°$ [127, 128, 129]. In such environment, where should the UAV position itself in order to minimize its VDOP or WVDOP?

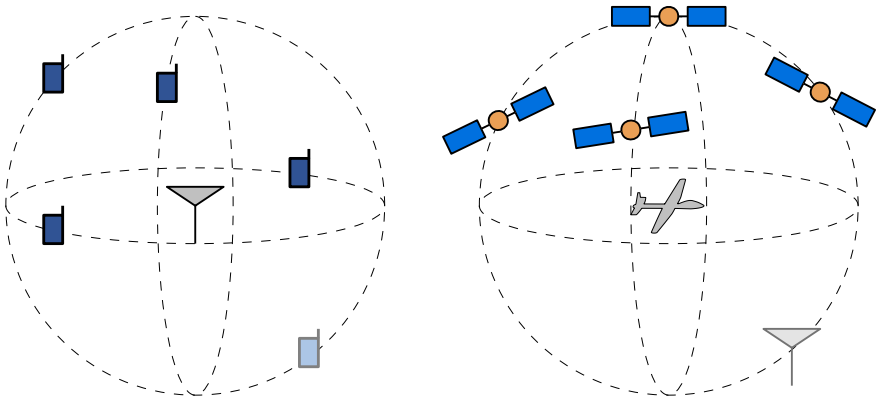

(a) (b)

Figure 7.1: Two motivating examples: (a) Placing an additional sensor for optimal source localization. (b) Solving for relative SOP position to minimize VDOP or WVDOP.

At the core, these problems are identical: they both boil down to minimizing the WGDOP or elements within the WGDOP matrix over a unit vector that corresponds to the relative position vector between the additional sensor (navigation source) and the source (UAV). In order to solve these problems, this chapter first formulates the core WGDOP minimization problem as a quadratically constrained fractional quadratic program, to which numerical solutions yielding the global optimum have been developed in the nonconvex optimization

literature [130]. Next, the algorithm for solving this minimization problem is detailed. Then, Monte Carlo simulation for the two DOP minimization problems illustrated in Fig. 7.1 along with numerical convergence and complexity analyses associated with the proposed approach versus existing approaches. An additional application of the proposed approach for source localization with a mobile agent is also presented.

7.2 Model Description and Problem Formulation

In this section, the models adopted in the chapter are described and the DOP minimization problem is subsequently formulated.

7.2.1 Model Description

The state to be estimated is $\boldsymbol{\eta} \triangleq \left[\boldsymbol{r}_s^{\mathsf{T}}, c\delta t_s\right]^{\mathsf{T}}$, which is composed of the 3-D position vector $\boldsymbol{r}_s \triangleq [x_s, y_s, z_s]^{\mathsf{T}}$ of the source (UAV) and its clock bias $c\delta t_s$ expressed in meters, where c is the speed of light and δt_s is the source's (UAV's) clock bias expressed in seconds. A prior for $\boldsymbol{\eta}$ may be given, denoted by $\hat{\boldsymbol{\eta}}$, with the associated initial covariance $\mathbf{P}_0 \succ \mathbf{0}$. The position vector of the jth sensor (navigation source) is given by $\boldsymbol{r}_{r_j} \triangleq \left[x_{r_j}, y_{r_j}, z_{r_j}\right]^{\mathsf{T}}$ and its clock bias by $c\delta t_{r_j}$, $j = 1, \ldots, N$, where $N \geq 5$ is the total number of sensors (navigation sources). It is assumed that the positions and clock biases of all the sensors (navigation sources) are known at any time-step. Moreover, each sensor is making a pseudorange measurement to the source. Alternatively, the UAV is making pseudorange measurements to each navigation source. The pseudorange measurements may be expressed as

$$z_j = \left\|\boldsymbol{r}_{r_j} - \boldsymbol{r}_s\right\|_2 + c \cdot \left[\delta t_{r_j} - \delta t_s\right] + v_j,$$

where $\boldsymbol{v} \triangleq [v_1, \ldots, v_N]^{\mathsf{T}}$ is the measurement noise vector, which is modeled as a zero-mean Gaussian random vector with covariance $\mathbf{R}_N$ [131]. Note that the measurement noise may be correlated; hence, $\mathbf{R}_N$ is an arbitrary symmetric positive-definite matrix. In the case of the navigation sources being GNSS satellites, it is assumed that z_j has been corrected for ionospheric and tropospheric delays. The Jacobian matrix $\mathbf{H}_N$ of the measurement vector $\boldsymbol{z} \triangleq [z_1, \ldots, z_N]^{\mathsf{T}}$ is given by

$$\mathbf{H}_N = [\boldsymbol{h}_1 \quad \ldots \quad \boldsymbol{h}_N]^{\mathsf{T}}, \quad \boldsymbol{h}_j \triangleq \left[\frac{\boldsymbol{r}_s^{\mathsf{T}} - \boldsymbol{r}_{r_j}^{\mathsf{T}}}{\left\| \boldsymbol{r}_s - \boldsymbol{r}_{r_j} \right\|_2}, -1 \right]^{\mathsf{T}}.$$

Subsequently, the estimation error covariance matrix of a weighted nonlinear least-squares (WNLS) estimator with N sensors (navigation sources), denoted $\mathbf{P}_N$, is given by

$$\mathbf{P}_N \triangleq \left(\mathbf{P}_0^{-1} + \mathbf{H}_N^{\mathsf{T}} \mathbf{R}_N^{-1} \mathbf{H}_N \right)^{-1}.$$

7.2.2 Problem Formulation

The problem addressed in this chapter is the optimal placement of an additional sensor (navigation source) to a set of $N - 1 \geq 4$ pre-deployed sensors (navigation sources) in order to optimize a functional of the localization (navigation solution) estimation error covariance. To this end, two cost functions are defined

$$g(\mathbf{P}_N) \triangleq \operatorname{tr}\left[\mathbf{T} \mathbf{P}_N \mathbf{T}^{\mathsf{T}} \right], \qquad g'(\mathbf{P}_N) \triangleq \det\left[\mathbf{T}' \mathbf{P}_N \mathbf{T}'^{\mathsf{T}} \right],$$

where $\operatorname{tr}[\cdot]$ is the matrix trace, $\det[\cdot]$ is the matrix determinant, $\mathbf{T}$ is an arbitrary $L \times 4$ matrix and L is a positive integer, and $\mathbf{T}'$ is an arbitrary $L' \times 4$ matrix with rank L' and L' is a positive integer with $0 < L' \leq 4$. These conditions on $\mathbf{T}'$ ensure that $g'(\mathbf{P}_N)$ is nonzero. Note that $\mathbf{H}_N = \left[\mathbf{H}_{N-1}^{\mathsf{T}} \quad \boldsymbol{h}_N \right]^{\mathsf{T}}$ and $\left\{ \boldsymbol{r}_{r_j} \right\}_{j=1}^{N-1}$ and $\boldsymbol{r}_s$ are fixed. Therefore, $\mathbf{H}_{N-1}$

is constant. The problem is to find $\boldsymbol{r}_{r_N}$ that minimizes $g(\mathbf{P}_N)$ or $g'(\mathbf{P}_N)$. The vector $\boldsymbol{h}_N$ may be expressed as $\boldsymbol{h}_N = \begin{bmatrix}\boldsymbol{x}^\mathsf{T} & -1\end{bmatrix}^\mathsf{T}$ where $\boldsymbol{x} \triangleq \frac{\boldsymbol{r}_s - \boldsymbol{r}_{r_N}}{\left\|\boldsymbol{r}_s - \boldsymbol{r}_{r_N}\right\|_2}$ is the unit LOS vector from the source (UAV) to the Nth sensor (navigation source). One can parameterize $\boldsymbol{x}$ in terms of the elevation angle θ and the azimuth angle ϕ according to

$$\boldsymbol{x} = \left[\cos\theta\,\cos\phi \quad \cos\theta\,\sin\phi \quad \sin\theta\right]^\mathsf{T},$$

where $-\frac{\pi}{2} \leq \theta \leq \frac{\pi}{2}$ is the elevation angle and $0 \leq \phi < 2\pi$ is the azimuth angle. It can be seen that any sensor (navigation source) position on the ray whose direction is given by $\boldsymbol{x}$ yields the same estimation error covariance. Subsequently, the problem boils down to finding the vector $\boldsymbol{x}$ on the unit sphere that minimizes $g(\mathbf{P}_N)$ or $g'(\mathbf{P}_N)$, given by the following the optimization problems

$$\underset{\boldsymbol{x}^\mathsf{T}\boldsymbol{x}=1}{\text{minimize}} \quad g(\mathbf{P}_N) = \operatorname{tr}\left[\mathbf{T}\mathbf{P}_N\mathbf{T}^\mathsf{T}\right], \tag{7.1}$$

$$\underset{\boldsymbol{x}^\mathsf{T}\boldsymbol{x}=1}{\text{minimize}} \quad g'(\mathbf{P}_N) = \det\left[\mathbf{T}\mathbf{P}_N\mathbf{T}^\mathsf{T}\right]. \tag{7.2}$$

In the rest of the chapter, these two problems are generally referred to as the DOP minimization problem. In order to visualize $g(\mathbf{P}_N)$ and $g'(\mathbf{P}_N)$, the following two motivating examples are considered.

In the first example, 4 sensors are randomly placed on the unit sphere, which was gridded by uniformly sampling the domain of $\theta \in \left[-\frac{\pi}{2}, \frac{\pi}{2}\right]$ and $\phi \in [0, 2\pi]$. Next, $g(\mathbf{P}_N)$ and $g'(\mathbf{P}_N)$ were evaluated for $\mathbf{T} = \mathbf{T}' = \mathbf{I}$ at each (θ, ϕ) pair and were plotted in two ways as shown in Figs. 7.2 and 7.3: (a) as a 3-D pattern plot where $g(\mathbf{P}_N)$ and $g'(\mathbf{P}_N)$ are proportional to the radial distance to the 3-D surface and the corresponding sensor location is its projection onto the unit sphere and (b) as a surface plot as a function of the azimuth and elevation angles. It can be seen from Figs. 7.2 and 7.3 that $g(\mathbf{P}_N)$ and $g'(\mathbf{P}_N)$ are nonconvex and have several maxima and minima.

In the second example, a UAV is assumed to have access to 4 GNSS satellites. The satellite elevation mask was set to 10°, i.e., satellites below such elevation mask are not used to produce the navigation solution (this is common in GNSS-based navigation to avoid severely attenuated GNSS signals and multipath). The UAV is trying for solve to its relative position to a terrestrial SOP in order to minimize its VDOP, given by $g(\mathbf{P}_N) = \mathrm{tr}\left[\boldsymbol{e}_3^\mathsf{T}\mathbf{P}_N\boldsymbol{e}_3\right] = \boldsymbol{e}_3^\mathsf{T}\mathbf{P}_N\boldsymbol{e}_3$, where $\boldsymbol{e}_3 \triangleq [0,0,1,0]^\mathsf{T}$. Note that the distance to the GNSS satellites is significantly large such that the unit LOS vectors form the UAV to the satellites do not change while the UAV is positioning itself with respect to the SOP. Hence, this problem becomes equivalent to the sensor placement problem whose solution is the desired relative position of the SOP with respect to the UAV. This scenario is illustrated in Fig. 7.4, where the dark blue marks indicate the endpoints of the unit LOS vectors to the 4 GNSS satellites and the red mark indicates the relative position of the SOP that minimizes the WVDOP. Since $\boldsymbol{e}_3^\mathsf{T}\mathbf{P}_N\boldsymbol{e}_3$ is a scalar, then $g(\mathbf{P}_N) = g'(\mathbf{P}_N)$. Subsequently, only $g(\mathbf{P}_N)$ is plotted. It can be seen from Fig. 7.4 that $g(\mathbf{P}_N)$ (and consequently $g'(\mathbf{P}_N)$) is nonconvex and has several local minima and maxima.

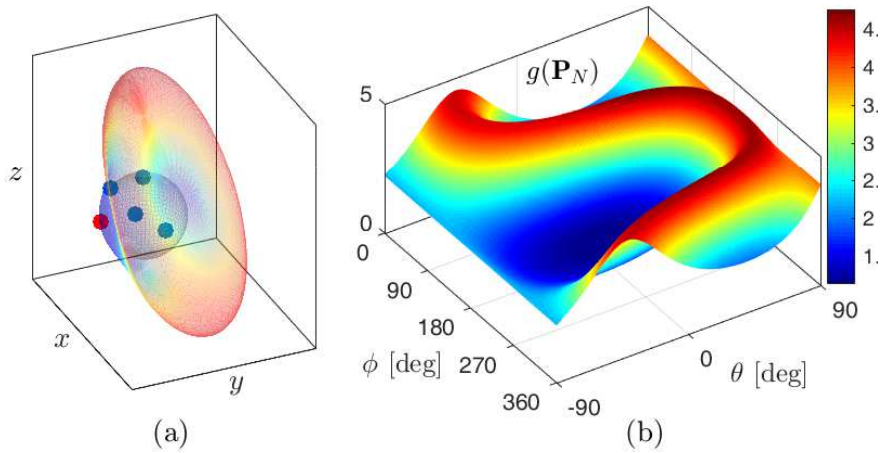

Figure 7.2: Visualization of $g(\mathbf{P}_N) = \mathrm{tr}[\mathbf{P}_N]$. (a) 3-D pattern plot where $g(\mathbf{P}_N)$ is proportional to the radial distance to the 3-D surface and the corresponding sensor location is its projection onto the unit sphere. The dark blue markers indicate the endpoints of the unit LOS vectors to 4 pre-deployed sensors. The red marker indicates the endpoint of the vector $\boldsymbol{x}$ that minimizes $g(\mathbf{P}_N)$. (b) Surface plot showing $g(\mathbf{P}_N)$ as a function of the azimuth angle ϕ and elevation angle θ.

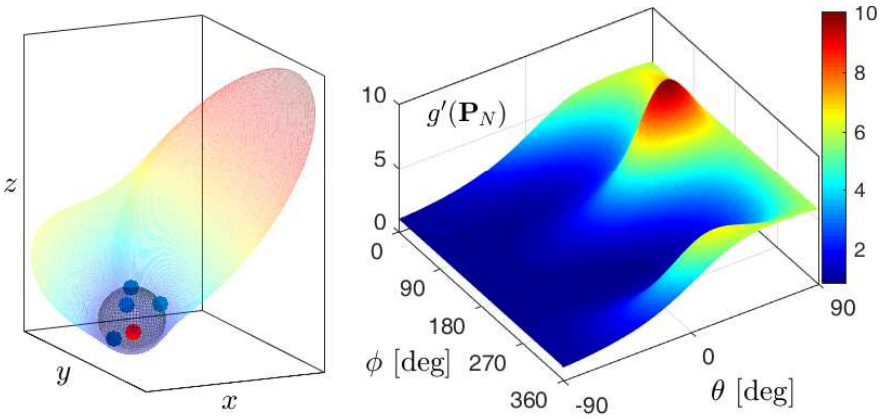

(a) (b)

Figure 7.3: Visualization of $g'(\mathbf{P}_N) = \det[\mathbf{P}_N]$. (a) 3-D pattern plot where $g'(\mathbf{P}_N)$ is proportional to the radial distance to the 3-D surface and the corresponding sensor location is its projection onto the unit sphere. The dark blue markers indicate the endpoints of the unit LOS vectors to 4 pre-deployed sensors. The red marker indicates the endpoint of the vector $\boldsymbol{x}$ that minimizes $g'(\mathbf{P}_N)$. (b) Surface plot showing $g'(\mathbf{P}_N)$ as a function of the azimuth angle ϕ and elevation angle θ.

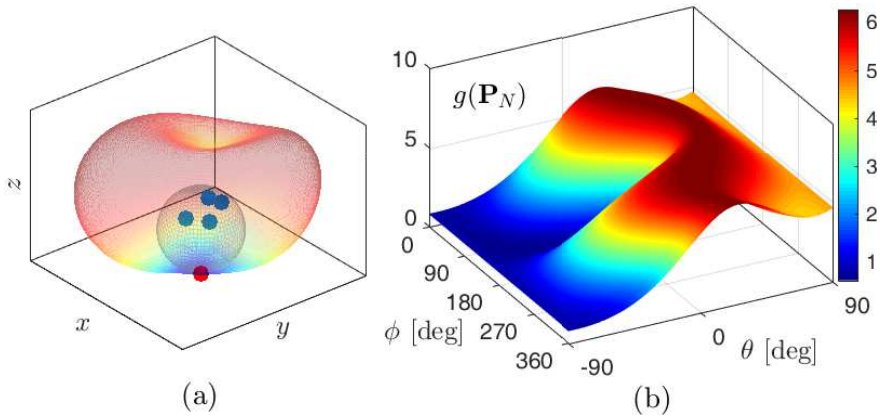

(a) (b)

Figure 7.4: Visualization of $g(\mathbf{P}_N) = \boldsymbol{e}_3^{\mathsf{T}}\mathbf{P}_N\boldsymbol{e}_3$. (a) 3-D pattern plot where the VDOP $g(\mathbf{P}_N)$ is proportional to the radial distance to the 3-D surface and the corresponding sensor location is its projection onto the unit sphere. The dark blue markers indicate the endpoints of the unit LOS vectors to 4 GNSS satellites. The red marker indicates the endpoint of the vector $\boldsymbol{x}$ that minimizes the WVDOP. (b) Surface plot showing the WVDOP as a function of the azimuth angle ϕ and elevation angle θ.

In the next section, a method for obtaining the global minimum of $g(\mathbf{P}_N)$ is developed.

7.3 DOP Minimization

In this section, the minimization problems (7.1) and (7.2) are formulated as quadratically constrained fractional quadratic programs and the global solutions are subsequently discussed.

7.3.1 DOP Minimization as a Quadratically Constrained Fractional Quadratic Program

Let the measurement noise covariance $\mathbf{R}_N$ after placing the Nth sensor (navigation source) have the following partitioning

$$\mathbf{R}_N = \begin{bmatrix} \mathbf{R}_{N-1} & \boldsymbol{r}_N \\ \boldsymbol{r}_N^{\mathsf{T}} & \sigma_N^2 \end{bmatrix}.$$

Let its inverse $\mathbf{Y}_N$ be partitioned according to

$$\mathbf{Y}_N \triangleq \mathbf{R}_N^{-1} = \begin{bmatrix} \mathbf{Y}_{N-1} & \boldsymbol{y}_N \\ \boldsymbol{y}_N^{\mathsf{T}} & \mu_N^2 \end{bmatrix}.$$

The estimation error covariance matrix after placing the Nth sensor (navigation source) may then be expressed as

$$\begin{aligned} \mathbf{P}_N &\triangleq \left(\mathbf{P}_0^{-1} + \mathbf{H}_N^{\mathsf{T}}\mathbf{R}_N^{-1}\mathbf{H}_N\right)^{-1} \\ &= \left(\mathbf{P}_0^{-1} + \mathbf{H}_{N-1}^{\mathsf{T}}\mathbf{Y}_{N-1}\mathbf{H}_{N-1} + \mu_N^2\boldsymbol{h}_N\boldsymbol{h}_N^{\mathsf{T}} + \boldsymbol{h}_N\boldsymbol{y}_N^{\mathsf{T}}\mathbf{H}_{N-1} + \mathbf{H}_{N-1}^{\mathsf{T}}\boldsymbol{y}_N\boldsymbol{h}_N^{\mathsf{T}}\right)^{-1} \\ &= \left(\mathbf{M} + \boldsymbol{u}\boldsymbol{u}^{\mathsf{T}}\right)^{-1}, \end{aligned} \tag{7.3}$$

where $\boldsymbol{u} \triangleq \mu_N \boldsymbol{h}_N + \frac{1}{\mu_N}\mathbf{H}_{N-1}^{\mathsf{T}}\boldsymbol{y}_N$ and $\mathbf{M} \triangleq \mathbf{P}_0^{-1} + \mathbf{H}_{N-1}^{\mathsf{T}}\left(\mathbf{Y}_{N-1} - \frac{1}{\mu_N^2}\boldsymbol{y}_N\boldsymbol{y}_N^{\mathsf{T}}\right)\mathbf{H}_{N-1}$. Using the matrix inversion lemma, it can be shown that $\mathbf{M} = \mathbf{P}_0^{-1} + \mathbf{H}_{N-1}^{\mathsf{T}}\mathbf{R}_{N-1}^{-1}\mathbf{H}_{N-1}$. If a prior is available, then $\mathbf{H}_{N-1}$ does not need to be full column rank. If no prior is available, then $\mathbf{M} = \mathbf{H}_{N-1}^{\mathsf{T}}\mathbf{R}_{N-1}^{-1}\mathbf{H}_{N-1}$, in which case $\mathbf{H}_{N-1}$ must be full column rank. Either way, $\mathbf{M}$ is positive definite and so is its inverse. Using the matrix inversion lemma, $\mathbf{P}_N$ may be expressed as

$$\mathbf{P}_N = \mathbf{M}^{-1} - \frac{\mathbf{M}^{-1}\boldsymbol{u}\boldsymbol{u}^{\mathsf{T}}\mathbf{M}^{-1}}{1 + \boldsymbol{u}^{\mathsf{T}}\mathbf{M}^{-1}\boldsymbol{u}}. \tag{7.4}$$

Next, $g(\mathbf{P}_N)$ and $g'(\mathbf{P}_N)$ are re-expressed as fractional quadratic cost functions.

Trace Minimization

Using (7.4), $g(\mathbf{P}_N)$ may be expressed as

$$g(\mathbf{P}_N) = C - \frac{\operatorname{tr}\left[\mathbf{T}\mathbf{M}^{-1}\boldsymbol{u}\boldsymbol{u}^{\mathsf{T}}\mathbf{M}^{-1}\mathbf{T}^{\mathsf{T}}\right]}{1 + \boldsymbol{u}^{\mathsf{T}}\mathbf{M}^{-1}\boldsymbol{u}},$$

where $C \triangleq \operatorname{tr}\left[\mathbf{T}\mathbf{M}^{-1}\mathbf{T}^{\mathsf{T}}\right]$. Using the cyclic properties of the trace, the cost function may be expressed as

$$g(\mathbf{P}_N) = C + \frac{\boldsymbol{u}^{\mathsf{T}}\mathbf{Q}\boldsymbol{u}}{1 + \boldsymbol{u}^{\mathsf{T}}\mathbf{M}^{-1}\boldsymbol{u}}, \tag{7.5}$$

where $\mathbf{Q} \triangleq -\mathbf{M}^{-1}\mathbf{T}^{\mathsf{T}}\mathbf{T}\mathbf{M}^{-1}$. Note that $\boldsymbol{h}_N = \left[\boldsymbol{x}^{\mathsf{T}}, -1\right]^{\mathsf{T}}$ and let $\mathbf{Q}$, $\mathbf{M}^{-1}$, $\boldsymbol{\zeta} \triangleq \mathbf{Q}\mathbf{H}_{N-1}^{\mathsf{T}}\boldsymbol{y}_N$, and $\boldsymbol{\psi} \triangleq \mathbf{M}^{-1}\mathbf{H}_{N-1}^{\mathsf{T}}\boldsymbol{y}_N$ have the following partitioning

$$\mathbf{Q} = \begin{bmatrix} \bar{\mathbf{A}}_1 & \bar{\boldsymbol{b}}_1 \\ \bar{\boldsymbol{b}}_1^{\mathsf{T}} & \bar{c}_1 \end{bmatrix},\ \mathbf{M}^{-1} = \begin{bmatrix} \bar{\mathbf{A}}_2 & \bar{\boldsymbol{b}}_2 \\ \bar{\boldsymbol{b}}_2^{\mathsf{T}} & \bar{c}_2 \end{bmatrix},\ \boldsymbol{\zeta} = \begin{bmatrix} \boldsymbol{\zeta}_1 \\ \zeta_2 \end{bmatrix},\ \boldsymbol{\psi} = \begin{bmatrix} \boldsymbol{\psi}_1 \\ \psi_2 \end{bmatrix}.$$

Then, $g\left(\mathbf{P}_N\right)$ may be expressed as

$$g\left(\mathbf{P}_N\right) = g(\boldsymbol{x}) \triangleq C + \frac{g_1(\boldsymbol{x})}{g_2(\boldsymbol{x})},$$

where $g_n(\boldsymbol{x}) \triangleq \boldsymbol{x}^{\mathsf{T}}\mathbf{A}_n\boldsymbol{x} - 2\boldsymbol{b}_n^{\mathsf{T}}\boldsymbol{x} + c_n$, $n = 1, 2$, and

$$\begin{aligned}
\mathbf{A}_1 &\triangleq \mu_N^2\bar{\mathbf{A}}_1,\\
\boldsymbol{b}_1 &\triangleq \mu_N^2\bar{\boldsymbol{b}}_1 - \boldsymbol{\zeta}_1,\\
c_1 &\triangleq \mu_N^2\bar{c}_1 + \frac{1}{\mu_N^2}\boldsymbol{y}_N^{\mathsf{T}}\mathbf{H}_{N-1}\mathbf{Q}\mathbf{H}_{N-1}^{\mathsf{T}}\boldsymbol{y}_N - 2\zeta_2,\\
\mathbf{A}_2 &\triangleq \mu_N^2\bar{\mathbf{A}}_2,\\
\boldsymbol{b}_2 &\triangleq \mu_N^2\bar{\boldsymbol{b}}_2 - \boldsymbol{\psi}_1,\\
c_2 &\triangleq \mu_N^2\bar{c}_2 + \frac{1}{\mu_N^2}\boldsymbol{y}_N^{\mathsf{T}}\mathbf{H}_{N-1}\mathbf{M}^{-1}\mathbf{H}_{N-1}^{\mathsf{T}}\boldsymbol{y}_N - 2\psi_2 + 1.
\end{aligned}$$

Subsequently, the DOP minimization problem in (7.1) may be posed as

$$\underset{\boldsymbol{x}\in\mathcal{F}}{\text{minimize}} \quad g(\boldsymbol{x}), \tag{7.6}$$

where $\mathcal{F} = \left\{\boldsymbol{x} \in \mathbb{R}^3 : \boldsymbol{x}^{\mathsf{T}}\boldsymbol{x} = 1\right\}$.

Determinant Minimization

Using (7.4) and Sylvester's determinant theorem, $g'(\mathbf{P}_N)$ may be expressed as

$$g'(\mathbf{P}_N) = C'\left(1 + \frac{\boldsymbol{u}^{\mathsf{T}}\mathbf{Q}'\boldsymbol{u}}{1 + \boldsymbol{u}^{\mathsf{T}}\mathbf{M}^{-1}\boldsymbol{u}}\right), \tag{7.7}$$

where $\mathbf{Q}' \triangleq -\mathbf{M}^{-1}\mathbf{T}'^{\mathsf{T}}\left(\mathbf{T}'\mathbf{M}^{-1}\mathbf{T}'^{\mathsf{T}}\right)^{-1}\mathbf{T}'\mathbf{M}^{-1}$ and $C' \triangleq \det\left[\mathbf{T}'\mathbf{M}^{-1}\mathbf{T}'^{\mathsf{T}}\right]$. Let $\mathbf{Q}'$ and $\boldsymbol{\zeta}' \triangleq \mathbf{Q}'\mathbf{H}_{N-1}^{\mathsf{T}}\boldsymbol{y}_N$ have the following partitioning

$$\mathbf{Q}' = \begin{bmatrix} \bar{\mathbf{A}}_1' & \bar{\boldsymbol{b}}_1' \\ \bar{\boldsymbol{b}}_1'^{\mathsf{T}} & \bar{c}_1' \end{bmatrix}, \quad \boldsymbol{\zeta}' = \begin{bmatrix} \boldsymbol{\zeta}_1' \\ \zeta_2' \end{bmatrix}.$$

Then, $g'(\mathbf{P}_N)$ may be expressed as

$$g'(\mathbf{P}_N) = g'(\boldsymbol{x}) \triangleq C' + \frac{g_1'(\boldsymbol{x})}{g_2(\boldsymbol{x})},$$

where $g_1'(\boldsymbol{x}) \triangleq \boldsymbol{x}^{\mathsf{T}}\mathbf{A}_1'\boldsymbol{x} - 2\boldsymbol{b}_1'^{\mathsf{T}}\boldsymbol{x} + c_1'$, and

$$\begin{aligned} \mathbf{A}_1' &\triangleq \mu_N^2\bar{\mathbf{A}}_1', \\ \boldsymbol{b}_1' &\triangleq \mu_N^2\bar{\boldsymbol{b}}_1' - \boldsymbol{\zeta}_1', \\ c_1' &\triangleq \mu_N^2\bar{c}_1' + \frac{1}{\mu_N^2}\boldsymbol{y}_N^{\mathsf{T}}\mathbf{H}_{N-1}\mathbf{Q}'\mathbf{H}_{N-1}^{\mathsf{T}}\boldsymbol{y}_N - 2\zeta_2'. \end{aligned}$$

Subsequently, the DOP minimization problem in (7.2) may be posed as

$$\underset{\boldsymbol{x}\in\mathcal{F}}{\text{minimize}} \quad g'(\boldsymbol{x}). \tag{7.8}$$

Note that (7.6) and (7.8) are of the form

$$\underset{\boldsymbol{x}\in\mathcal{F}}{\text{minimize}} \quad f(\boldsymbol{x}) = C_0 + \frac{f_1(\boldsymbol{x})}{f_2(\boldsymbol{x})}, \tag{7.9}$$

where $f(\boldsymbol{x})$, $f_1(\boldsymbol{x})$, $f_2(\boldsymbol{x})$, and C_0 can be either $g(\boldsymbol{x})$, $g_1(\boldsymbol{x})$, $g_2(\boldsymbol{x})$, and C; or $g'(\boldsymbol{x})$, $g_1'(\boldsymbol{x})$, $g_2(\boldsymbol{x})$, and C', respectively.

Remark: Note that this analysis is readily extendable to range measurements instead of

pseudorange, i.e, $z_j = \left\|\boldsymbol{r}_{r_j} - \boldsymbol{r}_s\right\| + v_j$. In this case, $\mathbf{A}_n$, $\boldsymbol{b}_n$, c_n, $\mathbf{A}'_n$, $\boldsymbol{b}'_n$, and c'_n for $n = 1, 2$ become

$$
\begin{aligned}
\mathbf{A}_1 &\triangleq \mu_N^2 \mathbf{Q}, \\
\boldsymbol{b}_1 &\triangleq -\mathbf{Q}\mathbf{H}_{N-1}^{\mathsf{T}} \boldsymbol{y}_N, \\
c_1 &\triangleq \frac{1}{\mu_N^2} \boldsymbol{y}_N^{\mathsf{T}} \mathbf{H}_{N-1} \mathbf{Q} \mathbf{H}_{N-1}^{\mathsf{T}} \boldsymbol{y}_N, \\
\mathbf{A}_2 &\triangleq \mu_N^2 \mathbf{M}^{-1}, \\
\boldsymbol{b}_2 &\triangleq -\mathbf{M}^{-1} \mathbf{H}_{N-1}^{\mathsf{T}} \boldsymbol{y}_N, \\
c_2 &\triangleq \frac{1}{\mu_N^2} \boldsymbol{y}_N^{\mathsf{T}} \mathbf{H}_{N-1} \mathbf{M}^{-1} \mathbf{H}_{N-1}^{\mathsf{T}} \boldsymbol{y}_N + 1. \\
\mathbf{A}'_1 &\triangleq \mu_N^2 \mathbf{Q}', \\
\boldsymbol{b}'_1 &\triangleq -\mathbf{Q}' \mathbf{H}_{N-1}^{\mathsf{T}} \boldsymbol{y}_N, \\
c'_1 &\triangleq \frac{1}{\mu_N^2} \boldsymbol{y}_N^{\mathsf{T}} \mathbf{H}_{N-1} \mathbf{Q}' \mathbf{H}_{N-1}^{\mathsf{T}} \boldsymbol{y}_N.
\end{aligned}
$$

7.3.2 Domain Approximation

Although (7.9) minimizes the ratio of two quadratic forms, it is not a quadratically constrained fractional quadratic program due to the feasible domain. As discussed in [130], the constraint was shown to take the form

$$
C_1^2 \leq \boldsymbol{x}^{\mathsf{T}} \mathbf{G} \boldsymbol{x} \leq C_2^2, \tag{7.10}
$$

where $C_2^2 > C_1^2 \geq 0$ and $\mathbf{G}$ is a positive definite matrix. In what follows, a method for transforming the constraint in (7.9) into the form of (7.10) is presented.

First, it must be established that $f(\boldsymbol{x})$ is continuous. It can be seen from (7.5) and (7.7) that both denominators are greater than one since $\mathbf{M}^{-1} \succ 0$, i.e., $g_2(\boldsymbol{x}) \geq 1$ and $g'_2(\boldsymbol{x}) \geq 1$.

Consequently $f(\boldsymbol{x})$ is continuous. Next, denote $\boldsymbol{x}_0^\star$ the true optimal solution of (7.9). Since $f(\boldsymbol{x})$ is continuous, then for every $\delta_0 > 0$ where $\|\boldsymbol{x} - \boldsymbol{x}_0^\star\|_2 < \delta_0$, there exists $\epsilon_0 > 0$ such that $|f(\boldsymbol{x}) - f(\boldsymbol{x}_0^\star)| < \epsilon_0$. Now, let $\epsilon_0 \equiv \epsilon^\star < \min_{\boldsymbol{x}\in\mathcal{L}} |f(\boldsymbol{x}) - f(\boldsymbol{x}_0^\star)|$, where $\mathcal{L}$ is the set of local minima on $\mathcal{F}$ excluding $\boldsymbol{x}_0^\star$. Therefore, there exists $\delta^\star$ such that $\|\boldsymbol{x} - \boldsymbol{x}_0^\star\|_2 < \delta^\star$. In order to satisfy the form of the constraint given in (7.10), the set $\mathcal{F}$ is approximated with

$$\mathcal{F}_2 = \left\{\boldsymbol{x} \in \mathbb{R}^3 : 1 \leq \boldsymbol{x}^\mathsf{T}\boldsymbol{x} \leq 1 + \delta\right\}, \tag{7.11}$$

where $\delta > 0$ is made infinitely small. This approximation is needed to formulate the DOP minimization problem as the quadratically constrained fractional quadratic problem discussed in the next subsection. It can be seen that

$$\lim_{\delta\to 0} \mathcal{F}_2 = \mathcal{F}.$$

Denote $\boldsymbol{x}_\delta^\star$ the solution to

$$\underset{\boldsymbol{x}\in\mathcal{F}_2}{\text{minimize}} \quad f(\boldsymbol{x}).$$

Since $\mathcal{F}_2$ is not strictly the unit sphere, then $\boldsymbol{x}_\delta^\star$ may not be a unit vector. Define $\boldsymbol{x}^\star$ to be a unit vector along $\boldsymbol{x}_\delta^\star$ as

$$\boldsymbol{x}^\star \triangleq \frac{\boldsymbol{x}_\delta^\star}{\|\boldsymbol{x}_\delta^\star\|_2}. \tag{7.12}$$

This vector $\boldsymbol{x}^\star$ will be shown to converge to the optimal solution of (7.9) $\boldsymbol{x}_0^\star$. Let δ be small enough such that $\|\boldsymbol{x}_0^\star - \boldsymbol{x}_\delta^\star\|_2 < \delta^\star$. Moreover, it can be seen from Fig. 7.5 that $\|\boldsymbol{x}_0^\star - \boldsymbol{x}^\star\|_2 < \|\boldsymbol{x}_0^\star - \boldsymbol{x}_\delta^\star\|_2$ since $\boldsymbol{x}^\star$ is the projection of $\boldsymbol{x}_\delta^\star$ onto the unit sphere.

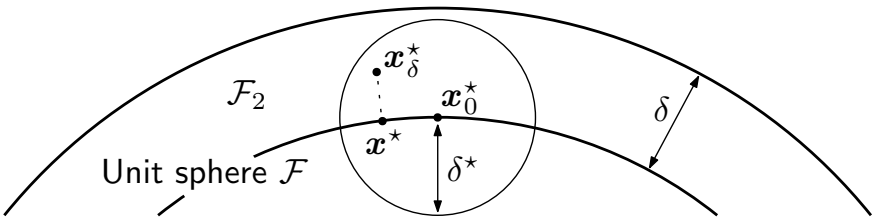

Figure 7.5: Visualization of $\mathcal{F}$ and $\mathcal{F}_2$ and the relationship between $\boldsymbol{x}^\star$, $\boldsymbol{x}^\star_0$, and $\boldsymbol{x}^\star_\delta$.

Consequently, for a sufficiently small δ, the following holds

$$\|\boldsymbol{x}^\star_0 - \boldsymbol{x}^\star\|_2 < \delta^\star \quad \Rightarrow \quad |f(\boldsymbol{x}^\star_0) - f(\boldsymbol{x}^\star)| < \epsilon^\star,$$

implying that $\boldsymbol{x}^\star$ converges to the solution of (7.9). Since C is independent of $\boldsymbol{x}$, the original optimization problem in (7.9) may be approximated with

$$\underset{\boldsymbol{x}\in\mathcal{F}_2}{\text{minimize}} \quad \frac{f_1(\boldsymbol{x})}{f_2(\boldsymbol{x})}. \tag{7.13}$$

7.3.3 Quadratically Constrained Fractional Quadratic Program Solution

The quadratically constrained fractional quadratic program was studied in [130]. Note that $\mathbf{A}_1$ ($\mathbf{A}'_1$) and $\mathbf{A}_2$ are symmetric and there are no conditions on their definiteness. In case $\mathbf{A}_n$ ($\mathbf{A}'_n$) is not symmetric, it can be replaced by $\frac{\mathbf{A}_n+\mathbf{A}_n^\mathsf{T}}{2}$ $\left(\frac{\mathbf{A}'_n+\mathbf{A}'^\mathsf{T}_n}{2}\right)$ without changing the problem. In (7.13), $\mathbf{A}_2 \succ 0$ ($\mathbf{A}'_2 \succ 0$), since it is a diagonal block of a positive definite matrix. The only assumption needed to solve (7.13) is that $f_2(\boldsymbol{x})$ is bounded below on $\mathcal{F}_2$ by a positive number γ. It can be seen from (7.5) and (7.7) that this assumption is trivially satisfied with $f_2(\boldsymbol{x}) \geq 1$. An iterative bisection algorithm for obtaining an ϵ-global optimal solution $\boldsymbol{x}^\star$ for the problem (7.13) was developed in [130], specifically

$$\alpha^\star \leq \frac{f_1(\boldsymbol{x}^\star)}{f_2(\boldsymbol{x}^\star)} \leq \alpha^\star + \epsilon,$$

where $\boldsymbol{x}^\star \in \mathcal{F}_2$, $\alpha^\star \triangleq \min\limits_{\boldsymbol{x}\in\mathcal{F}_2}\left\{\frac{f_1(\boldsymbol{x})}{f_2(\boldsymbol{x})}\right\}$, and ϵ is an arbitrarily small positive number. An upper and lower bound m and M, respectively, on $\min\limits_{\boldsymbol{x}\in\mathcal{F}_2}\left\{\frac{f_1(\boldsymbol{x})}{f_2(\boldsymbol{x})}\right\}$ must first be established. The following bounds may be established on f_1 and f_2

$$f_1(\boldsymbol{x}) = \begin{cases} \boldsymbol{u}^\mathsf{T}\mathbf{Q}\boldsymbol{u} \leq 0, \\ \boldsymbol{u}^\mathsf{T}\mathbf{Q}'\boldsymbol{u} \leq 0, \end{cases}, \quad f_2(\boldsymbol{x}) = 1 + \boldsymbol{u}^\mathsf{T}\mathbf{M}^{-1}\boldsymbol{u} \geq 1,$$

since $\mathbf{Q} \preceq 0$, $\mathbf{Q}' \preceq 0$, and $\mathbf{M}^{-1} \succ 0$. Subsequently, m and M may be chosen to be

$$M = 0, \qquad m \leq -\max_{\boldsymbol{x}\in\mathcal{F}_2} -f_1(\boldsymbol{x}) = \begin{cases} -\max\limits_{\boldsymbol{x}\in\mathcal{F}_2} -g_1(\boldsymbol{x}), \\ -\max\limits_{\boldsymbol{x}\in\mathcal{F}_2} -g_1'(\boldsymbol{x}), \end{cases}. \tag{7.14}$$

Noting that $\|\boldsymbol{h}_N\|_2^2 \leq h + \delta$, where $h = 2$ for pseudorange measurements and $h = 1$ for range measurements, the following inequality holds

$$0 \leq \|\boldsymbol{u}\|_2 \leq \mu_N\sqrt{h+\delta} + \frac{1}{\mu_N}\left\|\mathbf{H}_{N-1}^\mathsf{T}\boldsymbol{y}_N\right\|_2.$$

Therefore, m may be chosen to be

$$m = -\begin{cases} \left[\mu_N\sqrt{h+\delta} + \frac{1}{\mu_N}\left\|\mathbf{H}_{N-1}^\mathsf{T}\boldsymbol{y}_N\right\|_2\right]^2 \lambda_{\max}(-\mathbf{Q}), \\ \left[\mu_N\sqrt{h+\delta} + \frac{1}{\mu_N}\left\|\mathbf{H}_{N-1}^\mathsf{T}\boldsymbol{y}_N\right\|_2\right]^2 \lambda_{\max}(-\mathbf{Q}'). \end{cases} \tag{7.15}$$

where $\lambda_{\max}(\cdot)$ denotes the largest eigenvalue.

The following equivalency was shown in [132]

$$\min_{\boldsymbol{x}\in\mathcal{F}_2}\left\{\frac{f_1(\boldsymbol{x})}{f_2(\boldsymbol{x})}\right\} \leq \alpha \quad \Leftrightarrow \quad \min_{\boldsymbol{x}\in\mathcal{F}_2}\{f_1(\boldsymbol{x}) - \alpha f_2(\boldsymbol{x})\} \leq 0.$$

This equivalency enables (7.13) to be solved using a bisection algorithm, which is summarized in Algorithm 1.

Algorithm 1 DOP Minimization

Given: m, M (cf. (7.14) and (7.15)), and ϵ,
Initialization: $l_0 = m, \qquad u_0 = M,$
$\Delta_{ul} = 1 + \epsilon,$
while $\Delta_{ul} > \epsilon,\ k \geq 1,$ **do**
    $\alpha_k = \frac{l_{k-1}+u_{k-1}}{2},$
    Solve $\underset{\boldsymbol{x}\in\mathcal{F}_2}{\text{minimize}} \quad \beta_k = f_1(\boldsymbol{x}) - \alpha_k f_2(\boldsymbol{x}),$
    if $\beta_k^\star \leq 0$ **then**
        $l_k \leftarrow l_{k-1}, \quad u_k \leftarrow \alpha_k,$
    else
        $l_k \leftarrow \alpha_k, \qquad u_k \leftarrow u_{k-1},$
    $\Delta_{ul} \leftarrow u_k - l_k,$
Return $\boldsymbol{x}^\star = \underset{\boldsymbol{x}\in\mathcal{F}_2}{\text{argmin}}\{f_1(\boldsymbol{x}) - u_k f_2(\boldsymbol{x})\}.$

Next, the algorithm for minimizing $f_1(\boldsymbol{x}) - \alpha f_2(\boldsymbol{x})$ is described. It can be seen that minimizing $f_1(\boldsymbol{x}) - \alpha f_2(\boldsymbol{x})$ is equivalent to minimizing $\boldsymbol{x}^\mathsf{T}\tilde{\mathbf{A}}\boldsymbol{x} - 2\tilde{\boldsymbol{b}}^\mathsf{T}\boldsymbol{x} + \tilde{c}$, where

$$\tilde{\mathbf{A}} \triangleq \mathbf{A}_1 - \alpha\mathbf{A}_2, \qquad \tilde{\boldsymbol{b}} \triangleq \boldsymbol{b}_1 - \alpha\boldsymbol{b}_2, \qquad \tilde{c} \triangleq c_1 - \alpha c_2.$$

In the case of minimizing $g'(\mathbf{P}_N)$, $\mathbf{A}_n$, $\boldsymbol{b}_n$, and c_n are replaced by $\mathbf{A}'_n$, $\boldsymbol{b}'_n$, and c'_n, respectively. Note that $\tilde{\mathbf{A}}$ is symmetric; therefore, it is diagonalizable with the following eigenvalue decomposition

$$\tilde{\mathbf{A}} = \mathbf{U}\boldsymbol{\Lambda}\mathbf{U}^\mathsf{T},$$

where $\mathbf{U}$ is orthonormal and $\boldsymbol{\Lambda}$ is a diagonal matrix whose diagonal elements are the eigenvalues of $\tilde{\mathbf{A}}$, denoted λ_i. The eigenvalues and eigenvectors of $\tilde{\mathbf{A}}$ are re-ordered such that $\lambda_1 \geq \lambda_2 \geq \lambda_3$. With the change of variable $\boldsymbol{x} \triangleq \mathbf{U}\boldsymbol{s}$ and defining $\boldsymbol{w} \triangleq \mathbf{U}^\mathsf{T}\boldsymbol{b} = [w_1, w_2, w_3]^\mathsf{T}$, the following optimization problems are equivalent

$$\underset{\boldsymbol{x}\in\mathcal{F}_2}{\text{minimize}}\, f_1(\boldsymbol{x}) - \alpha f_2(\boldsymbol{x}) \quad \Leftrightarrow \quad \underset{\boldsymbol{s}\in\mathcal{F}_2}{\text{minimize}}\ \boldsymbol{s}^\mathsf{T}\boldsymbol{\Lambda}\boldsymbol{s} - 2\,\boldsymbol{w}^\mathsf{T}\boldsymbol{s} + \tilde{c}. \tag{7.16}$$

The solution of (7.16) is given by $\boldsymbol{s}^\star = [s_1^\star, s_2^\star, s_3^\star]^\mathsf{T}$ [130], with

$$s_i^\star = \frac{w_i}{\lambda_i - \eta^\star - \xi^\star},$$

$$(\eta^\star, \xi^\star) = \begin{cases} (\bar{\eta}, 0)\,, & \text{if } \lambda_3 \leq 0 \\ (\bar{\eta}, 0)\,, & \text{if } \lambda_3 > 0 \text{ and } h(\bar{\eta}, 0) > h(0, \bar{\xi}) \\ \left(0, \bar{\xi}\right), & \text{otherwise,} \end{cases}$$

and $\bar{\eta}$ and $\bar{\xi}$ are the solutions to the optimization problems

$$\underset{\eta \leq \min\left\{\lambda_3^-, 0\right\}}{\text{maximize}} \; h\left(\eta, 0\right) \tag{7.17}$$

$$\underset{0 \leq \xi < \lambda_3}{\text{maximize}} \; h\left(0, \xi\right), \tag{7.18}$$

respectively, where λ_3^- is the left-hand limit of λ_3 and

$$h\left(\eta, \xi\right) \triangleq -\sum_{i=1}^{3} \frac{w_i^2}{\lambda_i - \eta - \xi} + (1+\delta)\eta + \xi + \tilde{c}.$$

The functions $h_1(\eta) \triangleq h(\eta, 0)$ and $h_2(\xi) \triangleq h(0, \xi)$ are called secular functions [132]. These functions are strictly concave for $\eta, \xi < \lambda_3$, making (7.17) and (7.18) convex optimization problems. Therefore, one may solve for $h_1'(\eta) \equiv 0$ ($h_2'(\xi) \equiv 0$) using iterative methods (e.g., Newton's method) and if $\bar{\eta} \geq 0$ $\left(\bar{\xi} \leq 0\right)$, set $\bar{\eta} \equiv 0$ $\left(\bar{\xi} \equiv 0\right)$. Finally, $\boldsymbol{x}_\delta^\star$ is obtained from $\boldsymbol{x}_\delta^\star = \mathbf{U}\boldsymbol{s}^\star$ and $\boldsymbol{x}^\star$ is obtained from (7.12).

7.4 Simulation Results

In this section, three sets of Monte Carlo (MC) simulations are performed to validate the proposed approach. In the first set, described in Subsection 7.4.1, the solution obtained

with the proposed algorithm is plotted against the global optimal solution obtained by exhaustively sweeping the entire feasible space, showing that the solution obtained with the proposed algorithm always converges to the global optimal solution. In the second set, described in Subsection 7.4.2, the solution obtained with the proposed algorithm is plotted against the solution obtained with a general purpose solver, showing that the proposed algorithm outperforms the general purpose solver. In the third set, described in Subsection 7.4.3, the solution obtained with the proposed algorithm is plotted against the solution of an existing method that aims at maximizing the area of the polygon formed by the endpoints of the unit LOS vectors pointing from the source to the sensor [1], showing the superiority of the proposed algorithm over the method in [1]. Moreover, the proposed algorithm is evaluated in the case of source localization and simulation results, provided in Subsection 7.4.5, show that the proposed algorithm always yields a lower WGDOP compared to the one obtained with a general purpose solver.

7.4.1 Proposed Algorithm versus Global Optimal Solution

In the first set of simulations, the two cost functions were evaluated for three cases: (1) the WGDOP, i.e., $\mathbf{T} = \mathbf{T}' = \mathbf{I}_{4\times4}$, (2) the WHDOP, i.e., $\mathbf{T} = \mathbf{T}' = [\mathbf{I}_{2\times2} \quad \mathbf{0}_{2\times2}]$, and (3) the WVDOP, i.e., $\mathbf{T} = \mathbf{T}' = \boldsymbol{e}_3^\mathsf{T}$. For each case, 10^4 MC runs were conducted for $N = 6$ and 8. The optimal solutions computed using the proposed approach, denoted $g(\boldsymbol{x}^\star)$ and $g'(\boldsymbol{x}^\star)$, were plotted against the global optimal solutions, denoted $g^\star(\mathbf{P}_N)$ and $g'^\star(\mathbf{P}_N)$, obtained by exhaustively sweeping the entire feasible set, respectively (see Figs. 7.6 and 7.7). The positions of the $N-1$ pre-deployed sensors were generated randomly by drawing $N-1$ elevation angles from $\mathcal{U}\left(-\frac{\pi}{2}, \frac{\pi}{2}\right)$ and $N-1$ azimuth angles from $\mathcal{U}\left(0, 2\pi\right)$, where $\mathcal{U}(a, b)$ denotes the uniform distribution with support over $[a, b]$. The measurement noise covariance $\mathbf{R}_N$ is also generated randomly at each iteration. It can be seen that the optimal solutions obtained by the proposed approach were identical to the optimal solution obtained

by exhaustively sweeping the feasible set. Note that the WVDOP results for $g'(\mathbf{P}_N)$ is not plotted since in the WVDOP problem, $g(\mathbf{P}_N) = g'(\mathbf{P}_N)$.

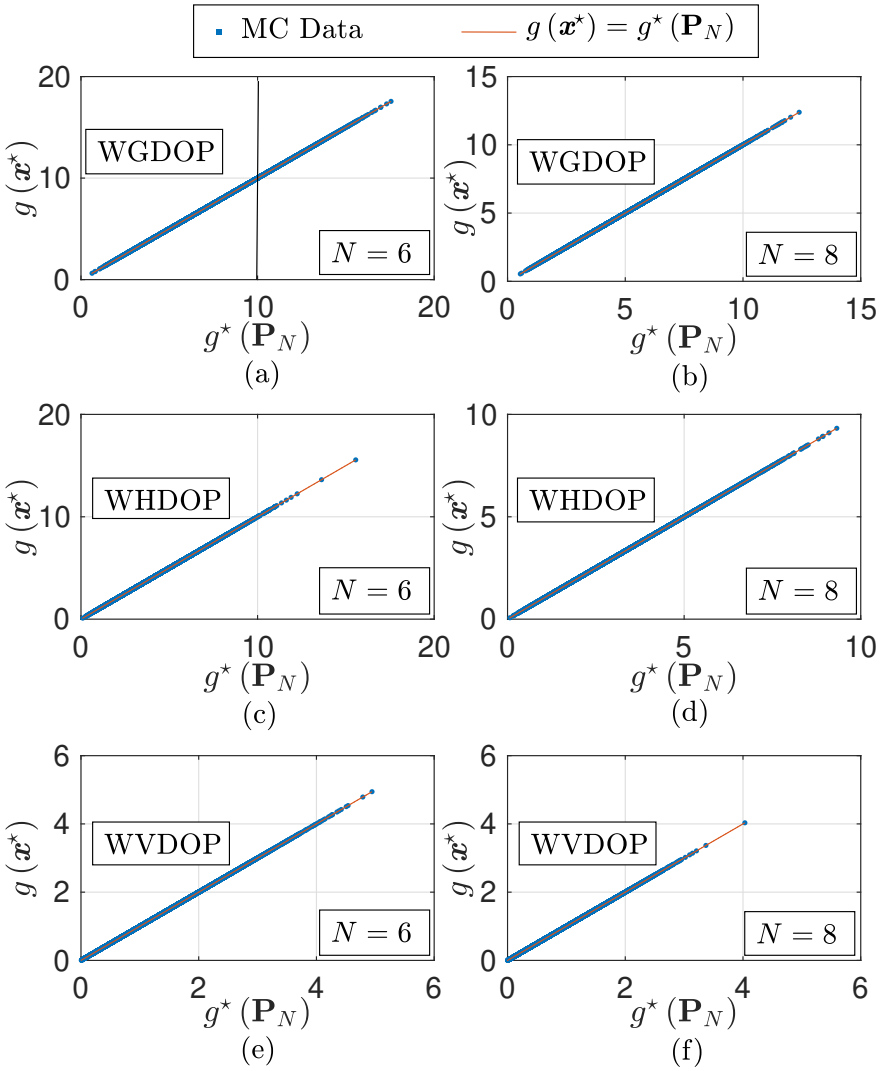

Figure 7.6: MC simulation results comparing the global optimal solution $g^\star(\mathbf{P}_N)$ obtained by exhaustively sweeping the feasible set versus the optimal solution $g(\boldsymbol{x}^\star)$ obtained with the proposed approach. Results corresponding to the WGDOP, WHDOP, and WVDOP problems are given for $N = 6$ and 8 sensors. MC points are overlayed over a line defined by $g(\boldsymbol{x}^\star) = g^\star(\mathbf{P}_N)$, showing a perfect match.

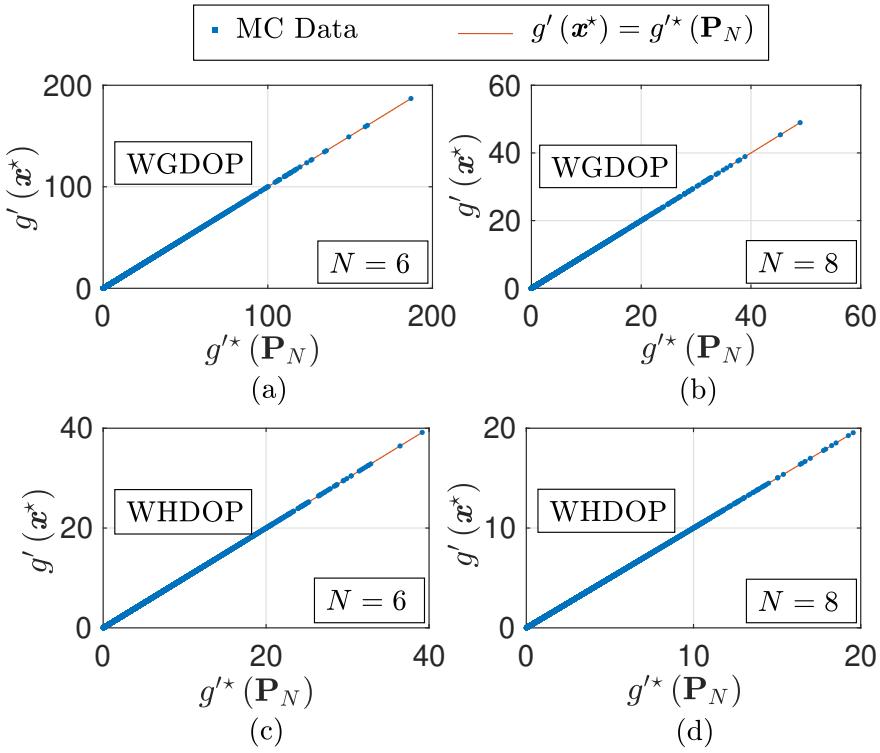

Figure 7.7: MC simulation results comparing the global optimal solution $g'^\star(\mathbf{P}_N)$ obtained by exhaustively sweeping the feasible set versus the optimal solution $g'(\boldsymbol{x}^\star)$ obtained with the proposed approach. Results corresponding to the WGDOP and WHDOP problems are given for $N = 6$ and 8 sensors. MC points are overlayed over a line defined by $g'(\boldsymbol{x}^\star) = g'^\star(\mathbf{P}_N)$, showing a perfect match.

7.4.2 Proposed Algorithm versus Nonlinear Numerical Optimization Solver Solution

In this second set of simulations, the two cost functions were evaluated for the same three cases. For each case, 10^4 MC runs were conducted for $N = 6$ and 8. The optimal solutions computed using the proposed approach was plotted against the global optimal solutions denoted $g^\star_{\texttt{fmincon}}(\mathbf{P}_N)$ and $g'^\star_{\texttt{fmincon}}(\mathbf{P}_N)$ obtained by using MATLAB's nonlinear numerical optimization solver `fmincon` (see Figs. 7.8 and 7.9). The MATLAB solver was initialized randomly. The position of the $N-1$ pre-deployed sensors and the measurement noise covariance $\mathbf{R}_N$ were generated the same way as in the first set of simulations. It can be seen that all MC simulation points lie either on or below the $g(\boldsymbol{x}^\star) = g^\star_{\texttt{fmincon}}(\mathbf{P}_N)$ and $g'(\boldsymbol{x}^\star) = g'^\star_{\texttt{fmincon}}(\mathbf{P}_N)$

lines, indicating that $g(\boldsymbol{x}^\star) \leq g^\star_{\texttt{fmincon}}(\mathbf{P}_N)$ and $g'(\boldsymbol{x}^\star) \leq g'^\star_{\texttt{fmincon}}(\mathbf{P}_N)$ for all MC runs. The proposed method outperforms MATLAB's `fmincon`, since `fmincon` may converge to a local minimum instead of the global minimum. Note that `fmincon` could be configured to employ one of four numerical algorithms (for the given constraints): `interior-point` (default), `sqp` (sequential quadratic program), `sqp-legacy`, and `active-set`. It was found that all four algorithms yielded $g(\boldsymbol{x}^\star) \leq g^\star_{\texttt{fmincon}}(\mathbf{P}_N)$ and $g'(\boldsymbol{x}^\star) \leq g'^\star_{\texttt{fmincon}}(\mathbf{P}_N)$ for all MC runs.

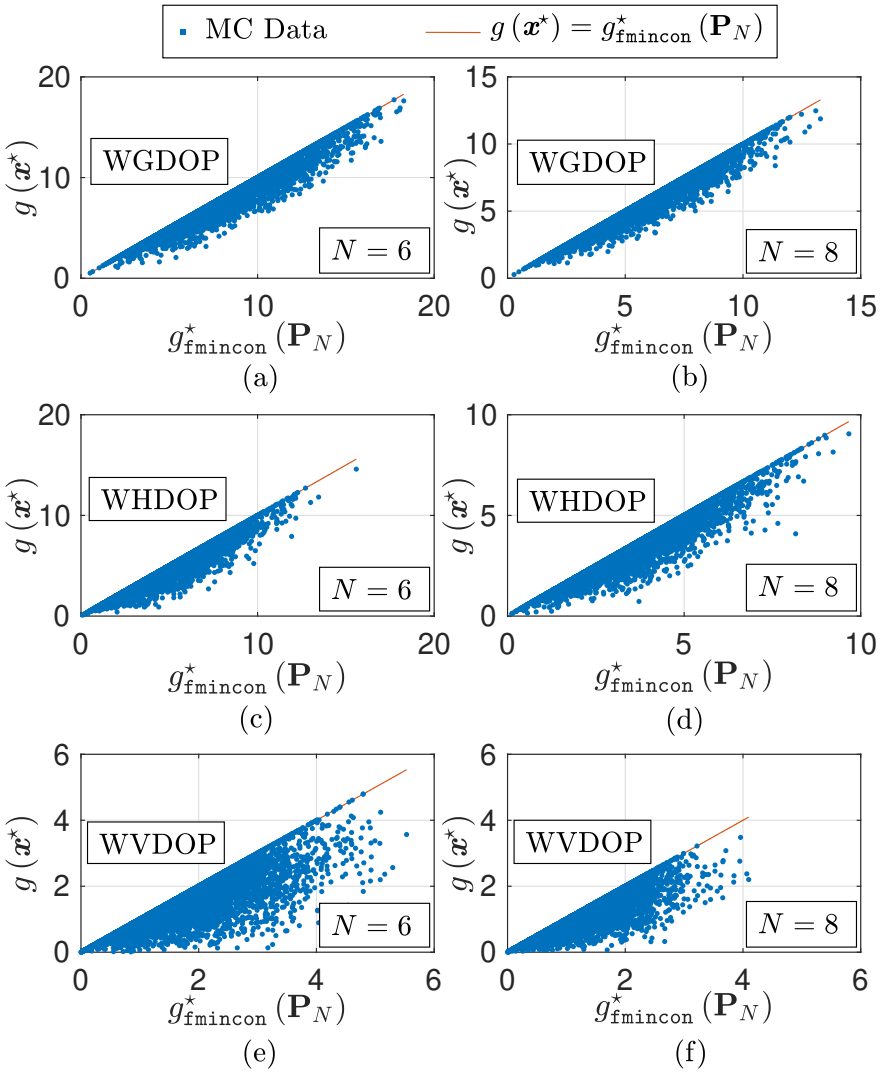

Figure 7.8: MC simulation results comparing the optimal solution $g^\star_{\texttt{fmincon}}(\mathbf{P}_N)$ obtained using MATLAB's `fmincon` versus the optimal solution $g(\boldsymbol{x}^\star)$ obtained with the proposed approach. Results corresponding to the WGDOP, WHDOP, and WVDOP problems are given for $N = 6$ and 8 sensors. MC points are overlayed over or lie beneath a line defined by $g(\boldsymbol{x}^\star) = g^\star_{\texttt{fmincon}}(\mathbf{P}_N)$, showing that $g(\boldsymbol{x}^\star) \leq g^\star_{\texttt{fmincon}}(\mathbf{P}_N)$.

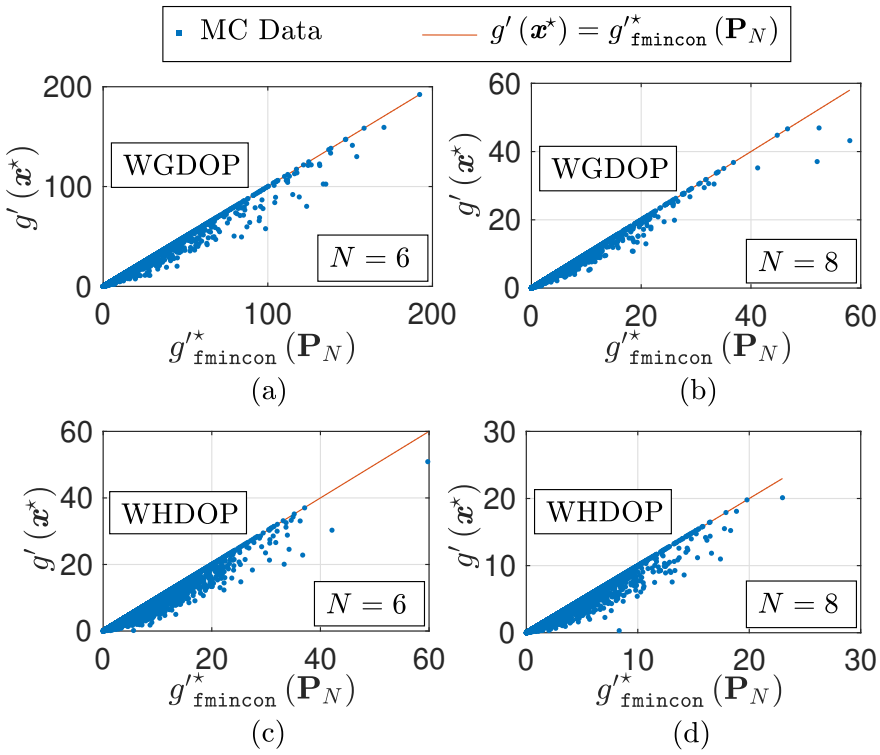

Figure 7.9: MC simulation results comparing the optimal solution $g'^\star_{\texttt{fmincon}}(\mathbf{P}_N)$ obtained using MATLAB's `fmincon` versus the optimal solution $g'(\boldsymbol{x}^\star)$ obtained with the proposed approach. Results corresponding to the WGDOP and WHDOP problems are given for $N = 6$ and 8 sensors. MC points are overlayed over or lie beneath a line defined by $g'(\boldsymbol{x}^\star) = g'^\star_{\texttt{fmincon}}(\mathbf{P}_N)$, showing that $g'(\boldsymbol{x}^\star) \leq g'^\star_{\texttt{fmincon}}(\mathbf{P}_N)$.

7.4.3 Proposed Algorithm versus Area Maximization Solution

In this third set of simulations, the proposed method is compared with the method described in [1]. In [1], the authors propose to maximize the area of the polygon whose vertices are the endpoints of the unit LOS vectors pointing from the source to the sensors in a 2-D environment. Area maximization is intimately related to DOP minimization, yielding a solution that is close to the one obtained by DOP minimization. The area maximization's elegant solution is shown to be the bisector of the largest angle between consecutive sensors on the unit circle [1]. To compare against the area maximization criterion, the proposed algorithm is adapted to a 2-D environment, i.e., $\boldsymbol{r}_{r_j} = \left[x_{r_j}, y_{r_j}\right]^\mathsf{T}$ and $\boldsymbol{r}_s = [x_s, y_s]^\mathsf{T}$, and thus $\boldsymbol{x} = [\cos(\phi) \quad \sin(\phi)]^\mathsf{T}$. The cost function considered was $g(\boldsymbol{x})$ with $\mathbf{T} = \mathbf{I}_{3\times3}$ and $\mathbf{R}_N = \mathbf{I}_{N\times N}$. A total of 10^4 MC runs were conducted for $N = 4$ and 6. The optimal

solutions computed using the proposed approach were plotted against the global optimal solutions obtained using the method in [1] denoted $g^{\star}_{area}(\mathbf{P}_N)$ in Fig. 7.10. The position of the $N-1$ pre-deployed sensors were generated the same way as in the first two sets of simulations. It can be seen that all MC simulation points lie either on or below the $g(\boldsymbol{x}^{\star}) = g^{\star}_{area}(\mathbf{P}_N)$ lines, indicating that $g(\boldsymbol{x}^{\star}) \leq g^{\star}_{area}(\mathbf{P}_N)$ for all MC runs. It can also be seen that the proposed method outperforms the one proposed in [1].

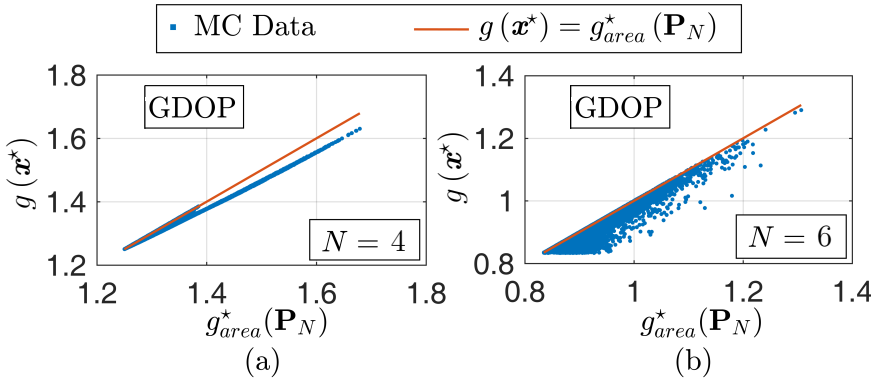

Figure 7.10: MC simulation results comparing the optimal solution $g^{\star}_{area}(\mathbf{P}_N)$ obtained using the method proposed in [1] versus the optimal solution $g(\boldsymbol{x}^{\star})$ obtained with the proposed approach. Results corresponding to the GDOP problems are given for (a) $N = 4$ and (b) $N = 6$ sensors. MC points are overlayed over or lie beneath a line defined by $g(\boldsymbol{x}^{\star}) = g^{\star}_{area}(\mathbf{P}_N)$, which shows that $g(\boldsymbol{x}^{\star}) \leq g^{\star}_{area}(\mathbf{P}_N)$.

7.4.4 Discussion

The simulation results presented in Subsections 7.4.1 and 7.4.2 reveal that while general-purpose nonlinear optimal solvers could converge to a local minimum, the proposed algorithm always converges to the global minimum, regardless of the configuration of the pre-deployed sensors (navigation sources) or the measurement noise covariance matrix. It is important to note that initialization affects the final solution in the general-purpose nonlinear numerical optimization solver. However, there is no way of knowing where the solver must be initialized to guarantee its convergence to the global optimal solution. This justifies why `fmincon` was initialized randomly on the unit sphere. In contrast, the proposed method does not

need any initialization and always converges to the global optimum. The simulation results presented in Subsection 7.4.3 reveal that although the area maximization problem is a good approximation of the DOP minimization problem, it does not yield a lower GDOP than the one obtained using the proposed method.

Next, the complexity of the proposed algorithm is analyzed. First, the complexity of obtaining the global minimum by exhaustively sweeping the feasible space is discussed. Consider a uniform gridding of the elevation and azimuth angles. Denote S to be the resulting number of discrete intervals in the elevation angle range. Since the azimuth angle range is twice as large as the elevation angle range, the resulting number of discrete intervals in the azimuth angle range will be $2S$. Therefore, there will be $2S^2$ feasible points to evaluate. However, the complexity of the proposed algorithm is independent of the gridding resolution. In [130], it is noted that the computationally expensive part of the proposed algorithm is computing the eigenvalues of $\tilde{\mathbf{A}}$, which has a complexity of $\mathcal{O}(n^3)$, where n is the size of the matrix. However, in the optimization problems addressed in this chapter, the size of $\tilde{\mathbf{A}}$ is always 3, which means that the cost of the proposed algorithm is constant; namely $\mathcal{O}(1)$ per iteration. Therefore, as S increases, the number of feasible solutions increases quadratically, whereas the complexity of the proposed algorithm remains constant. In the previous simulation results, ϵ was chosen to be $\epsilon \equiv 10^{-7}$. In order to obtain this resolution in the exhaustive sweeping approach, S must be greater than 6.28×10^7, which is impractically large. Note that both algorithms are comparable in memory allocation and do not require a lot of memory. The simulations were conducted on a desktop computer with an Intel i7 processor clocked at 3.6 GHz with 16 GB of RAM. For $S = 128$, the sweeping algorithm iteration took on average 0.185 seconds, while the proposed algorithm took 0.00183 seconds per iteration, which is approximately 200 times faster than the sweeping algorithm.

7.4.5 Application to Source Localization

In this section, the proposed algorithm is applied to source localization with a mobile agent. To this end, four sensors were pre-deployed randomly around an unknown source. The sensors are making pseudorange measurements to localize the unknown source. It is desired to deploy a mobile agent that chooses its next position so to minimize the WGDOP associated with localizing the source. The diagonal elements of the measurement noise covariance were set to $\{10, 11, 9, 8, 12\}$ and all the off-diagonal elements were set to 2. The measurements taken by the sensors and the moving agent are processed in a centralized, sequential manner. After each measurement taken by the sensors and the mobile agent, the prior $\mathbf{P}_0(k)$ is updated according to

$$\mathbf{P}_0^{-1}(k+1) = \mathbf{P}_0^{-1}(k) + \mathbf{H}_N^{\mathsf{T}}(k)\mathbf{R}_N^{-1}\mathbf{H}_N(k),$$

where k is the time-step index and $\mathbf{H}_N(k)$ is the measurement Jacobian evaluated at the sensors' fixed positions and the mobile agent's current position. The mobile agent's optimal position was determined for 10 successive time-steps using the proposed algorithm as well as MATLAB's `fmincon` for comparison purposes. The simulation results are shown in Fig. 7.11, from which it can be seen that the proposed method outperforms `fmincon`. It is important to note that this method can also be applied to the case of a mobile source or to the case where the sensors are making range measurements to a mobile target.

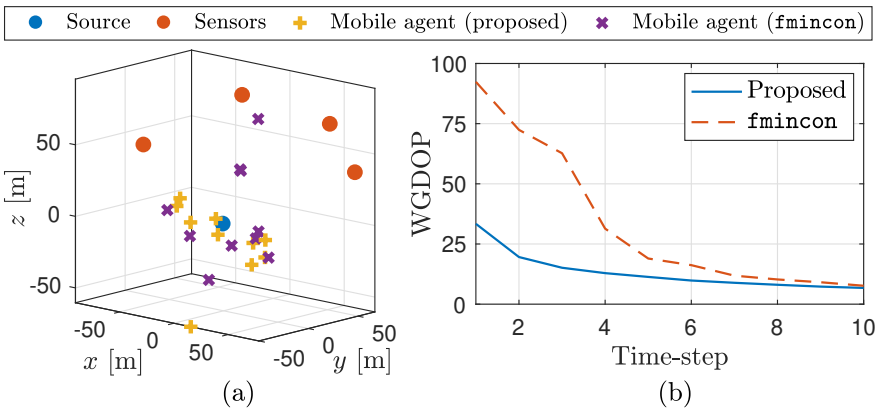

Figure 7.11: Simulation results demonstrating the application of the proposed algorithm to source localization. (a): Four sensors are pre-deployed around a source and are making pseudorange measurements to localize it. A mobile agent is then deployed to minimize the WGDOP for 10 consecutive time-steps. (b): WGDOP results for the proposed algorithm and MATLAB's `fmincon`.

Chapter 8

Performance Evaluation of TOA Positioning in Asynchronous 4G and 5G Networks: A Stochastic Geometry Approach

This chapter is organized as follows. Section 8.1 describes the TOA measurement model. Section 8.2 presents the positioning cases, characterizes their corresponding SPEBs, and establishes relationships between the SPEBs. Section 8.3 provides numerical simulation results evaluating the cumulative density function (cdf) of the SPEBs and validating the established relationships. The notation in this chapter is independent from the one used in previous chapters.

Notation: In the rest of the paper, lower-case bold variables (e.g., $\boldsymbol{x}$) indicate column vectors and upper-case bold variables (e.g., $\mathbf{X}$) indicate matrices. The matrix $\mathbf{I}_N$ indicates the $N \times N$ identity matrix. The vector $\mathbf{1}_N$ indicates an $N \times 1$ vector of ones. Let $\text{diag}\left[x_1, \ldots, x_N\right]$ denote

the diagonal matrix whose elements are $x_1, \ldots, x_N$.

8.1 System Model

In the following, let $\boldsymbol{p}_{\mathrm{UE}} \triangleq [x_{\mathrm{UE}}, y_{\mathrm{UE}}]^{\mathsf{T}}$ denote the UE's two-dimensional (2–D) position and $\boldsymbol{p}_{\mathrm{BS}_n} \triangleq [x_{\mathrm{BS}_n}, y_{\mathrm{BS}_n}]^{\mathsf{T}}$ denote the n-th BS's 2–D position, where $n = 1, \ldots, N$, and N is the total number of available BSs. The TOA measurement made by the UE on the n-th BS, expressed in meters, can be parameterized as

$$z_n = d_n + c \cdot [\delta t_{\mathrm{UE}} - \delta t_{\mathrm{BS}_n}] + v_n, \tag{8.1}$$

where $d_n \triangleq \|\boldsymbol{p}_{\mathrm{UE}} - \boldsymbol{p}_{\mathrm{BS}_n}\|$, δt_{UE} and δt_{BS_n} are the UE's and the n-th BS's clock biases, respectively, and v_n is the measurement noise, which is modeled as a zero-mean Gaussian random variable with variance σ_n^2. Several models of σ_n^2 as a function of the signal-to-noise ratio, distance, bearing angle, signal bandwidth, etc. were established [133]. The measurement noise variance also accounts for errors due to multipath propagation. In 5G applications, where the transmission bandwidths are sufficiently large, it is assumed that the first path, i.e., the direct path (DP), does not overlap with other multipath components. In this case, the DP is resolvable and the multipath signal boils down to a signal that is composed of the DP only for positioning, thereby attaining its maximum accuracy. Therefore, assuming limited interference between BSs, σ_n^2 is modeled as

$$\sigma_n^2 = \frac{c^2}{8\pi^2\beta^2} \left(\frac{d_n}{d_{\min}}\right)^{\alpha} \frac{1}{S/N_0},$$

where β is the effective signal bandwidth, α is the path-loss exponent, S is the transmitted signal power, and N_0 is the power spectral density of the additive white Gaussian channel noise [81]. Moreover, it is assumed that $\delta t_{\mathrm{UE}} \sim \mathcal{N}\left(0, \sigma_{\delta t_{\mathrm{UE}}}^2\right)$, $\delta t_{\mathrm{BS}_n} \sim \mathcal{N}\left(0, \sigma_{\delta t_{\mathrm{BS}}}^2\right)$, and v_n

and v_m are uncorrelated for $n \neq m$. Equation (8.1) can be written in vector form as

$$\boldsymbol{z}_N = \boldsymbol{d}_N + c\delta t_{\mathrm{UE}}\mathbf{1}_N - c\boldsymbol{\delta} t_{\mathrm{BS}_N} + \boldsymbol{v}_N,$$

$$\begin{aligned} \boldsymbol{z}_N &\triangleq [z_1, \ldots, z_N]^{\mathsf{T}}, & \boldsymbol{d}_N &\triangleq [d_1, \ldots, d_N]^{\mathsf{T}}, \\ \boldsymbol{\delta} t_{\mathrm{BS}_N} &\triangleq [\delta t_{\mathrm{BS}_1}, \ldots, \delta t_{\mathrm{BS}_N}]^{\mathsf{T}}, & \boldsymbol{v}_N &\triangleq [v_1, \ldots, v_N]^{\mathsf{T}}. \end{aligned}$$

Furthermore, define the following quantities

$$\begin{aligned} \boldsymbol{\Sigma}_v &\triangleq \mathrm{cov}\left[\boldsymbol{v}_N\right] = \mathrm{diag}\left[\sigma_1^2, \ldots, \sigma_N^2\right], \\ \boldsymbol{\Sigma}_{\delta t_{\mathrm{BS}}} &\triangleq \mathrm{cov}\left[\boldsymbol{\delta} t_{\mathrm{BS}_N}\right] = \sigma_{\delta t_{\mathrm{BS}}}^2 \mathbf{I}_N, \quad \boldsymbol{\Sigma}_{\delta t_{\mathrm{UE}}} \triangleq \sigma_{\delta t_{\mathrm{UE}}}^2 \mathbf{1}_N \mathbf{1}_N^{\mathsf{T}}. \end{aligned}$$

8.2 UE Positioning Cases and SPEB Characterization

This section analyzes three positioning cases and the SPEB is formulated for each case.

8.2.1 UE Positioning Cases

Consider the following three cases with different UE prior knowledge about its clock bias statistics:

Case I: The UE is estimating its position only and knows the statistics of its own and the BSs' clock biases. Hence, the parameter $\boldsymbol{\theta}_I$ associated with this case and the resulting likelihood function $p_I(\boldsymbol{z}; \boldsymbol{\theta}_I)$ are defined as

$$\boldsymbol{\theta}_I \triangleq \boldsymbol{p}_{\mathrm{UE}}, \quad p_I(\boldsymbol{z}; \boldsymbol{\theta}_I) = \mathcal{N}\left(\boldsymbol{z}; \boldsymbol{d}, \boldsymbol{\Sigma}_I\right), \tag{8.2}$$

where $\mathbf{\Sigma}_I \triangleq \mathbf{\Sigma}_v + c^2\mathbf{\Sigma}_{\delta t_{\mathrm{BS}}} + c^2\mathbf{\Sigma}_{\delta t_{\mathrm{UE}}}$.

Case II: The UE is estimating its position and clock bias and knows the statistics of the BSs' clock biases only. Hence, the parameter $\boldsymbol{\theta}_{II}$ associated with this case and the resulting likelihood function $p_{II}(\boldsymbol{z};\boldsymbol{\theta}_{II})$ are defined as

$$\boldsymbol{\theta}_{II} \triangleq \left[\boldsymbol{p}_{\mathrm{UE}}^{\mathsf{T}}, \delta t_{\mathrm{UE}}\right]^{\mathsf{T}},\ p_{II}(\boldsymbol{z};\boldsymbol{\theta}_{II}) = \mathcal{N}\left(\boldsymbol{z};\boldsymbol{\rho},\mathbf{\Sigma}_{II}\right), \tag{8.3}$$

where $\boldsymbol{\rho} \triangleq \boldsymbol{d} + c\delta t_{\mathrm{UE}}\mathbf{1}_N$ and $\mathbf{\Sigma}_{II} \triangleq \mathbf{\Sigma}_v + c^2\mathbf{\Sigma}_{\delta t_{\mathrm{BS}}}$.

Case III: The UE is estimating its position only, knows the statistics of the BSs' clock biases, and assumes the UE is synchronized with the system, i.e., δt_{UE} is assumed to be zero, which is not necessarily true. Hence, the parameter $\boldsymbol{\theta}_{III}$ associated with this case and the resulting likelihood function $p_{III}(\boldsymbol{z};\boldsymbol{\theta}_{III})$ are defined similarly to Case I as

$$\boldsymbol{\theta}_{III} \triangleq \boldsymbol{\theta}_I, \quad p_{III}(\boldsymbol{z};\boldsymbol{\theta}_{III}) = p_I(\boldsymbol{z};\boldsymbol{\theta}_I). \tag{8.4}$$

Remark 1. *The main difference between Case I and Case III is that the UE assumes its bias is zero; hence, the CRLB of Case I cannot be achieved in Case III. This assumption is often made in the TOA localization literature and the goal of this paper is to show the drastic effect of this assumption. To study Case III, an estimator that achieves the CRLB in the absence of UE clock bias, i.e., Case I with $\sigma^2_{\delta t_{\mathrm{UE}}} = 0$, is applied and its MSE is studied.*

8.2.2 SPEB General Definition

The position MSE of any estimator will be lower-bounded according to MSE $\geq$ SPEB. In this paper, maximum likelihood estimators (MLEs) are used to estimate the UE position and/or clock bias from TOA measurements. Such MLEs will closely approach the CRLB, with small differences due to linearization errors. For estimators that achieve the CRLB, the

position MSE becomes the SPEB; hence the choice of SPEB as a performance metric to be studied. It is important to note that the purpose of this paper is not to obtain an analytical expression of the distribution of the SPEB, but explicitly express the SPEB as a function of random variables whose distributions are known and have been validated (e.g., bearing angles and distances between the UE and BSs). In addition to the fact that obtaining analytical expressions is intractable, such analysis would require a rigorous treatment that cannot fit into this letter. Instead, this work aims to characterize through Monte Carlo simulations the SPEB of the three different aforementioned cases and to draw key observations. Moreover, this paper aims to compare analytically the SPEBs of each cases in a deterministic sense, i.e., for a given BPP realization. The SPEB for each case is defined as

$$\text{SPEB} \triangleq \text{trace}\left\{\left[\left(\mathcal{I}(\boldsymbol{\theta})\right)^{-1}\right]_{2\times 2}\right\},$$

where $\mathcal{I}(\boldsymbol{\theta})$ is the Fisher information matrix (FIM) of parameter $\boldsymbol{\theta}$ and $[\mathbf{A}]_{2\times 2}$ indicates the upper 2×2 diagonal block of matrix $\mathbf{A}$. In the case of the FIM, this block corresponds to the two position parameters.

SPEB for Case I

From $p_I(\boldsymbol{z}; \boldsymbol{\theta}_I)$, the FIM for Case I can be shown to be

$$\mathcal{I}(\boldsymbol{\theta}_I) = \mathbf{G}^{\mathsf{T}}\Sigma_I^{-1}\mathbf{G}, \quad \mathbf{G} \triangleq \begin{bmatrix} \cos\phi_1, \ldots, \cos\phi_N \\ \sin\phi_1, \ldots, \sin\phi_N \end{bmatrix}^{\mathsf{T}},$$

where ϕ_n is the n-th BS's bearing angle, and the SPEB is given by

$$\text{SPEB}_I = \text{trace}\left[\left(\mathbf{G}^{\mathsf{T}}\boldsymbol{\Sigma}_I^{-1}\mathbf{G}\right)^{-1}\right].$$

It is worth mentioning that SPEB_I is achievable. A weighted nonlinear least-squares (WNLS) estimator with weighting matrix $\boldsymbol{\Sigma}_I^{-1}$, which is the MLE of $\boldsymbol{\theta}_I$, can achieve SPEB_I.

SPEB for Case II

From $p_{II}(\boldsymbol{z};\boldsymbol{\theta}_{II})$, the FIM for Case II can be shown to be

$$\mathcal{I}(\boldsymbol{\theta}_{II}) = \mathbf{H}^{\mathsf{T}}\Sigma_{II}^{-1}\mathbf{H}, \quad \mathbf{H} = [\mathbf{G}\ \mathbf{1}_N]\,.$$

Using block matrix inversion, the SPEB for Case II can be shown to be

$$\text{SPEB}_{II} = \text{trace}\left[\left(\mathbf{G}^{\mathsf{T}}\boldsymbol{\Psi}_{II}\mathbf{G}\right)^{-1}\right],$$

$$\boldsymbol{\Psi}_{II} = \boldsymbol{\Sigma}_{II}^{-1} - \frac{\boldsymbol{\Sigma}_{II}^{-1}\mathbf{1}_N\mathbf{1}_N^{\mathsf{T}}\boldsymbol{\Sigma}_{II}^{-1}}{\mathbf{1}_N^{\mathsf{T}}\boldsymbol{\Sigma}_{II}^{-1}\mathbf{1}_N}.$$

Similarly to Case I, a WNLS estimator with weighting matrix $\boldsymbol{\Sigma}_{II}^{-1}$ is the MLE of $\boldsymbol{\theta}_{II}$ and can achieve SPEB_{II}. Note that not knowing the statistics of δt_{UE} is equivalent to having a diffuse prior.

SPEB for Case III

The CRLB in Case III cannot be achieved because of the model mismatch. Therefore, instead of SPEB, the MSE of a WNLS with weighting matrix $\boldsymbol{\Sigma}_{II}^{-1}$ estimating the UE position is used to characterize Case III. This case arises when the estimator assumes full synchronization of the UE with the network. Instead of using MSE_{III}, the SPEB_{III} notation is abused in order to keep the notation consistent with SPEB_I and SPEB_{II}. Subsequently, SPEB_{III} can

be shown to be

$$\text{SPEB}_{III} = \text{trace}\left[\mathbf{K}\boldsymbol{\Sigma}_{III}\mathbf{K}^{\mathsf{T}}\right],$$

where $\mathbf{K} \triangleq \left(\mathbf{G}^{\mathsf{T}}\boldsymbol{\Sigma}_{II}^{-1}\mathbf{G}\right)^{-1}\mathbf{G}^{\mathsf{T}}\boldsymbol{\Sigma}_{II}^{-1}$ and $\boldsymbol{\Sigma}_{III} \triangleq \boldsymbol{\Sigma}_{I}$.

8.2.3 Performance Comparison

First, define SPEB_0 as the SPEB where there is no UE clock bias, which is the case often assumed in the literature. This SPEB can be expressed as

$$\text{SPEB}_0 = \text{trace}\left[\left(\mathbf{G}^{\mathsf{T}}\boldsymbol{\Sigma}_{II}^{-1}\mathbf{G}\right)^{-1}\right].$$

The following three lemmas establish relationships between the SPEB for each case and SPEB_0.

Lemma 8.2.1. *The SPEB for Case I can be expressed as*

$$\text{SPEB}_I = \text{SPEB}_0 + \frac{c^2\sigma^2_{\delta t_{\text{UE}}}}{1 + c^2\sigma^2_{\delta t_{\text{UE}}}\gamma^2}\kappa^2, \tag{8.5}$$

for some $\kappa^2 \geq 0$ and $\gamma^2 > 0$ that are a function of the BSs' positions.

Proof. Using the matrix inversion lemma, $\boldsymbol{\Sigma}_I^{-1}$ may be expressed as

$$\boldsymbol{\Psi}_I \triangleq \boldsymbol{\Sigma}_I^{-1} = \boldsymbol{\Sigma}_{II}^{-1} - \frac{c^2\sigma^2_{\delta t_{\text{UE}}}\boldsymbol{\Sigma}_{II}^{-1}\mathbf{1}_N\mathbf{1}_N^{\mathsf{T}}\boldsymbol{\Sigma}_{II}^{-1}}{1 + c^2\sigma^2_{\delta t_{\text{UE}}}\left(\mathbf{1}_N^{\mathsf{T}}\boldsymbol{\Sigma}_{II}^{-1}\mathbf{1}_N\right)}.$$

Using the matrix inversion lemma again, the following can be shown

$$\left(\mathbf{G}^{\mathsf{T}}\boldsymbol{\Sigma}_I^{-1}\mathbf{G}\right)^{-1} = \left(\mathbf{G}^{\mathsf{T}}\boldsymbol{\Sigma}_{II}^{-1}\mathbf{G}\right)^{-1} + \frac{\mathbf{K}\mathbf{1}_N\mathbf{1}_N^{\mathsf{T}}\mathbf{K}^{\mathsf{T}}}{\frac{1}{c^2\sigma^2_{\delta t_{\text{UE}}}} + \mathbf{1}_N^{\mathsf{T}}\boldsymbol{\Psi}_0\mathbf{1}_N}, \tag{8.6}$$

where $\mathbf{\Psi}_0 \triangleq \mathbf{\Sigma}_{II}^{-1} - \mathbf{\Sigma}_{II}^{-1}\mathbf{G}\left(\mathbf{G}^{\mathsf{T}}\mathbf{\Sigma}_{II}^{-1}\mathbf{G}\right)^{-1}\mathbf{G}^{\mathsf{T}}\mathbf{\Sigma}_{II}^{-1}$. The matrix $\mathbf{\Psi}_0$ may be expressed as

$$\mathbf{\Psi}_0 = \mathbf{\Sigma}_{II}^{-\frac{1}{2}}\mathbf{P}\mathbf{\Sigma}_{II}^{-\frac{1}{2}},$$

where $\mathbf{\Sigma}_{II}^{-\frac{1}{2}}$ is a square-root of $\mathbf{\Sigma}_{II}^{-1}$ and $\mathbf{P} \triangleq \mathbf{I}_N - \mathbf{\Sigma}_{II}^{-\frac{1}{2}}\mathbf{G}\left(\mathbf{G}^{\mathsf{T}}\mathbf{\Sigma}_{II}^{-1}\mathbf{G}\right)^{-1}\mathbf{G}^{\mathsf{T}}\mathbf{\Sigma}_{II}^{-\frac{1}{2}}$ is an idempotent orthogonal projection matrix, i.e., $\mathbf{PP} = \mathbf{P}$. Subsequently, the quadratic form $\mathbf{1}_N^{\mathsf{T}}\mathbf{\Psi}_0\mathbf{1}_N$ may be expressed as

$$\mathbf{1}_N^{\mathsf{T}}\mathbf{\Psi}_0\mathbf{1}_N = \mathbf{1}_N^{\mathsf{T}}\mathbf{\Sigma}_{II}^{-\frac{1}{2}}\mathbf{P}\mathbf{P}\mathbf{\Sigma}_{II}^{-\frac{1}{2}}\mathbf{1}_N = \left\|\mathbf{P}\mathbf{\Sigma}_{II}^{-\frac{1}{2}}\mathbf{1}_N\right\|^2 \triangleq \gamma^2.$$

It is important to note that although $\left\|\mathbf{P}\mathbf{\Sigma}_{II}^{-\frac{1}{2}}\mathbf{1}_N\right\|^2 \geq 0$, it is assumed for simplicity that the trivial case is never achieved; hence $\gamma^2 > 0$. Taking the trace of (8.6), using the linear and cyclic properties of the matrix trace, and defining $\kappa^2 \triangleq \|\mathbf{K}\mathbf{1}_N\|^2$, (8.5) is deduced. □

Lemma 8.2.2. *The SPEB for Case II does not depend on $\sigma^2_{\delta t_{\mathrm{UE}}}$ and can be expressed as*

$$\mathrm{SPEB}_{II} = \mathrm{SPEB}_0 + \frac{1}{\gamma^2}\kappa^2, \tag{8.7}$$

for $\gamma^2 > 0$.

Proof. The proof of Lemma 8.2.2 follows the same steps as in Lemma 8.2.1, for the same values of γ^2 and κ^2 defined earlier. □

It is important to note that since SPEB_{II} does not depend on $\sigma^2_{\delta t_{\mathrm{UE}}}$, accurate positioning is possible in Case II even when $\sigma^2_{\delta t_{\mathrm{UE}}}$ is very large.

Lemma 8.2.3. *The SPEB for Case III can be expressed as*

$$\mathrm{SPEB}_{III} = \mathrm{SPEB}_0 + c^2\sigma^2_{\delta t_{\mathrm{UE}}}\kappa^2. \tag{8.8}$$

Proof. The proof of Lemma 8.2.3 follows the same steps as in Lemma 8.2.1, for the same value of κ^2 defined earlier. □

The lemmas stated above expose the relationships between the SPEBs of each case. It can be seen that

$$\text{SPEB}_I \leq \text{SPEB}_{II}, \quad \text{SPEB}_I \leq \text{SPEB}_{III}.$$

At the limits of $c^2\sigma^2_{\delta t_{\text{UE}}}$, the following can be observed

$$\lim_{\sigma^2_{\delta t_{\text{UE}}} \to \infty} \text{SPEB}_I = \text{SPEB}_{II},$$

$$\lim_{\sigma^2_{\delta t_{\text{UE}}} \to 0} \text{SPEB}_I = \lim_{\sigma^2_{\delta t_{\text{UE}}} \to 0} \text{SPEB}_{III} = \text{SPEB}_0.$$

Recall that a WNLS estimator with weighting matrix $\mathbf{\Sigma}_I^{-1}$ closely approaches SPEB_I for Case I, with small differences due to linearization errors. This in turn means that the aforementioned WNLS estimator, although not explicitly formulated as such, is equivalent to a WNLS estimating the UE clock bias when $\sigma^2_{\delta t_{\text{UE}}}$ is very large. On the other hand, when $\sigma^2_{\delta t_{\text{UE}}}$ is zero, there will be a constant "loss of information" between Case I and Case II since in Case II, some information from the measurements are going to estimate a non-existing quantity.

Another interesting observation is that SPEB_{III} is not always greater than SPEB_{II}, and the sign of the inequality between SPEB_{III} and SPEB_{II} depends on the values of γ^2 and $\sigma^2_{\delta t_{\text{UE}}}$. This result is somewhat counter-intuitive: in some cases, ignoring the existence of the UE bias yields better performance than estimating it along with the UE position. This happens when $\frac{1}{\gamma^2} > c^2\sigma^2_{\delta t_{\text{UE}}}$. For example, for $N = 4$, $\{\phi_n\}_{n=1}^4 = \{10°, 175°, 250°, 330°\}$,

$\mathbf{\Sigma}_{II} = 4\mathbf{I}$, and $c^2\sigma^2_{\delta t_{\text{UE}}} = 16$, then $\frac{1}{\gamma^2} \approx 19.4 > 16$. This can be explained as the tradeoff between (i) losing information on the UE position from the TOA measurements when more parameters are being estimated and (ii) additional error in the measurement. In practice however, $c^2\sigma^2_{\delta t_{\text{UE}}} \gg \frac{1}{\gamma^2}$, hence SPEB_{II} will be practically lower than SPEB_{III}.

8.3 Numerical Analysis

This section presents the BS position model and Monte Carlo simulation results to numerically analyze the cdf of the SPEBs in an asynchronous cellular network. For each Monte Carlo simulation, 10^4 realizations of the SPEB are generated to calculate the cdf.

8.3.1 BS Position Model

The BS network is modeled as a BPP, where $N \geq 3$ BSs are independently and uniformly distributed over an annular region centered at the origin o, i.e., $\mathbb{B}_o(d_{\min}, d_{\max}) = \pi(d^2_{\max} - d^2_{\min})$ [76], where $d_{\min}$ is the minimum distance required for the far-field assumption to hold and $d_{\max}$ is the maximum distance for which ranging signals can be detected by the receiver (see Fig. 8.1(a) for $N = 15$). Such model has been proven to accurately describe the distribution of BSs in 4G networks [78]. The location of the n-th BS can be represented by (d_n, ϕ_n), as shown in Fig. 8.1(b).

8.3.2 Numerical Analysis Settings

The path-loss exponent was chosen to be $\alpha = 3.7$ to characterize the path-loss in deep urban and indoor environments. The number of BSs was varied between $5, 10, 15$, and 20. The Monte Carlo simulation parameters are shown in Table 8.1.

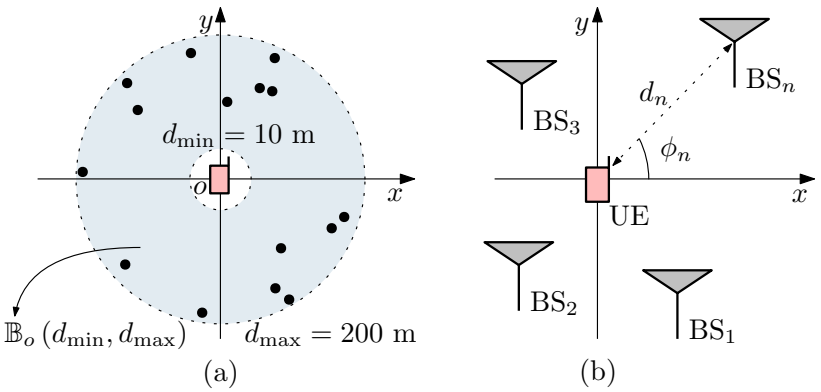

Figure 8.1: (a) BPP realization with $N = 15$. (b) Parametrization of the n-th BS position by its range d_n and bearing angle ϕ_n to the UE.

The 3GPP2 protocol requires BS clock biases to be bounded by $\epsilon \sim 3\mu$s [49]. Assuming the BS clock biases to be uniformly distributed between $-\epsilon$ and ϵ, a moment matching method can be used to approximate a Gaussian pdf for δt_{BS_n} in order to maintain the Gaussian assumption in the analysis, leading to the values in Table 8.1. The UE clock bias was chosen similarly. Although there are no synchronization requirements for the UE, UEs will get timing information from the servicing BS and synchronize to it. Therefore, reasonably small values of the UE clock bias are considered in the numerical analysis.

Table 8.1: Parameter values for Monte Carlo simulations

Parameter	**Value/Assumption**
Wireless network model	BPP
N (number of BSs)	5, 10, 15, 20
α (path-loss exponent)	3.7
S/N_0	60 dB
$d_{\min}$	10 m
$d_{\max}$	200 m
β (effective bandwidth)	100 MHz

8.3.3 Numerical Results

Numerical results are provided next for several simulation scenarios. Note that the cdf of the PEB $= \sqrt{\text{SPEB}}$ is provided for a more intuitive visualization.

Best Case Scenario: Perfectly Synchronized Network

The best case scenario is provided for comparison purposes. In this scenario, the UE and BS clock biases are assumed to be zero, i.e., perfectly synchronized UE-BS network. Note that in this scenario, Case I and Case III will perform similarly and Case II is expected to perform worse. The results for all cases shown in Fig. 8.2 for $N = 5, 10, 15$, and 20.

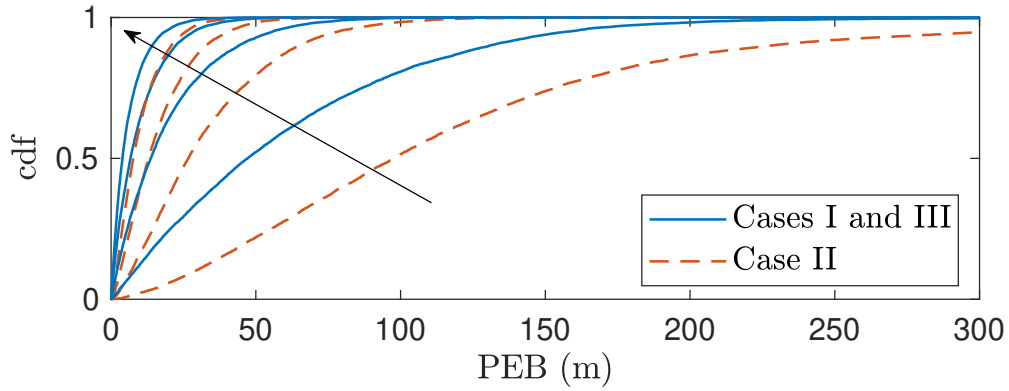

Figure 8.2: Cdf of $\text{PEB}_I = \text{PEB}_{III}$ and PEB_{II} in the absence of UE and BS clock biases for $N = 5, 10, 15$, and 20. The black arrow indicates the direction of change of the cdf as N increases.

Effect of BS Clock Biases

Next, the effect of BS clock biases is evaluated by setting $N = 15$ and $\sqrt{3}\sigma_{\delta t_{UE}} = 1\mu$s, and $\sigma_{\delta t_{BS}}$ was varied. The results are shown in Fig. 8.3.

The effect of BS clock bias can be seen by comparing Figs. 8.2 and 8.3: all the cdfs are shifted to the right. Moreover, Fig. 8.3 shows that as $\sigma_{\delta t_{BS}}$ decreases and $\sigma_{\delta t_{UE}}$ becomes

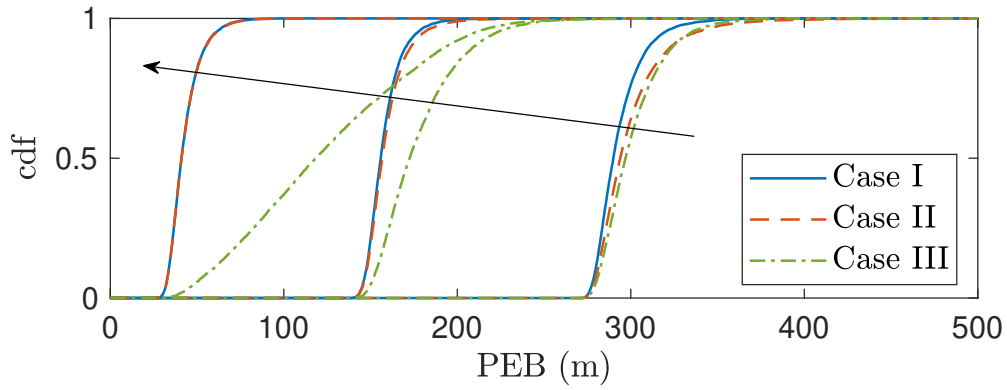

Figure 8.3: Cdf of PEB_I, PEB_{II} and PEB_{III} for $N = 15$, $\sqrt{3}\sigma_{\delta t_{UE}} = 1$ μs and $\sqrt{3}\sigma_{\delta t_{BS}} = 0.25, 1.5$, and 3 μs. The black arrow indicates the direction of change of the cdf as $\sigma_{\delta t_{BS}}$ decreases.

more dominant, Cases I and II still improve significantly but Case III almost saturates since the UE bias is taking over.

Effect of UE Clock Biases

Next, the effect of UE clock bias is evaluated by setting $N = 15$ and $\sqrt{3}\sigma_{\delta t_{BS}} = 0.25\mu$s, and $\sigma_{\delta t_{UE}}$ was varied. The results are shown in Fig. 8.4.

Fig. 8.4 shows how sensitive Case III is to the UE clock bias, while, as expected, the cdf of SPEB_{II} does not change with $\sigma_{\delta t_{UE}}$. When $\sigma_{\delta t_{UE}}$ becomes very small, Case I and Case III coincide, also as expected. The key takeaway from Fig. 8.4 is the importance of estimating the UE clock bias, even if some performance may be sacrificed. The difference between Case II and Case III (Case II performs better) is enormous for large values $\sigma_{\delta t_{UE}}$, while it is only very small (Case III performs better) when $\sigma_{\delta t_{UE}}$ is small.

Effect of Number of BSs

Next, the effect of N is evaluated. To this end, $\sqrt{3}\sigma_{\delta t_{BS}}$ was fixed to 0.25 μs, $\sqrt{3}\sigma_{\delta t_{UE}}$ to 1 μs, and N was varied. The results are shown in Fig. 8.5.

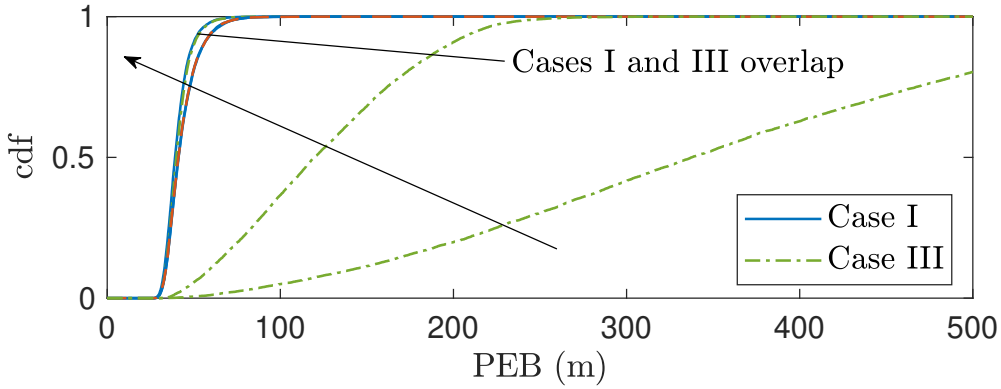

Figure 8.4: Cdf of PEB_I, PEB_{II} and PEB_{III} for $N = 15$, $\sqrt{3}\sigma_{\delta t_{BS}} = 0.25$ μs and $\sqrt{3}\sigma_{\delta t_{UE}} = 0.1, 1,$ and 3 μs. The black arrow indicates the direction of change of the cdf as $\sigma_{\delta t_{UE}}$ decreases.

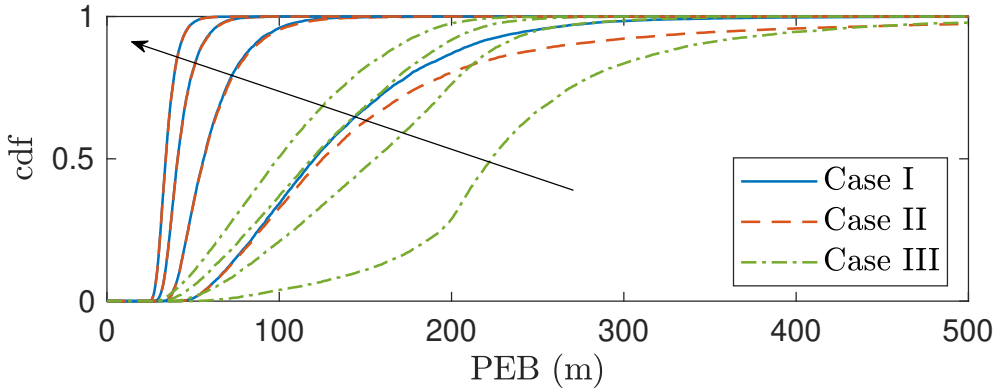

Figure 8.5: Cdf of PEB_I, PEB_{II} and PEB_{III} for $\sqrt{3}\sigma_{\delta t_{BS}} = 0.25$ μs, $\sqrt{3}\sigma_{\delta t_{UE}} = 1$ μs and $N = 5, 10, 15,$ and 20. The black arrow indicates the direction of change of the cdf as N increases.

Fig. 8.5 shows the intuitive result of the performance improving as N increases. It was noticed that the PEB is decreasing at a much slower rate than in the absence of biases, as can be seen by comparing Fig. 8.5 to Fig. 8.2. This reduction is due to the tradeoff that comes with adding more BSs: improvement in the UE-BS geometry at the cost of additional biases.

Chapter 9

Conclusions

This dissertation presented an SDR architecture for cellular CDMA-based navigation. Models of the cellular CDMA signals were first developed and optimal extraction of relevant positioning and timing information was discussed. Next, a description of the acquisition and tracking stages of a LabVIEW-based SDR was presented. The statistics of the pseudorange error of the proposed SDR in an additive white Gaussian channel were derived. Furthermore, the discrepancy between the clock biases observed by a receiver in two different sectors of the BTS cell was analyzed and modeled as a stochastic dynamic sequence. The consistency of the obtained model was experimentally analyzed in different locations, at different times, and for different cellular providers. Experimental results validating the pseudoranges produced by the proposed SDR were presented, in which the SDR's pseudoranges followed closely the true range between mobile UAV-mounted and car-mounted receivers and two cellular BTSs.

Next, a navigation a differential framework for navigating with pseudorange measurements from cellular SOPs was presented. Theoretical lower bounds on the navigation performance under errors due to the discrepancy between BTS sector clock biases were derived and analyzed. Moreover, a lower bound on the logarithm of the determinant of the estimation

error covariance was derived for non-identical measurement noise variances and a receiver–BTS configuration that achieves this bound was identified. A practical upper bound on the position error due to the discrepancy between sector clock biases was characterized. Experimental results showed an improvement of nearly 11 m in the RMSE when the discrepancy is accounted for utilizing the statistical model relating observed clock biases from different sectors of the same BTS cell.

For more precise navigation, a differential framework for navigation using carrier phase measurements from cellular SOPs was proposed. The proposed CD-cellular framework requires no prior knowledge of the receiver's position and achieves centimeter-level accuracy. MC simulations were presented to characterize the performance of the proposed framework as a function of the total number of hearable BTSs and the size of the batch estimator. A preliminary study of a CD-cellular network design in terms of number of bases needed, communication and synchronization requirements, and software and hardware considerations for real-time implementation was provided. Experimental results were presented demonstrating a UAV navigating with sub-meter-level accuracy exclusively using the proposed framework.

Next, a non-differential framework for navigating using carrier phase measurements from cellular SOPs that leverages the relative stability of quasi-synchronous cellular BTSs clocks was discussed. This stability also allows to parameterize the SOP clock biases by a common term plus some small deviations from the common term, which alleviates the need for a reference receiver. The clock deviations were subsequently modeled as a stochastic sequence using experimental data. Next, performance bounds were established for this framework. Experimental data show that a single UAV can navigate with sub-meter level accuracy for more than 5 minutes using this framework.

An EKF-based framework for navigation with carrier phase measurements from asynchronous cellular signals was then presented. It was shown that (i) this framework is observable and (ii) the EKF error state is asymptotically stable in a mean square sense and bounded with

probability one. A lower bound for the EKF's estimation error covariance was provided. MC simulations showed that this bound is not violated and studied the performance of the proposed framework for varying (i) number of BTSs, (ii) initial receiver speeds, and (iii) receiver clock qualities. Two sets of experimental results on two different UAVs showed that this framework can achieve meter-level accuracy.

In addition to navigation frameworks, a method for obtaining a global minimum for the DOP minimization problem was proposed. Two equivalent problems were formulated, where it was assumed that a receiver (navigation source) was to be added to a set of pre-deployed receivers (navigation sources) to optimally estimate the 3-D position and clock bias of a source or target. To deal with the nonconvexity of the problem, a method for obtaining the global minimum was presented by formulating the DOP minimization problem as a quadratically constrained fractional quadratic problem. Simulation results were provided validating the global optimality of the solution obtained from the proposed algorithm.

Finally, this dissertation evaluated the SPEB of UE positioning in asynchronous 4G and 5G networks for three cases: (i) the UE bias statistics are known and only the UE position is estimated, (ii) the UE bias statistics are unknown and UE clock bias is estimated along with its position, and (iii) the UE clock bias statistics are unknown and only the UE position is estimated. The SPEB for each case was derived and the cdf of the SPEB for each case was evaluated numerically using stochastic geometry models.

Appendices

A Derivation of Equation (3.22)

Using (3.20), the limit of $\log\det\left[\mathbf{P}^{\star}_{x,y}\right]$ can be expressed as

$$\begin{aligned}\lim_{k\to\infty}\log\det\left[\mathbf{P}^{\star}_{x,y}\right] &= \lim_{k\to\infty}\log\left[4\left(\sigma^2_{\text{eq}}\right)^2\right]\\ &= \log\left[4\left(\lim_{k\to\infty}\sigma^2_{\text{eq}}\right)^2\right],\end{aligned} \tag{A.1}$$

It follows from (3.21) that

$$\begin{aligned}\lim_{k\to\infty}\sigma^2_{\text{eq}} &= \frac{\left(\sigma^2_\eta+\frac{c^2\lambda^2}{\alpha}\right)\sigma^2_\eta}{N\sigma^2_\eta+(N-N_s)\frac{c^2\lambda^2}{\alpha}}\\ &= \frac{\left(1+\frac{\sigma^2_\eta}{\frac{c^2\lambda^2}{\alpha}}\right)\sigma^2_\eta}{N\frac{\sigma^2_\eta}{\frac{c^2\lambda^2}{\alpha}}+(N-N_s)}.\end{aligned} \tag{A.2}$$

Based on experimental data [85], $\sigma_\eta \approx 1$ to 2 m, $c\lambda \approx 0.4$ to 4 m, and $\alpha \approx 10^{-4}$ to 10^{-3} Hz. Therefore, the ratio $\frac{\sigma^2_\eta}{\frac{c^2\lambda^2}{\alpha}}$ is negligible, hence

$$\lim_{k\to\infty}\sigma^2_{\text{eq}} \approx \frac{\sigma^2_\eta}{N-N_s},$$

therefore (A.1) becomes

$$\lim_{k\to\infty} \log\det\left[\mathbf{P}^{\star}_{x,y}\right] \approx \log\left[4\left(\frac{\sigma_\eta^2}{N-N_s}\right)^2\right].$$

B Derivation of Equation (3.23)

Using (3.20), $\log\det\left[\mathbf{P}^{\star}_{x,y}\right]$ can be expressed as

$$\begin{aligned}\log\det\left[\mathbf{P}^{\star}_{x,y}\right] &= \log\left[4\left(\sigma_{\text{eq}}^2\right)^2\right] \\ &= \log(4) - 2\log\left(\frac{1}{\sigma_{\text{eq}}^2}\right), \end{aligned} \tag{B.3}$$

Noting that $\sigma_{\text{eq}}^2 = \frac{\sigma_\eta^2\left[\sigma_\eta^2+\sigma_\epsilon^2(k)\right]}{N_s\sigma_\eta^2+(N-N_s)\left[\sigma_\eta^2+\sigma_\epsilon^2(k)\right]}$, (B.3) becomes

$$\begin{aligned}\log\det\left[\mathbf{P}^{\star}_{x,y}\right] &= \log(4) - 2\log\left[\frac{N_s}{\sigma_\eta^2+\sigma_\epsilon^2(k)} + \frac{N}{\sigma_\eta^2} - \frac{N_s}{\sigma_\eta^2}\right] \\ &= \log(4) - 2\log\left\{\frac{N}{\sigma_\eta^2}\left[1-\frac{N_s}{N}\left(1-\frac{\sigma_\eta^2}{\sigma_\eta^2+\sigma_\epsilon^2(k)}\right)\right]\right\} \\ &= -2\log\left[1-\frac{N_s}{N}\left(1-\frac{\sigma_\eta^2}{\sigma_\eta^2+\sigma_\epsilon^2(k)}\right)\right] \\ &\quad + \underbrace{\log(4) - 2\log\left(\frac{N}{\sigma_\eta^2}\right)}_{\triangleq\ \xi\ \text{(constant)}}.\end{aligned}$$

For large k, the ratio $\frac{\sigma_\eta^2}{\sigma_\eta^2+\sigma_\epsilon^2(k)} = 1 - \frac{1}{1+\frac{\sigma_\eta^2}{\sigma_\epsilon^2(k)}}$ becomes negligible (see Appendix A), therefore

$$\log\det\left[\mathbf{P}^{\star}_{x,y}\right] \approx -2\log\left(1-\frac{N_s}{N}\right) + \xi.$$

C Derivation of Equation (3.25)

In this appendix, the expression for the optimal estimation error covariance for the batch estimator given in (3.25) is derived. From (3.24), $\bar{\sigma}_\epsilon^2(k)$ may be expressed as $\bar{\sigma}_\epsilon^2(k) = k\bar{\sigma}_\epsilon^2(1)$. Therefore, the elements of $\mathbf{R}_\epsilon$ can be approximated by $[\mathbf{R}_\epsilon]_{m,n} \approx \min\{m,n\}\,\bar{\sigma}_\epsilon^2(1)$, hence

$$\mathbf{R}_\epsilon \approx \bar{\sigma}_\epsilon^2(1)\mathbf{\Gamma}_K,$$

where $[\mathbf{\Gamma}_K]_{m,n} = \min\{m,n\}\,,\ m,n = 1,\ldots,K$. For the batch estimator, the sum $\sum_{l=1}^{L} N_l \mathbf{1}_K^\mathsf{T}\mathbf{R}_l^{-1}\mathbf{1}_K$ becomes

$$\begin{aligned}
\sum_{l=1}^{L} N_l \mathbf{1}_K^\mathsf{T}\mathbf{R}_l^{-1}\mathbf{1}_K &= N_s \mathbf{1}_K^\mathsf{T}\left(\sigma_\eta^2\mathbf{I}_{K\times K} + \mathbf{R}_\epsilon\right)^{-1}\mathbf{1}_K \\
&\quad + (N-N_s)\,\mathbf{1}_K^\mathsf{T}\left(\sigma_\eta^2\mathbf{I}_{K\times K}\right)^{-1}\mathbf{1}_K \\
&= N_s \mathbf{1}_K^\mathsf{T}\left(\sigma_\eta^2\mathbf{I}_{K\times K} + \bar{\sigma}_\epsilon^2(1)\mathbf{\Gamma}_K\right)^{-1}\mathbf{1}_K \\
&\quad + \frac{(N-N_s)\,K}{\sigma_\eta^2} \\
&= \frac{N_s}{\bar{\sigma}_\epsilon^2(1)}\mathbf{1}_K^\mathsf{T}\left(\frac{\sigma_\eta^2}{\bar{\sigma}_\epsilon^2(1)}\mathbf{I}_{K\times K} + \mathbf{\Gamma}_K\right)^{-1}\mathbf{1}_K \\
&\quad + \frac{(N-N_s)\,K}{\sigma_\eta^2}.
\end{aligned}$$

By defining $\beta \triangleq \frac{\sigma_\eta^2}{\bar{\sigma}_\epsilon^2(1)}$ and $\gamma(\beta,K) \triangleq \mathbf{1}_K^\mathsf{T}\left(\beta\mathbf{I}_{K\times K} + \mathbf{\Gamma}_K\right)^{-1}\mathbf{1}_K$, the above expression simplifies to

$$\sum_{l=1}^{L} N_l \mathbf{1}_K^\mathsf{T}\mathbf{R}_l^{-1}\mathbf{1}_K = \frac{N_s}{\bar{\sigma}_\epsilon^2(1)}\gamma(\beta,K) + \frac{(N-N_s)\,K}{\sigma_\eta^2}. \tag{C.4}$$

It can be shown that $\mathbf{\Gamma}_K = \mathbf{U}\mathbf{U}^\mathsf{T}$, where $\mathbf{U}$ is a lower triangular matrix with all its nonzero elements equal to one. Subsequently, using the matrix inversion lemma, $\gamma(\beta,K)$ can be

expressed as

$$\gamma(\beta, K) = \mathbf{1}_K^{\mathsf{T}} \left[\frac{1}{\beta}\mathbf{I} - \frac{1}{\beta^2}\mathbf{U}\left(\mathbf{I} + \frac{1}{\beta}\mathbf{U}^{\mathsf{T}}\mathbf{U}\right)^{-1}\mathbf{U}^{\mathsf{T}} \right] \mathbf{1}_K,$$

where the $K \times K$ subscript on the identity matrices is dropped for compactness of notation. The above expression may be expressed as

$$\gamma(\beta, K) = \frac{K}{\beta}\left[1 - \frac{1}{K\beta}\mathbf{1}_K^{\mathsf{T}}\mathbf{U}\left(\beta\mathbf{I} + \mathbf{U}^{\mathsf{T}}\mathbf{U}\right)^{-1}\mathbf{U}^{\mathsf{T}}\mathbf{1}_K\right].$$

A plot of $\gamma(\beta, K)$ as a function of K and β is shown in Fig. C.1 (a). It can be seen that for a given β, $\gamma(\beta, K)$ approaches a finite value for relatively large K. This function is defined as $f(\beta) = \gamma(\beta, K_0)$, where $K_0 > 10$, and is shown in Fig. C.1 (b). Note that $f(\beta)$ in Fig. C.1 (b) was obtained by evaluating $\gamma(\beta, K)$ at $K = 15$.

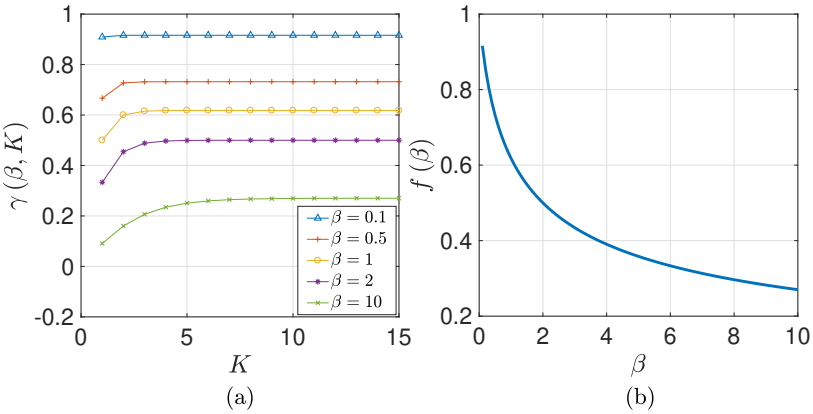

Figure C.1: Plot of (a) $\gamma(\beta, K)$ and (b) $f(\beta) = \gamma(\beta, K_0)$ where $K_0 > 10$.

For large K (greater than 10), (C.4) becomes

$$\sum_{l=1}^{L} N_l \mathbf{1}_K^{\mathsf{T}} \mathbf{R}_l^{-1} \mathbf{1}_K = \frac{N_s f(\beta)\sigma_\eta^2 + (N - N_s)\, K\bar{\sigma}_\epsilon^2(1)}{\bar{\sigma}_\epsilon^2(1)\sigma_\eta^2}. \tag{C.5}$$

It follows from the definition of $\mathbf{R}$ that

$$\sum_{l=1}^{L} N_l \mathbf{R}_l^{-1} = N_s \mathbf{R}_\epsilon^{-1} + \frac{(N - Ns)}{\sigma_\eta^2} \mathbf{I}_{K \times K}. \tag{C.6}$$

From (C.5)–(C.6) and (3.17) in Theorem 3.2, the estimation error covariance matrix with the minimum determinant is given by (3.25).

D Derivation of the Maximum Likelihood Estimate for EKF Initialization

This appendix derives $\hat{\boldsymbol{x}}_{\mathrm{ML_{ini}}}$ and $\mathbf{P}_{\mathrm{ML_{ini}}}$ used in the EKF initialization. For a sufficiently small T, the receiver velocity at $k = 1$ may be expressed as

$$\dot{\boldsymbol{r}}_r(1) = \frac{1}{T}\left[\boldsymbol{r}_r(1) - \boldsymbol{r}_r(0)\right], \tag{D.7}$$

and the n-th BTS's clock drift at $k = 1$ as

$$c\dot{\delta}t_n(1) \approx \frac{1}{T}\left[c\delta t_n(1) - c\delta t_n(0)\right]. \tag{D.8}$$

From (D.7) and (D.8), one may express $\boldsymbol{x}(0)$ as

$$\boldsymbol{x}(0) = \mathbf{F}^{-1}\boldsymbol{x}(1). \tag{D.9}$$

Using (6.2), (6.5), and (D.9), the following measurement equation is obtained

$$\boldsymbol{z}_{\mathrm{ini}} = \boldsymbol{h}_{\mathrm{ini}}\left[\boldsymbol{x}(1)\right] + \boldsymbol{v}_{\mathrm{ini}}, \tag{D.10}$$

where the vector-valued function $\boldsymbol{h}_{\mathrm{ini}}$ is given by

$$\boldsymbol{h}_{\mathrm{ini}}\left[\boldsymbol{x}(1)\right] = \begin{bmatrix} \boldsymbol{r}_r(1) \\ \boldsymbol{r}_r(1) - T\dot{\boldsymbol{r}}_r(1) \\ \boldsymbol{h}\left[\boldsymbol{x}(1)\right] \\ \boldsymbol{h}\left[\mathbf{F}^{-1}\boldsymbol{x}(1)\right] \end{bmatrix},$$

and the measurement noise vector is given

$$\boldsymbol{v}_{\text{ini}} = \left[\boldsymbol{v}_{\boldsymbol{r}_r}^{\mathsf{T}}(1),\ \boldsymbol{v}_{\boldsymbol{r}_r}^{\mathsf{T}}(0),\ \boldsymbol{v}^{\mathsf{T}}(1),\ \boldsymbol{v}^{\mathsf{T}}(0)\right]^{\mathsf{T}},$$

which is a zero-mean white Gaussian random vector with the block-diagonal covariance matrix

$$\boldsymbol{\Sigma}_{\text{ini}} = \text{diag}\left[\boldsymbol{\Sigma}_{\boldsymbol{r}_r}(1), \boldsymbol{\Sigma}_{\boldsymbol{r}_r}(0), \mathbf{R}(1), \mathbf{R}(0)\right].$$

The ML estimate of $\boldsymbol{x}(1)$ can be therefore obtained from (D.10) according to

$$\hat{\boldsymbol{x}}_{\text{ML}_{\text{ini}}} = \underset{\boldsymbol{x}(1)}{\text{argmax}}\ \Lambda\left[\boldsymbol{z}_{\text{ini}}; \boldsymbol{x}(1)\right], \tag{D.11}$$

where $\Lambda\left[\boldsymbol{z}_{\text{ini}}; \boldsymbol{x}(1)\right]$ is the likelihood function of $\boldsymbol{z}_{\text{ini}}$ parameterized by $\boldsymbol{x}(1)$, which is the multivariate Gaussian probability density function with zero-mean and covariance $\boldsymbol{\Sigma}_{\text{ini}}$. The maximization problem in (D.11) is equivalent to

$$\hat{\boldsymbol{x}}_{\text{ML}_{\text{ini}}} = \underset{\boldsymbol{x}(1)}{\text{argmin}} \left\{\boldsymbol{z}_{\text{ini}} - \boldsymbol{h}_{\text{ini}}[\boldsymbol{x}(1)]\right\}^{\mathsf{T}} \boldsymbol{\Sigma}_{\text{ini}}^{-1} \left\{\boldsymbol{z}_{\text{ini}} - \boldsymbol{h}_{\text{ini}}[\boldsymbol{x}(1)]\right\},$$

which can be solved using the Gauss-Newton method. It can be shown that

$$\begin{aligned}
\hat{\boldsymbol{x}}_{\text{ML}_{\text{ini}}} = \Big[& \hat{\boldsymbol{r}}_{r,\text{ML}_{\text{ini}}}^{\mathsf{T}},\ c\hat{\delta}t_{1,\text{ML}_{\text{ini}}},\ \ldots,\ c\hat{\delta}t_{N,\text{ML}_{\text{ini}}}, \\
& \hat{\dot{\boldsymbol{r}}}_{r,\text{ML}_{\text{ini}}}^{\mathsf{T}},\ c\hat{\dot{\delta}}t_{1,\text{ML}_{\text{ini}}},\ \ldots,\ c\hat{\dot{\delta}}t_{N,\text{ML}_{\text{ini}}} \Big]^{\mathsf{T}},
\end{aligned}$$

$$\hat{\boldsymbol{r}}_{r,\text{ML}_{\text{ini}}} = \boldsymbol{z}_{\boldsymbol{r}_r}(1), \tag{D.12}$$

$$\hat{\dot{\boldsymbol{r}}}_{r,\text{ML}_{\text{ini}}} = \frac{1}{T}\left[\boldsymbol{z}_{\boldsymbol{r}_r}(1) - \boldsymbol{z}_{\boldsymbol{r}_r}(0)\right], \tag{D.13}$$

$$c\hat{\delta}t_{n,\text{ML}_{\text{ini}}} = z_n(1) - d_{r,n}(1), \tag{D.14}$$

$$c\hat{\dot{\delta}}t_{n,\text{ML}_{\text{ini}}} = \frac{1}{T}\left[z_n(1) - z_n(0) + d_{r,n}(0) - d_{r,n}(1)\right], \tag{D.15}$$

with $d_{r,n}(j) \triangleq \|\boldsymbol{z}_{\boldsymbol{r}_r}(j) - \boldsymbol{r}_{s_n}\|$ for $j = 0, 1$. It can also be shown that the estimation error covariance associated with $\hat{\boldsymbol{x}}_{\mathrm{ML}_{\mathrm{ini}}}$ is given by

$$\mathbf{P}_{\mathrm{ML}_{\mathrm{ini}}} = \mathbf{A}_{\mathrm{ini}} \boldsymbol{\Sigma}_{\mathrm{ini}} \mathbf{A}_{\mathrm{ini}}^{\mathsf{T}}, \tag{D.16}$$

$$\mathbf{A}_{\mathrm{ini}} \triangleq \begin{bmatrix} \mathbf{I}_{2\times 2} & \mathbf{0}_{2\times 2} & \mathbf{0}_{2\times N} & \mathbf{0}_{2\times N} \\ -\boldsymbol{h}_{r,1}^{\mathsf{T}}(1) & \mathbf{0}_{1\times 2} & \boldsymbol{e}_{N,1}^{\mathsf{T}} & \mathbf{0}_{1\times N} \\ \vdots & \vdots & \vdots & \vdots \\ -\boldsymbol{h}_{r,N}^{\mathsf{T}}(1) & \mathbf{0}_{1\times 2} & \boldsymbol{e}_{N,N}^{\mathsf{T}} & \mathbf{0}_{1\times N} \\ \frac{1}{T}\mathbf{I}_{2\times 2} & -\frac{1}{T}\mathbf{I}_{2\times 2} & \mathbf{0}_{2\times N} & \mathbf{0}_{2\times N} \\ -\frac{1}{T}\boldsymbol{h}_{r,1}^{\mathsf{T}}(1) & \frac{1}{T}\boldsymbol{h}_{r,1}^{\mathsf{T}}(0) & \frac{1}{T}\boldsymbol{e}_{N,1}^{\mathsf{T}} & -\frac{1}{T}\boldsymbol{e}_{N,1}^{\mathsf{T}} \\ \vdots & \vdots & \vdots & \vdots \\ -\frac{1}{T}\boldsymbol{h}_{r,N}^{\mathsf{T}}(1) & \frac{1}{T}\boldsymbol{h}_{r,N}^{\mathsf{T}}(0) & \frac{1}{T}\boldsymbol{e}_{N,N}^{\mathsf{T}} & -\frac{1}{T}\boldsymbol{e}_{N,N}^{\mathsf{T}} \end{bmatrix},$$

with $\boldsymbol{h}_{r,n}(j) \triangleq \frac{\boldsymbol{z}_{\boldsymbol{r}_r}(j) - \boldsymbol{r}_{s_n}}{d_{r,n}(j)}$ for $j = 0, 1$, and $\boldsymbol{e}_{N,n} \in \mathbb{R}^N$ is the standard basis vector consisting of a one at the n-th element and zeros elsewhere.

E Derivation of the Upper Bounds in (6.6)

In this appendix, the estimation error covariance associated with the initial speed estimate $\hat{v}_{r_1} \triangleq \left\|\hat{\dot{\boldsymbol{r}}}_{r,\mathrm{ML}_{\mathrm{ini}}}\right\|$ and the initial velocity direction unit vector estimate $\hat{\boldsymbol{u}}_{r_1} \triangleq \frac{\hat{\dot{\boldsymbol{r}}}_{r,\mathrm{ML}_{\mathrm{ini}}}}{\left\|\hat{\dot{\boldsymbol{r}}}_{r,\mathrm{ML}_{\mathrm{ini}}}\right\|}$ are studied. Let $v_{r_1} \triangleq \|\dot{\boldsymbol{r}}_r(1)\|$ denote the true initial speed and $\boldsymbol{u}_{r_1} \triangleq \frac{\dot{\boldsymbol{r}}_r}{\|\dot{\boldsymbol{r}}_r\|}$ denote the true initial direction unit vector. Using first-order Taylor series expansion around $\dot{\boldsymbol{r}}_r(1)$, the initial speed estimate may be approximated with

$$\hat{v}_{r_1} \approx v_{r_1} - \boldsymbol{u}_{r_1}^{\mathsf{T}} \tilde{\dot{\boldsymbol{r}}}_{r,\mathrm{ini}}, \tag{E.17}$$

where $\tilde{\dot{\boldsymbol{r}}}_{r,\text{ini}} \triangleq \dot{\boldsymbol{r}}_r(1) - \hat{\dot{\boldsymbol{r}}}_{r,\text{ML}_\text{ini}}$. The initial speed estimation error can be calculated from (E.17) as

$$\tilde{v}_{r_1} \triangleq v_{r_1} - \hat{v}_{r_1} = \boldsymbol{u}_{r_1}^\mathsf{T} \tilde{\dot{\boldsymbol{r}}}_{r,\text{ini}},$$

and its associated estimation error variance may obtained according

$$\sigma_{v_{r_1}}^2 \triangleq \mathbb{E}\left[\tilde{v}_{r_1}^2\right] = \boldsymbol{u}_{r_1}^\mathsf{T} \mathbb{E}\left[\tilde{\dot{\boldsymbol{r}}}_{r,\text{ini}} \tilde{\dot{\boldsymbol{r}}}_{r,\text{ini}}^\mathsf{T}\right] \boldsymbol{u}_{r_1}.$$

It can be shown from (D.13) and (D.16) that

$$\mathbf{P}_{\dot{r},\text{ini}} \triangleq \mathbb{E}\left[\tilde{\dot{\boldsymbol{r}}}_{r,\text{ini}} \tilde{\dot{\boldsymbol{r}}}_{r,\text{ini}}^\mathsf{T}\right] = \frac{1}{T^2} \bar{\boldsymbol{\Sigma}}_{\boldsymbol{r}_r},$$

where $\bar{\boldsymbol{\Sigma}}_{\boldsymbol{r}_r} \triangleq \boldsymbol{\Sigma}_{\boldsymbol{r}_r}(0) + \boldsymbol{\Sigma}_{\boldsymbol{r}_r}(1)$. Since $\boldsymbol{u}_{r_1}$ is a unit vector, $\sigma_{v_{r_1}}^2$ may bounded according to

$$\sigma_{v_{r_1}}^2 \leq \frac{\lambda_{\max,\dot{r}}}{T^2}, \tag{E.18}$$

where $\lambda_{\max,\dot{r}}$ denotes the maximum eigenvalue of $\bar{\boldsymbol{\Sigma}}_{\boldsymbol{r}_r}$. Note that since $\bar{\boldsymbol{\Sigma}}_{\boldsymbol{r}_r}$ is positive definite, then $\lambda_{\max,\dot{r}}$ is a positive real number that only depends on $\bar{\boldsymbol{\Sigma}}_{\boldsymbol{r}_r}$.

Next, the estimation error covariance of $\hat{\boldsymbol{u}}_{r_1}$ is characterized. Using first-order Taylor series expansion around $\dot{\boldsymbol{r}}_r$, $\hat{\boldsymbol{u}}_{r_1}$ may be approximated with

$$\hat{\boldsymbol{u}}_{r_1} \approx \boldsymbol{u}_{r_1} - \boldsymbol{\Psi} \tilde{\dot{\boldsymbol{r}}}_{r,\text{ini}}, \tag{E.19}$$

where $\boldsymbol{\Psi} \triangleq \frac{1}{v_{r_1}} \left(\mathbf{I}_{2\times 2} - \boldsymbol{u}_{r_1} \boldsymbol{u}_{r_1}^\mathsf{T}\right)$. The initial direction unit vector estimation error can be calculated from (E.19) as

$$\tilde{\boldsymbol{u}}_{r_1} \triangleq \boldsymbol{u}_{r_1} - \hat{\boldsymbol{u}}_{r_1} = \boldsymbol{\Psi} \tilde{\dot{\boldsymbol{r}}}_{r,\text{ini}},$$

The matrix $\boldsymbol{\Psi}$ is an annihilator matrix; therefore, $\|\boldsymbol{\Psi}\| = 1$. The estimation error covariance associated with $\tilde{\boldsymbol{u}}_{r_1}$ is given by

$$\mathbf{P}_{\boldsymbol{u}_{r_1}} \triangleq \mathbb{E}\left[\tilde{\boldsymbol{u}}_{r_1}\tilde{\boldsymbol{u}}_{r_1}^{\mathsf{T}}\right] = \frac{1}{v_{r_1}^2}\boldsymbol{\Psi}\bar{\boldsymbol{\Sigma}}_{\boldsymbol{r}_r}\boldsymbol{\Psi}^{\mathsf{T}}. \tag{E.20}$$

Using (D.7) and (E.20), $\left\|\mathbf{P}_{\boldsymbol{u}_{r_1}}\right\|$ may be bounded according to

$$\sigma_{\boldsymbol{u}_{r_1}}^2 \triangleq \left\|\mathbf{P}_{\boldsymbol{u}_{r_1}}\right\| \leq \frac{\lambda_{\max,\dot{\boldsymbol{r}}}}{\left\|\boldsymbol{r}_r(1) - \boldsymbol{r}_r(0)\right\|^2}. \tag{E.21}$$

F Theoretical Background on Observability and EKF Estimation Error Bounds

This appendix provides relevant theoretical background on observability and EKF estimation error bounds.

F.1 Observability of Linear and Nonlinear Systems

Consider the discrete-time linear time-varying system

$$\boldsymbol{x}(k+1) = \mathbf{F}(k)\,\boldsymbol{x}(k) + \boldsymbol{\Gamma}(k)\,\boldsymbol{u}(k)\,, \tag{F.22}$$

$$\boldsymbol{y}(k) = \mathbf{H}(k)\,\boldsymbol{x}(k)\,, \tag{F.23}$$

where $\boldsymbol{x} \in \mathbb{R}^{n_x}$ is the system's state, $\boldsymbol{u} \in \mathbb{R}^{n_u}$ is the input, and $\boldsymbol{y} \in \mathbb{R}^{n_y}$ is the measurement.

Observability of the discrete-time linear time-varying system defined in (F.22)–(F.23) is usually determined by studying the rank of either the observability Gramian or the observability matrix. The following theorem from [134] states a necessary and sufficient condition

for observability of linear time-varying systems through the l-step observability matrix.

Theorem F.1. *The discrete-time linear time-varying system defined in* (F.22)–(F.23) *is l-step observable if and only if the l-step observability matrix, defined as*

$$\boldsymbol{\mathcal{O}}(k, k+l) \triangleq \begin{bmatrix} \mathbf{H}(k) \\ \mathbf{H}(k+1)\,\boldsymbol{\Phi}(k+1,k) \\ \vdots \\ \mathbf{H}(k+l-1)\,\boldsymbol{\Phi}(k+l-1,k) \end{bmatrix} \tag{F.24}$$

is full rank, i.e., $\operatorname{rank}[\boldsymbol{\mathcal{O}}(k, k+l)] = n_x$. *The matrix function $\boldsymbol{\Phi}(k, j)$ is the discrete-time state transition matrix, which is defined as*

$$\boldsymbol{\Phi}(k, j) \triangleq \begin{cases} \mathbf{F}(k-1)\,\mathbf{F}(k-2)\cdots\mathbf{F}(j), & k \geq j+1 \\ \mathbf{I}, & k = j. \end{cases}$$

Linear observability tools may be applied to nonlinear systems by linearizing the dynamics and measurements to obtain $\mathbf{F}(k)$, $\boldsymbol{\Gamma}(k)$, and $\mathbf{H}(k)$ [33]. The observability results in such case are only valid locally.

F.2 EKF Error Bounds

The following useful lemma from [135] establishes bounds on the Kalman filter's estimation error covariance.

Lemma F.1. *Consider the discrete-time linear time-varying stochastic system*

$$\boldsymbol{x}(k+1) = \mathbf{F}(k)\,\boldsymbol{x}(k) + \boldsymbol{\Gamma}(k)\,\boldsymbol{u}(k) + \boldsymbol{w}(k), \tag{F.25}$$

$$\boldsymbol{z}(k) = \mathbf{H}(k)\,\boldsymbol{x}(k) + \boldsymbol{v}(k), \tag{F.26}$$

where $\boldsymbol{x} \in \mathbb{R}^{n_x}$ *is the system's state,* $\boldsymbol{u} \in \mathbb{R}^{n_u}$ *is the input,* $\boldsymbol{w} \in \mathbb{R}^{n_x}$ *is a zero-mean white sequence with covariance* $\mathbf{Q}(k)$*,* $\boldsymbol{z} \in \mathbb{R}^{n_z}$ *is the measurement, and* $\boldsymbol{v} \in \mathbb{R}^{n_z}$ *is a zero-mean white sequence with covariance* $\mathbf{R}(k)$*. Assume that* $\boldsymbol{w}(k)$ *and* $\boldsymbol{v}(j)$ *are uncorrelated for all* k *and* j*. Let* $\mathbf{P}(k+1|k)$ *be a solution to the matrix Riccati difference equation in the Kalman filter estimating the state of system* (F.25)–(F.26) *given by*

$$\begin{aligned}\mathbf{P}(k+1|k) = \mathbf{F}(k) \big\{ &\mathbf{P}(k|k-1) - \mathbf{P}(k|k-1)\mathbf{H}^{\mathsf{T}}(k) \cdot \\ &\big[\mathbf{H}(k)\mathbf{P}(k|k-1)\mathbf{H}^{\mathsf{T}}(k) + \mathbf{R}(k)\big]^{-1} \cdot \\ &\mathbf{H}(k)\mathbf{P}(k|k-1)\big\} \mathbf{F}^{\mathsf{T}}(k) + \mathbf{Q}(k).\end{aligned}$$

Let the following hold:

1. *There are real numbers* $\underline{q}, \bar{q}, \underline{r}, \bar{r} > 0$ *such that* $\mathbf{Q}(k)$ *and* $\mathbf{R}(k)$ *are bounded by*

$$\underline{q}\mathbf{I} \preceq \mathbf{Q}(k) \preceq \bar{q}\mathbf{I}, \qquad \underline{r}\mathbf{I} \preceq \mathbf{R}(k) \preceq \bar{r}\mathbf{I}.$$

2. *The matrices* $\mathbf{F}(k)$ *and* $\mathbf{H}(k)$ *satisfy the uniform observability condition.*

3. *The initial condition* $\mathbf{P}(1|0)$ *of the matrix Riccati difference equation in the Kalman filter is positive definite.*

Then, there are real numbers $\underline{p}, \bar{p} > 0$ *such that* $\mathbf{P}(k+1|k)$ *is bounded via*

$$\underline{p}\mathbf{I} \preceq \mathbf{P}(k+1|k) \preceq \bar{p}\mathbf{I}, \qquad \forall\, k > 0.$$

Next, theoretical background on EKF estimation error bounds is provided. Consider the

discrete-time nonlinear stochastic system

$$\boldsymbol{x}(k+1) = \boldsymbol{f}\left[\boldsymbol{x}(k), \boldsymbol{u}(k)\right] + \boldsymbol{w}(k) \tag{F.27}$$

$$\boldsymbol{z}(k) = \boldsymbol{h}\left[\boldsymbol{x}(k)\right] + \boldsymbol{v}(k), \tag{F.28}$$

where $\boldsymbol{x} \in \mathbb{R}^{n_x}$ is the system's state, $\boldsymbol{u} \in \mathbb{R}^{n_u}$ is the input, $\boldsymbol{w} \in \mathbb{R}^{n_x}$ is a zero-mean white sequence with covariance $\mathbf{Q}(k)$, $\boldsymbol{z} \in \mathbb{R}^{n_z}$ is the measurement, and $\boldsymbol{v} \in \mathbb{R}^{n_z}$ is a zero-mean white sequence with covariance $\mathbf{R}(k)$.

An EKF is employed to estimate $\boldsymbol{x}(k)$. Define the EKF linearization errors

$$\begin{aligned}\boldsymbol{\varphi}(k) \triangleq\ & \boldsymbol{f}\left[\boldsymbol{x}(k), \boldsymbol{u}(k)\right] - \boldsymbol{f}\left[\hat{\boldsymbol{x}}(k|k), \boldsymbol{u}(k)\right] \\ & - \mathbf{F}(k)\left[\boldsymbol{x}(k) - \hat{\boldsymbol{x}}(k|k)\right]\end{aligned} \tag{F.29}$$

$$\begin{aligned}\boldsymbol{\chi}(k) \triangleq\ & \boldsymbol{h}\left[\boldsymbol{x}(k)\right] - \boldsymbol{h}\left[\hat{\boldsymbol{x}}(k+1|k)\right] \\ & - \mathbf{H}(k)\left[\boldsymbol{x}(k) - \hat{\boldsymbol{x}}(k+1|k)\right],\end{aligned} \tag{F.30}$$

where $\mathbf{F}(k)$ and $\mathbf{H}(k)$ are the dynamics and observation Jacobians, respectively, evaluated at $\hat{\boldsymbol{x}}(k|k)$ and $\hat{\boldsymbol{x}}(k+1|k)$, respectively. The main theorem from [117] that establishes conditions for the boundedness of $\tilde{\boldsymbol{x}}(k|k)$ is stated.

Theorem F.2. *Consider the system defined in* (F.27)–(F.28) *and consider an EKF estimating its state vector. Moreover, let the following assumptions hold*

1. *There are positive real numbers* $\bar{f}, \bar{h}, \underline{p}, \bar{p}, \underline{q}, \underline{r} > 0$ *such that the following bounds hold*

for every $k > 0$

$$\|\mathbf{F}(k)\| \leq \bar{f} \tag{F.31}$$

$$\|\mathbf{H}(k)\| \leq \bar{h} \tag{F.32}$$

$$\underline{p}\mathbf{I} \preceq \mathbf{P}(k+1|k) \preceq \bar{p}\mathbf{I} \tag{F.33}$$

$$\underline{q}\mathbf{I} \preceq \mathbf{Q}(k) \tag{F.34}$$

$$\underline{r}\mathbf{I} \preceq \mathbf{R}(k). \tag{F.35}$$

2. *The matrix* $\mathbf{F}(k)$ *is nonsingular for every* $k > 0$.

3. *There are positive real numbers* $\epsilon_\varphi, \epsilon_\chi, \kappa_\varphi, \kappa_\chi > 0$ *such that the nonlinear functions* $\boldsymbol{\varphi}(k)$ *and* $\boldsymbol{\chi}(k)$ *are bounded via*

$$\|\boldsymbol{\varphi}(k)\| \leq \kappa_\varphi \|\tilde{\boldsymbol{x}}(k|k)\|^2 \tag{F.36}$$

$$\|\boldsymbol{\chi}(k)\| \leq \kappa_\chi \|\tilde{\boldsymbol{x}}(k|k)\|^2, \tag{F.37}$$

with $\|\tilde{\boldsymbol{x}}(k|k)\| \leq \epsilon_\varphi$ *and* $\|\tilde{\boldsymbol{x}}(k|k)\| \leq \epsilon_\chi$.

Then, the estimation error $\tilde{\boldsymbol{x}}(k|k)$ *is exponentially bounded in mean square and bounded with probability one as per Definitions 6.3.1 and 6.3.2, respectively, provided that (i) the initial estimation error satisfies*

$$\|\tilde{\boldsymbol{x}}(1|1)\| \leq \epsilon \tag{F.38}$$

and (ii) the covariance matrices of the noise terms are bounded via

$$\mathbf{Q}(k) \preceq \delta\mathbf{I}, \quad \mathbf{R}(k) \preceq \delta\mathbf{I}, \tag{F.39}$$

for some $\epsilon, \delta > 0$.

Bibliography

[1] J. Morales and Z. Kassas, "Optimal collaborative mapping of terrestrial transmitters: receiver placement and performance characterization," *IEEE Transactions on Aerospace and Electronic Systems*, vol. 54, no. 2, pp. 992–1007, April 2018.

[2] 3GPP2, "Physical layer standard for cdma2000 spread spectrum systems (C.S0002-E)," 3rd Generation Partnership Project 2 (3GPP2), TS C.S0002-E, June 2011.

[3] G. Seco-Granados, J. Lopez-Salcedo, D. Jimenez-Banos, and G. Lopez-Risueno, "Challenges in indoor global navigation satellite systems: unveiling its core features in signal processing," *IEEE Signal Processing Magazine*, vol. 29, no. 2, pp. 108–131, March 2012.

[4] J. Grabowski, "Personal privacy jammers: locating Jersey PPDs jamming GBAS safety-of-life signals," *GPS World Magazine*, pp. 28–37, April 2012.

[5] C. Günther, "A survey of spoofing and counter-measures," *NAVIGATION, Journal of the Institute of Navigation*, vol. 61, no. 3, pp. 159–177, 2014.

[6] P. Misra and P. Enge, *Global Positioning System: Signals, Measurements, and Performance*, 2nd ed. Ganga-Jamuna Press, 2010.

[7] J. Seo, Y. Chen, D. De Lorenzo, S. Lo, P. Enge, D. Akos, and J. Lee, "A real-time capable software-defined receiver using GPU for adaptive anti-jam GPS sensors," *Sensors*, vol. 11, no. 9, pp. 8966–8991, September 2011.

[8] A. Kerns, D. Shepard, J. Bhatti, and T. Humphreys, "Unmanned aircraft capture and control via GPS spoofing," *Journal of Field Robotics*, vol. 31, no. 4, pp. 617–636, 2014.

[9] D. He, S. Chan, and M. Guizani, "Communication security of unmanned aerial vehicles," *IEEE Wireless Communications*, vol. 24, no. 4, pp. 134–139, August 2017.

[10] S. Saab and Z. Kassas, "Power matching approach for GPS coverage extension," *IEEE Transactions on Intelligent Transportation Systems*, vol. 7, no. 2, pp. 156–166, June 2006.

[11] F. Caron, M. Davy, E. Duflos, and P. Vanheeghe, "Particle filtering for multisensor data fusion with switching observation models: application to land vehicle positioning," *IEEE Transactions on Signal Processing*, vol. 55, no. 6, pp. 2703–2719, June 2007.

[12] Y. Wu, J. Wang, and D. Hu, "A new technique for INS/GNSS attitude and parameter estimation using online optimization," *IEEE Transactions on Signal Processing*, vol. 62, no. 10, pp. 2642–2655, May 2014.

[13] J. Raquet and R. Martin, "Non-GNSS radio frequency navigation," in *Proceedings of IEEE International Conference on Acoustics, Speech and Signal Processing*, March 2008, pp. 5308–5311.

[14] L. Merry, R. Faragher, and S. Schedin, "Comparison of opportunistic signals for localisation," in *Proceedings of IFAC Symposium on Intelligent Autonomous Vehicles*, September 2010, pp. 109–114.

[15] Z. Kassas, "Collaborative opportunistic navigation," *IEEE Aerospace and Electronic Systems Magazine*, vol. 28, no. 6, pp. 38–41, 2013.

[16] Z. Kassas, "Analysis and synthesis of collaborative opportunistic navigation systems," Ph.D. dissertation, The University of Texas at Austin, USA, 2014.

[17] J. McEllroy, "Navigation using signals of opportunity in the AM transmission band," Master's thesis, Air Force Institute of Technology, Wright-Patterson Air Force Base, Ohio, USA, 2006.

[18] S. Fang, J. Chen, H. Huang, and T. Lin, "Is FM a RF-based positioning solution in a metropolitan-scale environment? A probabilistic approach with radio measurements analysis," *IEEE Transactions on Broadcasting*, vol. 55, no. 3, pp. 577–588, September 2009.

[19] M. Joerger, L. Gratton, B. Pervan, and C. Cohen, "Analysis of Iridium-augmented GPS for floating carrier phase positioning," *NAVIGATION, Journal of the Institute of Navigation*, vol. 57, no. 2, pp. 137–160, 2010.

[20] K. Pesyna, Z. Kassas, and T. Humphreys, "Constructing a continuous phase time history from TDMA signals for opportunistic navigation," in *Proceedings of IEEE/ION Position Location and Navigation Symposium*, April 2012, pp. 1209–1220.

[21] M. Rabinowitz and J. Spilker, Jr., "A new positioning system using television synchronization signals," *IEEE Transactions on Broadcasting*, vol. 51, no. 1, pp. 51–61, March 2005.

[22] P. Thevenon, S. Damien, O. Julien, C. Macabiau, M. Bousquet, L. Ries, and S. Corazza, "Positioning using mobile TV based on the DVB-SH standard," *NAVIGATION, Journal of the Institute of Navigation*, vol. 58, no. 2, pp. 71–90, 2011.

[23] R. Martin, C. Yan, H. Fan, and C. Rondeau, "Algorithms and bounds for distributed TDOA-based positioning using OFDM signals," *IEEE Transactions on Signal Processing*, vol. 59, no. 3, pp. 1255–1268, March 2011.

[24] I. Bilik, K. Adhikari, and J. R. Buck, "Shannon capacity bound on mobile station localization accuracy in urban environments," *IEEE Transactions on Signal Processing*, vol. 59, no. 12, pp. 6206–6216, December 2011.

[25] C. Yang, T. Nguyen, and E. Blasch, "Mobile positioning via fusion of mixed signals of opportunity," *IEEE Aerospace and Electronic Systems Magazine*, vol. 29, no. 4, pp. 34–46, April 2014.

[26] K. Shamaei, J. Khalife, and Z. Kassas, "Performance characterization of positioning in LTE systems," in *Proceedings of ION GNSS Conference*, September 2016, pp. 2262–2270.

[27] R. Faragher, C. Sarno, and M. Newman, "Opportunistic radio SLAM for indoor navigation using smartphone sensors," in *Proceedings of IEEE/ION Position Location and Navigation Symposium*, April 2012, pp. 120–128.

[28] J. Prieto, S. Mazuelas, A. Bahillo, P. Fernandez, R. Lorenzo, and E. Abril, "Adaptive data fusion for wireless localization in harsh environments," *IEEE Transactions on Signal Processing*, vol. 60, no. 4, pp. 1585–1596, April 2012.

[29] J. Khalife, Z. Kassas, and S. Saab, "Indoor localization based on floor plans and power maps: Non-line of sight to virtual line of sight," in *Proceedings of ION GNSS Conference*, September 2015, pp. 2291–2300.

[30] K. Pesyna, Z. Kassas, J. Bhatti, and T. Humphreys, "Tightly-coupled opportunistic navigation for deep urban and indoor positioning," in *Proceedings of ION GNSS Conference*, September 2011, pp. 3605–3617.

[31] K. Pesyna, K. Wesson, R. Heath, and T. Humphreys, "Extending the reach of GPS-assisted femtocell synchronization and localization through tightly-coupled opportunistic navigation," in *Proceedings of IEEE GLOBECOM Workshops*, December 2011, pp. 242–247.

[32] Z. Kassas and T. Humphreys, "Observability and estimability of collaborative opportunistic navigation with pseudorange measurements," in *Proceedings of ION GNSS Conference*, September 2012, pp. 621–630.

[33] Z. Kassas and T. Humphreys, "Observability analysis of collaborative opportunistic navigation with pseudorange measurements," *IEEE Transactions on Intelligent Transportation Systems*, vol. 15, no. 1, pp. 260–273, February 2014.

[34] Z. Kassas and T. Humphreys, "Motion planning for optimal information gathering in opportunistic navigation systems," in *Proceedings of AIAA Guidance, Navigation, and Control Conference*, August 2013, pp. 4551–4565.

[35] Z. Kassas and T. Humphreys, "Receding horizon trajectory optimization in opportunistic navigation environments," *IEEE Transactions on Aerospace and Electronic Systems*, vol. 51, no. 2, pp. 866–877, April 2015.

[36] Z. Kassas, A. Arapostathis, and T. Humphreys, "Greedy motion planning for simultaneous signal landscape mapping and receiver localization," *IEEE Journal of Selected Topics in Signal Processing*, vol. 9, no. 2, pp. 247–258, March 2015.

[37] Z. Kassas and T. Humphreys, "The price of anarchy in active signal landscape map building," in *Proceedings of IEEE Global Conference on Signal and Information Processing*, December 2013, pp. 165–168.

[38] E. Kaplan and C. Hegarty, *Understanding* GPS*: Principles and Applications*, 2nd ed. Artech House, 2005.

[39] TIA/EIA-95-B, "Mobile station-base station compatibility standard for dual-mode spread spectrum systems," October 1998.

[40] B. Horn. (2014) How to install a cellular repeater. [Online]. Available: http://people.csail.mit.edu/bkph/CellTracker

[41] Z. Kassas, V. Ghadiok, and T. Humphreys, "Adaptive estimation of signals of opportunity," in *Proceedings of ION GNSS Conference*, September 2014, pp. 1679–1689.

[42] D. Shin and T. Sung, "Comparisons of error characteristics between TOA and TDOA positioning," *IEEE Transactions on Aerospace and Electronic Systems*, vol. 38, no. 1, pp. 307–311, January 2002.

[43] L. Romero and J. Mason, "Geolocation using TOA, FOA, and altitude information at singular geometries," *IEEE Transactions on Aerospace and Electronic Systems*, vol. 51, no. 2, pp. 1069–1078, April 2015.

[44] N. Patwari, J. Ash, S. Kyperountas, A. Hero, R. Moses, and N. Correal, "Locating the nodes: cooperative localization in wireless sensor networks," *IEEE Signal Processing Magazine*, vol. 22, no. 4, pp. 54–69, July 2005.

[45] M. Bshara, U. Orguner, F. Gustafsson, and L. Van Biesen, "Robust tracking in cellular networks using HMM filters and cell-ID measurements," *IEEE Transactions on Vehicular Technology*, vol. 60, no. 3, pp. 1016–1024, March 2011.

[46] Z. Abu-Shaban, X. Zhou, and T. Abhayapala, "A novel TOA-based mobile localization technique under mixed LOS/NLOS conditions for cellular networks," *IEEE Transactions on Vehicular Technology*, vol. 65, no. 11, pp. 8841–8853, 2016.

[47] A. Tahat, G. Kaddoum, S. Yousefi, S. Valaee, and F. Gagnon, "A look at the recent wireless positioning techniques with a focus on algorithms for moving receivers," *IEEE Access*, vol. 4, pp. 6652–6680, 2016.

[48] 3GPP2, "Recommended minimum performance standards for cdma2000 spread spectrum base stations," 3rd Generation Partnership Project 2 (3GPP2), TS C.S0010-E, March 2014. [Online]. Available: http://www.arib.or.jp/english/html/overview/doc/STD-T64v7_00/Specification/ARIB_STD-T64-C.S0010-Ev2.0.pdf

[49] 3GPP, "Evolved universal terrestrial radio access (E-UTRA); requirements for support of radio resource management," 3rd Generation Partnership Project (3GPP), TS 36.133, April.

[50] J. Wennervirta and T. Wigren, "RTT positioning field performance," *IEEE Transactions on Vehicular Technology*, vol. 59, no. 7, pp. 3656–3661, September 2010.

[51] A. Yeredor, "On passive TDOA and FDOA localization using two sensors with no time or frequency synchronization," in *Proceedings of IEEE International Conference on Acoustics, Speech and Signal Processing*, May 2013, pp. 4066–4070.

[52] J. Barnes, A. Chi, R. Andrew, L. Cutler, D. Healey, D. Leeson, T. McGunigal, J. Mullen, W. Smith, R. Sydnor, R. Vessot, and G. Winkler, "Characterization of frequency stability," *IEEE Transactions on Instrumentation and Measurement*, vol. 20, no. 2, pp. 105–120, May 1971.

[53] J. Morales, P. Roysdon, and Z. Kassas, "Signals of opportunity aided inertial navigation," in *Proceedings of ION GNSS Conference*, September 2016, pp. 1492–1501.

[54] E. Kaplan and C. Hegarty, *Understanding* GPS/GNSS*: Principles and applications*, 3rd ed. Artech House, 2017.

[55] T. Humphreys, M. Psiaki, P. Kintner, and B. Ledvina, "GNSS receiver implementation on a DSP: Status, challenges, and prospects," in *Proceedings of ION GNSS Conference*, September 2006, pp. 1567–1575.

[56] M. Tsatsanis and Z. Xu, "Performance analysis of minimum variance CDMA receivers," *IEEE Transactions on Signal Processing*, vol. 46, no. 11, pp. 3014–3022, November 1998.

[57] Z. Xu, "Effects of imperfect blind channel estimation on performance of linear CDMA receivers," *IEEE Transactions on Signal Processing*, vol. 52, no. 10, pp. 2873–2884, October 2004.

[58] K. Zarifi and A. Gershman, "High SNR performance analysis of blind minimum output energy receivers for large DS-CDMA systems," *IEEE Transactions on Signal Processing*, vol. 56, no. 7, pp. 3248–3260, July 2008.

[59] I. Sharp, K. Yu, and Y. Guo, "GDOP analysis for positioning system design," *IEEE Transactions on Vehicular Technology*, vol. 58, no. 7, pp. 3371–3382, 2009.

[60] J. Perez-Ramirez, D. Borah, and D. Voelz, "Optimal 3-D landmark placement for vehicle localization using heterogeneous sensors," *IEEE Transactions on Vehicular Technology*, vol. 62, no. 7, pp. 2987–2999, September 2013.

[61] J. Kim and S. Sukkarieh, "Autonomous airborne navigation in unknown terrain environments," *IEEE Transactions on Aerospace and Electronic Systems*, vol. 40, no. 3, pp. 1031–1045, July 2004.

[62] K. Dogancay, "UAV path planning for passive emitter localization," *IEEE Transactions on Aerospace and Electronic Systems*, vol. 48, no. 2, pp. 1150–1166, April 2012.

[63] S. Monica and G. Ferrari, "UWB-based localization in large indoor scenarios: optimized placement of anchor nodes," *IEEE Transactions on Aerospace and Electronic Systems*, vol. 51, no. 2, pp. 987–999, April 2015.

[64] S. Martinez and F. Bullo, "Optimal sensor placement and motion coordination for target tracking," *Automatica*, vol. 42, no. 4, pp. 661–668, April 2006.

[65] K. Punithakumar, T. Kirubarajan, and M. Hernandez, "Multisensor deployment using PCRLBS, incorporating sensor deployment and motion uncertainties," *IEEE Transactions on Aerospace and Electronic Systems*, vol. 42, no. 4, pp. 1474–1485, October 2006.

[66] C. Yang, L. Kaplan, E. Blasch, and M. Bakich, "Optimal placement of heterogeneous sensors for targets with Gaussian priors," *IEEE Transactions on Aerospace and Electronic Systems*, vol. 49, no. 3, pp. 1637–1653, July 2013.

[67] F. Penna, M. Caceres, and H. Wymeersch, "Cramér-Rao bound for hybrid GNSS-terrestrial cooperative positioning," *IEEE Communications Letters*, vol. 14, no. 11, pp. 1005–1007, November 2010.

[68] J. Spilker, Jr., *Global Positioning System: Theory and Applications*. Washington, D.C.: American Institute of Aeronautics and Astronautics, 1996, ch. 5: Satellite Constellation and Geometric Dilution of Precision, pp. 177–208.

[69] N. Levanon, "Lowest GDOP in 2-D scenarios," *IEE Proceedings Radar, Sonar and Navigation*, vol. 147, no. 3, pp. 149–155, 2000.

[70] N. Blanco-Delgado and F. Nunes, "Satellite selection method for multi-constellation GNSS using convex geometry," *IEEE Transactions on Vehicular Technology*, vol. 59, no. 9, pp. 4289–4297, November 2010.

[71] R. Santerre, A. Geiger, and S. Banville, "Geometry of GPS dilution of precision: revisited," *Proceedings of the IEEE*, vol. 21, no. 4, pp. 1747–1763, October 2017.

[72] S. Xu and K. Dogancay, "Optimal sensor placement for 3-D angle-of-arrival target localization," *IEEE Transactions on Aerospace and Electronic Systems*, vol. 53, no. 3, pp. 1196–1211, June 2017.

[73] P. Massat and K. Rudnick, "Geometric formulas for dilution of precision calculations," *NAVIGATION, Journal of the Institute of Navigation*, vol. 37, no. 4, pp. 379–391, 1990.

[74] N. Blanco-Delgado, F. Nunes, and G. Seco-Granados, "Relation between GDOP and the geometry of the satellite constellation," in *International Conference on Localization and GNSS*, June 2011, pp. 175–180.

[75] J. Morales and Z. Kassas, "Optimal receiver placement for collaborative mapping of signals of opportunity," in *Proceedings of ION GNSS Conference*, September 2015, pp. 2362–2368.

[76] M. Haenggi, J. Andrews, F. Baccelli, O. Dousse, and M. Franceschetti, "Stochastic geometry and random graphs for the analysis and design of wireless networks," *IEEE Journal on Selected Areas in Communications*, vol. 27, no. 7, pp. 1029–1046, September 2009.

[77] J. Andrews, F. Baccelli, and R. Ganti, "A tractable approach to coverage and rate in cellular networks," *IEEE Transactions on Communications*, vol. 59, no. 11, pp. 3122–3134, November 2011.

[78] J. Schloemann, H. Dhillon, and R. Buehrer, "Toward a tractable analysis of localization fundamentals in cellular networks," *IEEE Transactions on Wireless Communications*, vol. 15, no. 3, pp. 1768–1782, March 2016.

[79] S. Aditya, A. Molisch, and H. Behairy, "A survey on the impact of multipath on wideband time-of-arrival based localization," *Proceedings of the IEEE*, vol. 106, no. 7, pp. 1183–1203, July 2018.

[80] C. O'Lone, H. Dhillon, and R. Buehrer, "A statistical characterization of localization performance in wireless networks," *IEEE Transactions on Wireless Communications*, vol. 17, no. 9, pp. 5841–5856, September 2018.

[81] S. Aditya, H. Dhillon, A. Molisch, R. Buehrer, and H. Behairy, "Characterizing the impact of SNR heterogeneity on time-of-arrival-based localization outage probability," *IEEE Transactions on Wireless Communications*, vol. 18, no. 1, pp. 637–649, January 2019.

[82] J. Khalife, K. Shamaei, and Z. Kassas, "A software-defined receiver architecture for cellular CDMA-based navigation," in *Proceedings of IEEE/ION Position, Location, and Navigation Symposium*, April 2016, pp. 816–826.

[83] J. Khalife and Z. Kassas, "Characterization of sector clock biases in cellular CDMA systems," in *Proceedings of ION GNSS Conference*, September 2016, pp. 2281–2285.

[84] J. Khalife and Z. Kassas, "Evaluation of relative clock stability in cellular networks," in *Proceedings of ION GNSS Conference*, September 2017, pp. 2554–2559.

[85] J. Khalife, K. Shamaei, and Z. Kassas, "Navigation with cellular CDMA signals – part I: Signal modeling and software-defined receiver design," *IEEE Transactions on Signal Processing*, vol. 66, no. 8, pp. 2191–2203, April 2018.

[86] J. Lee and L. Miller, *CDMA Systems Engineering Handbook*, 1st ed. Norwood, MA, USA: Artech House, 1998.

[87] W. Lee, "Overview of cellular CDMA," *IEEE Transactions on Vehicular Technology*, vol. 40, no. 2, pp. 291–302, May 1991.

[88] R. Vaughn, N. Scott, and D. White, "The theory of bandpass sampling," *IEEE Transactions on Signal Processing*, vol. 39, no. 9, pp. 1973–1984, September 1991.

[89] 3GPP2, "Upper layer (layer 3) signaling standard for cdma2000 spread spectrum systems," 3rd Generation Partnership Project 2 (3GPP2), TS C.S0005-F v2.0, May 2014.

[90] 3GPP2, "Medium access control (MAC) standard for cdma2000 spread spectrum systems," 3rd Generation Partnership Project 2 (3GPP2), TS C.S0003-F v2.0, May 2014.

[91] D. van Nee and A. Coenen, "New fast GPS code-acquisition technique using FFT," *Electronics Letters*, vol. 27, no. 2, pp. 158–160, January 1991.

[92] A. van Dierendonck, P. Fenton, and T. Ford, "Theory and performance of narrow correlator spacing in a GPS receiver," *NAVIGATION, Journal of the Institute of Navigation*, vol. 39, no. 3, pp. 265–283, September 1992.

[93] L. Ljung, *System identification: Theory for the user*, 2nd ed. Prentice Hall PTR, 1999.

[94] J. Proakis and D. Manolakis, *Digital signal processing*. Prentice-Hall, Upper Saddle River, NJ, 1996.

[95] R. Norton, "The double exponential distribution: Using calculus to find a maximum likelihood estimator," *The American Statistician*, vol. 38, no. 2, pp. 135–136, May 1984.

[96] T. Humphreys, J. Bhatti, T. Pany, B. Ledvina, and B. O'Hanlon, "Exploiting multicore technology in software-defined GNSS receivers," in *Proceedings of ION GNSS Conference*, September 2009, pp. 326–338.

[97] J. Khalife and Z. Kassas, "Navigation with cellular CDMA signals – part II: Performance analysis and experimental results," *IEEE Transactions on Signal Processing*, vol. 66, no. 8, pp. 2204–2218, April 2018.

[98] J. Khalife and Z. Kassas, "Modeling and analysis of sector clock bias mismatch for navigation with cellular signals," in *Proceedings of American Control Conference*, May 2017, pp. 3573–3578.

[99] D. Uciński, *Optimal Measurement Methods for Distributed Parameter System Identification*. CRC Press, 2005.

[100] A. Thompson, J. Moran, and G. Swenson, *Interferometry and Synthesis in Radio Astronomy*, 2nd ed. John Wiley & Sons, 2001.

[101] Y. Bar-Shalom, X. Li, and T. Kirubarajan, *Estimation with Applications to Tracking and Navigation*. New York, NY: John Wiley & Sons, 2002.

[102] J. Khalife and Z. Kassas, "Precise UAV navigation with cellular carrier phase measurements," in *Proceedings of IEEE/ION Position, Location, and Navigation Symposium*, April 2018, pp. 978–989.

[103] J. Khalife, K. Shamaei, S. Bhattacharya, and Z. Kassas, "Centimeter-accurate UAV navigation with cellular signals," in *Proceedings of ION GNSS Conference*, September 2018, pp. 2321–2331.

[104] X. Li and V. Jilkov, "Survey of maneuvering target tracking. Part I: Dynamic models," *IEEE Transactions on Aerospace and Electronic Systems*, vol. 39, no. 4, pp. 1333–1364, 2003.

[105] 3GPP, "Evolved universal terrestrial radio access (E-UTRA); physical channels and modulation," 3rd Generation Partnership Project (3GPP), TS 36.211, January 2011. [Online]. Available: http://www.3gpp.org/ftp/Specs/html-info/36211.htm

[106] K. Shamaei, J. Khalife, S. Bhattacharya, and Z. Kassas, "Computationally efficient receiver design for mitigating multipath for positioning with LTE signals," in *Proceedings of ION GNSS Conference*, September 2017, pp. 3751–3760.

[107] K. Shamaei, J. Khalife, and Z. Kassas, "Exploiting LTE signals for navigation: Theory to implementation," *IEEE Transactions on Wireless Communications*, vol. 17, no. 4, pp. 2173–2189, April 2018.

[108] J. del Peral-Rosado, J. Lopez-Salcedo, G. Seco-Granados, F. Zanier, P. Crosta, R. Ioannides, and M. Crisci, "Software-defined radio LTE positioning receiver towards future hybrid localization systems," in *Proceedings of International Communication Satellite Systems Conference*, October 2013, pp. 14–17.

[109] B. Pervan and B. Parkinson, "Cycle ambiguity estimation for aircraft precision landing using the Global Positioning System," *Journal of Guidance, Control, and Dynamics*, vol. 20, no. 4, pp. 681–689, July–August 1997.

[110] J. Mendel, *Lessons in Estimation Theory for Signal Processing, Communications, and Control*, 2nd ed. Prentice Hall, 1995.

[111] N. Bulusu, J. Heidemann, and D. Estrin, "GPS-less low-cost outdoor localization for very small devices," *IEEE Personal Communications*, vol. 7, no. 5, pp. 28–34, October 2000.

[112] P. J. G. Teunissen, "The least-squares ambiguity decorrelation adjustment: a method for fast gps integer ambiguity estimation," *Journal of Geodesy*, vol. 70, no. 1, pp. 65–82, November 1995.

[113] S. Verhagen and B. Li, "LAMBDA software package - MATLAB implementation, version 3.0. Delft Uuniversity of Technology," 2012.

[114] A. Van Dierondonck, *Global Positioning System: Theory and Applications*. Washington D.C.: American Institute of Aeronautics and Astronautics, 1996, ch. 8: GPS Receivers, pp. 329–408.

[115] J. Khalife and Z. Kassas, "Opportunistic UAV navigation with carrier phase measurements from asynchronous cellular signals," *IEEE Transactions on Aerospace and Electronic Systems*, 2019, accepted.

[116] R. Brown and P. Hwang, *Introduction to Random Signals and Applied Kalman Filtering*, 3rd ed. John Wiley & Sons, 2002.

[117] K. Reif, S. Gunther, E. Yaz, and R. Unbehauen, "Stochastic stability of the discrete-time extended Kalman filter," *IEEE Transactions on Automatic Control*, vol. 44, no. 4, pp. 714–728, April 1999.

[118] T. Song and J. Speyer, "A stochastic analysis of a modified gain extended Kalman filter with applications to estimation with bearings only measurements," *IEEE Transactions on Automatic Control*, vol. 30, no. 10, pp. 940–949, October 1985.

[119] M. Yeddanapudi, Y. Bar-Shalom, and K. Pattipati, "IMM estimation for multitarget-multisensor air traffic surveillance," *Proceedings of the IEEE*, vol. 85, no. 1, pp. 80–96, January 1997.

[120] P. Hanlon and P. Maybeck, "Multiple-model adaptive estimation using a residual correlation Kalman filter bank," *IEEE Transactions on Aerospace and Electronic Systems*, vol. 36, no. 2, pp. 393–406, April 2000.

[121] Z. Kowalczuk and M. Sankowski, "Soft- and hard-decision multiple-model estimators for air traffic control," *IEEE Transactions on Aerospace and Electronic Systems*, vol. 46, no. 4, pp. 2056–2065, October 2010.

[122] S. Stein and R. Filler, "Kalman filter analysis for real time applications of clocks and oscillators," in *Proceedings of the Frequency Control Symposium*, June 1988, pp. 447–452.

[123] C. Zucca and P. Tavella, "The clock model and its relationship with the Allan and related variances," *IEEE Transactions on Ultrasonics, Ferroelectrics, and Frequency Control*, vol. 52, no. 2, pp. 289–296, February 2005.

[124] K. Wesson, K. Pesyna, J. Bhatti, and T. Humphreys, "Opportunistic frequency stability transfer for extending the coherence time of GNSS receiver clocks," in *Proceedings of ION GNSS Conference*, September 2010, pp. 2959–2968.

[125] J. Morales and Z. Kassas, "Information fusion strategies for collaborative radio SLAM," in *Proceedings of IEEE/ION Position Location and Navigation Symposium*, April 2018, pp. 1445–1454.

[126] J. Khalife and Z. Kassas, "Optimal sensor placement for dilution of precision minimization via quadratically constrained fractional programming," *IEEE Transactions on Aerospace and Electronic Systems*, vol. 55, no. 4, pp. 2086–2096, August 2019.

[127] J. Morales, J. Khalife, and Z. Kassas, "GNSS vertical dilution of precision reduction using terrestrial signals of opportunity," in *Proceedings of ION International Technical Meeting Conference*, January 2016, pp. 664–669.

[128] J. Morales, J. Khalife, and Z. Kassas, "Opportunity for accuracy," *GPS World Magazine*, vol. 27, no. 3, pp. 22–29, March 2016.

[129] Z. Kassas, J. Khalife, K. Shamaei, and J. Morales, "I hear, therefore I know where I am: Compensating for GNSS limitations with cellular signals," *IEEE Signal Processing Magazine*, pp. 111–124, September 2017.

[130] A. Beck, A. Ben-Tal, and M. Teboulle, "Finding a global optimal solution for a quadratically constrained fractional quadratic problem with applications to the regularized total least squares," *SIAM Journal on Matrix Analyis and Applications*, vol. 28, no. 2, pp. 425–445, May 2006.

[131] Z. Kassas and T. Humphreys, "Observability analysis of opportunistic navigation with pseudorange measurements," in *Proceedings of AIAA Guidance, Navigation, and Control Conference*, vol. 1, August 2012, pp. 1209–1220.

[132] W. Dinkelbach, "On nonlinear fractional programming," *Management Science*, vol. 13, no. 7, pp. 492–498, March 1967.

[133] Y. Shen and M. Win, "Fundamental limits of wideband localization–Part I: A general framework," *IEEE Transactions on Information Theory*, vol. 56, no. 10, pp. 4956–4980, October 2010.

[134] W. Rugh, *Linear System Theory*, 2nd ed. Upper Saddle River, NJ: Prentice Hall, 1996.

[135] B. Anderson and J. Moore, "Detectability and stabilisability of time-varying discrete-time linear systems," *SIAM Journal on Control and Optimiaztion*, vol. 19, pp. 20–32, 1981.